



DEEP EMISSION STUDIES OF HIGH REDSHIFT ABSORPTION SELECTED GALAXIES

Probing the Galaxy Population With Beacons From Afar

Dissertation submitted for the degree of

PHILOSOPHIÆ DOCTOR

to the PhD School of The Faculty of Science, University of Copenhagen

on May 31st 2019, by

Nils Henrik Pehlivan Rhodin

Principal Advisor:

Assoc. Prof. Lise Bech Christensen

Committee:

Dr. Valentina D'Odorico

National Institute of Astrophysics, Italy

Prof. Tom Theuns

Durham University, United Kingdom

Assoc. Prof. Darach Jafar Watson

University of Copenhagen, Denmark

DEEP EMISSION STUDIES OF HIGH REDSHIFT ABSORPTION SELECTED GALAXIES

Probing the Galaxy Population With Beacons From Afar

...there is a grandeur and majesty in the concept [of island universes] and an agreement with the general cosmical continuity expected on philosophical grounds, which is both inspiring and alluring. Few greater concepts have ever been formed in the mind of thinking man than this one, namely, - that we, the microbic inhabitants of a minor satellite of one of the millions of suns which form our galaxy, may look out beyond its confines and behold other similar galaxies, tens of thousands of light-years in diameter, each composed, like ours, of a thousand million or more suns, and that, in so doing, we are penetrating the greater cosmos to distances of from half a million to a hundred million light years.

- H. D. Curtis, 1924

ABSTRACT

In its heart, astronomy is an *empirical* science: what we see is what we get. This detection-driven approach gives us remarkable insights on the nature and contents of the Universe that we inhabit, including galaxies. However, these results often rely on observations that select on luminosity, and conclusions are therefore biased to the *tip of the iceberg*. This effect becomes increasingly severe when we attempt to understand the earliest stages of galaxy formation in the young, high redshift Universe.

This thesis attempts to mitigate these shortcomings by studying galaxies with a complementary technique, utilising a gas cross-section selection. This is made possible by favourable chance alignments in nature which occur when galaxies intervene the line of sight towards distant beacons of light; quasars. For gaseous galaxies, these configurations imprint characteristic neutral hydrogen (H I) Lyman alpha absorption features in quasar continua, and thereby provide a tell-tale for galaxy position and redshift. With targeted follow-up studies, the galaxies responsible for the absorption can be studied in great detail, utilising the complementary powers of imaging and absorption- and emission spectroscopy.

Part I provides context to the research. Chapter 1 presents a brief overview of galaxy formation and evolution, mechanisms regulating galaxy growth, and how such objects are studied to large redshifts. Chapter 2 substantiates the notion that strong H I absorbers probe galaxy environments, before delving into a discussion on how the field has progressed in recent years, the original research contribution of this thesis, and future outlooks. Part II presents the three first author publications which form the base to this thesis, attached in journal format.

In Paper I, I used ground-based long-slit spectroscopy to follow-up and confirm ten candidate absorbing galaxies at redshift $z \sim 0.7$. By combining pre-existing photometry of the quasar fields with my spectroscopic redshifts, I derived stellar masses and show that absorbing galaxies fall on predicted mass-metallicity relations, but systematically display sub-main-sequence star formation. In Paper II, I confronted state-of-the-art cosmological zoom-in simulations of a Milky Way mass galaxy with a recent compilation of spectroscopically confirmed galaxies harbouring strong H I absorbers. The simulation captures observed distributions of projected separations between absorbers and their galaxy counterparts. I show that both extended H I discs and haloes play a role at all redshifts. The recovery of absorbers at high impact parameters is only made possible by efficient feedback and high numerical resolution, which reveals that such line-of-sights are associated with dwarf satellites in the main halo, stripped metal-rich gas and outflows. In Paper III, I present the results of a photometric follow-up of ten spectroscopically confirmed absorbing galaxies at a complementary redshift $z \sim 2 - 3$. Utilising the exquisite spatial resolution reached with the Hubble Space Telescope, this paper presents the first

systematic morphological characterisation of absorbing galaxies at high redshifts. Combined with stellar masses and a heterogeneous set of star formation rate indicators, I show that the absorbing galaxies are consistent with the low-mass end of late-type star-forming galaxy populations at high-redshifts.

In summary, the results from observations and simulations presented in this thesis support the idea that strong H I absorbers probe neutral gas across galaxy environments. By contributing to the detection and characterisation of these objects in emission, I have helped the field mature and to undergo a transition to a stage where the properties of absorbing galaxies can directly be compared with standard luminosity selected galaxy samples.

RESUMÉ PÅ DANSK

Astronomy er i sin helt basale grundform en empirisk videnskab: vores viden bygger på det vi ser. Denne observationsdrevne tilgang har givet os stor indsigt i vores univers og dets indhold, blandt andet dets galakser. Desværre betyder dette også, at vores viden er baseret på observationer af de stærkest lysende objekter, som kun udgør en lille brøkdel af hele populationen. Denne effekt har specielt stor betydning, når vi prøver at forstå udviklingen af de første galakser, dannet helt tilbage i universets ungdom.

Målet med denne afhandling er at overkomme dette bias ved brug af en anderledes teknik, hvor man benytter observationer baseret på gas tværsnit. Dette opstår når en galakse tilfældigvis befinder sig foran i lyskeglen fra et af universets fjerneste og stærkeste lysende objekter, kvasarer. Den neutrale hydrogen fra den gasfyldte galakse i forgrunden, vil hermed danne en karakteristisk Lyman alpha (H I) absorptionslinje i kvasarens kontinuums spektrum, som kan fortælle os noget om galaksens egen position og rødforskydning. Ved målrettet at observere kvasarer med denne slags absorptionslinjer, kan man lave detaljerede studier af disse galakser ved at kombinere resultater fra billedanalyse og absorptions- og emissionspektroskopi.

I første del af denne afhandling beskrives konteksten for undersøgelsen. I kapitel 1 præsenteres læseren kort for historien om galaksers dannelse og udvikling, hvilke mekanismer der har indflydelse på deres vækst, og hvordan disse objekter indtil videre er blevet studeret ved høj rødforskydning. I kapitel 2 underbygges antagelsen om, at observationer af stærke HI absorptionslinjer kan bruges til at beskrive galakser i forgrunden. Derefter følger en uddybende diskussion om, hvordan denne type observationer er blevet udbygget de sidste par år, samt hvilke bidrag der er produceret i denne afhandling, og til sidst en vurdering af fremtidsudsigterne. Del 2 indeholder også de tre første-forfatter artikler, som udgør hoveddelen af denne afhandling.

I den første artikel brugte jeg jord-baseret spalte-spektroskopi til at følge op på og bekræfte ti kandidater af absorberende forgrundsgalakser med rødforskydning $z \sim 0.7$. Ved at kombinere eksisterende fotometri af kvasarfelterne og mine beregninger af rødforskydningen, udledte jeg stjerne massen i galakserne og kunne derpå vise, at disse absorberende galakser passer med den nuværende teori, om forholdet mellem deres masse og metalitet, samt at de har en systematisk lavere rate af stjernedannelse. I den anden artikel sammenlignede jeg state-of-the-art kosmologiske zoom-in computersimuleringer af en Mælkevejslignende galakse, med en nylig samling af spektroskopisk bekræftede galakser med stærk hydrogen absorption. Simuleringen indfanger de observerede fordelinger af projicerede afstande, mellem hydrogen absorptionen og den galakse der forårsager den. Jeg viser, at både den udbredte skive af H I og haloen, spiller en rolle ved alle rødforskydninger. Opdagelsen af H I absorption ved store

projicerede afstande er kun muliggjort af den effektive feedback og høje numeriske opløsning, hvilket viser at sådanne sigtelinjer er forbundet med dværggalakser i den centrale halo, berøvet for metal-rig gas og påvirket af udstrømmende gas. I artikel tre, præsenterer jeg den fotometriske opfølgning af ti absorberende galakser, spektroskopisk bekræftet til at ligge mellem rødforskydning 2 og 3. Ved at udnytte den udsøgte rumlige opløsning som Hubble-teleskopet leverer, præsenterer denne artikel den første systematiske morfologiske karakterisering af sådanne galakser ved høj rødforskydning. Ved at kombinere stjernemasser og forskellige stjernedannelsesindikatorer, viser jeg, at de absorberende galakser er konsistente med den lav-masse del af spiralgalakse populationen, som den ser ud ved høj rødforskydning.

Resultaterne fra både observationerne og simuleringerne der er blevet præsenteret i denne afhandling støtter den ide, at stærk absorption fra H I er et direkte tegn på den neutrale gas, på tværs af galaksemiljøer. Ved at detektere og karakterisere disse objekter via emission, har jeg hjulpet med at modne feltet til et stadie hvor vi endelig kan sammenligne egenskaberne af disse galakser direkte med de sædvanligvis luminositetsudvalgte galakser.

ACKNOWLEDGEMENTS

Many deserve my sincerest gratitudes. Lise Christensen, for opportunity, guidance and support. You gave me the freedom to explore the depths of the data. For that I am grateful. Oscar Agertz, for inspiring science and for making cosmic simulations a little less frightening. Palle Møller, for unparalleled directness; you were always my hardest critic. Johan Fynbo, for providing elegant solutions to complex problems, and for granting me the opportunity to observe with the *NOT* and assist you during the observing school on La Palma. Göran Östlin and the Galaxy Group at Stockholm University for hosting me for my stay abroad. Marianne Vestergaard for always providing useful feedback. To all friends and colleagues in the various constellations of Dark Cosmology Centre, DARK and DAWN, for a wonderful, friendly work atmosphere. My family, for listening to endless problems and for your support. Above all, my wife Aslı for believing in me, always.

LIST OF PUBLICATIONS

This thesis is based on the following three first-author publications:

I **Stellar masses, metallicity gradients, and suppressed star formation revealed in a new sample of absorption selected galaxies**

N. H. P. Rhodin, L. Christensen, P. Møller, T. Zafar, and J. P. U. Fynbo (2018),
Astronomy & Astrophysics, vol. 618, A129 (20 pp.)

II **The nature of strong H I absorbers probed by cosmological simulations: satellite accretion and outflows**

N. H. P. Rhodin, O. Agertz, L. Christensen, F. Renaud and J. P. U. Fynbo (2019),
Monthly Notices of the Royal Astronomical Society, *accepted for publication*

III **Absorption-selected galaxies trace the low-mass, late-type, star-forming population at $z \sim 2 - 3$**

N. H. P. Rhodin, J. -K. Krogager, L. Christensen, F. Valentino, K. E. Heintz, P. Møller, T. Zafar, and J. P. U. Fynbo (2019), The Astrophysical Journal, *in manuscript form*

Publications not included in this thesis:

I Testing strong line metallicity diagnostics at $z \sim 2$

V. Patrício, L. Christensen, **H. Rhodin**, R. Cañameras, and M. A. Lara-López (2018),
Monthly Notices of the Royal Astronomical Society, vol. 481, 3520 (14 pp.)

II ALMA observations of a metal-rich damped Ly α absorber at $z = 2.5832$: evidence for strong galactic winds in a galaxy group

J. P. U. Fynbo, K. E. Heintz, M. Neeleman, L. Christensen, M. Dessauges-Zavadsky,
N. Kanekar, P. Møller, J. X. Prochaska, **N. H. P. Rhodin**, and M. Zwaan (2018),
Monthly Notices of the Royal Astronomical Society, vol. 479, 2126 (7 pp.)

III Massive, Absorption-selected Galaxies at Intermediate Redshifts

N. Kanekar, J. X. Prochaska, L. Christensen, **N. H. P. Rhodin**, M. Neeleman, M. A. Zwaan,
P. Møller, M. Dessauges-Zavadsky, J. P. U. Fynbo, and T. Zafar (2018),
The Astrophysical Journal Letters, vol. 856, L23 (6 pp.)

IV ALMA + VLT observations of a damped Lyman- α absorbing galaxy: massive, wide CO emission, gas-rich but with very low SFR

P. Møller, L. Christensen, M. A. Zwaan, N. Kanekar, J. X. Prochaska, **N. H. P. Rhodin**,
M. Dessauges-Zavadsky, J. P. U. Fynbo, M. Neeleman, and T. Zafar (2018),
Monthly Notices of the Royal Astronomical Society, vol. 474, 4039 (17 pp.)

CONTENTS

Abstract	v
Resumé på Dansk	vii
Acknowledgements	ix
List of Publications	x
Contents	xii
I RESEARCH CONTEXT	1
1 Galaxies	3
1.1 A Standard Framework	3
1.2 Galaxy Formation and Evolution	4
1.3 High- z Galaxy Populations	9
2 Quasar Absorbers	12
2.1 Quasars as Cosmic Beacons of Light	12
2.2 Intervening Clouds of Neutral Hydrogen	15
2.3 An inferred galaxy connection	19
2.4 Absorption selected galaxies	24
2.5 Research Summary	27
2.6 Conclusions and Future Outlooks	29
Bibliography	31
II RESEARCH PAPERS	39
Paper I	41
Paper II	63
Paper III	79

PART I
RESEARCH CONTEXT

1

GALAXIES

Galaxies are complicated systems, governed by diverse processes that act on a range of physical scales. This Chapter presents a brief overview of fundamental concepts, with emphasis on the aspects required to give context to the galaxy population probed by damped Ly- α absorbers (DLAs) and sub-DLAs in quasar spectra. Section 1.1 outlines the current framework of cosmic structure formation in a Λ CDM Universe. Section 1.2 introduces the census on galaxy formation and evolution. Finally, Section 1.3 focuses on high redshift galaxy populations and techniques for detecting them. This provides a baseline for the discussions pursued in Chapter 2, which treat absorption selected galaxies that are the focal point of this thesis.

1.1 A Standard Framework

The physics of galaxies connects the Bohr radius, the natural length scale of the atom at $\sim 10^{-11}$ m, to the overwhelming vastness of cosmic filaments spanning scales of $\sim 10^{25}$ m. The current paradigm of galaxy formation is therefore confronted with the tremendous task of building a coherent model that bridges ~ 36 orders of magnitude in length, capable of describing the ~ 13.8 billion years of cosmic history that our universe has undergone.

One of the greatest scientific achievements of the past century, was to reconcile a growing body of observational data into a standard cosmology: that of a flat, homogenous, isotropic Universe on large scales (e.g. Hogg et al. 2005), initially in a state of extreme smoothness as revealed through the uniformity of the cosmic microwave background (CMB, Penzias & Wilson 1965), and currently undergoing accelerated expansion (Riess et al. 1998; Perlmutter et al. 1999). Parallel to its dynamic evolution we also have detailed information on its contents, with energy densities split into 69.2% dark energy parametrised as a cosmological constant (Ω_Λ), and 30.8% matter (Ω_m) split into 26.0% collisionless cold dark matter (CDM, Ω_c); and 4.8% ordinary baryonic matter (Ω_b) (Planck Collaboration et al. 2016). Together with the Hubble constant $H_0 = 67.8 \pm 0.9$ km s $^{-1}$ Mpc $^{-1}$, these quantities outline the standard cosmology referred to as the Λ CDM ‘concordance’ model, and provides a framework for cosmic structure formation and the study of galaxies.

In the Λ CDM framework, the foundation for structure formation is encoded in density fluctuations which were frozen-in during a period of accelerated expansion, *cosmic inflation*, in the earliest stages of the Universe. Such density fluctuations exist on the level of $\sim 10^{-5}$ as CMB anisotropies (Planck

Collaboration et al. 2014a,b). These overdensities grow hierarchically under the influence of gravity, and assemble into a cosmic dark matter network of sheets, filaments and knots in the expanding Universe, collectively referred to as the *cosmic web*. On surpassing the critical density required for self-gravity to triumph over cosmic expansion, knots break off from the Hubble flow and form gravitationally bound dark matter halos. As ordinary matter couples to dark matter through gravity, baryons in the form of pristine gas flows along the dark matter network and assembles in the cores of these halos where it fragments and forms stars (White & Rees 1978; White & Frenk 1991; Springel et al. 2005; Cole et al. 2008). This star formation produces feedback and galactic winds, which mixes with infalling matter to produce a diffuse, multiphase circum-galactic medium (CGM, Tumlinson, Peebles, & Werk 2017), itself embedded in the hot inter-galactic medium (IGM) that permeates the Universe. Whilst halos grow hierarchically by accretion and sequential mergers, the stars together with their reprocessed radiation shine as luminous galaxies.

Indeed, the ability of numerical simulations (Bond, Kofman, & Pogosyan 1996; Springel, Frenk, & White 2006) to explain the observed distribution of galaxies across the cosmic web as uncovered by large galaxy surveys such as the 2-degree Field Galaxy Redshift Survey (2dFGRS Colless et al. 2001) and the Sloan Digital Sky Survey (SDSS York et al. 2000) is profound. However, the ability to accurately describe the Universe on large scales does not imply that we understand how galaxies at different redshifts are related; nor the details that regulate their growth, or drives their evolution towards the plethora of galaxies observed today. These questions are hard to address from first principles, but insights can be gained from observations of galaxies. This will be the topic of the next chapter.

1.2 Galaxy Formation and Evolution

In the hierarchical model of structure formation outlined above, galaxies in the local Universe are the end-products of a history of cosmic mergers of dark matter halos and their baryonic contents. However, local galaxies do not come in one shape and size, nor do they live in isolation; they represent a class of dynamically evolving systems and display a diverse range of morphologies. Here, we discuss this diversity, and how it is believed to arise based on the underlying physics.

1.2.1 The Evolving Hubble Sequence

A century ago, Hubble (1926), in a seminal work, categorised the observed galaxy morphologies of local galaxies into four broad classes: the elliptical galaxies (E); the lenticular galaxies (S0); the spiral (barred) galaxies (S/SB); and the irregular galaxies (Irr), today known as the *Hubble classes*, which collectively form the *Hubble sequence*, exemplified in Figure 1.1. Contrary to the suggestive chronological connotation, Hubble, based on similar traits of visual complexity, originally referred to E+S0 collectively as “early-type” galaxies, and S/SB+Irr as “late type” galaxies; a terminology which is still in broad use today.

However, the Hubble sequence in its original form is fundamentally flawed as a unique classifier of galaxies. In a non-exhaustive list of arguments:

1. The Hubble sequence is subjective in appearance and sensitive to the wavelength it is observed in, as opposed to providing an objective metric of fundamental physical properties.

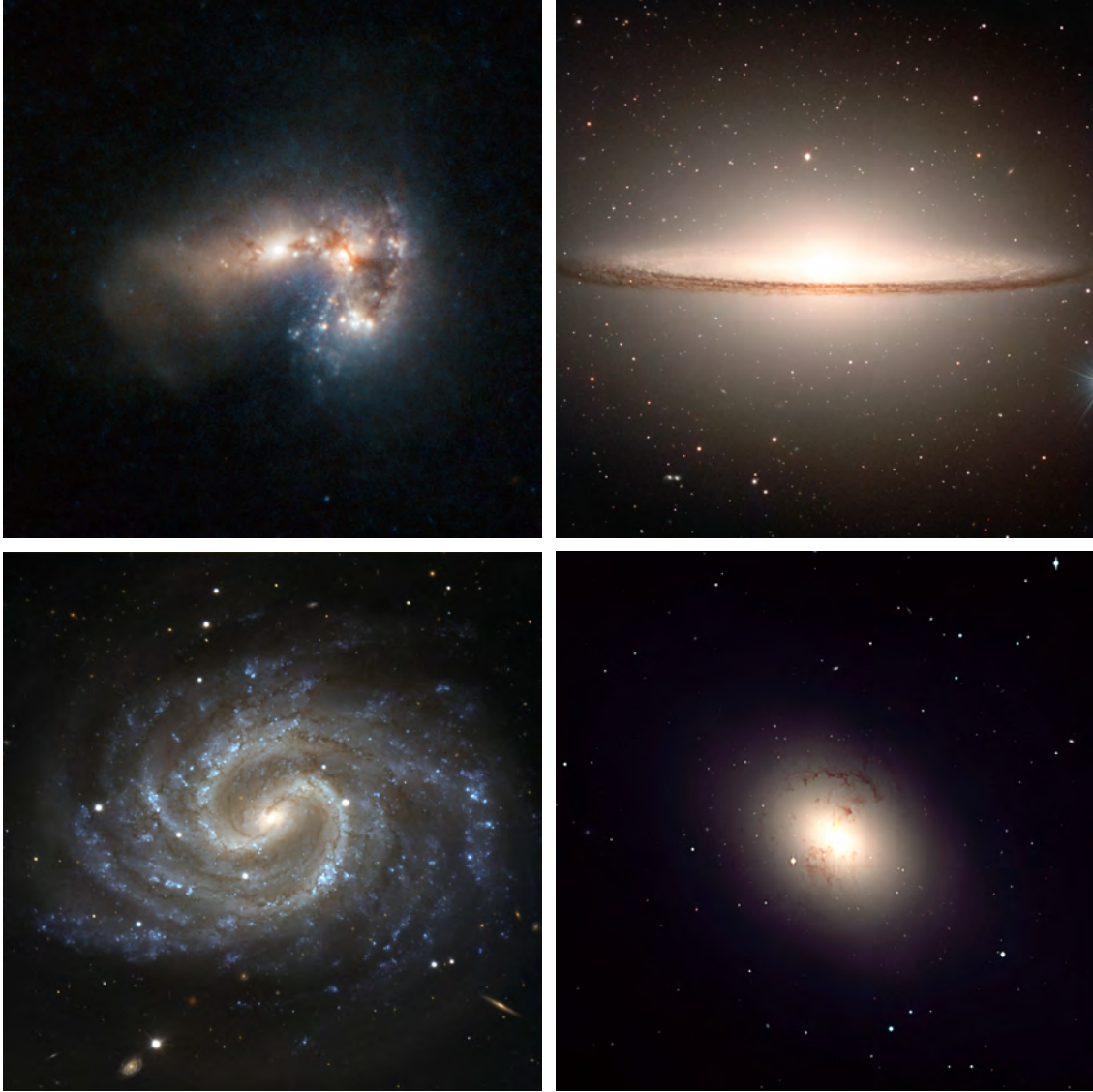


Figure 1.1 A portrayal of the Hubble sequence. *Top left*: Haro 11, star-burst dwarf irregular. *Top right*: M104/NGC4594 (the “Sombrero”), massive, edge-on lenticular. *Bottom left*: NGC 4535, face-on barred spiral. *Bottom Right*: NGC 1316, giant elliptical. Image Credits in order of appearance: ESO/ESA/Hubble and NASA; ESO/P. Barthel, with acknowledgments to Mark Neeser (Kapteyn Institute, Groningen) and Richard Hook (ST/ECF, Garching, Germany); ESO; ESO.

2. The Hubble Sequence is incomplete as it makes no reference to highly varying quantities such as mass. Galaxy stellar masses ($M_{\star}(M_{\odot})$) span more than seven order of magnitude from the least massive ($\sim 10^5 M_{\odot}$) gas-poor population of Milky Way dwarf spheroidals (dSph, $\sim 10^5 M_{\odot}$, Kirby et al. 2013) and local group gas-rich dwarf irregulars (dIrr, $\sim 10^6 M_{\odot}$, Kirby et al. 2017), to the spirals like the Milky Way ($\sim 5 \times 10^{10} M_{\odot}$, McMillan 2017) to the Bright Cluster Galaxy (BCG); a member of Abell 3827, and believed to be the most massive galaxy of the local Universe, with a stellar mass $M_{\star} \gtrsim 10^{11.7} M_{\odot}$ (Gu, Conroy, & Brammer 2018) and a total mass of $\sim 10^{13} M_{\odot}$ (Carrasco et al. 2010)
3. The Hubble sequence does not capture the nature of galaxies as dynamic and evolving systems sampled in transient phases (e.g. Steinmetz & Navarro 2002) as it categorises them by instantaneous

visual morphology.

Understanding the origin and significance of the Hubble sequence and how it evolved through cosmic time represents one of the main goals of modern astrophysics. Indeed, cosmological distances only allow for direct morphological classification of sources at relatively low redshifts. Such systematic morphological studies suggest an evolution in the relative frequencies of galaxies in each Hubble class, which is dominated by the transformation of galaxies with peculiar morphologies at $z \sim 0.7$ into spirals in the local Universe (Delgado-Serrano et al. 2010). Indeed, the prominence of compact, peculiar galaxies with irregular morphologies and star-forming clumps at high redshifts ($z \sim 2 - 3$) has since been confirmed independently (e.g. Wuyts et al. 2012).

1.2.2 Correlating Observables

Beyond Hubble classes, morphology correlates with stellar content, gas content, luminosity, surface brightness, colour and star formation locally (Roberts & Haynes 1994; Blanton & Moustakas 2009; González Delgado et al. 2015), and at high ($z \gtrsim 2$) redshifts (Cassata et al. 2008). Such studies show that physical properties largely separate galaxies in a bimodal distribution; the optically red, dead, bulge-dominated spheroids with little or no gas, dispersion-dominated stellar dynamics and concentrated light distributions (reminiscent of early-types); and the blue, young, star-forming galaxies, rich on gas and with rotationally supported discs and exponentially declining light-distributions (reminiscent of late-types).

These statistical correlations between galaxy observables (direct measurements and derived quantities) allow us to test models of galaxy formation, simulate observed morphologies, and isolate parameters that drive galaxy evolution on a variety of scales and as a function of redshift. In particular, positively correlated ‘scaling relations’ exist between luminosity and gas-phase metallicity, the ‘luminosity-metallicity (LZ) relation’ (Garnett & Shields 1987), stellar mass and the gas-phase metallicity, the ‘mass-metallicity (MZ) relation’ in the redshift range $z \sim 0.1 - 3.5$ (Tremonti et al. 2004; Savaglio et al. 2005; Erb et al. 2006; Maiolino et al. 2008); between stellar mass and star formation rate, the ‘main sequence of star forming galaxies’ (MS) in the redshift range $z \sim 0.5 - 2.5$ (Noeske et al. 2007; Whitaker et al. 2014); and between stellar mass and galaxy size, the ‘mass size relation’ (MR) in the redshift range $z \sim 0 - 3$ (van der Wel et al. 2014). These relations evolve, such that at progressively higher redshifts, galaxies at fixed stellar mass have higher star-formation rates, lower metallicities, and smaller sizes.

One may naively expect that these scaling relations form a fundamental plane, as gas flows modulate the access to the fuel required for star formation; therefore affecting the stellar mass growth as well as the chemical enrichment of the ISM via stellar winds and supernovae (for a discussion on feedback, see Section 1.2.3). Motivated by such arguments, Mannucci et al. (2010) described the MZ-relation and MSSF as projections of a fundamental, redshift-invariant relation that ties stellar mass, metallicity and star formation rate together. The existence of such a fundamental plane is, however, disputed, and alternative explanations attribute its existence to selection bias (Zahid et al. 2014). Additionally, the MR-relation has revealed that on average, early types display more compact morphologies, a stronger dependency on mass, and steeper size evolutions with redshift than that of late type galaxies. This may reflect different evolutionary modes for early- and late types (van der Wel et al. 2014).

The existence of these scaling relations undeniably couples the physical conditions that regulate galactic growth to observed morphology. It is, therefore, imperative that we understand the mechanisms by which baryons are accreted onto a halo and into the galaxy, and how star formation feeds into the environment to set up these self-regulating systems.

1.2.3 Galaxy Growth

The conditions for galaxy formation can be understood in terms of three competing time-scales; the Hubble time t_H , which measures the characteristic time-scale for the cosmological expansion, the free-fall time t_{ff} , which measures the characteristic time-scale on which a pressureless region undergoes gravitational collapse, and the cooling time t_c , which measures the capacity of a system to radiate away energy. Fundamentally, structure formation must beat the cosmological expansion to form bound structures. If $t_{\text{ff}} < t_c$, the inability to cool efficiently inhibits gravitational collapse by continuously re-establishing hydrostatic equilibrium during contraction. This is inefficient for fragmentation of gas. If, on the other hand, $t_c < t_{\text{ff}}$, energy is radiated sufficiently quick to allow for gravitational collapse, and such conditions can trigger star formation. In the Λ CDM Universe, these time-scales - and thereby ultimately what determines/governs galaxy growth - is primarily set by *accretion*, *mergers*, and star-formation's back-reaction on the environment; *feedback*.

Mergers

The sequential merging of dark matter haloes is intrinsic to the Λ CDM paradigm. If galaxies are embedded in merging dark matter halos, the merging process can lead to loss of orbital energy and angular momentum by dynamical friction, and these processes will alter the resulting structure of galaxy remnants. Traditionally, mergers are separated by the merging galaxies mass ratios; major ($\sim 1 : 1$)- and minor ($\lesssim 1 : 3$) mergers, and by their gas contents; wet (gas-rich)- and dry (gas-poor) mergers. These labels carry physical significance as they lead to qualitatively different evolutions. In major mergers, the existing stellar masses of the merging components are added; and if wet, will compress gas to trigger episodes of major star-bursts, which yields further mass-growth. Any rotationally supported disc structures in the progenitors are expected to be destroyed and replaced by a remnant with dispersion-dominated dynamics (Mihos & Hernquist 1994, 1996; Barnes & Hernquist 1996), a process labeled morphological transformation. Such major mergers of disc progenitors is the most commonly accepted formation channel of early-type galaxies in the local Universe. By dissipating energy, gas from gas-rich encounters can flow to the center. Therefore, wet mergers provides a mechanism to regulate the buildup of a compact central stellar bulge, and sizes that can be reconciled with observations by varying progenitor gas fractions (Cox et al. 2006).

In contrast, minor mergers are expected to leave the dynamical structure of the main galaxy intact, but may through gravitational interaction lead to a size growth, and - if wet - tidal forces can strip gas from satellite galaxies. Minor mergers are therefore the traditional mechanism by which to maintain and grow disc galaxies. Recently, however, it has been suggested that major mergers may play a vital role in the formation of the present Hubble sequence, through the rebuilding of disks at late times (Hammer et al. 2009).

Accretion

Although mergers are expected to contribute significantly, galaxies can grow by accumulating gas from their surrounding cosmic environments. This accretion is bimodal, with the distinguishing feature being whether the temperature of the infalling gas reaches the virial temperature of the halo (*hot mode accretion*, $T \gg 10^5 K$) or not (*cold mode accretion*, $T \sim 10^4 K$) (Katz et al. 2003; Kereš et al. 2005). In hot mode accretion, gas accretes spherically onto the halo; but is there shock-heated. This causes it to become pressure-supported, and the gas is inhibited from sinking deeper into the potential unless the excess energy is removed by cooling radiation. Cold mode accretion arises because dark matter halos tend to be located at the intersection of filaments. Due to a strong density-dependence of the cooling function (and therefore on t_c), cold flows avoid a build-up of temperature and pressure by channeling gas along such high-density, cosmic filaments.

The relative contribution of hot to cold mode accretion depends on redshift and dark matter halo mass. At high redshifts, enhanced baryon densities facilitate efficient cooling. Combined with lower gas temperatures reached by falling onto lower average dark matter halo masses, this promotes cold mode accretion. Reciprocally, lower redshifts are characterised by lower mean baryon densities and higher mass haloes: conditions that favour hot mode accretion. Such dependence was verified by van de Voort et al. (2011a), who showed that whilst cold mode accretion peaks at $z \sim 3$, hot mode strongly dominates the global accretion rate on to halos in the local Universe. However, whereas hot-mode accretion can dominate the gas accumulation onto halos, cold-mode accretion is essential for transporting gas from the halo and onto the galaxies for all halos and at all redshifts (van de Voort et al. 2011b). These results echo the results of Dekel et al. (2009), who proposed cold mode accretion as the main mode of galaxy formation - and has been suggested to significantly contribute to observations of strong H I absorbers (see Section 2.3.1 and Part II Paper II).

Galaxy Feedback

Galaxies do not grow unhindered. In addition to accretion and mergers, galaxy growth is regulated by feedback processes. *A priori*, feedback is predicted from stellar evolution theory as mass-loss on the asymptotic giant branch (AGB) and by core-collapse supernovae explosions associated with massive stars. Its existence is inferred observationally from the presence of stellar winds (Steidel et al. 1996b) and starburst driven outflows (Noterdaeme et al. 2012b) in galaxies; and from the detection of metals (typically C IV (Ellison et al. 2000; D’Odorico et al. 2013)) in the IGM. Indeed, its significance has been demonstrated with numerical simulations which, absent feedback, unable to capture star formation histories, morphologies, or to match empirical scaling relations (Somerville et al. 2008; Kereš et al. 2009; Hopkins, Quataert, & Murray 2011). Detailed meta-studies such as the Aquila Comparison Project (Scannapieco et al. 2012) and the AGORA project (Kim et al. 2014, 2016) show that even if feedback is present, if inefficient it cannot suppress star formation at high redshifts; and an inability to remove low angular momentum gas leads to central baryon concentrations at odds with observations. Likewise, too efficient feedback inhibits (re)accretion of gas and disc formation at low redshifts; and despite required in order to capture cold gas in the CGM, often destroys star-forming gas discs in the process (Liang, Kravtsov, & Agertz 2016, 2018).

Feedback in the form of mass, momentum, energy, metals and dust injection into the ISM results from embedded stars, core-collapse supernovae (SNII), Type Ia supernovae (SNIa); and active galactic nuclei (AGN). Owing to their varied physical natures, these agents operate on different characteristic temporal- and spatial scales. Supernovae feedback preferentially dominates in low-mass galaxies due to the weak gravitational potential well (Dekel & Silk 1986); powerful active galactic nuclei (AGN) are favoured in massive galaxies (Benson et al. 2003) and are indeed required to launch galactic winds in the these deeper potential wells; and at all galaxy masses, stars produce radiation and mass-loss (Leitner & Kravtsov 2011) over the course of their lifetimes. In fact, cumulative momentum injection by winds and radiation pressure into the ISM from massive, young, hot stars over time is comparable to supernovae explosions, and this can significantly impact their native giant molecular clouds (Agertz et al. 2013).

On average, the response of a medium subject to feedback is to heat, thereby prolonging cooling times and suppressing fragmentation on local scales. If energetic enough this can drive chemically enriched galactic winds into the surrounding CGM and IGM, which can be re-accreted at later times. In essence, the interplay between gas accretion, star formation, and feedback results in a self-regulated cycle and depending on the strength of the feedback it promotes the formation of either bulge or disc dominated galaxies (Übler et al. 2014). Studying the gas that will form stars across redshift is therefore vital for our understanding of galaxy evolution. As I show in Sections 2.3 and 2.4 DLAs have historically been associated with extended H I discs and can therefore provide insights. The use of simulations to understand the nature of strong H I absorbers and their connection to galaxies, as presented in Part II Paper II of this thesis, therefore requires realistic feedback implementations that captures the relevant physics across a dynamic range of scales.

1.3 High- z Galaxy Populations

With the launch of the Hubble Space Telescope (*HST*) in 1995, galaxy evolution was given a new, sensitive eye which could stare into the depths of space, unhindered by the telluric atmosphere below. Perhaps its capacities are most vividly captured by the rich galaxy diversity across cosmic time observed in the *Hubble Deep Field* (HDF, Williams et al. 1996), shown in Figure 1.2. Spearheaded by *HST*'s discovery of such variety in galaxy populations at early times, and with the advent of 10-meter class telescopes, such as Keck on Hawaii, new photometric pre-selections targeting faint high-redshift galaxy populations in the early Universe based on known rest-frame spectral energy distribution (SED) features emerged.¹ In a non-exhaustive list, this led to the discovery of Lyman Break Galaxies (LBGs, Steidel et al. 1996a, 2003), selected by targeting the rest-frame $\lambda 912\text{\AA}$ Lyman break of galaxies at $z = 2.4 - 3.4$ with UGR filters; distant red galaxies (DRGs, Franx et al. 2003), selected to avoid the UV-bias present in LBG samples by targeting the rest-frame $\lambda 3646\text{\AA}$ Balmer break and the $\lambda 4000\text{\AA}$ break of galaxies at $z \sim 2$ with JK filters; and Lyman- α emitters (LAEs, Cowie & Hu 1998; Hu, Cowie, & McMahon 1998), selected to target the rest-frame $\lambda 1216\text{\AA}$ Ly- α line in the redshift range $z \sim 3-6$, with appropriate narrow-band filters.

Classifying galaxies by *selection* rather than by *morphology* replaces the Hubble sequence at high redshifts, where targets are faint and difficult to resolve. Despite targeting particular features and using a range of photometric colours, such selections often encounter difficulties in comparing the populations

¹For a review of such selections, see Dunlop (2013).

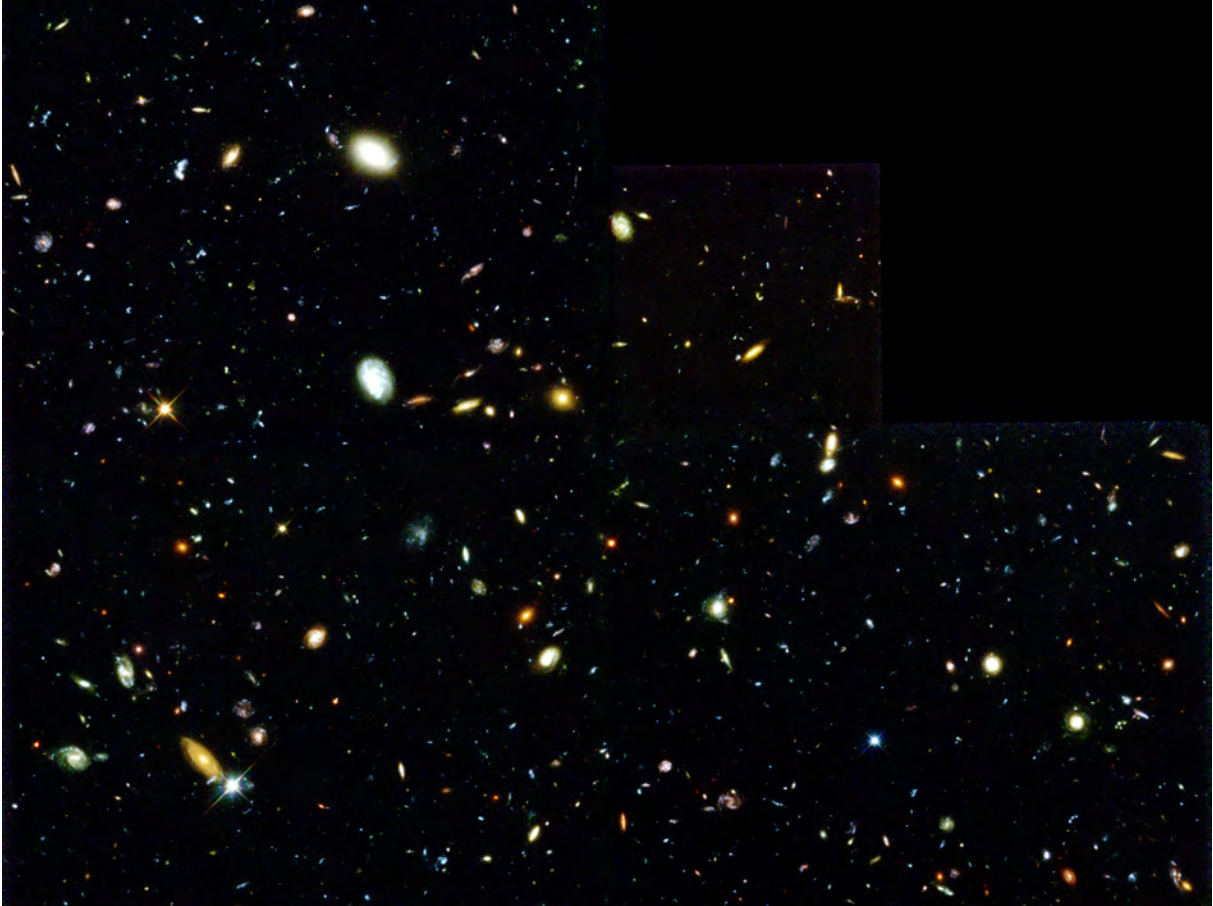


Figure 1.2 Assembled by staring at a seemingly empty piece of the cosmos for ten consecutive days, the *Hubble Deep Field* (HDF) reveals a rich galaxy diversity already in place in the young Universe. Image credits: Robbert Williams and the Hubble Deep Field Team (STScI) and NASA/ESA.)

traced because objects can fulfil multiple selection criteria, leading to target overlap. Therefore, the relations between samples, how they are drawn from the total galaxy population at any redshift, and their selection bias must be analysed to reach a census for galaxy evolution.

Of particular relevance to the research presented in this thesis, the Lyman break technique pre-selects on a discontinuity in the far-UV continuum, and therefore selects actively star forming galaxies largely unaffected by dust reddening. Nonetheless, a strong Lyman break is indicative of young, massive stellar populations capable of producing H I ionizing radiation. Naively, the reprocessed ionizing radiation results in an intrinsically bright Ly α line emission, which should allow the galaxy to be detected as a LAE. However, owing to the resonance nature of Ly α , which is known to affect observations of high- z galaxy populations (Verhamme et al. 2008; Laursen, Razoumov, & Sommer-Larsen 2009; Hayes et al. 2010) and its efficient destruction by dust in more chemically enriched, massive and luminous galaxies, the escape fraction and hence emerging line-flux in Ly α is uncertain. Even after establishing the causal link between the two populations, their selection criteria introduce different bias. Whereas the UV-continuum is proportional to the number of massive stars which causes a LBG selection to favour massive galaxies; LAEs are sensitive to the contrast between line emission and continuum, and are, therefore, biased to low-mass galaxies with high star formation rates, i.e. biased to high specific star formation rates. Observations now indicate that LAEs represent such a low-mass subset of LBGs (Fynbo, Møller, & Thomsen 2001).

The above discussion highlights that if galaxies are regulated by a set of fundamental, underlying physical conditions manifested in their integrated SED, selections based thereon can give valuable insights to the high-redshift Universe and galaxy evolution. Yet, care has to be taken to account for the underlying selection functions before we can hope to understand how different populations are related. Common to the selections discussed here, they are based on photometric techniques and therefore suffer from a fundamental luminosity bias towards the brightest objects at any redshift. For extended galaxies, this effect is enhanced by surface brightness dimming which is a strong function of redshift; and the presence of a Malmquist bias which leads to an overestimate of the average brightness of the parent population at all redshifts. These considerations have for a long time left the field attempting to characterise galaxy populations detected with alternative selection methods. The gas cross section selection against background sources provides an efficient and complementary detection technique, and this method will be discussed in great depths in the following Chapter.

2

QUASAR ABSORBERS

Complementing standard luminosity selections, galaxies can be selected on gas cross-section. This technique is extremely powerful for detecting high-redshift galaxies as it is insensitive to the galaxy luminosity - and thus surpasses the “tip of the iceberg” of the galaxy population at any redshift. However, detected as absorption, the gas cross-section selection requires a bright background source to provide a continuum. This Chapter treats galaxies selected via their gas cross-section along the line of sight towards distant quasars. Section 2.1 discusses quasars, with emphasis given to the role they play as background light-sources. Section 2.2 introduces the framework to quasar absorbers. Section 2.3 provides indirect evidence to support the interpretation of strong H I absorbers as “smoking guns” for galaxy environments. Section 2.4 relates the absorbers to their host galaxies observed in emission directly. In Section 2.5, I outline my research contribution to the field, before ending the Chapter with some reflections on standing issues and possible ways forward in Section 2.6.

2.1 Quasars as Cosmic Beacons of Light

Quasi-stellar objects (QSOs) - or quasars - refer to some of the intrinsically most luminous non-transient astrophysical objects. Conceptually, their luminosity is believed to be powered by actively accreting supermassive ($M > 10^6 M_{\odot}$) black holes (SMBH), embedded in gravitationally infalling gas, dust, and matter at the centres of galaxies (Lynden-Bell 1969). Conservation of angular momentum leads to the formation of an accretion disc surrounding the SMBH, which converts the gravitational potential energy to thermal energy by internal friction in the turbulent accretion flows (see Frank, King, & Raine 2002, for an introduction to accretion discs). In an active period of mass accretion onto the SMBH, this conversion of gravitational to thermal energy can be very efficient and is responsible for the emerging electromagnetic radiation which - by far - outshines its host galaxy. In some cases, the quasar may further drive non-relativistic wide-angle outflows (e.g. Fabian 2012) or relativistic collimated jets (e.g. Urry & Padovani 1995). These flows of gas allow the SMBH to interact with the surrounding medium in complex ways, which may impact the host galaxy evolution on local scales as well as spatial scales extending into the CGM (Ishibashi & Fabian 2016). Indeed, the mass of the SMBH is observed to correlate with properties of the host galaxy, in particular with stellar velocity dispersion, stellar luminosity, and bulge stellar mass, which suggests a co-evolution (see Kormendy & Ho 2013, for a review).

In light of the framework presented above, which suggests temporal, spatial and dynamic complexity, we are therefore confronted - and justified - in asking: *what properties do quasars display that allow them*

to act as background light-sources for analysis of absorption-line systems?

(I) Quasars are intrinsically bright and have been detected at cosmological redshifts of $z \sim 6 - 7.5$ (Fan et al. 2006; Mortlock et al. 2011; Bañados et al. 2018). These redshifts correspond to a Universe of merely $\sim 690 - 900$ Myr age, or equivalently, $\sim 5 - 6$ per cent of its current value. With a reported bolometric luminosity of $L \sim 4 \times 10^{13} L_{\odot}$ at redshift $z = 7.54$, the quasar reported in Bañados et al. (2018) outshines our Galaxy which has a bolometric luminosity of order $L_{\text{MW}} \sim 5 \times 10^{10} L_{\odot}$, by a factor ~ 800 . On its own, this has two implications: there was a quasar population in the early Universe; and as light beacons, quasars give us unprecedented access to study the Universe to redshifts $z \sim 7$ by providing a continuum (see property (III) below) on which to map intervening absorption (see Section 2.2). This has enabled “Ly- α forest tomography” which maps over- and under-densities in 3D (two spatial dimensions, one redshift dimension) large-scale cosmic environments, (e.g. Lee et al. 2016, 2018), and can provide insights on the nature and evolution of the intergalactic medium (e.g. Simcoe, Sargent, & Rauch 2004; Prochaska, Herbert-Fort, & Wolfe 2005; Mas-Ribas et al. 2018).

(II) Quasars are compact objects and can therefore be modelled as (unresolved) point sources. In contrast to galaxies, which are extended objects and therefore suffer from cosmological surface brightness dimming with redshift $F \propto (1 + z)^{-4}$, quasars as point sources do not. Together with the intrinsic brightness (see property (I) above), this differential response of flux to redshift implies that the contamination of the quasar host galaxy to the observed SED is reduced dramatically for progressively higher redshift.¹ This is what makes it difficult to detect and analyse quasar hosts observationally (Peng et al. 2006; Kim et al. 2008; Schramm, Wisotzki, & Jahnke 2008). By imaging a galaxy at an intervening redshift and at low projected separation from the background quasar, we can therefore neglect the quasar host galaxy, which reduces the complexity of the problem from modelling {quasar + quasar host galaxy + intervening galaxy} to modelling {PSF + intervening galaxy}. Here, we use the definition of the Point Spread Function (PSF), which by construction describes the response of the optical system to an imaged point source, and therefore is independent of the morphology of the object imaged.

(III) Quasar continua can be fitted with power-laws of the form $f_{\lambda} \propto \lambda^{\alpha_{\lambda}}$, or equivalently $f_{\nu} \propto \nu^{\alpha_{\nu}}$. Such slopes can take on different values, with reported ranges of optical spectral indices α_{ν} from -2.5 to $+0.3$ and a mean value of -0.5 (Richstone & Schmidt 1980). The power-law behaviour is believed to originate in thermal emission generated by accretion disc dynamics. Indeed, it is predicted based on standard geometrically thin but optically thick accretion discs (Lynden-Bell 1969; Shakura & Sunyaev 1973). Being optically thick, each annulus of the accretion disc will radiate with a blackbody luminosity given by the temperature structure of the disc. The integral of the blackbody luminosities across the disc annuli results in the power-law continuum. Together with characteristic spectral features -typically broad emission lines generated by high velocity clouds in the broad line region deep in the gravitational potential - this allows us to accurately model quasar spectra. In extension, this implies that we can separate the quasar spectrum from intervening absorbers, and therefore identify the spectral features of the absorbing galaxy in emission.

¹Indeed, surface brightness dimming can explain why galaxies at high- z mostly appear as compact objects (Bouwens et al. 2004; Calvi et al. 2014).

(IV) Quasars have temporally stable flux outputs on the time-scales required for deep spectroscopic and photometric detection-thresholds of intervening absorbing galaxies. This is particularly important to ensure a good baseline quasar continuum measurement on which intensity contrasts can be mapped. Albeit not categorised as transient phenomena, quasars typically display aperiodic flux variability of $\sim 10 - 20$ per cent on timescales of order of months to years (Collier & Peterson 2001; MacLeod et al. 2010). Indeed, in Rhodin et al. (2018, see Part II Paper I) I quantified the combined uncertainty of atmospheric conditions, slit-losses and quasar variability based on the scatter between individual sensitivity functions of five quasars. I found an RMS of the same order as the typical integrated line-flux uncertainties, from which I concluded that quasar variability, on average, was a minor source of noise for our study.

Complementary sources to quasars on which to base absorption analysis include long-duration gamma-ray bursts (GRBs)² and background galaxies. GRBs are compact, transient phenomena associated to the deaths of massive stars. Like quasars, GRBs afterglows have intrinsically bright peak luminosities ($L_{\text{GRB}} \sim 10^{48} - 10^{55} \text{ erg s}^{-1}$ assuming isotropic emission (e.g. Kulkarni et al. 1999; Kumar & Zhang 2015), and display featureless power-law spectra generated by synchrotron radiation at early times (e.g. Hjorth et al. 2003), before diminishing in strength to reveal a core-collapse supernovae spectrum at late times³ (Galama et al. 1998; Fruchter et al. 2006), and finally fading away. These characteristics allow for an absorption analysis of intervening material along the traced pencil-beam at early times, and follow-up analysis of the host or the intervening material in emission at late times, when the GRB afterglow spectrum vanishes. Indeed, this has become a standard practise to study actively star-forming GRB hosts (Hjorth et al. 2012; Perley et al. 2016; Selsing et al. 2018) allowing targeted detections to redshifts $z \sim 6$ (McGuire et al. 2016), and for unrelated, intervening absorbers (Savaglio 2006; Christensen et al. 2017). However, as the afterglows fade quickly, there is only a limited window of opportunity to secure high-quality spectra that encode intervening absorption. Therefore, GRB afterglow follow-ups initially relied on low-resolution spectroscopy ($R \sim \lambda/\Delta\lambda < 1000$) spectroscopy, (e.g. Fynbo et al. 2009), but has by dedicated efforts improved, now providing intermediate resolution ($R \sim 6500 - 12000$) with varying signal-to-noise ratios of $S/N \sim 1 - 50$ per pixel,⁴ which at best is comparable to regular quasar surveys (Christensen et al. 2017; Selsing et al. 2018).⁵ The situation is, perhaps, most evident by considering typical sample statistics, with the X-shooter GRB afterglow legacy sample reporting $N_{\text{GRB}} \sim 10^2$ (Selsing et al. 2018), whilst low-resolution SDSS spectroscopy has identified $N_{\text{QSO}} \sim 10^5$ quasars with intervening absorption (Noterdaeme et al. 2012a), which can be followed up at the desired resolution at later times (e.g. Rafelski et al. 2012).

The use of background galaxies to provide a continuum on which to map intervening absorption is a novel technique (Mawatari et al. 2016; Cooke & O’Meara 2015). This method has the advantage of being able to constrain the size of the H I gas by measuring the covering fraction of the intervening foreground absorber over the extended background. In addition, and as opposed to the use of quasars and

²GRBs are traditionally classified into *long*- and *short*- duration GRBs, following a bimodal distribution of burst duration, with a division at a duration-time of $t \sim 2$ seconds, following Kouveliotou et al. (1993).

³This confirms the stellar origin of the GRB progenitor.

⁴Depending on burst brightness, wavelength coverage, and response time.

⁵But see also Thöne et al. (2007), Prochaska et al. (2007) and Ledoux et al. (2009) for exceptional cases of $R > 20000$ GRB afterglow spectra.

GRBs, the relatively low brightness contrast between the background- and intervening galaxies allows a more robust identification of emission counterparts at low projected separations (for a discussion on counterpart detections in emission, see Section 2.4). However, as previously outlined, surface brightness dimming limits the redshift coverage for which extended background sources is practically feasible, with the notable exception of lensed systems. In particular, a study by [Lopez et al. \(2018\)](#) was able to use observations of a lensed galaxy to provide spatially resolved maps revealing a clumpy distribution of an intervening Mg II absorber. In addition, as outlined in Chapter 1, galaxies come in a range of sizes, masses and morphologies which affect the integrated spectral energy distribution. This complicates their modelling, and can introduce uncertainties in continuum normalisation and contaminating spectral features intrinsic to the background source which blend with the intervening absorber.

In this section, I addressed quasars as cosmic beacons of light, and I placed them in the context of other candidate sources. Although quasars share favourable characteristics with both GRBs and galaxies, their hallmark is temporal stability combined with luminous, regular SEDs observed to great distances. Whilst this leads to large brightness contrasts which complicates the detection and modelling of the absorber counterpart in emission, quasars give us unprecedented access to arbitrarily high signal-to-noise ratios and spectral resolutions on which to base absorption analysis. This is indeed the great advantage of quasars over GRBs and background galaxies in the study of intervening matter.

2.2 Intervening Clouds of Neutral Hydrogen

2.2.1 The H I Ly- α forest

Ly- α absorption results when the energy of incident photons match the energy separation between the 1S \rightarrow 2P electronic states in neutral hydrogen, H I. The finite lifetime of the excited state will produce an allowed de-excitation to the ground state, causing Ly- α to resonantly scatter in random directions relative to the original light. This light-matter interaction effectively removes light at a rest-frame wavelength of $\lambda_{\text{Ly-}\alpha} = 1216 \text{ \AA}$ from the incident quasar spectrum. Simultaneously, cosmic expansion causes photons that are blue-wards of the quasar Ly- α line to progressively redshift into resonance with the rest-frame Ly- α transition of intervening neutral hydrogen clouds. Each discrete hydrogen cloud along the redshift path therefore generates discrete Ly- α absorption profiles at progressively higher frequencies in the quasar spectrum; collectively referred to as the *Ly- α forest*.

The application of the large scattering cross-section of Ly- α transition to study the intervening intergalactic medium (IGM) in absorption towards background quasars was first proposed by [Gunn & Peterson \(1965\)](#). In theory, this approach allows us to study H I gas from the local Universe up to the redshifts $z \sim 6$, at which point reionization was completed. Prior to this redshift, the universe was neutral - and thus the discrete Ly- α absorption profiles would be replaced by a continuous Gunn-Peterson trough immediately bluewards of the quasar Ly- α emission line ([Becker et al. 2001](#); [Fan et al. 2006](#)). In practise, however, ground-based observations are limited by the atmospheric cut-off at $\lambda_{\text{atm}} \sim 3200 \text{ \AA}$, and the study Ly- α absorption is limited to redshifts above $z_{\text{abs}} \gtrsim (\lambda_{\text{atm}}/\lambda_{\text{Ly-}\alpha}) - 1 \simeq 1.6$. Therefore, observing lower redshift absorbers requires space-based UV instruments such as the Hubble Space Telescope (*HST*).

Without direct access to the 3D spatial information and density, Ly- α absorbers are classified by the H I column density; the integral measure of the density that gives rise to the absorption profile along the line of sight, and measured in units of $[N_{\text{HI}}] = \text{cm}^{-2}$. Formally, these absorbers are defined as Ly- α forest for $\log_{10}[N_{\text{HI}} (\text{cm}^{-2})] < 17$ (Lynds 1971); Lyman Limit Systems (LLS; $17 < \log_{10}[N_{\text{HI}} (\text{cm}^{-2})] < 19$, (Tytler 1982)); Sub-Damped Ly- α Absorbers (sub-DLAs; $19 < \log_{10}[N_{\text{HI}} (\text{cm}^{-2})] < 20.3$, e.g. Péroux et al. (2003); Zafar et al. (2013)); and the Damped Ly- α Absorbers (DLAs, $\log_{10}[N_{\text{HI}} (\text{cm}^{-2})] > 20.3$, Wolfe et al. (1986)).

Despite forming a continuous sequence of column densities, there are important physical as well as phenomenological differences between the classes of absorbers. The lower column density limit of LLSs represents the column density at which the gas becomes optically thick to photons blue-wards of the Lyman continuum edge at $\lambda = 912 \text{ \AA}$. This causes a characteristic, sharp break in the quasar spectrum that is easily identified even in low resolution, noisy observations. At wavelengths $\lambda < 912 \text{ \AA}$ in the Ly- α absorber's rest frame, the flux is redistributed in nebular continuum and line emission. This implies an effective zero flux level, which lies below any practical detection limit. Sub-DLA and DLAs imprint saturated Ly- α absorption profiles, with pronounced Lorentzian damping wings, and are always accompanied by low-ionization metal line complexes (see 2.3.1). The H I gas becomes increasingly self-shielding to UV background radiation above $\log_{10}[N_{\text{HI}} (\text{cm}^{-2})] \gtrsim 18$, and is completely self-shielded above the DLA limit. This implies that DLAs are precise tracers for hydrogen and metal columns, and do not require ionization corrections to account for (unobserved) ionised ion fractions (see Section 2.3.2 for a developed discussion). Sub-DLAs, however, lie in a transition regime in physical densities that causes the dominant ionization state to vary from predominantly ionised to predominantly neutral gas (Lehner et al. 2014; Fumagalli, O'Meara, & Prochaska 2016; Zafar et al. 2017). This introduces varying degrees of ionization corrections to individual ions and individual systems (Som et al. 2013). Observations suggest that the required ionization corrections are of order ~ 0.2 dex, and thus small relative to measurement uncertainties (Dessauges-Zavadsky et al. 2003; Péroux et al. 2007, 2008). Unless otherwise specified, sub-DLAs and DLAs will therefore uniformly be referred to as strong H I absorbers throughout the remainder of this thesis.

2.2.2 The column density distribution function

The statistical properties of H I absorbers are encoded in the H I column density frequency distribution function, $f(N_{\text{HI}}, X)$. This function is the absorption equivalent of galaxy luminosity functions, and is defined in terms of the number of absorbers, $d^2\mathcal{N}$, along a random line of sight (LOS) in the redshift range $(z, z + dz)$ with column densities in the range $(N_{\text{HI}}, N_{\text{HI}} + dN_{\text{HI}})$. It is derived by considering the effective cross-section of the population as follows. With geometric gas cross-section $\sigma_{N_{\text{HI}}}(z)$, and a comoving number density $n_{N_{\text{HI}}}$

$$d^2\mathcal{N} = n_{N_{\text{HI}}}(z)\sigma_{N_{\text{HI}}}(z)dN_{\text{HI}}\frac{dl_p}{dz}dz, \quad (2.1)$$

where $\sigma_{N_{\text{HI}}}(z)$ and $n_{N_{\text{HI}}}$ are explicitly allowed to be functions of redshift, and the proper distance interval along the LOS, dl_p is re-cast in terms of redshift dz as this is the natural variable to consider. For a non-evolving population, the cross-section is constant and the expression reduces to $\sigma_{N_{\text{HI}}}(z) = \sigma_{N_{\text{HI}}}(0) \equiv \sigma_{N_{\text{HI}}}$, whereas for the comoving number density, which scales with redshift cubed,

$n_{\text{N}_{\text{HI}}}(z) = n_{\text{N}_{\text{HI}}}(0)(1+z)^3 \equiv n_{\text{N}_{\text{HI}}}(1+z)^3$. The equation becomes,

$$d^2\mathcal{N} = n_{\text{N}_{\text{HI}}}\sigma_{\text{N}_{\text{HI}}}(1+z)^3 dN_{\text{HI}} \frac{dl_p}{dz} dz . \quad (2.2)$$

Here, it is convenient to solve for the ratio of the proper distance interval to redshift interval which light emanating from the background quasar travels along the LOS. By expanding the proper path length,

$$dl_p = c dt = c \frac{dt}{da} \frac{da}{dz} dz , \quad (2.3)$$

where, c is the speed of light, dt is the time interval required for the radiation to travel dl_p , and utilizing the definition of the Hubble parameter, $H(z) \equiv \dot{a}/a$ and the scale factor $a = 1/(1+z)$,

$$\frac{da}{dt} \equiv \dot{a} \rightarrow \frac{dt}{da} = \frac{1}{\dot{a}} \quad ; \quad \frac{da}{dz} = \frac{d}{dz} \left(\frac{1}{1+z} \right) = -\frac{1}{(1+z)^2} . \quad (2.4)$$

Substituting expressions 2.4 into Eq. 2.3,

$$dl_p = \frac{c}{\dot{a}} \left(-a^2 \right) dz = -\frac{c}{H(z)} \frac{dz}{(1+z)} , \quad (2.5)$$

from which it follows that

$$d^2\mathcal{N} = n_{\text{N}_{\text{HI}}}\sigma_{\text{N}_{\text{HI}}} \frac{c}{H(z)} (1+z)^2 dN_{\text{HI}} dz . \quad (2.6)$$

We now isolate quantities intrinsic to the absorber population from those depending on cosmology, and construct a unitless integration variable $dX \equiv \frac{H_0}{H(z)} (1+z)^2 dz$, which when integrated defines the measured *absorption distance*, X (Bahcall & Peebles 1969). The absorption distance ensures that a non-evolving population with constant comoving spatial density and physical cross-section has a constant line-of-sight density per unit X - a result which does not hold for redshift. With absorption-spectroscopy of single sightlines, the geometric cross-section of single absorbers is degenerate with the number density of clouds at the inferred redshift. Therefore, these quantities⁶ are collapsed into a measure of the effective number of absorbers per unit column density and redshift; namely the function $f(N_{\text{HI}}, X)$ which introduces the chapter. We, thus, find what we set out to show,

$$d^2\mathcal{N} = n_{\text{N}_{\text{HI}}}(N_{\text{HI}}, z)\sigma_{\text{N}_{\text{HI}}}(z)(1+z)^3 \frac{dl_p}{dz} dN_{\text{HI}} dz \equiv f(N_{\text{HI}}, X) dN_{\text{HI}} dX . \quad (2.7)$$

Eq. 2.7 is a standard result and formalises the quasar absorption line framework for simulators and observers alike. Absorber data give us an observationally determined $f(N_{\text{HI}}, X)$ by simply counting absorption-systems. The observations can then be fitted with more or less physically motivated functional forms. Commonly, $f(N_{\text{HI}}, X)$ is parametrized by a Gamma function, as this is analogous to the Schechter function which is used to fit luminosity functions and H I mass function (e.g. Zwaan et al. (Z05, 2005b), Noterdaeme et al. (N09, 2009), Zafar et al. (Z13, 2013)). Therefore, if H I absorbers trace galaxies, we expect them to follow similar relations. Other parametrizations include a broken power-law, also used by N09, as this would be expected if absorbers sample a population of randomly inclined exponential discs (Fall & Pei 1993; Wolfe et al. 1995), and Prochaska et al. (P14, 2014) describe the

⁶together with a factor c/H_0 , to compensate for making dX unitless

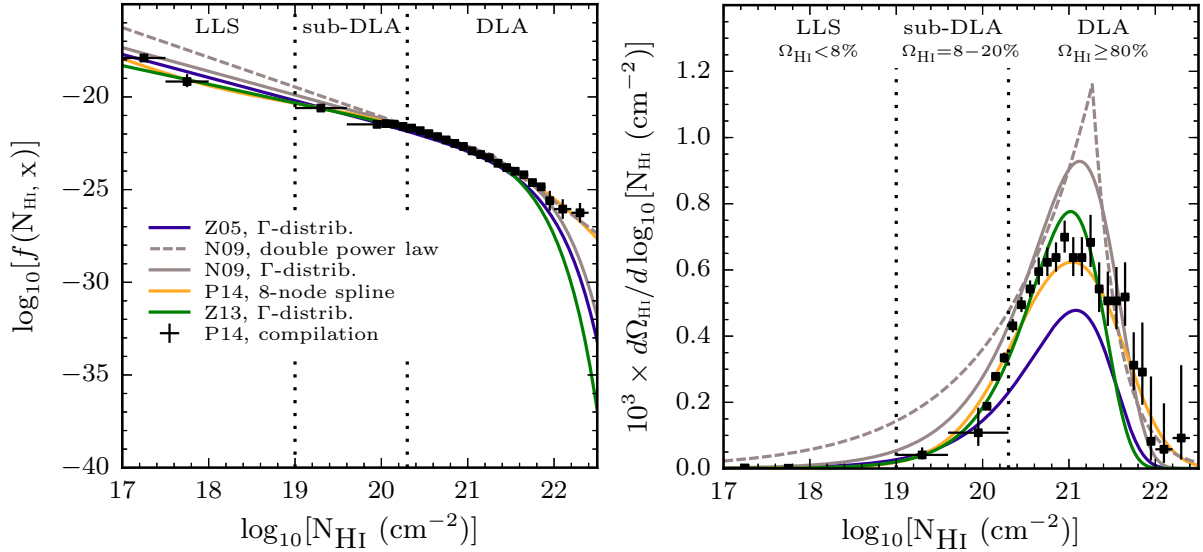


Figure 2.1 *Left*: column density frequency distribution function $f(N_{\text{HI}}, X)$ as a function of the column density. Take note of the logarithmic quantity plotted, which implies that the frequency of low-column density absorbers vastly outnumbers high column-density systems. *Right*: differential contribution of the cosmological mass density of neutral gas, Ω_g^{HI} , per logarithmic unit of column density. This panel demonstrates that the majority of neutral gas is contained in gas structures which give rise to column densities $\log_{10}[N_{\text{HI}} (\text{cm}^{-2})] \sim 21$.

distribution with a spline model. These descriptions are not homogenous, as they are built on different selection functions; with data sets that span different redshift ranges, and often are driven to reproduce certain column density intervals.

Based on this formalism, the total neutral gas mass density (ρ_{HI}), expressed in terms of the critical density ($\rho_{\text{crit}} = 3H_0^2/8\pi G$) can now be calculated as

$$\Omega_g^{\text{HI}}(X)dX \equiv \frac{\rho_{\text{HI}}}{\rho_{\text{crit}}} = \frac{\mu m_{\text{H}} H_0}{c \rho_{\text{crit}}} \int_0^\infty N_{\text{HI}} f(N_{\text{HI}}, X) dN_{\text{HI}} dX, \quad (2.8)$$

where $\mu = 1.3$, is the mean molecular mass of a gas with 75% hydrogen, and 25% helium by weight, giving a mean mass per hydrogen atom of μm_{H} , and ρ_c is the current critical density. Here, we have implicitly equated dz to dX at $z = 0$, and made use of Equation 2.5 to convert column density per absorption path to column density per proper path length ($l_p = c/H_0$), i.e. giving the required dimension of “per volume”.

In Figure 2.1 I plot the compilation of column density frequency distribution functions described above (*left*), and the associated differential contribution of the cosmological HI gas mass density (*right*) per $\log_{10}[N_{\text{HI}} (\text{cm}^{-2})]$. In addition, I plot the most recent compilation of observational data, also presented in P14, with $\log_{10}[N_{\text{HI}} (\text{cm}^{-2})] > 20$ measurements from [Noterdaeme et al. \(2012a\)](#). The shape of the column density distribution function implies that there are many more low-column density absorbers; and the sharp turnover towards the high column-density end of the distribution results from the conversion of dense, neutral gas into molecular hydrogen. To correctly describe this behaviour and avoid

an excess of absorbers with $\log_{10}[N_{\text{HI}} (\text{cm}^{-2})] \gtrsim 21$, simulations must therefore establish realistic star formation - feedback cycles (Erkal, Gnedin, & Kravtsov 2012; Altay et al. 2013).

Remarkably, Equation 2.8 provides a method for determining the cosmological neutral gas fraction independent of the origin, nature or size of the absorbing population. Considering that the number of absorbers strongly depends on column density - in particular at column-densities above the turnover at $\log_{10}[N_{\text{HI}} (\text{cm}^{-2})] \sim 21$, it is remarkable to see that DLAs contain more than 80% of the neutral gas at all redshifts $z < 5$ (Prochaska, Herbert-Fort, & Wolfe 2005; Noterdaeme et al. 2009, 2012a; Crighton et al. 2015; Sánchez-Ramírez et al. 2016). Combined with the contribution from sub-DLAs (Zafar et al. 2013), these classes of absorbers do, to within current estimates, account for the entire neutral gas budget. Therefore, damped H I systems have long been considered the reservoirs of neutral gas that inevitably must be linked to star formation. If so, the population is expected to evolve with redshift, and hold a direct link to galaxies. These topics will be treated in Sections 2.3 and 2.4.

2.3 An inferred galaxy connection

2.3.1 The evolving gas budget

One of the main goals of modern astrophysics is to understand the conditions for star formation. This is extremely challenging and probably lacks a closed form analytical solution, as gas flows regulates the access to stellar birth material; and star formation in turn impacts gas flows by stellar feedback. If star formation ensues from the collapse of (and therefore traces) molecular hydrogen (Bigiel et al. 2008), and the high H I column-density end of the distribution function encloses the bulk neutral gas and provides a sanctuary from hard, ionizing radiation, DLAs are viable reservoirs of the gas that feeds star formation.

To understand this role in star formation, and how absorber populations contribute to the cosmic baryon cycle, efforts have been made to quantify the redshift evolution of the distribution function (see Section 2.2.2 for formalism). Heterogenous samples (direct detection of Ly- α absorption at high redshifts (~ 5 (Crighton et al. 2015); $z = 3 - 4$ (Prochaska, Herbert-Fort, & Wolfe 2005; Noterdaeme et al. 2012a); objects originally selected as Mg II absorbers for $z < 1.6$ (Rao & Turnshek 2000; Rao, Turnshek, & Nestor 2006); and 21-cm H I emission-line detections in the local universe (Zwaan et al. 2005a; Martin et al. 2010)) consistently show that DLAs dominate the neutral gas budget. Accounting for the H I contribution from absorbers below the DLA column-density threshold, Crighton et al. (2015) describe the redshift evolution of the cosmological H I mass density from $z = 0 - 5$ by the functional form $\Omega_{\text{HI}}(z) \propto (1 + z)^{0.4}$. This weak evolution implies that the cosmic H I mass density only evolves by a factor ~ 1.7 from $z = 3$ to the local universe. From a naive closed-box-model of galaxy formation, one expects that $d\Omega_{\star}/dz \approx -d\Omega_{\text{HI}}(z)/dz$, i.e. that a decrease in the cosmic gas fraction with time (or here, with redshift z) is mirrored by the corresponding increase in stellar mass. But observations in the past decade robustly identified a dramatic build-up of stellar mass over the same ($z = 3 - 0$) redshift range, as encoded in the cosmic star formation history (Heavens et al. 2004; Behroozi, Wechsler, & Conroy 2013; Madau & Dickinson 2014; Khostovan et al. 2015).

Figure 2.2 is taken from Crighton et al. (2015), and illustrates the simultaneous buildup of comoving mass

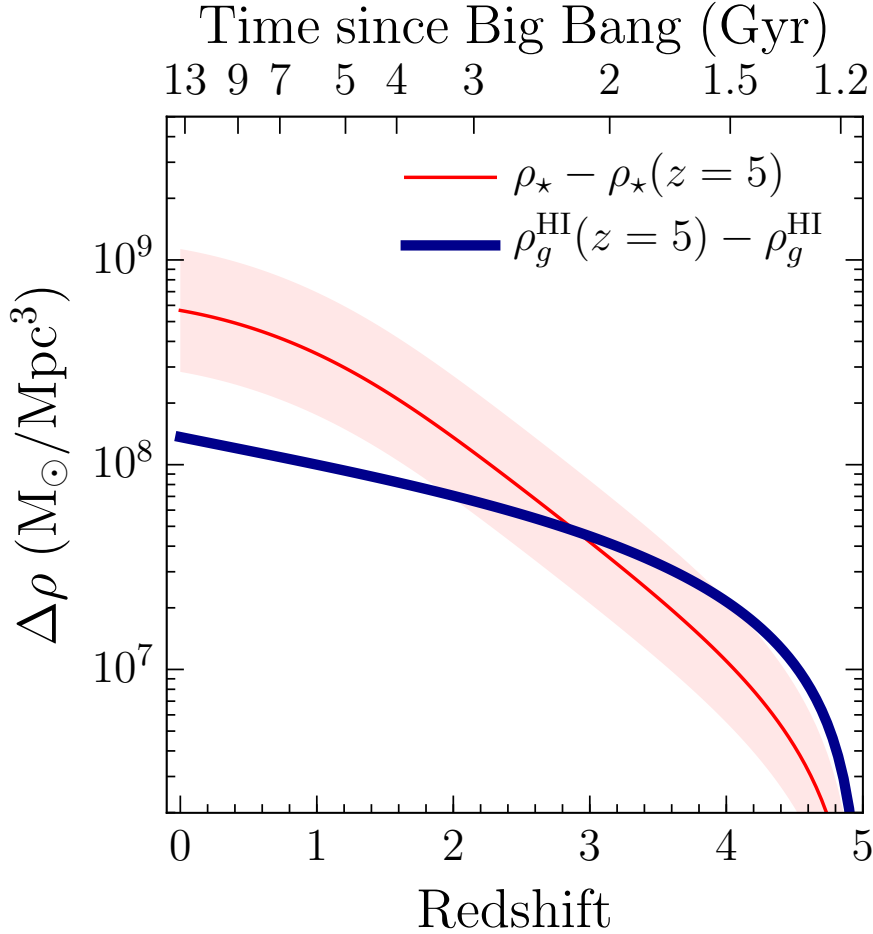


Figure 2.2 The buildup of stellar mass density (red) and the simultaneous decrease in comoving gas mass density as traced by DLAs and corrected for contributions from lower-column-density absorbers. Below $z \sim 3$ the H I gas phase mass density evolution is too weak to account for the stars formed. Therefore, the H I must be continuously replenished, for example by recombining ionized gas. The Figure is taken from [Crighton et al. \(2015, their Figure 13\)](#).

density in stars (functional parametrization from [Madau & Dickinson \(2014\)](#)) and decrease of comoving H I mass density (functional parametrization from [Crighton et al. \(2015\)](#)) from redshift $z = 5$. Note that the gas mass density evolution (a *decreasing* function with time) is reflected to facilitate comparison of any differential behaviour in the relations. At high redshift $z \sim 5$, the H I mass density is large enough to account for stars observed at $z \sim 3$. However, for redshifts $z < 3$, the evolution of H I mass density is a factor of $\sim 5 - 6$ too weak to explain the buildup in stellar mass at low redshifts.

Indeed, the redshift evolution of these functions not posing mirror images of one another is often interpreted as refutation of the closed box model, in favour of an open-box model of galaxy formation. According to such a framework, a galaxy is affected by its cosmic environment and cannot be treated as an isolated system. In addition to the conversion of gas to stars, gas is then replenished by inflows of pristine gas from the CGM, by accretion of stripped satellite gas from wet interactions, and from recycled winds. In that case, DLAs are more likely to represent an intermediate, transitory phase of gas which ends up fuelling star formation ([Prochaska, Herbert-Fort, & Wolfe 2005; Davé et al. 2013](#)),

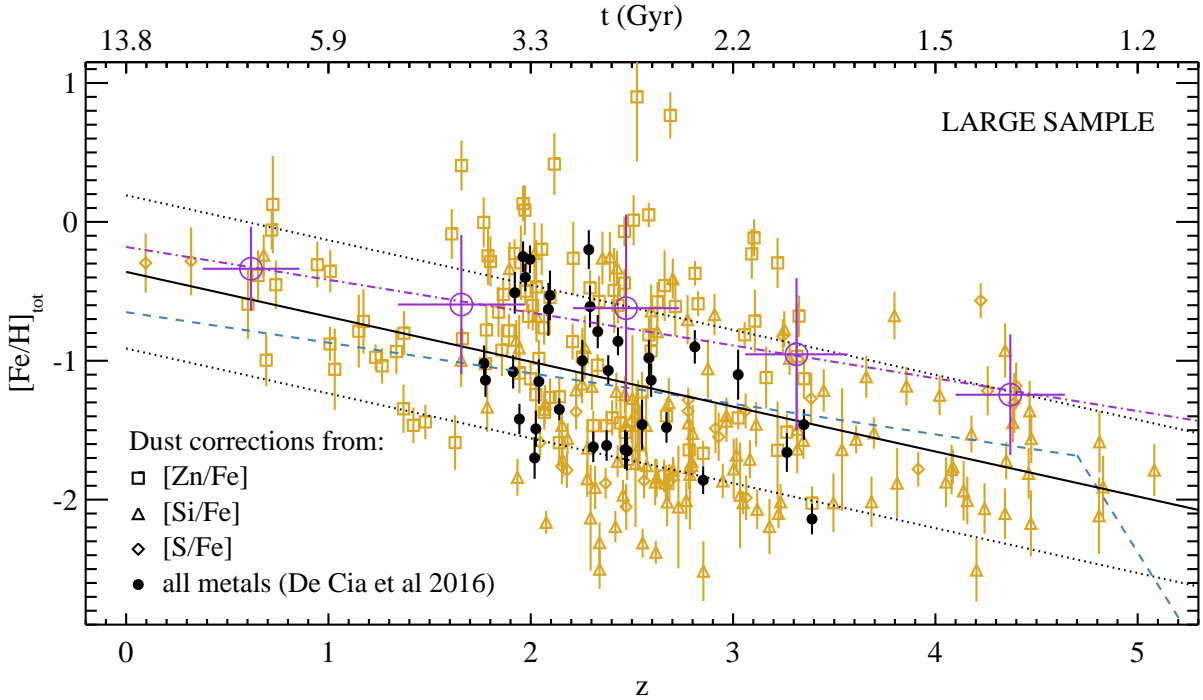


Figure 2.3 Global chemical enrichment of gas traced by DLAs with time. The presence of metals and the metal-evolution both support the notion that DLAs are associated with galaxy environments. Note that at $z \sim 5$ DLAs sample the cosmic metallicity of a Universe 10% of its current age. The Figure is taken from De Cia et al. (2018, their Figure 4).

continuously replenished by recombining highly ionized gas from the IGM or recycled galactic outflows. The main contributors to such inflows are believed to be cold-mode accretion (see Dekel et al. 2009; Fumagalli et al. 2011) and recycled winds (see Oppenheimer et al. 2010), with the former expected to become increasingly important towards higher redshifts.

2.3.2 A metallicity evolution

The second argument which suggests that strong HI absorbers are related to galaxy environments rests on metallicity measurements. Observations show that both sub-DLAs and DLAs are always accompanied by low-ionization metal absorption lines at the redshift of the absorber (Prochaska et al. 2003; Noterdaeme et al. 2012a; Rafelski et al. 2014). By combining the column density measurements for a metal ion and hydrogen, the metallicity of the absorber is recovered ($[M/H]_{\text{abs}}$). Here, $[M/H]_{\text{abs}}$ is defined as the abundance ratio of an element, relative to the solar abundance ratio for the same element.

Of course, care has to be taken to ensure the metal ion is an accurate tracer of the metal content in the absorbing gas. Typically, volatile elements such as zinc (Zn) and sulphur (S) are used as tracers of metallicity as these are believed to be minimally depleted onto dust. However, recent work suggests that even for Zn, dust corrections of order 0.1 – 0.2 dex are often needed (De Cia et al. 2018). In addition, an element in the gas can exist in multiple ionization states. Therefore, ionization corrections must be applied to account for the fraction of the element enclosed in different ionization states. For DLAs, HI is self-shielded to ionizing radiation and therefore ionization corrections are small. In addition, their conditions ensure that most metals embedded in DLAs exist in singly ionized states such as Si II,

Fe II, S II and Zn II. Therefore, measurements of column densities in these ions give a measure of their metallicity. However, below $\log_{10}[\text{N}_{\text{HI}} (\text{cm}^{-2})] \sim 20$, ionization can be severe, and depending on the state and metallicity of the gas, it can significantly affect metallicity measurements in sub-DLAs (Lehner et al. 2014; Fumagalli, O’Meara, & Prochaska 2016; Zafar et al. 2017).

Having accounted for depletion- and ionization effects, such absorption studies provide us with some of the most precise information on the metal content in dense, neutral gas out to high ($z \sim 5$) redshifts. Such information is typically inaccessible with conventional techniques to these depths as they are flux-limited, rely on particular emission line detections, and because metallicity measurements rely on tying line-ratios to empirically derived abundance calibrations which may themselves evolve with time. With large compilations of DLAs, it has been shown that the probed gas experiences a global chemical enrichment (Pettini et al. 1994; Rafelski et al. 2012, 2014). In Figure 2.3 I show a revised version of this enrichment evolution which accounts for dust-corrections, as presented in De Cia et al. (2018). Data for individual absorbers is shown in gold and black markers, and black solid and dotted lines display the linear fit that parametrizes the evolution and the intrinsic scatter in the relation. The purple open circles depict the mean HI column density weighted metallicities, in bins of redshift, with the purple dot-dashed line presenting the associated linear fit. For reference, the dashed blue curve refers to the evolution derived in Rafelski et al. (2012, 2014).

Both the presence of metals in such absorbers and the observed metallicity-evolution suggest an association with a gaseous medium affected by chemical enrichment from galaxy feedback. However, Figure 2.3 reveals a sub-solar cosmic mean metallicity⁷ at all redshifts, which may be indicative of sampling galaxies in early stages of chemical evolution, and a large ~ 0.5 dex intrinsic scatter in the underlying data at all redshifts. Under the assumption that DLAs are associated with galaxies, these properties of the DLA population can be understood as a consequence of a gas cross-section selection. DLAs arise from pencil-beam line-of-sights through individual galaxies, themselves drawn from the total gaseous galaxy population at any redshift. Therefore, the scatter in the DLA metallicity evolution reflects local variations (random ones originating in an inhomogeneous, turbulent medium and systematic ones expected from radial abundance gradients) *within* a galaxy, as well as the variations in chemical enrichment *in between* galaxies, introduced by galaxies being in different stages of their chemical evolution.

This connection to galaxy environments and the access to precise metallicity measurements have provoked attention to identify stellar populations whose chemical signatures match those of DLAs. Although the high metallicity distributions in Milky Way thin- and thick disc stars are incompatible with typical DLAs, Rafelski et al. (2012) suggest that halo stars may have formed out of the gas we detect as DLAs at $z > 2$. Recent work by Berg et al. (2015) also show that metal-rich DLAs share some abundance patterns with the Local Group dSphs. Correlating properties from absorbers and galaxies separated by half the Universe’s age is an intriguing idea, but its success hinges on the gas in absorption being converted into stars at later times. Without a direct confirmation of the DLA counterparts in emission and with only a pencil-beam line-of-sight through a hypothesised galaxy, it is impossible to understand whether this is truly the fate of the absorbing gas.

⁷The solar metallicity, by definition, is zero.

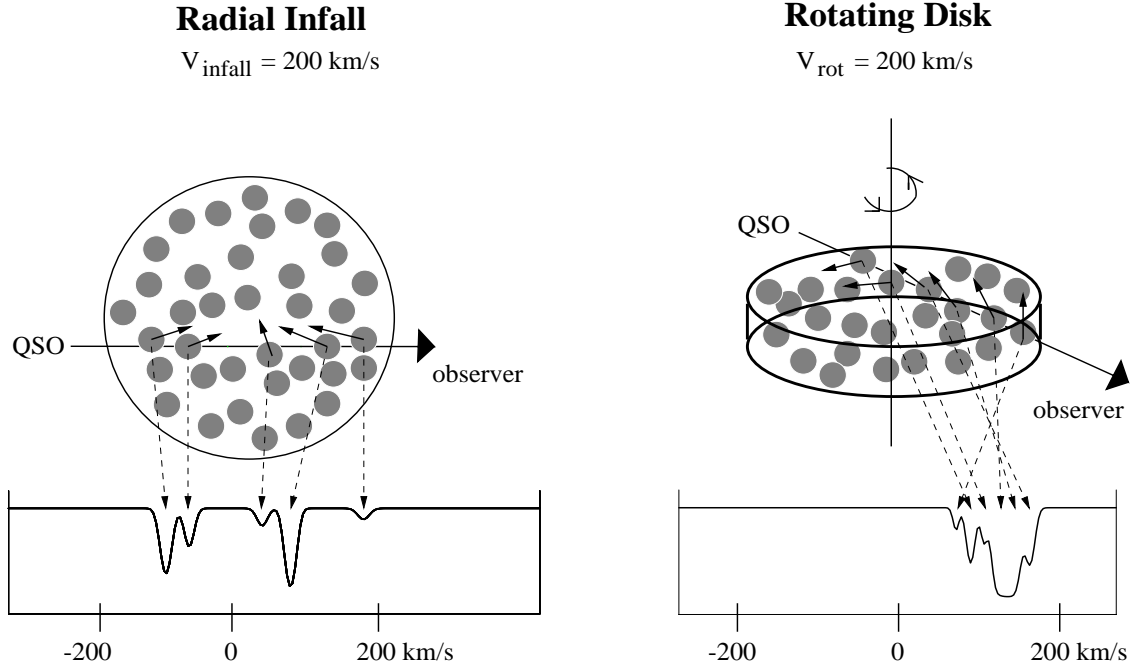


Figure 2.4 Idealized kinematic models of gas clouds and the associated absorption imprint in a flat quasar spectrum. *Left*: Radial infall, giving rise to a symmetric velocity structure centered on the systemic velocity of the potential. *Right*: Gas clouds distributed in a galactic disc and participating in rotational motion, preferentially favouring clustered, edge-leading velocity profiles relative to the systemic velocity of the host galaxy. The Figure is taken from [Charlton & Churchill \(2000, their Figure 5\)](#).

2.3.3 Complex kinematics

Apart from providing a measure of the metallicity in the absorbing gas, the advent of 10-meter class telescopes coupled with high-resolution spectrographs has had a remarkable impact. Instruments such as *VLT/UVES* which holds a resolution power of $R = \lambda/\Delta\lambda = c/\Delta v = 40000$ and *KECK/HIRES* with $R \sim 45000$ allow velocity structures of $\Delta v \sim 6 \text{ km s}^{-1}$ (or equivalently $\Delta\lambda \sim 0.1 \text{ \AA}$) at a typical observed wavelength of $\lambda \sim 5500 \text{ \AA}$ to be resolved. Such instruments now regularly reveal that the metal lines discussed in Section 2.3.2 often show multiple velocity components. The velocity structure of these ‘metal complexes’ encodes detailed information on the kinematics of the gas that contributes to a given absorber.

Historically, two idealized kinematic structures were considered: clouds in a spherical distribution radially infalling towards a mass-centre; and clouds distributed in a disc participating in its rotation. By discriminating between these kinematic modes, observers hoped to answer whether such absorbers were preferentially probing extended H I discs of *pre-existing* spiral galaxies, or the earliest moments of *a galaxy in the making*; the assembly its gaseous building blocks. These models together with their hypothetical kinematic imprints on a flat quasar spectrum are shown in Figure 2.4. If strong H I absorbers preferentially probe radially infalling gas clouds, then for a given line of sight, velocity components are expected to fall symmetrically over the range of velocities $\sim 200 - 400 \text{ km s}^{-1}$, centred on the systemic velocity ([Charlton & Churchill 2000](#)). In addition, it is unlikely that clouds are observed at the systemic velocity, and therefore a characteristic double peak from red- and blue-shifted material is expected. If, in contrast, absorbers probe rotating discs, the observational signature is expected to be

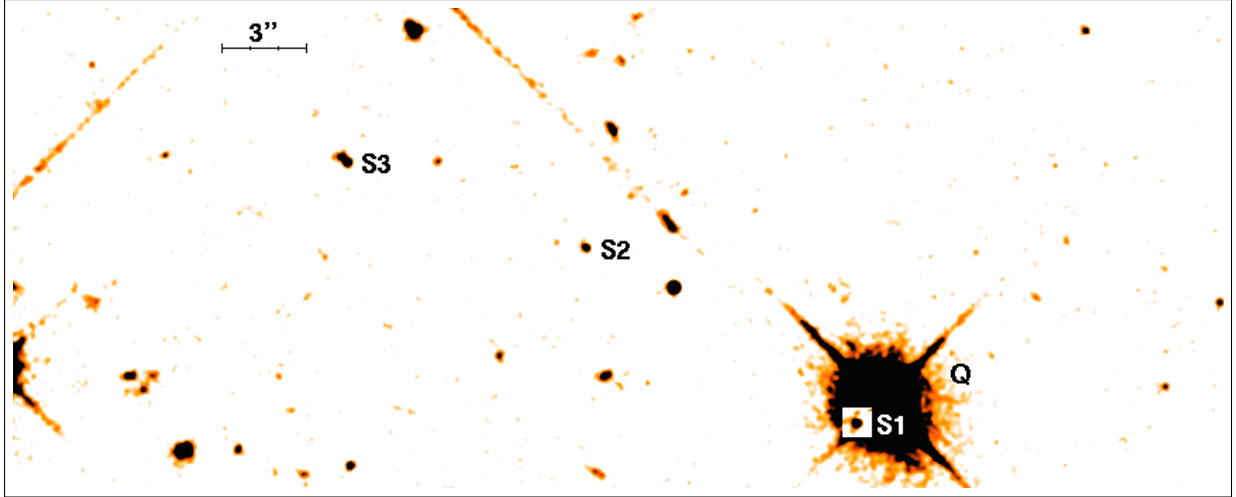


Figure 2.5 An *HST/WFC2* image cutout of the quasar field PKS 0528 -250 which hosts the first detection of a DLA galaxy counterpart, originally reported in Møller & Warren (1993). In the field, the quasar (Q), and a group of three galaxies (S1, S2 and S3) have been labeled, and overlap in redshift with the $z = 2.81$ DLA. The inset panel reveals the object S1, hiding underneath the quasar point-spread function. The Figure is taken from Møller & Warren (1998, their Figure 1) .

asymmetric line-profiles with leading edges and individual velocity components clustered around the mean rotational velocity component along the line of sight.

Early observations favoured the latter (Wolfe et al. 1986; Prochaska & Wolfe 1997), and were supported by models of disc formation (Mo, Mao, & White 1998). We now understand these idealized templates as limiting cases. Cosmological hydrodynamic simulations (Haehnelt, Steinmetz, & Rauch 1998) and semi-analytic models (Maller et al. 2001) demonstrated that the absorption kinematics could equally well be explained by irregular proto-galactic clumps in dark matter halos subject to a combination of rotation, random motions, gas flows, and mergers. With observations, Prochaska et al. (2008) confirmed the diverse, complex kinematics of strong H I absorbers, displaying velocities ranging from tens to several hundreds of km s^{-1} . Indeed, recent work now shows that the kinematics is sensitive to ionization states of a multi-phase ISM and CGM (Liang, Kravtsov, & Agertz 2018; Peebles et al. 2019), gas motions (Fumagalli et al. 2011; Rahmati & Schaye 2014), and the star formation - feedback cycle (Bird et al. 2014, 2015; Liang, Kravtsov, & Agertz 2016).

Finally, whereas simulations can measure the systemic velocity of the galaxy, such a measurement cannot be derived from observations of a single, randomly intersecting sight line piercing a galaxy halo. Re-emphasizing the message of the previous sections; without direct confirmation of the galaxy in emission, it is, therefore, hard to robustly put the kinematic structure of the absorber in a galactic context.

2.4 Absorption selected galaxies

From the arguments presented in the previous Sections, it is clear that strong H I absorbers sample chemically enriched and kinematically complex gaseous media in a transient phase of the cosmic baryon cycle that is, somehow, linked to star formation. However, most of these arguments are indirect and

derived based on an inferred galaxy connection and from the results of simulations. Even though such studies provide important clues as to their nature, astronomy is at its heart an empirical science and we, therefore, seek to confirm such an intrinsic connection by observing absorbing galaxies directly in emission.

The early attempts at studying galaxies harbouring strong H I absorbers in emission were often unsuccessful, with a representative detection-rate of $\sim 10\%$ as compiled by [Krogager et al. \(2017\)](#), and references therein). This was primarily driven by the observational strategy. At cosmological redshifts, the combination of low angular separations and the inherent brightness contrast between the bright background quasar and the faint intervening galaxy makes it difficult to identify and separate their respective contributions to the imaged light. In addition, as an extended object at cosmological redshifts, the absorbing galaxy suffers from increased surface brightness dimming with redshift. The first confirmation of a DLA galaxy counterpart was, therefore, only reported in [Møller & Warren \(1993\)](#), using Ly- α narrow-band imaging that targeted a $z_{\text{abs}} = 2.81$ absorber in the quasar field PKS 0528-250. By the year 2002, only two additional spectroscopic confirmations of the galaxy counterparts were made. Based on the three spectroscopically confirmed DLA galaxy counterparts, at the time [Møller et al. \(2002\)](#) claimed that DLA galaxies were consistent with the faint end of LBGs.

These pioneering studies identified the need for performing PSF-subtractions of the quasar in the spatial and spectral domains to search for excess flux related to the intervening galaxy ([Møller 2000](#); [Møller et al. 2000](#)). Indeed, as it can be seen from [Figure 2.5](#), the existence of a faint counterpart in emission hiding in the projected sky proximity of the bright background quasar is a fundamental challenge, and the ultimate reason these objects are not detected in luminosity selected surveys in the first place.

In an attempt to capture the statistical properties describing the relation between DLAs and their galaxy counterparts in terms of luminosity, metallicity and luminosity, [Fynbo et al. \(2008\)](#) modelled the absorbers as arising from sight-lines through optically thick slabs of gas smeared on an infinitely thin, randomly inclined disc-geometry. Despite the simplicity, the model was able to reconcile the metallicity distributions of GRBs, DLAs, and LBGs. This suggested that the objects represented different selections of the same parent population. We now understand the impact parameter distributions spanned in observations as an effect of the governing, underlying scaling relations at work. More massive galaxies are, on average, larger (allowing a larger span in possible projected separations) and more metal-rich. This is shown in the right panel of [Figure 2.7](#). Likewise, plotting the impact parameter as a function of the H I column density has also become standard practise, and is shown in the left panel of the same [Figure](#). Here, the results of simulations are taken from [Rahmati & Schaye \(2014\)](#). Despite a large scatter within 1σ regions, the systematically larger impact parameters returned by observations relative to the mean simulation relation were interpreted as an observational selection bias by the authors. Such a bias would wrongfully detect a more massive and therefore more luminous galaxy in the sky vicinity. I address this issue directly in [Paper II](#).

We now understand these low detection-rates on the basis of scaling relation arguments, which suggest that emission-lines often fall below detection-limits in blind surveys ([Krogager et al. 2017](#)), whilst pre-selecting on the absorption metallicity is found to be a viable strategy to achieve higher ($\sim 60 - 70\%$)

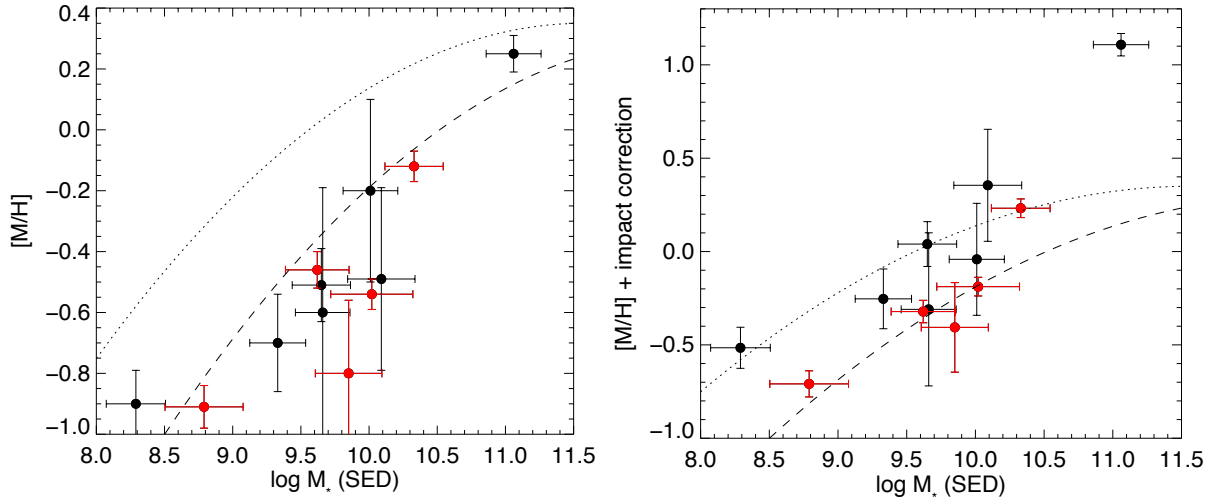


Figure 2.6 Reconciling observations of absorption selected galaxies with the [Maiolino et al. \(2008\)](#) MZ-relation for luminosity selected samples at redshift $z = 0.7$ and $z = 2.2$, plotted as dotted and dashed lines, respectively. Note the different scales on the y-axis. *Left:* The absorption metallicity is taken to be a proxy for the luminosity-selected metallicity. All objects fall systematically below their luminosity-based relations. *Right:* The absorption metallicity is updated to include an impact-parameter dependent correction factor. The inclusion of this correction factor allows the luminosity-selected relations to be recovered. Although the majority of galaxies now follow the relation, objects with large impact parameters unphysically over-shoot the assumed luminosity relations by > 0.5 dex, as visible from the data point in the top right. The Figure is taken from [Christensen et al. \(2014, their Figure 4\)](#).

detection rates in observational campaigns ([Fynbo et al. 2010, 2011](#); [Péroux et al. 2011](#); [Fynbo et al. 2013](#)). This is understood as a consequence of a scaling relation between velocity widths and the metallicity in absorption, the so called $\Delta v_{90} - [M/H]_{\text{abs}}$ relation, and is interpreted as the absorber equivalent of the MZ-relation ([Ledoux et al. 2006](#); [Møller et al. 2013](#); [Neeleman et al. 2013](#); [Som et al. 2015](#)).

In fact, using absorption kinematics as a tracer of stellar mass and calibrating the relation to the MZ-relation presented in [Maiolino et al. \(2008\)](#), [Møller et al. \(2013\)](#) was able to predict the stellar mass of the galaxy harbouring the absorber in functional form. This prediction uses absorption metallicity, redshift, and a free parameter $C_{[M/H]}$ which was introduced to reconcile the difference between absorption- and emission-line metallicities as inputs. The relation was verified directly by comparing the stellar mass prediction to stellar mass measurements derived from spectral energy distribution (SED) fits by [Christensen et al. \(2014\)](#). In the same work, [Christensen et al. \(2014\)](#) reinterpreted $C_{[M/H]}$ as an average metallicity gradient Γ which was allowed to act over the impact parameter that connected the absorber and emitter. The resulting, inferred emission-line metallicity based on absorption properties could then be placed on the luminosity-selected MZ-relation. In Figure 2.6 I show the result of this metallicity-gradient correction explicitly. Indeed, populating this relation with more data to verify its robustness is a key result, as presented in Paper I of this thesis.

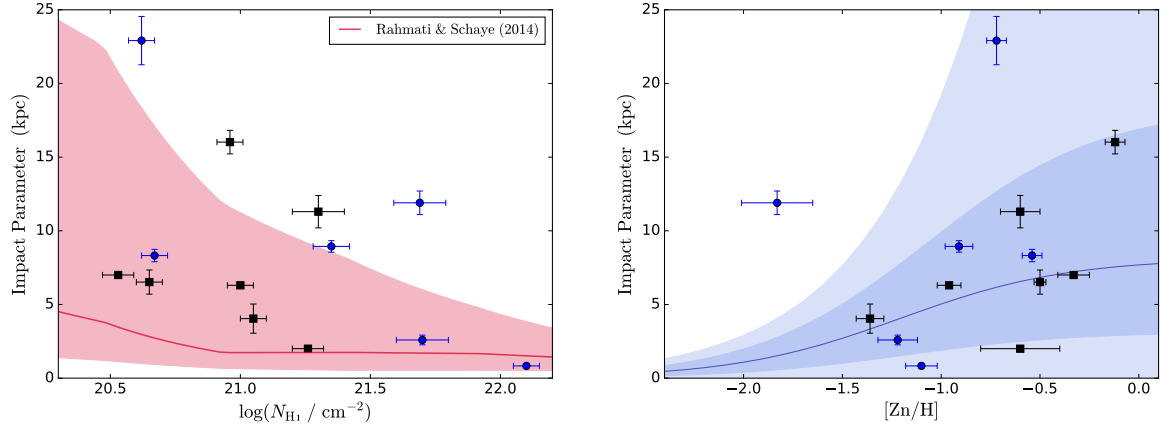


Figure 2.7 Distributions with projected separation between the absorber and the spectroscopically confirmed galaxy counterparts. *Left*: The distribution is plotted as a function of the neutral H I column density. The red, underlying contour correspond to the mean and 1σ simulation predictions based on galaxies at $z \sim 3$ from (Rahmati & Schaye 2014). Note that, all but one spectroscopically confirmed systems have impact parameters above the mean prediction. *Right*: The distribution is plotted as a function of the absorption metallicity. Larger galaxies allow for a larger range of impact parameters and are associated with higher metallicities. The blue underlying contour shows the predict median, 1σ , and envelope contours based on the (Fynbo et al. 2008) model. The Figures are taken from Krogager et al. (2017, their Figures 8 and 9, respectively).

2.5 Research Summary

The original work and contribution to the field of absorption selected galaxies are presented as attached first-author articles in Part II of this thesis. In this work, I have addressed many of the most pressing concerns raised. Perhaps the most immediate contribution to the field is the increased number of spectroscopically confirmed absorber-galaxy pairs, characterised in both absorption and emission. Although the properties of the absorbers often exist by construction as the targeted galaxies were selected on gas cross section, complementary information on the emission from these galaxies is frequently partial or missing completely.

This is caused by an observationally expensive selection strategy. If, after selection, an absorber is followed-up photometrically, all candidate hosts in the quasar field can be identified but neither can be spectroscopically confirmed as the host (e.g. Rao et al. 2011). If instead, after selection, an absorber is pursued with long-slit spectroscopy, an efficient observing strategy as employed in the X-shooter campaign (Fynbo et al. 2010; Krogager et al. 2017), can identify the correct host, but often leaves the observer wondering whether the identified object is part of a larger group environment, just beyond slit coverage. Absent data from integral field units which are ideal for these studies (e.g. Péroux et al. 2011), a confirmation therefore requires an initial quasar spectrum to identify the absorbers in and complementary spectroscopic- and photometric observations to study all objects in the quasar field. Only then can the galaxy responsible for the quasar absorber be robustly identified and characterised.

This thesis, therefore, presents extensive work on the emission properties on this intriguing high redshift galaxy population, both in the form of long-slit spectroscopy utilising *VLT/FORS* data presented in

Paper I and broad-band photometric imaging *HST/WFC3* data presented in Paper III. In numbers, this thesis contributes with 14 new and 3 re-analysed emission characterisations of absorption selected galaxies, with derived stellar masses sampling a broad range of $8 \lesssim \log_{10}[M_{\star} (M_{\odot})] < 11$. This implies a contribution of $\sim 30\%$ to the 43 spectroscopically confirmed systems to date (Møller & Christensen 2019; Christensen et al. 2019). Out of the subsample of these, which have SED-based stellar masses, the work presented in this thesis contributes with $\sim 50\%$.

In Paper I, I employed *VLT/FORS2* long-slit spectroscopy to confirm photometrically determined candidate hosts of ten (sub-)DLAs at intermediate ($z \sim 0.7$) redshift and pre-selected to have high ($[M/H]_{\text{abs}} > -1$) metallicity. The campaign saw a success-rate of 70% and was able to confirm galaxy group environments for two absorbers at separate redshifts based on a single slit orientation in the quasar field of Q 1436-0051. Building on the methodology developed in Møller et al. (2013) and Christensen et al. (2014), I revisited their intriguing result which suggests a mean, linear metallicity-gradient that unifies measurements in emission and absorption. By incorporating our new detections, we retrieve the same mean metallicity gradient of $\Gamma = -0.022 \text{ dex kpc}^{-1}$ first reported in Christensen et al. (2014). This suggests that such a metallicity gradient is robust, significant and real. In addition, we introduce an observationally motivated truncation radius to inhibit the metallicity gradient from extending to infinity, and fix it to 12 kpc based on oxygen abundance gradients in low redshift galaxy discs (Sánchez et al. 2014). We show that albeit crude, such an *ad hoc* cut-off leads to a statistically improved match to absorption- and emission based mass-metallicity relations alike.

In the same paper, $H\beta$ and $[O\text{ II}]$ emission line diagnostics were used to derive spectroscopic star formation rates. Combining these with the SED-based stellar mass estimates, we show that a sub-sample of absorption selected galaxies with stellar masses above $\log_{10}[M_{\star} (M_{\odot})] \sim 10$ systematically probe sub-main-sequence star formation. This result is remarkable as that the objects are selected on gas cross-section and considering that a parallel ALMA programme exploring a sub-sample of the objects analysed in Paper I have large molecular gas masses, $M_{\text{mol}} \sim (0.6 - 8.2) \times 10^{10} M_{\odot}$, and gas fractions in the range $f_{\text{mol}} \sim 0.3 - 0.9$ (Møller et al. 2018; Kanekar et al. 2018).

In Paper II, I present the results from an initial study which confronts state-of-the-art cosmological hydrodynamic zoom-in simulations of a Milky Way mass galaxy (to be presented in Agertz et al. in prep.) with a recent compilation of spectroscopically confirmed galaxies hosting strong H I absorbers at $z \sim 0.4 - 3$ (Møller & Christensen 2019; Christensen et al. 2019). This work is motivated in part to explain detections of absorbers at large projected separations ($\gtrsim 20 \text{ kpc}$) from their hosts and in part, and more fundamentally, to answer which sight-lines through a galaxy produce sub-DLAs and which produce DLAs. By building probability functions in observationally spanned parameter spaces, we show that at all redshifts, the confirmed absorber-emitter systems are captured by the simulation outputs. This is a rather spectacular and observationally encouraging discovery, as it means that high impact parameter absorbers are not necessarily a selection effect. Whereas large-scale cosmological simulation (e.g. Rahmati & Schaye 2014) have difficulties explaining such absorbers, apparent from Figure 2.7, we here show that with high numerical resolution and efficient feedback, such sight-lines emerge from the combination of dwarf satellites in the main halo, stripped metal-rich gas, and outflows.

With these simulations, we show that the circum-galactic medium plays an increasingly important role in producing strong H I absorption towards progressively higher redshifts. However, even at $z \sim 0.4 - 1$, when an H I disc is in place, the CGM contributes with $\sim 20\%$ of absorbers above DLA column densities, and with $\sim 40\%$ above the sub-DLA limit.

In Paper III we present the results from an *HST* imaging follow-up campaign of ten spectroscopically confirmed galaxies harbouring strong H I absorbers at redshift $z \sim 2 - 3$. With Wide Field Camera 3 (WFC3), we secure broad-band photometry in the Ultraviolet-Visible *UVIS* channel *UVIS/F606W* and the Infrared (IR) channel *IR/F105W* and *F160W* filters, selected to cover the Balmer break. Combined with pre-existing spectroscopic redshifts, we determine stellar masses in the range $\log_{10}[M_{\star} (M_{\odot})] \sim 8 - 10$. With the high spatial resolution achieved in the drizzled science images, we show that a majority of the targets exhibit complex, clumpy star-forming morphologies. This enables us to measure half-light radii, which we determine to be in the range $r_{1/2} \sim 0.5 - 2.5$ kpc. Placed on luminosity-selected scaling relations, we show that our targets have the expected star formation rates at their respective mass and redshift of star-forming galaxies (Whitaker et al. 2014) and that their sizes are consistent with being drawn from the population of late-type galaxies (van der Wel et al. 2014). Combined with the relatively low stellar masses, we therefore conclude that absorption-selected galaxies at $z \sim 2 - 3$ trace the low-mass, late-type, star-forming galaxy populations - in agreement with the results of the only prior study of this kind (Møller et al. 2002).

2.6 Conclusions and Future Outlooks

The study of absorption selected galaxies has now reached a mature stage. We know what measures are needed to identify them (e.g. PSF and SPSF subtractions); we know that by pre-selecting on absorption metallicity we maximise campaign success rates; and we now have a sample of spectroscopically confirmed absorber-galaxy pairs, characterised in both emission and absorption, that is large enough to compare their statistical properties with other galaxy populations and alternative selection techniques. Parallel to these observational achievements, numerical simulations have seen an equally impressive development. With increased computing power, numerical resolution is shown to be a key to capture the CGM (Hummels et al. 2018; van de Voort et al. 2019; Peebles et al. 2019).

The research presented in this thesis has helped moving the field from being primarily concerned with absorbing clouds, to being concerned with their emission counterparts - thereby allowing them to be compared luminosity selected surveys. My work shows that absorption-selected galaxies preferentially samples (and overlaps with) the low-mass end of galaxy populations probed with luminosity-selected surveys at all redshifts. An absorption selection, therefore, provides a viable path-way towards studying faint galaxies, which with luminosity selections will only become possible with the next generation ground-based observatories like the Extremely Large Telescope (*ELT*) and with the launch of James Web Space Telescope (*JWST*).

At present, many questions concerning the nature of gas cross-section selected galaxies that harbour damped H I absorbers remain unanswered. However, the prospects for reconciling these objects with other galaxy populations and galaxy evolution at large are promising. To this end, I see three main

research foci following on the immediate results of this thesis. These concern metallicity gradients, star formation, and the life-cycle of gas parcels detected as sub-DLAs and DLAs.

With the data accumulated only since the start of this thesis, it is timely to revisit the linear metallicity gradient and its *ad hoc* truncation radius. Although its existence is robustly identified and consistent across three studies (Møller et al. 2013; Christensen et al. 2014; Rhodin et al. 2018), its form is less certain. Based on the data at hand, an immediate extension of these studies would, therefore, be to fit and compare different functional forms. If, as predicted by galaxy downsizing, stellar mass is a catalyst for evolution, we should - with enough data - test the hypothesis that the metallicity gradient is a function of stellar mass. Despite attempting to identify such a correlation in Rhodin et al. (2018), the data only allowed for a formal 2σ detection, and therefore we could not test the hypothesis of a metallicity-gradient-stellar-mass correlation.

Understanding the star formation of these objects is more challenging. In part because it requires addressing absorbing galaxy populations at different redshifts and in part because data for these samples are largely incomplete. An immediate extension is to secure *ALMA* data for the high-redshift *HST* sample for which spectroscopic confirmations and stellar mass estimates exist and are presented in Paper III of this thesis. Such data could provide important information on the molecular gas masses and gas fractions at a complementary redshift range to the results presented in Kanekar et al. (2018). This would allow us to test whether high gas masses is intrinsic to the absorbing galaxy population or a function of redshift. Either positive or negative results on large gas fractions and molecular gas masses will have important implications for our understanding of star formation in these objects.

A viable alternative is to directly test the hypothesis posed in Møller et al. (2018), namely that absorbing galaxies probe a short-lived post-starburst phase of galaxy evolution. This could be achieved by securing deep spectroscopic data to search for strong Balmer line absorption and a pronounced 4000\AA break. Both of these spectral features are expected to arise in a post-starburst phase for which A- and F- type stellar populations dominate (e.g. Wild et al. 2009). Such a programme, however, is extremely challenging. Targets have to be selected and studied at spatial resolutions capable of resolving the galaxy from the quasar and deep enough to robustly trace the intervening galaxy continuum rather than just focusing on its emission lines. This is something that current SPSF subtractions cannot do when the intervening system is at low impact parameters, as these methods rely on the contrast between an underlying continuum and an emission line to signal the presence of an absorbing galaxy.

Besides their usefulness as means of selecting targets, a final reflection concerns the *nature* of strong H I absorbers. If these truly sample a continuously replenished, transient phase of gas in the star formation-feedback cycle, the gas must relate to the cosmic baryon cycle at large. Using tracer particle methods to follow the evolution of parcels of gas that eventually produces the structures sampled with sub-DLAs and DLAs, simulations may be able to help us assess their role. Perhaps only then, we will be able to move beyond the formal column density definitions, and gain insights into what exactly strong H I absorbers are.

BIBLIOGRAPHY

- Agertz, O., Kravtsov, A. V., Leitner, S. N., & Gnedin, N. Y. 2013, *ApJ*, 770, 25
- Altay, G., Theuns, T., Schaye, J., Booth, C. M., & Dalla Vecchia, C. 2013, *MNRAS*, 436, 2689
- Bañados, E., Venemans, B. P., Mazzucchelli, C., et al. 2018, *Nature*, 553, 473
- Bahcall, J. N., & Peebles, P. J. E. 1969, *ApJ*, 156, L7
- Barnes, J. E., & Hernquist, L. 1996, *ApJ*, 471, 115
- Becker, R. H., Fan, X., White, R. L., et al. 2001, *AJ*, 122, 2850
- Behroozi, P. S., Wechsler, R. H., & Conroy, C. 2013, *ApJ*, 770, 57
- Benson, A. J., Bower, R. G., Frenk, C. S., et al. 2003, *ApJ*, 599, 38
- Berg, T. A. M., Ellison, S. L., Prochaska, J. X., Venn, K. A., & Dessauges-Zavadsky, M. 2015, *MNRAS*, 452, 4326
- Bigiel, F., Leroy, A., Walter, F., et al. 2008, *AJ*, 136, 2846
- Bird, S., Haehnelt, M., Neeleman, M., et al. 2015, *MNRAS*, 447, 1834
- Bird, S., Vogelsberger, M., Haehnelt, M., et al. 2014, *MNRAS*, 445, 2313
- Blanton, M. R., & Moustakas, J. 2009, *ARA&A*, 47, 159
- Bond, J. R., Kofman, L., & Pogosyan, D. 1996, *Nature*, 380, 603
- Bouwens, R. J., Illingworth, G. D., Blakeslee, J. P., Broadhurst, T. J., & Franx, M. 2004, *ApJ*, 611, L1
- Calvi, V., Stiavelli, M., Bradley, L., Pizzella, A., & Kim, S. 2014, *ApJ*, 796, 102
- Carrasco, E. R., Gomez, P. L., Verdugo, T., et al. 2010, *ApJ*, 715, L160
- Cassata, P., Cimatti, A., Kurk, J., et al. 2008, *A&A*, 483, L39
- Charlton, J., & Churchill, C. 2000, *Quasistellar Objects: Intervening Absorption Lines*, ed. P. Murdin, 2366
- Christensen, L., Møller, P., Rhodin, N. H. P., Heintz, K., & Fynbo, J. P. U. 2019, *MNRAS*
- Christensen, L., Møller, P., Fynbo, J. P. U., & Zafar, T. 2014, *MNRAS*, 445, 225

Christensen, L., Vergani, S. D., Schulze, S., et al. 2017, *A&A*, 608, A84

Cole, S., Helly, J., Frenk, C. S., & Parkinson, H. 2008, *MNRAS*, 383, 546

Colless, M., Dalton, G., Maddox, S., et al. 2001, *MNRAS*, 328, 1039

Collier, S., & Peterson, B. M. 2001, *ApJ*, 555, 775

Cooke, J., & O’Meara, J. M. 2015, *ApJ*, 812, L27

Cowie, L. L., & Hu, E. M. 1998, *AJ*, 115, 1319

Cox, T. J., Dutta, S. N., Di Matteo, T., et al. 2006, *ApJ*, 650, 791

Crighton, N. H. M., Murphy, M. T., Prochaska, J. X., et al. 2015, *MNRAS*, 452, 217

Davé, R., Katz, N., Oppenheimer, B. D., Kollmeier, J. A., & Weinberg, D. H. 2013, *MNRAS*, 434, 2645

De Cia, A., Ledoux, C., Petitjean, P., & Savaglio, S. 2018, *A&A*, 611, A76

Dekel, A., & Silk, J. 1986, *ApJ*, 303, 39

Dekel, A., Birnboim, Y., Engel, G., et al. 2009, *Nature*, 457, 451

Delgado-Serrano, R., Hammer, F., Yang, Y. B., et al. 2010, *A&A*, 509, A78

Dessauges-Zavadsky, M., Péroux, C., Kim, T.-S., D’Odorico, S., & McMahon, R. G. 2003, *MNRAS*, 345, 447

D’Odorico, V., Cupani, G., Cristiani, S., et al. 2013, *MNRAS*, 435, 1198

Dunlop, J. S. 2013, in *Astrophysics and Space Science Library*, Vol. 396, *The First Galaxies*, ed. T. Wiklind, B. Mobasher, & V. Bromm, 223

Ellison, S. L., Songaila, A., Schaye, J., & Pettini, M. 2000, *AJ*, 120, 1175

Erb, D. K., Shapley, A. E., Pettini, M., et al. 2006, *ApJ*, 644, 813

Erkal, D., Gnedin, N. Y., & Kravtsov, A. V. 2012, *ApJ*, 761, 54

Fabian, A. C. 2012, *ARA&A*, 50, 455

Fall, S. M., & Pei, Y. C. 1993, *ApJ*, 402, 479

Fan, X., Strauss, M. A., Becker, R. H., et al. 2006, *AJ*, 132, 117

Frank, J., King, A., & Raine, D. J. 2002, *Accretion Power in Astrophysics: Third Edition*, 398

Franx, M., Labbé, I., Rudnick, G., et al. 2003, *ApJ*, 587, L79

Fruchter, A. S., Levan, A. J., Strolger, L., et al. 2006, *Nature*, 441, 463

Fumagalli, M., O’Meara, J. M., & Prochaska, J. X. 2016, *MNRAS*, 455, 4100

Fumagalli, M., Prochaska, J. X., Kasen, D., et al. 2011, *MNRAS*, 418, 1796

- Fynbo, J. P. U., Prochaska, J. X., Sommer-Larsen, J., Dessauges-Zavadsky, M., & Møller, P. 2008, *ApJ*, 683, 321
- Fynbo, J. P. U., Jakobsson, P., Prochaska, J. X., et al. 2009, *ApJS*, 185, 526
- Fynbo, J. P. U., Laursen, P., Ledoux, C., et al. 2010, *MNRAS*, 408, 2128
- Fynbo, J. P. U., Ledoux, C., Noterdaeme, P., et al. 2011, *MNRAS*, 413, 2481
- Fynbo, J. P. U., Geier, S. J., Christensen, L., et al. 2013, *MNRAS*, 436, 361
- Fynbo, J. U., Møller, P., & Thomsen, B. 2001, *A&A*, 374, 443
- Galama, T. J., Vreeswijk, P. M., van Paradijs, J., et al. 1998, *Nature*, 395, 670
- Garnett, D. R., & Shields, G. A. 1987, *ApJ*, 317, 82
- González Delgado, R. M., García-Benito, R., Pérez, E., et al. 2015, *A&A*, 581, A103
- Gu, M., Conroy, C., & Brammer, G. 2018, *ApJ*, 862, L18
- Gunn, J. E., & Peterson, B. A. 1965, *ApJ*, 142, 1633
- Haehnelt, M. G., Steinmetz, M., & Rauch, M. 1998, *ApJ*, 495, 647
- Hammer, F., Flores, H., Puech, M., et al. 2009, *A&A*, 507, 1313
- Hayes, M., Östlin, G., Schaerer, D., et al. 2010, *Nature*, 464, 562
- Heavens, A., Panter, B., Jimenez, R., & Dunlop, J. 2004, *Nature*, 428, 625
- Hjorth, J., Sollerman, J., Møller, P., et al. 2003, *Nature*, 423, 847
- Hjorth, J., Malesani, D., Jakobsson, P., et al. 2012, *ApJ*, 756, 187
- Hogg, D. W., Eisenstein, D. J., Blanton, M. R., et al. 2005, *ApJ*, 624, 54
- Hopkins, P. F., Quataert, E., & Murray, N. 2011, *MNRAS*, 417, 950
- Hu, E. M., Cowie, L. L., & McMahon, R. G. 1998, *ApJ*, 502, L99
- Hubble, E. P. 1926, *ApJ*, 64
- Hummels, C. B., Smith, B. D., Hopkins, P. F., et al. 2018, arXiv e-prints
- Ishibashi, W., & Fabian, A. C. 2016, *MNRAS*, 457, 2864
- Kanekar, N., Prochaska, J. X., Christensen, L., et al. 2018, *ApJ*, 856, L23
- Katz, N., Keres, D., Dave, R., & Weinberg, D. H. 2003, in *Astrophysics and Space Science Library*, Vol. 281, *The IGM/Galaxy Connection. The Distribution of Baryons at $z=0$* , ed. J. L. Rosenberg & M. E. Putman, 185
- Kereš, D., Katz, N., Davé, R., Fardal, M., & Weinberg, D. H. 2009, *MNRAS*, 396, 2332

Kereš, D., Katz, N., Weinberg, D. H., & Davé, R. 2005, *MNRAS*, 363, 2

Khostovan, A. A., Sobral, D., Mobasher, B., et al. 2015, *MNRAS*, 452, 3948

Kim, J.-h., Abel, T., Agertz, O., et al. 2014, *ApJS*, 210, 14

Kim, J.-h., Agertz, O., Teyssier, R., et al. 2016, *ApJ*, 833, 202

Kim, M., Ho, L. C., Peng, C. Y., Barth, A. J., & Im, M. 2008, *ApJS*, 179, 283

Kirby, E. N., Boylan-Kolchin, M., Cohen, J. G., et al. 2013, *ApJ*, 770, 16

Kirby, E. N., Rizzi, L., Held, E. V., et al. 2017, *ApJ*, 834, 9

Kormendy, J., & Ho, L. C. 2013, *ARA&A*, 51, 511

Kouveliotou, C., Meegan, C. A., Fishman, G. J., et al. 1993, *ApJ*, 413, L101

Krogager, J.-K., Møller, P., Fynbo, J. P. U., & Noterdaeme, P. 2017, *MNRAS*, 469, 2959

Kulkarni, S. R., Djorgovski, S. G., Odewahn, S. C., et al. 1999, *Nature*, 398, 389

Kumar, P., & Zhang, B. 2015, *Phys. Rep.*, 561, 1

Laursen, P., Razoumov, A. O., & Sommer-Larsen, J. 2009, *ApJ*, 696, 853

Ledoux, C., Petitjean, P., Fynbo, J. P. U., Møller, P., & Srianand, R. 2006, *A&A*, 457, 71

Ledoux, C., Vreeswijk, P. M., Smette, A., et al. 2009, *A&A*, 506, 661

Lee, K.-G., Hennawi, J. F., White, M., et al. 2016, *ApJ*, 817, 160

Lee, K.-G., Krolewski, A., White, M., et al. 2018, *ApJS*, 237, 31

Lehner, N., O’Meara, J. M., Fox, A. J., et al. 2014, *ApJ*, 788, 119

Leitner, S. N., & Kravtsov, A. V. 2011, *ApJ*, 734, 48

Liang, C. J., Kravtsov, A. V., & Agertz, O. 2016, *MNRAS*, 458, 1164

—. 2018, *MNRAS*, 479, 1822

Lopez, S., Tejos, N., Ledoux, C., et al. 2018, *Nature*, 554, 493

Lynden-Bell, D. 1969, *Nature*, 223, 690

Lynds, R. 1971, *ApJ*, 164, L73

MacLeod, C. L., Ivezić, Ž., Kochanek, C. S., et al. 2010, *ApJ*, 721, 1014

Madau, P., & Dickinson, M. 2014, *ARA&A*, 52, 415

Maiolino, R., Nagao, T., Grazian, A., et al. 2008, *A&A*, 488, 463

Maller, A. H., Prochaska, J. X., Somerville, R. S., & Primack, J. R. 2001, *MNRAS*, 326, 1475

Mannucci, F., Cresci, G., Maiolino, R., Marconi, A., & Gnerucci, A. 2010, *MNRAS*, 408, 2115

Martin, A. M., Papastergis, E., Giovanelli, R., et al. 2010, *ApJ*, 723, 1359

Mas-Ribas, L., Riemer-Sørensen, S., Hennawi, J. F., et al. 2018, *ApJ*, 862, 50

Mawatari, K., Inoue, A. K., Kousai, K., et al. 2016, *ApJ*, 817, 161

McGuire, J. T. W., Tanvir, N. R., Levan, A. J., et al. 2016, *ApJ*, 825, 135

McMillan, P. J. 2017, *MNRAS*, 465, 76

Mihos, J. C., & Hernquist, L. 1994, *ApJ*, 431, L9

—. 1996, *ApJ*, 464, 641

Mo, H. J., Mao, S., & White, S. D. M. 1998, *MNRAS*, 295, 319

Møller, P., & Christensen, L. 2019, *MNRAS*

Møller, P. 2000, *The Messenger*, 99, 31

Møller, P., Fynbo, J. P. U., Ledoux, C., & Nilsson, K. K. 2013, *MNRAS*, 430, 2680

Møller, P., & Warren, S. J. 1993, *A&A*, 270, 43

—. 1998, *MNRAS*, 299, 661

Møller, P., Warren, S. J., Fall, S. M., Fynbo, J. U., & Jakobsen, P. 2002, *ApJ*, 574, 51

Møller, P., Warren, S. J., Fall, S. M., Jakobsen, P., & Fynbo, J. U. 2000, *The Messenger*, 99, 33

Møller, P., Christensen, L., Zwaan, M. A., et al. 2018, *MNRAS*, 474, 4039

Mortlock, D. J., Warren, S. J., Venemans, B. P., et al. 2011, *Nature*, 474, 616

Neeleman, M., Wolfe, A. M., Prochaska, J. X., & Rafelski, M. 2013, *ApJ*, 769, 54

Noeske, K. G., Weiner, B. J., Faber, S. M., et al. 2007, *ApJ*, 660, L43

Noterdaeme, P., Petitjean, P., Ledoux, C., & Srianand, R. 2009, *A&A*, 505, 1087

Noterdaeme, P., Petitjean, P., Carithers, W. C., et al. 2012a, *A&A*, 547, L1

Noterdaeme, P., Laursen, P., Petitjean, P., et al. 2012b, *A&A*, 540, A63

Oppenheimer, B. D., Davé, R., Kereš, D., et al. 2010, *MNRAS*, 406, 2325

Peebles, M. S., Corlies, L., Tumlinson, J., et al. 2019, *ApJ*, 873, 129

Peng, C. Y., Impey, C. D., Rix, H.-W., et al. 2006, *ApJ*, 649, 616

Penzias, A. A., & Wilson, R. W. 1965, *ApJ*, 142, 419

Perley, D. A., Krühler, T., Schulze, S., et al. 2016, *ApJ*, 817, 7

Perlmutter, S., Aldering, G., Goldhaber, G., et al. 1999, *ApJ*, 517, 565

Péroux, C., Bouché, N., Kulkarni, V. P., York, D. G., & Vladilo, G. 2011, *MNRAS*, 410, 2237

Péroux, C., Dessauges-Zavadsky, M., D’Odorico, S., Kim, T.-S., & McMahon, R. G. 2003, *MNRAS*, 345, 480

—. 2007, *MNRAS*, 382, 177

Péroux, C., Meiring, J. D., Kulkarni, V. P., et al. 2008, *MNRAS*, 386, 2209

Pettini, M., Smith, L. J., Hunstead, R. W., & King, D. L. 1994, *ApJ*, 426, 79

Planck Collaboration, Ade, P. A. R., Aghanim, N., et al. 2014a, *A&A*, 571, A19

—. 2014b, *A&A*, 571, A16

—. 2016, *A&A*, 594, A13

Prochaska, J. X., Chen, H.-W., Dessauges-Zavadsky, M., & Bloom, J. S. 2007, *ApJ*, 666, 267

Prochaska, J. X., Chen, H.-W., Wolfe, A. M., Dessauges-Zavadsky, M., & Bloom, J. S. 2008, *ApJ*, 672, 59

Prochaska, J. X., Gawiser, E., Wolfe, A. M., Castro, S., & Djorgovski, S. G. 2003, *ApJ*, 595, L9

Prochaska, J. X., Herbert-Fort, S., & Wolfe, A. M. 2005, *ApJ*, 635, 123

Prochaska, J. X., Madau, P., O’Meara, J. M., & Fumagalli, M. 2014, *MNRAS*, 438, 476

Prochaska, J. X., & Wolfe, A. M. 1997, *ApJ*, 487, 73

Rafelski, M., Neeleman, M., Fumagalli, M., Wolfe, A. M., & Prochaska, J. X. 2014, *ApJ*, 782, L29

Rafelski, M., Wolfe, A. M., Prochaska, J. X., Neeleman, M., & Mendez, A. J. 2012, *ApJ*, 755, 89

Rahmati, A., & Schaye, J. 2014, *MNRAS*, 438, 529

Rao, S. M., Belfort-Mihalyi, M., Turnshek, D. A., et al. 2011, *MNRAS*, 416, 1215

Rao, S. M., & Turnshek, D. A. 2000, *ApJS*, 130, 1

Rao, S. M., Turnshek, D. A., & Nestor, D. B. 2006, *ApJ*, 636, 610

Rhodin, N. H. P., Christensen, L., Møller, P., Zafar, T., & Fynbo, J. P. U. 2018, *A&A*, 618, A129

Richstone, D. O., & Schmidt, M. 1980, *ApJ*, 235, 361

Riess, A. G., Filippenko, A. V., Challis, P., et al. 1998, *AJ*, 116, 1009

Roberts, M. S., & Haynes, M. P. 1994, *ARA&A*, 32, 115

Sánchez, S. F., Rosales-Ortega, F. F., Iglesias-Páramo, J., et al. 2014, *A&A*, 563, A49

Sánchez-Ramírez, R., Ellison, S. L., Prochaska, J. X., et al. 2016, *MNRAS*, 456, 4488

Savaglio, S. 2006, *New Journal of Physics*, 8, 195

Savaglio, S., Glazebrook, K., Le Borgne, D., et al. 2005, *ApJ*, 635, 260

Scannapieco, C., Wadepuhl, M., Parry, O. H., et al. 2012, *MNRAS*, 423, 1726

Schramm, M., Wisotzki, L., & Jahnke, K. 2008, *A&A*, 478, 311

Selsing, J., Malesani, D., Goldoni, P., et al. 2018, arXiv e-prints

Shakura, N. I., & Sunyaev, R. A. 1973, *A&A*, 24, 337

Simcoe, R. A., Sargent, W. L. W., & Rauch, M. 2004, *ApJ*, 606, 92

Som, D., Kulkarni, V. P., Meiring, J., et al. 2013, *MNRAS*, 435, 1469

—. 2015, *ApJ*, 806, 25

Somerville, R. S., Hopkins, P. F., Cox, T. J., Robertson, B. E., & Hernquist, L. 2008, *MNRAS*, 391, 481

Springel, V., Frenk, C. S., & White, S. D. M. 2006, *Nature*, 440, 1137

Springel, V., White, S. D. M., Jenkins, A., et al. 2005, *Nature*, 435, 629

Steidel, C. C., Adelberger, K. L., Shapley, A. E., et al. 2003, *ApJ*, 592, 728

Steidel, C. C., Giavalisco, M., Dickinson, M., & Adelberger, K. L. 1996a, *AJ*, 112, 352

Steidel, C. C., Giavalisco, M., Pettini, M., Dickinson, M., & Adelberger, K. L. 1996b, *ApJ*, 462, L17

Steinmetz, M., & Navarro, J. F. 2002, *New Astronomy*, 7, 155

Thöne, C. C., Greiner, J., Savaglio, S., & Jehin, E. 2007, *ApJ*, 671, 628

Tremonti, C. A., Heckman, T. M., Kauffmann, G., et al. 2004, *ApJ*, 613, 898

Tumlinson, J., Peebles, M. S., & Werk, J. K. 2017, *ARA&A*, 55, 389

Tytler, D. 1982, *Nature*, 298, 427

Übler, H., Naab, T., Oser, L., et al. 2014, *MNRAS*, 443, 2092

Urry, C. M., & Padovani, P. 1995, *PASP*, 107, 803

van de Voort, F., Schaye, J., Booth, C. M., & Dalla Vecchia, C. 2011a, *MNRAS*, 415, 2782

van de Voort, F., Schaye, J., Booth, C. M., Haas, M. R., & Dalla Vecchia, C. 2011b, *MNRAS*, 414, 2458

van de Voort, F., Springel, V., Mandelker, N., van den Bosch, F. C., & Pakmor, R. 2019, *MNRAS*, 482, L85

van der Wel, A., Franx, M., van Dokkum, P. G., et al. 2014, *ApJ*, 788, 28

Verhamme, A., Schaerer, D., Atek, H., & Tapken, C. 2008, *A&A*, 491, 89

Whitaker, K. E., Franx, M., Leja, J., et al. 2014, *ApJ*, 795, 104

White, S. D. M., & Frenk, C. S. 1991, *ApJ*, 379, 52

- White, S. D. M., & Rees, M. J. 1978, MNRAS, 183, 341
- Wild, V., Walcher, C. J., Johansson, P. H., et al. 2009, MNRAS, 395, 144
- Williams, R. E., Blacker, B., Dickinson, M., et al. 1996, AJ, 112, 1335
- Wolfe, A. M., Lanzetta, K. M., Foltz, C. B., & Chaffee, F. H. 1995, ApJ, 454, 698
- Wolfe, A. M., Turnshek, D. A., Smith, H. E., & Cohen, R. D. 1986, ApJS, 61, 249
- Wuyts, S., Förster Schreiber, N. M., Genzel, R., et al. 2012, ApJ, 753, 114
- York, D. G., Adelman, J., Anderson, Jr., J. E., et al. 2000, AJ, 120, 1579
- Zafar, T., Møller, P., Péroux, C., et al. 2017, MNRAS, 465, 1613
- Zafar, T., Péroux, C., Popping, A., et al. 2013, A&A, 556, A141
- Zahid, H. J., Kashino, D., Silverman, J. D., et al. 2014, ApJ, 792, 75
- Zwaan, M. A., Meyer, M. J., Staveley-Smith, L., & Webster, R. L. 2005a, MNRAS, 359, L30
- Zwaan, M. A., van der Hulst, J. M., Briggs, F. H., Verheijen, M. A. W., & Ryan-Weber, E. V. 2005b, MNRAS, 364, 1467

PART II
RESEARCH PAPERS

Paper I

Stellar masses, metallicity gradients, and suppressed star formation revealed in a new sample of absorption selected galaxies

N. H. P. Rhodin¹, L. Christensen¹, P. Møller², T. Zafar³, and J. P. U. Fynbo⁴

¹ Dark Cosmology Centre, Niels Bohr Institute, University of Copenhagen, Juliane Maries Vej 30, 2100 Copenhagen Ø, Denmark
e-mail: henrikrhodin@dark-cosmology.dk

² European Southern Observatory, Karl-Schwarzschildstrasse 2, 85748 Garching bei München, Germany

³ Australian Astronomical Observatory, PO Box 915, North Ryde, NSW 1670, Australia

⁴ The Cosmic Dawn Center, Niels Bohr Institute, University of Copenhagen, Juliane Maries Vej 30, 2100 Copenhagen Ø, Denmark

Received 9 March 2018 / Accepted 2 July 2018

ABSTRACT

Context. Absorbing galaxies are selected via the detection of characteristic absorption lines which their gas-rich media imprint in the spectra of distant light-beacons. The proximity of the typically faint foreground absorbing galaxies to bright background sources makes it challenging to robustly identify these in emission, and hence to characterise their relation to the general galaxy population.

Aims. We search for emission to confirm and characterise ten galaxies hosting damped, metal-rich quasar absorbers at redshift $z < 1$.

Methods. We identified the absorbing galaxies by matching spectroscopic absorption -and emission redshifts and from projected separations. Combining emission-line diagnostics with existing absorption spectroscopy and photometry of quasar-fields hosting metal-rich, damped absorbers, we compare our new detections with reference samples and place them on scaling relations.

Results. We spectroscopically confirm seven galaxies harbouring damped absorbers (a 70% success-rate). Our results conform to the emerging picture that neutral gas on scales of tens of kpc in galaxies is what causes the characteristic H I absorption. Our key results are: (I) Absorbing galaxies with $\log_{10}[M_{\star} (M_{\odot})] \geq 10$ have star formation rates that are lower than predicted for the main sequence of star formation. (II) The distribution of impact parameter with H I column density and with absorption-metallicity for absorbing galaxies at $z \sim 2-3$ extends to $z \sim 0.7$ and to lower H I column densities. (III) A robust mean metallicity gradient of $\langle \Gamma \rangle = -0.022 \pm 0.001 \text{ dex kpc}^{-1}$. (IV) By correcting absorption metallicities for $\langle \Gamma \rangle$ and imposing a truncation-radius at 12 kpc, absorbing galaxies fall on top of predicted mass-metallicity relations, with a statistically significant decrease in scatter.

Key words. Galaxy: halo – galaxies: evolution – galaxies: distances and redshifts – galaxies: stellar content – galaxies: star formation

1. Introduction

Scaling relations between galaxy observables (direct measurements and derived quantities) allow us to probe what drives galaxy evolution, and act as standard tests for simulations. Historically, scaling relations have been derived for luminosity-selected samples. In particular, such selection criteria have revealed a redshift-dependent relation between the galaxy stellar mass (M_{\star}) and the gas-phase metallicity (Z_{gas}) in the redshift range $z \sim 0.1-3.5$ (Tremonti et al. 2004; Savaglio et al. 2005; Erb et al. 2006; Maiolino et al. 2008); and a relation between M_{\star} and star formation rate (SFR; Noeske et al. 2007). These relations were combined as projections of a fundamental redshift-invariant relation tying M_{\star} , Z_{gas} , and SFR together (Mannucci et al. 2010).

Complementing these luminosity selections, galaxies can be selected via their absorption cross-section in neutral gas when there is a chance alignment of the target with a background quasar along the line of sight. Such configurations imprint strong characteristic absorption lines in the quasar spectrum, caused by the high column density H I gas in either discs, circumgalactic material (CGM) or galaxy haloes. The strongest classes of absorbers are the damped Lyman- α systems (DLAs) with neutral hydrogen column densities $\log_{10}[N_{\text{HI}} (\text{cm}^{-2})] \geq 20.3$ (Wolfe et al. 1986), and the sub-DLAs with column densities of $19.0 \leq \log_{10}[N_{\text{HI}} (\text{cm}^{-2})] < 20.3$ (Péroux et al. 2003;

Zafar et al. 2013b). Both classes have characteristic Lorentzian damping wings associated with their Lyman- α profiles. Unless otherwise specified, we refer to sub-DLAs and DLAs uniformly as damped absorbers.

With a detectability that is independent of the host galaxy's brightness, damped absorbers are believed to sample the general galaxy population in a more representative manner, probing a larger dynamic range in stellar mass, gas-phase metallicity, star formation rate and morphology at any redshift. Indeed, this assertion was confirmed by comparing how absorption- and luminosity-selections sample the underlying luminosity function (Berry et al. 2016; Krogager et al. 2017).

This implies that a pure H I selection based on damped absorbers, on average samples lower-mass systems, often below the detection-limit in emission (Fynbo et al. 1999, 2008, 2010; Møller et al. 2002; Pontzen et al. 2008; Krogager et al. 2012; Rahmati & Schaye 2014; Fumagalli et al. 2015). In combination with a small projected separation to the absorption, which causes the quasar to dominate the light-throughout in a blended point spread function (PSF), this has led to a low average detection rate ($\sim 10\%$) of confirmed counterparts (Møller & Warren 1998; Christensen et al. 2007; Monier et al. 2009; Fynbo et al. 2010, 2011, 2013a; Meiring et al. 2011; Krogager et al. 2012, 2013; Noterdaeme et al. 2012a; Péroux et al. 2012; Rahmani et al. 2016). This has prevented us from characterising the connection the majority of absorbers hold to their galaxy hosts. But

presumably, sub-DLAs and DLAs on average sample different environments.

The DLA population contains the bulk of neutral gas throughout cosmic time ($\Omega_{\text{HI}}^{\text{DLA}} \gtrsim 80\%$; Prochaska et al. 2005; Noterdaeme et al. 2009, 2012b), and displays a weak redshift-evolution by a factor of ~ 3 from redshift $z \sim 5$ to the local universe (Neeleman et al. 2016a). Sub-DLAs account for the bulk of the remaining fraction in the redshift range $1.5 < z < 5.0$ ($\Omega_{\text{HI}}^{\text{sub-DLA}} \sim 8\text{--}20\%$; Zafar et al. 2013a), the Lyman limit systems (LLS, $17 \leq \log_{10}[N_{\text{HI}}(\text{cm}^{-2})] < 19.0$) and Ly α forest ($\log_{10}[N_{\text{HI}}(\text{cm}^{-2})] < 17.0$) only contributing minor fractions to the total neutral gas content (Songaila & Cowie 2010).

The chemical enrichment of the DLA population evolves from $\sim 1\%$ solar metallicity at $z = 5$ to $\sim 10\%$ solar metallicity in the local universe, with a ~ 2 dex metallicity-spread at all redshifts (Pettini et al. 1994; Ledoux et al. 2002; Prochaska et al. 2003; Rafelski et al. 2014). This evolution and its scatter is sensitive to the underlying selection function, and can be understood as an interplay between (i) drawing from the full galaxy population at every redshift; (ii) the existence of a mass-metallicity relation at every redshift (Ledoux et al. 2005; Møller et al. 2013; Christensen et al. 2014); and (iii) a metallicity gradient within each galaxy reflecting the gradual build-up of metals in the interstellar medium (ISM) and CGM by stellar feedback and supernovae explosions. Although metallicity measurements in sub-DLAs rely on ionisation corrections (see e.g., Zafar et al. 2017), these systems are believed to be more chemically enriched than DLAs on average – in particular at low redshifts (Péroux et al. 2006; Kulkarni et al. 2007; Meiring et al. 2009; Som et al. 2013, 2015), and there are indications that sub-DLAs arise in more massive galaxies (Kulkarni et al. 2010), which may be caused by selection biases (Dessauges-Zavadsky et al. 2009).

The existence of a statistically significant anti-correlation between $\log_{10}[N_{\text{HI}}(\text{cm}^{-2})]$ and projected separation based on photometric redshift identifications of hosts was demonstrated by Rao et al. (2011). This is consistent with spectroscopically confirmed systems which indicate that absorbers are distributed over different impact parameters; sub-DLAs showing larger and more scattered impact parameters than DLAs (Møller & Warren 1998; Christensen et al. 2007; Monier et al. 2009; Fynbo et al. 2010, 2011, 2013a; Meiring et al. 2011; Krogager et al. 2012, 2013; Noterdaeme et al. 2012a; Péroux et al. 2012; Rahmani et al. 2016). This distribution is observed in $z \gtrsim 2$ simulations, and is attributed to the complex distribution- and flow of HI-gas (Pontzen et al. 2008; Rahmati & Schaye 2014). In addition, the distribution of impact parameters correlates with absorption metallicity ($[M/H]_{\text{abs}}$), suggesting that DLAs probe the size of gaseous discs. This is supported by modelling DLAs as sight-lines through randomly inclined discs in high- z Lyman break galaxies (LBG), which shows that the two are drawn from the same underlying distribution above $z \sim 2$ (Møller et al. 2004; Fynbo et al. 2008; Krogager et al. 2017).

Recent developments found a scaling relation that tie velocity-widths of metal lines in absorption to the absorber metallicity (the $\Delta V_{90} - [M/H]_{\text{abs}}$ relation). This relation is redshift-dependent (Ledoux et al. 2006; Møller et al. 2013; Neeleman et al. 2013), column-density-dependent (Som et al. 2015), and is interpreted as the absorber equivalent of the MZ-relation. Recognising that the relation can be used to target the most metal-rich absorbers has significantly increased the detection rate of absorbing galaxies in emission to $\sim 60\text{--}70\%$, because these are associated with more massive and therefore more luminous galaxies (Fynbo et al. 2010, 2011,

2013a; Krogager et al. 2012, 2013; Noterdaeme et al. 2012a; Péroux et al. 2012; Bouché et al. 2013; Rahmani et al. 2016). Connecting the $\Delta V_{90} - [M/H]_{\text{abs}}$ relation to the MZ-relation, Møller et al. (2013) predicted stellar masses in functional form $f([M/H]_{\text{abs}}, z_{\text{abs}})$, including a free parameter $C_{[M/H]}$ to reconcile the difference between absorption- and emission-line metallicities. The relation was verified directly by comparing the stellar masses from the functional form to those derived from spectral energy distribution (SED)-fits, spanning three orders of magnitude in stellar mass (Christensen et al. 2014).

To characterise absorption selected galaxies and how they relate to the general galaxy population hinges on the low number of spectroscopically confirmed systems with complementary data in absorption and emission. Here, we attempt to rectify this issue by reporting our results from a long-slit spectroscopic follow-up of candidate hosts at redshifts $z < 1$.

The paper is organised as follows: Sect. 2 describes the sample selection, observations and archival data; Sect. 3 presents our spectroscopic measurements, extracted physical parameters and stellar masses of the absorbing galaxies. In Sect. 4 we combine with literature samples to investigate distributions and scaling relations. In Sect. 5 we summarise our conclusions. Throughout this paper we assume a flat Λ cold dark matter (Λ CDM) cosmology, with $H_0 = 70.4 \text{ km s}^{-1} \text{ Mpc}^{-1}$ and $\Omega_{\Lambda} = 0.727$ (Komatsu et al. 2011).

2. Observations and data-reduction

2.1. Sample selection

The sample represents the observed subset of targets as part of a programme to provide spectroscopic redshift-confirmation of damped absorber ($\log_{10}[N_{\text{HI}}(\text{cm}^{-2})] > 19.5$) counterparts at low ($z_{\text{abs}} < 1$) redshifts (programme ID 095.A-0890(A); PI: L. Christensen). We proposed ten quasar fields including 12 absorbers for long-slit spectroscopic observations with the ESO/VLT Focal Reducer and low dispersion Spectrograph 2 (FOR2; Appenzeller et al. 1998). See Sect. 2.2 for more details. However, only eight quasar fields containing ten absorbers were observed. Of these eight quasar fields, Q 1436–0051 and Q 1209+107 both contain two absorbers each. The spatial positions of the candidate-hosts of both absorbers towards Q 1436–0051 allowed them to be observed with a single slit placement, whilst the candidate-hosts in the Q 1209+107 quasar field required two different slit-alignments (PA1 and PA2). In sum, we therefore report the results for nine slit alignments targeting ten absorbers.

We selected targets with metallicities $[M/H]_{\text{abs}} \gtrsim -1$ as inferred from relative element ratios measured in high resolution spectra (Table 1 and references therein), and that have a tentative galaxy counterpart based on projected separation and photometric redshift solutions consistent with z_{abs} (Rao et al. 2011). Zinc is minimally depleted onto dust which allowed us to use it as a direct tracer-element for the absorption-metallicity (but see De Cia et al. 2018 for evidence of marginal depletion of zinc onto dust grains, in which case zinc represents a lower limit). For objects where we only had access to iron and chromium measurements, we inferred the absorption metallicity by applying a constant correction factor of 0.3 dex to account for depletion and α -enhancement (Rafelski et al. 2012, our Sect. 3.9). The physical properties of the targets are summarised in Table 1.

At $z < 1.65$, Ly α falls in the UV. This restricts HI column-density measurements to the systems observed with expensive

Table 1. Absorber characteristics and photometry of the candidate host galaxies explored with our FORS2 campaign.

Quasar field	E_{B-V}^* (mag)	z_{abs}	$\log_{10}[N_{\text{HI}} (\text{cm}^{-2})]$	$[M/H]_{\text{abs}}$		z_{phot}	Filter	Magnitude (AB)	A_{λ}^{\dagger} (mag)							
				Tracer	(dex)											
HE 1122-1649	0.0369	0.6819 ^a	20.45 ± 0.05 ^{a,b}	Fe	−1.40 ± 0.05 ^b	0.69 ^c	<i>U</i>	23.19 ± 0.08 ^c	+0.05 [‡]							
							<i>V</i>	23.01 ± 0.06 ^c	+0.03 [‡]							
							<i>I</i>	22.33 ± 0.03 ^c	+0.02 [‡]							
							<i>J</i>	22.10 ± 0.10 ^c	+0.01 [‡]							
							<i>H</i>	21.72 ± 0.09 ^c	+0.01 [‡]							
Q 0153+0009	0.0300	0.7714 ^d	19.70 ^{+0.08} _{−0.10} ^{d,e}	Cr	−0.52 ± 0.20 ^e	0.745 ± 0.040 ^f	<i>u'</i>	24.96 ± 0.70 ^g	0.15							
							<i>g'</i>	24.30 ± 0.38 ^f	0.11							
							<i>r'</i>	23.18 ± 0.24 ^f	0.08							
							<i>i'</i>	22.24 ± 0.18 ^f	0.06							
							<i>z'</i>	21.18 ± 0.50 ^f	0.04							
							<i>J</i>	21.43 ± 0.07 ^f	0.03							
							<i>H</i>	21.39 ± 0.10 ^f	0.02							
							<i>K</i>	21.01 ± 0.07 ^f	0.01							
							<i>g'</i>	<21.02 ^f	–							
							<i>i'</i>	21.93 ± 0.11 ^f	–							
Q 1209+107	0.0217	0.6295 ^d	20.30 ^{+0.18} _{−0.30} ^d	Fe	−0.9 ± 0.40 ^{h,†}	0.644 ± 0.100 ^f	<i>g'</i>	<21.02 ^f	–							
							<i>i'</i>	21.93 ± 0.11 ^f	–							
							<i>J</i>	21.36 ± 0.06 ^f	–							
							<i>H</i>	20.72 ± 0.05 ^f	–							
							<i>K</i>	19.89 ± 0.03 ^f	–							
		0.3930 ^d	19.46 ^{+0.08} _{−0.08} ^d	Zn	0.04 ± 0.20 ⁱ	0.3922 ± 0.0003 ^{j,***}	<i>u'</i>	23.21 ± 0.18 ^f	0.11							
	<i>g'</i>						21.55 ± 0.11 ^f	0.08								
	<i>r'</i>						22.68 ± 0.76 ^f	0.06								
	<i>i'</i>						21.48 ± 0.10 ^f	0.04								
	<i>J</i>						22.04 ± 0.11 ^f	0.02								
		0.7160 ^d	20.40 ^{+0.30} _{−0.40} ^k	Zn	0.40 ^{+0.3} _{−0.3} ^k	0.182 ± 0.244 ^f	<i>H</i>	22.64 ± 0.18 ^f	0.01							
	<i>K</i>						21.83 ± 0.13 ^f	0.01								
	<i>u'</i>						24.89 ± 0.81 ^f	0.12								
	<i>g'</i>						22.64 ± 0.22 ^f	0.09								
	<i>r'</i>						21.90 ± 0.14 ^f	0.06								
Q 1323−0021	0.0232	0.7160 ^d	20.40 ^{+0.30} _{−0.40} ^k	Zn	0.40 ^{+0.3} _{−0.3} ^k	0.182 ± 0.244 ^f	<i>i'</i>	22.03 ± 0.23 ^f	0.05							
							<i>z'</i>	20.20 ± 0.15 ^k	0.02							
							$m_{11200 \text{ \AA}}$	19.90 ± 0.25 ^k	0.02							
							$m_{13500 \text{ \AA}}$	19.16 ± 0.13 ^l	0.01							
							<i>K</i>	19.16 ± 0.13 ^l	0.01							
							Q 1436−0051	0.0321	0.7377 ^d	20.08 ^{+0.10} _{−0.12} ^d	Zn	−0.05 ± 0.12 ^m	–	<i>g'</i>	22.49 ± 0.10 ⁿ	–
														<i>r'</i>	21.62 ± 0.06 ⁿ	–
														<i>i'</i>	20.82 ± 0.05 ⁿ	–
														<i>z'</i>	20.69 ± 0.08 ⁿ	–
														<i>J</i>	20.19 ± 0.03 ^f	0.03
														<i>H</i>	19.82 ± 0.03 ^f	0.02
														<i>K</i>	17.54 ± 0.05 ^f	0.01
														<i>u'</i>	26.22 ± 1.20 ^f	0.16
														<i>g'</i>	23.72 ± 0.17 ⁿ	–
														<i>r'</i>	22.95 ± 0.12 ⁿ	–
	0.9281 ^d	18.4 ± 0.98 ^o	Zn	−0.05 ± 0.55 ^{o,p}	–	<i>i'</i>	22.14 ± 0.10 ⁿ	–								
<i>z'</i>						21.97 ± 0.15 ⁿ	–									
<i>J</i>						21.07 ± 0.06 ^f	0.03									
<i>H</i>						20.80 ± 0.06 ^f	0.02									
<i>K</i>						18.76 ± 0.15 ^f	0.01									
Q 2328+0022	0.0345	0.6519 ^d	20.32 ^{+0.06} _{−0.07} ^d	Zn	−0.49 ± 0.22 ^q	0.815 ± 0.242 ^f	<i>u'</i>	22.60 ± 0.78 ^f	0.17							
							<i>g'</i>	23.23 ± 0.14 ^f	0.13							
							<i>r'</i>	22.61 ± 0.17 ^f	0.09							
							<i>i'</i>	21.37 ± 0.11 ^f	0.07							
							<i>z'</i>	21.01 ± 0.45 ^f	0.05							
							<i>J</i>	>20.04 ± 0.13 ^f	0.03							
							<i>H</i>	>19.23 ± 0.02 ^f	0.02							
							<i>K</i>	>19.89 ± 0.04 ^f	0.01							
							<i>u'</i>	23.90 ± 0.78 ^s	0.29							
							<i>g'</i>	22.76 ± 0.14 ^s	0.23							
Q 2335+1501	0.0598	0.6798 ^{d,e}	19.70 ± 0.30 ^p	Zn	0.07 ± 0.34 ^p	–	<i>r'</i>	21.84 ± 0.09 ^s	0.16							
							<i>i'</i>	21.33 ± 0.09 ^s	0.12							
							<i>z'</i>	21.56 ± 0.48 ^s	0.09							
							<i>u'</i>	23.44 ± 0.59 ^s	0.13							
							<i>g'</i>	23.35 ± 0.23 ^s	0.10							
							<i>r'</i>	22.71 ± 0.18 ^s	0.07							
							<i>i'</i>	21.85 ± 0.13 ^s	0.05							
							<i>z'</i>	21.69 ± 0.37 ^s	0.04							
							<i>J</i>	20.48 ± 0.05 ^f	0.02							
							<i>H</i>	20.05 ± 0.04 ^f	0.01							
Q 2353−0028	0.0257	0.6044 ^d	21.54 ^{+0.15} _{−0.15} ^{d,r}	Zn	−0.92 ± 0.32 ^r	0.844 ± 0.300 ^f	<i>u'</i>	23.44 ± 0.59 ^s	0.13							
							<i>g'</i>	23.35 ± 0.23 ^s	0.10							
							<i>r'</i>	22.71 ± 0.18 ^s	0.07							
							<i>i'</i>	21.85 ± 0.13 ^s	0.05							
							<i>z'</i>	21.69 ± 0.37 ^s	0.04							
							<i>J</i>	20.48 ± 0.05 ^f	0.02							
							<i>H</i>	20.05 ± 0.04 ^f	0.01							
							<i>K</i>	19.27 ± 0.02 ^f	0.01							

Notes. (*) Galactic E_{B-V} reddening and A_{λ} towards the absorbing galaxy assuming the Schlafly & Finkbeiner (2011) re-calibrated extinction maps. (***) Cristiani (1987) identified emission-lines 2σ from z_{abs} , 7.1 arcsec from the quasar sightline. Le Brun et al. (1997) resolved the candidate into two interacting objects, the emission lines originating in one of them. (†) Boissé et al. (1998), their Table 6, report a metallicity and introduced a typical uncertainty of 0.1–0.2 dex. Due to a poorly constrained N_{HI} , we assign a conservative error of 0.40 dex. (‡) The magnitudes in Chen & Lanzetta (2003) were corrected for Schlegel & Finkbeiner Davis (1998) extinctions. Here we report the conversion to the Schlafly & Finkbeiner (2011) maps.

References. (a) de la Varga et al. (2000); (b) Ledoux et al. (2002); (c) Chen & Lanzetta (2003); (d) Rao et al. (2006); (e) Péroux et al. (2008); (f) Rao et al. (2011); (g) Ahn et al. (2014, SDSS DR10); (h) Boissé et al. (1998); (i) Péroux et al. (2011); (j) Cristiani (1987); (k) Möller et al. (2018); (l) Hewett & Wild (2007); (m) Meiring et al. (2008); (n) Meiring et al. (2011); (o) Straka et al. (2016); (p) Meiring et al. (2009); (q) Péroux et al. (2006); (r) Nestor et al. (2008)

Table 2. Observation log for the VLT/FORS2 long-slit spectroscopic observations of damped absorbing galaxies.

Quasar field	RA (J2000)	Dec (J2000)	Obs. date (YYYY-MM-DD)	$N_{\text{exp.}} \times t_{\text{exp.}}$ (s)	GRISM	Slit PA (deg)	Airmass	Seeing (arcsec)	$\Delta\lambda_{\text{sys.}}$ (Å)
HE 1122–1649	11:24:42.87	–17:05:17.50	2015-04-19	2×1800	600RI	–12.90	1.105	0.86–0.93	0.33
Q 0153+0009	01:53:18.19	+00:09:11.44	2015-09-(08:09)	4×1800	600z	73.40	1.172	0.73–0.84	–0.93
Q 1209+107 PA1	12:11:40.59	+10:30:02.04	2015-04-19	2×1300	600RI	96.70	1.323	1.12–1.27	–1.04
Q 1209+107 PA2	12:11:40.59	+10:30:02.04	2015-04-19	2×1300	600RI	43.30	1.236	1.24–1.32	–0.44
Q 1323–0021	13:23:23.78	–00:21:55.28	2015-04-(17:18)	4×1100	600RI	42.00	1.158	1.03–1.17	–0.64
Q 1436–0051	14:36:45.05	–00:51:50.59	2015-04-(13:14)	4×1800	600z	29.40	1.097	0.68–0.77	–0.72
Q 2328+0022	23:28:20.38	+00:22:38.24	2015-07-11	2×800	600RI	45.00	1.147	0.78–0.85	–0.38
Q 2335+1501	23:35:44.19	+15:01:18.37	2015-05-30	2×800	600RI	4.80	1.673	0.83–0.93	0.43
Q 2353–0028	23:53:21.62	–00:28:40.67	2015-07-11	4×1800	600RI	–2.30	1.143	0.90–0.95	0.35

Notes. RA and Dec refer to the coordinates of the quasar. The slit position angle (PA) was selected to match the candidate host galaxy from imaging data (Rao et al. 2011), and is defined so that $N=0$, $E=90^\circ$. All observations were taken with a slit-width of 1.31 arcsec. The tabulated airmass corresponds to the mean value calculated from the nominal header-values at start and end for each exposure. The seeing, as the FWHM of a summed profile in ten pixels along the dispersion direction, was measured in the combined spectrum of the quasar. As the seeing-measurements varied temporally and in wavelength non-trivially, we report the observed ranges. We define the systematic offset in the wavelength-solution as $\Delta\lambda_{\text{sys.}} = \lambda_{\text{calib.}} - \lambda_{\text{UVES}}$.

and competitive space-based observatories. However, damped HI absorbers are accompanied by low-ionisation metal absorption lines, including singly ionised magnesium which is a tracer of DLAs (Rao et al. 2006). For $z > 0.11$, the Mg II $\lambda\lambda 2796, 2803$ Å doublet falls in the optical spectral region, where it is an efficient proxy for damped absorbers (e.g., Ellison 2006; Berg et al. 2017). Our sample was therefore selected from a set of sub-DLA and DLAs with reliable HST HI column-density measurements, initially identified as strong Mg II absorbers.

A large fraction of our targeted absorbers are located at redshifts $z \sim 0.7$, originating from the redshift distribution of the imaging campaigns from which they were drawn¹. The distribution peaking at this value reflects the tradeoff between a lower number density of LLS, sub-DLAs, and DLAs towards low redshift (Rao et al. 2006; Zafar et al. 2013a) and an increased limiting luminosity towards higher redshifts which prevents the identification of candidate absorbing galaxies from photometric redshift methods (Rao et al. 2011). We targeted standard diagnostic nebulae lines in emission to characterise the galaxies. This allowed us to directly observe how absorbing galaxies fall relative to scaling relations derived from deep imaging surveys of luminosity-selected samples at similar redshifts (Savaglio et al. 2005; Maiolino et al. 2008; Karim et al. 2011; Stott et al. 2014; Whitaker et al. 2014).

2.2. VLT FORS2 data

Long-slit spectra were taken in nine slit-alignments². The log of observations for the different fields, including slit configuration and average seeing-conditions measured in the reduced spectra are listed in Table 2. The observations were taken with a 1.31 arcsec slit-width, and the slit was aligned to cover both the quasar and the candidate host with relative coordinates based on archival imaging. The observations were carried out with the 600RI and the 600z grisms, covering wavelength-ranges of $\lambda\lambda 5120 - 8450$ Å and $\lambda\lambda 7370 - 10\,700$ Å at a nominal spectral

resolution $\mathcal{R}_{600\text{RI}} = 1000$ and $\mathcal{R}_{600\text{z}} = 1390$ assuming 1.0 arcsec slit-widths, respectively (Boffin et al. 2015). For all the observations, we used a 2×2 binning configuration along spatial and spectral directions.

We performed a cosmic-ray removal on the raw data frames with P3D (Sandin et al. 2010), an adaptation of the L. A. Cosmic algorithm (van Dokkum 2001). Each frame was subsequently reduced in a standard manner by passing it through the ESO/Reflex pipeline version 5.1.4 (Freudling et al. 2013). Individual exposures were combined into 2D spectra for each object using the average pixel value and a sigma-clipping rejection. In three cases (Q 0153+0009, Q 1209+107 PA1, and Q 1436–0051), the pipeline did an unsatisfactory sky-subtraction, and we post-processed the intermediate Reflex products of those observations with standard TRAF tasks.

For each science-frame, the host-galaxy was flux-calibrated by extracting 1D-spectra of the quasar and target, scaling the quasar spectrum to its Sloan Digital Sky Survey data release 10 (SDSS DR10, Ahn et al. 2014) counterpart, and applying this scaling-solution to the target spectrum. For point-sources, this prevented temporally varying seeing and slit-losses from propagating into systematic errors which would have been introduced in calibrating against spectrophotometric standard stars. However, it did not account for any flux variation caused by intrinsic quasar variability. Based on the the same FORS2 data for Q 1323–0021, Møller et al. (2018) quantified the effect of quasar variability on the flux-calibration. In their work, they found that flux-measurements were correct to within a factor of two, with quasar variability responsible for $\sim 10\%$, and slit-losses for the remaining fraction.

The SDSS catalogue does not cover HE 1122–1649. In this field, we assumed that the transmission was the same as for the other fields observed with the same instrument settings. This allowed us to calculate an average sensitivity function which we used to flux-calibrate the target spectrum in the HE 1122–1649 field. Based on five sensitivity functions, we calculated an RMS of $0.5-0.8 \times 10^{-17}$ ergs s^{–1} cm^{–2} in the wavelength region $\lambda\lambda 6000 - 8000$ Å. This RMS value is of the same order as integrated line-flux uncertainties (see Table 3), and accounts for weather conditions, slit-losses and quasar variability effects. We therefore confirm that the flux-calibration is robust, and verify that quasar variability, on average, is a minor effect.

¹ See for example Rao et al. (2011) where $\sim 63\%$ of the systems were identified at the 3σ level in the redshift range $0.5 < z < 0.8$.

² See Sect. 2.1 for a detailed account of the number of fields, absorbers, and slits used.

Table 3. Line-flux measurements.

Quasar field	Host galaxy identifiers			Emission-line measurements			
	θ^a (")	b^b (kpc)	$z_{\text{em}}^{\text{SPEC}}$	Transition	λ_0 (Å)	$FWHM$ (Å)	Line-flux ($\times 10^{-17} \text{ erg s}^{-1} \text{ cm}^{-2}$)
HE 1122–1649	3.6 ^c	25.6	0.68249 ± 0.00003	[O II]	3727,3729	6.3 ± 0.7	17.7 ± 2.4
Q 0153+0009	4.9 ^d	36.6	0.77085 ± 0.00003	H β	4861.39	6.0 ± 0.5	4.8 ± 0.6
				H5	4340.47	9.5 ± 1.0	3.0 ± 0.4
				H β	4861.33	9.5 ± 0.6	6.3 ± 0.6
Q 1209+107	7.2 ^d	38.3	0.39238 ± 0.00001	[O III]	5007	9.8 ± 0.5	7.5 ± 0.5
				[O II]	3727,3729	6.7 ± 0.4	41.9 ± 1.5
				H5	4340.47	5.0 ± 0.5	7.0 ± 0.7
				H β	4861.33	5.5 ± 0.1	14.8 ± 0.4
				[O III]	4958.91	5.6 ± 0.1	23.3 ± 0.8
Q 1323–0021	1.4 ^d	10.2	0.71717 ± 0.00008	[O III]	5007	5.8 ± 0.2	72.1 ± 3.0
				[O II]	3727,3729	9.6 ± 1.7	3.1 ± 0.4
Q 1436–0051	6.2 ^e	45.5	0.73749 ± 0.00003	[O II]	3727,3729	10.2 ± 0.7 ^g	11.1 ± 0.8 ^g
				H β	4861.33	7.9 ± 1.4	1.5 ± 0.3
Q 1436–0051	4.4 ^d	34.9	0.92886 ± 0.00002	[O III]	5007	17.8 ± 2.7	1.3 ± 0.3
				[O III]	5007	5.6 ± 0.4	7.0 ± 0.7
Q 2328+0022	1.7 ^d	11.9	0.65194 ± 0.00006	[O II]	3727,3729	5.5 ± 0.7	7.0 ± 0.7
Q 2335+1501	3.8 ^f	27.0	0.67989 ± 0.00002	[O II]	3727,3729	6.7 ± 0.4	36.3 ± 1.4
				H β	4861.33	6.5 ± 0.2	15.6 ± 6.2

Notes. Values for $z_{\text{em}}^{\text{SPEC}}$ refer to the heliocentric rest-frame corrected measurement, with the quoted error reflecting the uncertainty in the profile-fit. θ is the angular separation between quasar and host, measured in arcsec. θ is translated into an impact parameter (b) measured in kpc using the spectroscopically determined emission-line redshift and the assumed cosmology. The fluxes were integrated across the profile, and corrected for Galactic extinction assuming the Galactic E_{B-V} values reported in Table 1. Full-width-half-maximum (FWHM) measurements have not been corrected for the instrumental resolution. ^(a)Un-binned angular distance relative to the quasar. ^(b)Projected distance relative to the quasar, measured at the spectroscopic redshift. ^(c)Chen & Lanzetta (2003); ^(d)Rao et al. (2011). ^(e)This work, based on Rao et al. (2011) K -band image (see Sect. 2.4). ^(f)This work, FORS2 spectrum. ^(g)This work, based on the Straka et al. (2016) spectrum (see Sects. 3.3, 3.6, and 3.8).

To test if a systematic offset in the wavelength-solution exists and to determine velocity-dispersions, we measured central wavelengths and the full-width-half-maximum (FWHM) of skylines proximate to object emission lines in the 2D spectra. Gaussian- and Voigt profile-fitting ensured accurate central wavelengths, but systematically underestimated the FWHM measurements. The central wavelengths were measured against the Ultra-Violet and Echelle Spectrograph (UVES) telluric line catalogue (Hanuschik 2003), yielding an effective offset in the wavelength-solution reported in Table 2. With non-parametric FWHM measurements, we confirm the nominal instrumental resolutions³ renormalised to a 1.31 arcsec slit-width which gives effective resolutions $\mathcal{R}_{600\text{RI}} = 763$ ($\sim 393 \text{ km s}^{-1}$) and $\mathcal{R}_{600z} = 1061$ ($\sim 283 \text{ km s}^{-1}$).

2.3. Archival data

In addition to the FORS2 observations described in Sect. 2.2, we compiled the archival data that we required in each of the targeted fields. This included the Galactic extinction towards the lines of sight, the absorber characteristics (z_{abs} , $\log_{10}[N_{\text{H}} I (\text{cm}^{-2})]$, $[M/H]_{\text{abs}}$) and the candidate host characteristics (z_{phot} and photometry).

The photometry was predominantly taken from Rao et al. (2011), with optical images obtained at the Kitt Peak National Observatory (KPNO) with standard SDSS u' , g' , r' , i' filters, and near-IR (NIR) images obtained at the Mauna Kea Observatory with the NASA Infrared Telescope’s NSFCAM J , H , K fil-

ter set. Exceptions to this included the HE 1122–1649 field, for which all photometry was taken with the du Pont Telescope at the Las Campanas Observatory (Chen & Lanzetta 2003) and the Q 1323–0021 $m_{11200\text{Å}}$ and $m_{13500\text{Å}}$, for which magnitudes were measured in the collapsed 1D-spectrum (Møller et al. 2018). Where required, we applied Galactic extinction corrections to the photometric magnitudes. Here we note that the magnitudes in the HE 1122-1649 field reported in Chen & Lanzetta (2003) were corrected for Schlegel & Finkbeiner Davis (1998) extinctions. We therefore calculated conversion factors to the recalibrated Schlafly & Finkbeiner (2011) maps and report these instead. All values and references to each entry are summarised in Table 1.

2.4. NIR photometry for Q 1436–0051

The vicinity of Q 1436–0051 has been studied extensively because it is a crowded field, hosting two absorbers in the quasar spectrum (a sub-DLA at $z_{\text{abs}} = 0.7377$ and a LLS at $z_{\text{abs}} = 0.9281$) and eight objects within a 30×30 arcsec perimeter centred on the quasar (Rao et al. 2011). Of special interest is an object at an impact parameter of 6.4 arcsec, where SDSS reports two source detections, classifying the combined object as a blend of an extended object with $z_{\text{phot}} = 0.622 \pm 0.139$ and a star. Rao et al. (2011) considered the same system to be a single object (their object 3), and therefore reported a combined magnitude. With optical photometry, Meiring et al. (2011) resolved the object into two extended objects (their objects 6 and 7) consistent with the redshift of the sub-DLA, likely forming an interacting pair of galaxies (Meiring et al. 2011; Straka et al. 2016).

³ <http://www.eso.org/sci/facilities/paranal/instruments/fors/inst.html>

The slit in our FORS2 observations of Q 1436–0051 was aligned to cover this galaxy configuration. To solve for the stellar mass of each component (see Sect. 3.6), we acquired the calibrated J , H , and K band images used in Rao et al. (2011) from private communication with Sandhya M. Rao, and performed aperture photometry with SExtractor (Bertin & Arnouts 1996) version 2.19.5. We obtained isophotal flux measurements for which we required a 2σ detection threshold above the RMS noise level in the image and that a source encompassed a minimum of five pixels in the detection isophote. With these criteria in place, we resolved the two objects in the K -band image and ensured that we measured a representative flux-ratio of the interacting galaxies by accounting for flux in the extended wings of their flux profiles. We constructed a K -band catalogue for object identification, and used it to extract the flux for each of the two galaxies in the J and H bands. The measured flux-ratios of the components in each band were combined with the total magnitudes (Rao et al. 2011) to assign individual magnitudes to each of the interacting components. The resulting magnitudes are reported in Table 1, and complement the optical photometry in the SED-fitting procedure (see Sect. 3.6).

3. Results

3.1. Spectral point spread function subtraction

To scan the quasar PSF for hidden objects and recover their spectral signatures in search for the absorbing galaxies, we subtracted the quasar continua in a process known as spectral PSF (SPSF) subtraction (Møller 2000; Møller et al. 2000). Conceptually, a model of the quasar trace in the 2D-spectrum was constructed. The model was then subtracted out to isolate line-emission from objects at small projected separations to the quasar. Variations of SPSF subtraction procedures have been used in prior studies, specifically constructed to find metal emission lines in high-redshift DLA galaxies (Møller et al. 2002, 2018; Fynbo et al. 2010, 2013a; Zafar et al. 2011; Krogager et al. 2013).

Here, we built a non-parametric, empirical model of the quasar PSF by averaging the observed spatial profile in two spectral windows immediately bluewards and redwards of each predicted emission-line feature for each science frame. We confirmed that the quasar trace has no gradient along the dispersion direction to within sub-pixel precision. We then assumed that the PSF profile did not vary with wavelength and that the quasar continuum emission could be modelled as a pure power-law across the covered wavelength range. With these assumptions in place, we scaled the strength of the modelled quasar PSF at each wavelength, and the resulting SPSF model was subtracted from the 2D-spectrum.

In eight out of ten targeted systems we identified the absorbing galaxy from emission lines at the expected wavelengths (see Table 3). In six of these systems emission lines were detected directly in the science frames, without performing SPSF subtractions. This allowed us to measure line-fluxes without the addition of noise. In passing, we note that the SPSF-subtracted spectrum of Q 1209+107 PA2 did not reveal hidden emission lines from an object at small impact parameter. Instead, we confirm the detection of emission lines at $z = 0.3922$ in the object first reported by Cristiani (1987) which then remains the best candidate host in that field. Two additional objects were identified as the absorbing galaxies after performing SPSF subtractions (Q 1323–0021 and Q 2328+0022, see Fig. 1). For these two systems, we varied the size and limits of the wavelength windows to see if the residual flux was real, or an artefact of the subtraction. In all realisations of the SPSF-subtraction residual flux was detected

at the same locations in the 2D spectra, which confirmed that the signals were real (see Fig. 1). 1D-spectra covering the recovered spectral features of the absorbing galaxies were then extracted with a simple extraction using standard IRAF tasks. By applying a simple extraction, we avoided biasing the flux-measurement by the signal gradient across the quasar PSF (Møller 2000); an effect which would result from the standard optimal extraction weighting scheme (Horne 1986). We defined the extraction apertures relative to the quasar trace, with aperture limits [+0.38″: +1.26″] and [+0.38″: +1.64″] for Q 1323–0021 and Q 2328+0022, respectively.

In the case of Q 1323–0021, the spatial structure observed in the emission line feature is indicative of a velocity gradient, which makes the redshift determination sensitive to the adopted aperture limits. We note that the extension of the signal below the quasar trace as observed in the 2D-spectrum appears to be real. However, the image statistics suggest that this extension is driven by noise. We therefore set a lower aperture limit ensuring that we only captured the real signal of the absorbing galaxy. Similarly, Møller et al. (2018) used the aperture limits [+0.25″: +2.5″] above the quasar trace, attributing apparent flux beyond the aperture limits to quasar noise residuals from an imperfect SPSF-subtraction. We determined the redshift to be $z_{[\text{O II}]} = 0.71717$ (see Tables 3 and 4) which is consistent with the Møller et al. (2018) measurement of $z_{\text{ref}} = 0.7170 \pm 0.0006$.

3.2. Emission line measurements

The FORS2 wavelength coverage allows us to make line detections in [O II] $\lambda\lambda 3727, 3729 \text{ \AA}$, H β $\lambda 4861 \text{ \AA}$ and [O III] $\lambda\lambda 4959, 5007 \text{ \AA}$. From here on, we use the abbreviations [O II], H β and [O III] to refer to these ion lines, respectively. We are able to confirm the counterparts to seven out of ten absorbers in eight quasar fields, that is, a conservative detection rate of 70% (see Sect. 3.4 for a discussion on an unlikely host, and Sect. 3.5 for a discussion on the two non-detections).

We extracted line-fluxes by fitting Gaussian profiles to each line, with continuum placement based on a linear fit to regions bluewards and redwards of the transition, free of telluric absorption and skylines. We allowed the slope and normalisation of the continuum and the centroid, linewidth, and amplitude of the line profile to vary in order to retrieve the optimal fit to all lines except for the [O II] line doublet. At the effective resolution of the FORS2 instrument and for the target redshifts, we could not resolve its individual components. We therefore fitted two Gaussian components simultaneously, fixing the linewidths to the same value, tying the centroid-separation to the redshift, and verifying that the best fit parameters yielded a line-ratio consistent with standard low-density nebulae conditions (Osterbrock & Ferland 2006).

Line-centres were converted to velocity space, helio-centric rest-frame corrections were applied, and each velocity solution was converted to a spectroscopic redshift (see Tables 3 and 4). We applied Galactic extinction corrections to the line-fluxes based on the E_{B-V} values provided by the Schlafly & Finkbeiner (2011) extinction maps. Uncertainties in the line-fluxes reflect the propagated statistical errors in the profile fit.

To convert the fitted line-widths to velocity dispersions, σ , we subtracted the instrumental broadening \mathcal{R} (km s^{-1}) (see Sect. 2.2) renormalised to the effective seeing, quadratically from the FWHM as

$$\sigma = \sqrt{FWHM^2 - \mathcal{R}^2} / (2\sqrt{\ln 2}). \quad (1)$$

To determine the value of each σ and its errors, we assumed that the FWHM measurements had Gaussian-distributed errors.

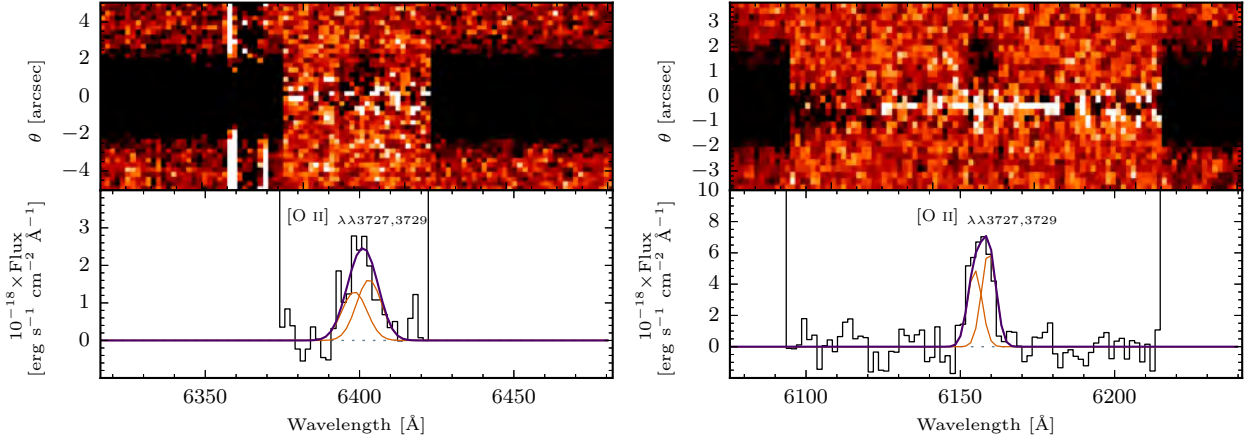


Fig. 1. Negative colour-mapped two-dimensional VLT/FORS2 SPSF-subtracted spectra (*top panels*), and the extracted one-dimensional spectra (black; *lower panels*), centred on the [O II] $\lambda\lambda 3727, 3729$ Å doublet. *Left panel:* Q 1323–0021 field shows excess emission from the DLA counterpart extending above the quasar-trace. *Right panel:* Q 2328+0022 reveals the presence of the DLA counterpart offset from the trace. In both panels, the fitted doublet-components are overlotted in orange, with the resulting emission profiles in purple.

Table 4. Resulting parameters for our sample of absorbing galaxies.

Quasar field	Host-galaxy identifiers			Modelled parameter								
	θ^*	b	$z_{\text{em}}^{\text{SPEC}}$	$E_{B-V}^{\text{nebulular}}$			$\log_{10}[M_{\star} (M_{\odot})]$	$\text{SFR}_{[\text{O II}]}$	$\text{SFR}_{\text{H}\alpha}$	σ	[O/H]	[M/H] _{em}
	(")	(kpc)		(mag) SED	(mag) BDEC	(mag) SFR		($M_{\odot} \text{ yr}^{-1}$)	($M_{\odot} \text{ yr}^{-1}$)	(km s^{-1})	(dex)	(dex)
HE 1122-1649	3.6 ^a	25.6	0.68249(3)	0.11	–	0.05 ^{+0.08} _{–0.04}	9.45 ^{+0.15} _{–0.19}	1.68 ± 0.23	1.55 ± 0.19	20 ⁺¹² _{–10}	8.70 ^{+0.17} _{–0.20}	–0.84 ± 0.05
Q 0153+0009	4.9 ^b	36.6	0.77085(3)	0.00	0.5 ^{+0.6} _{–0.4}	–	10.03 ^{+0.18} _{–0.08}	–	16.14 ± 1.54	121 ⁺⁸ _{–8}	8.75 ^{+0.03} _{–0.03}	0.04 ± 0.20
Q 1209+107 PA2	7.2 ^b	38.3	0.39238(1)	0.68	0.3 ^{+0.4} _{–0.2}	≤ 0	8.16 ^{+0.06} _{–0.06}	3.20 ± 0.12	3.34 ± 0.09	49 ⁺²² _{–22}	~8.05 [‡]	0.30 ± 0.20
Q 1323–0021	1.4 ^b	10.2	0.71717(8)	0.68	–	–	10.95 ^{+0.11} _{–0.14} [§]	0.27 ± 0.03	–	134 ⁺⁴⁴ _{–48}	–	0.62 ± 0.35
Q 1436–0051	6.2 ^c	45.5	0.73749(3)	0.68	–	≤ 0	10.41 ^{+0.09} _{–0.08}	1.02 ± 0.07 ^{**}	0.48 ± 0.10	99 ⁺²⁴ _{–26}	8.82 ^{+0.08} _{–0.08} ^{††}	0.21 ± 0.12
Q 1436–0051	4.4 ^b	34.9	0.92886(2)	1.02	–	–	10.20 ^{+0.11} _{–0.11}	–	–	33 ⁺¹⁰ _{–12}	–	0.21 ± 0.55
Q 2328+0022	1.7 ^b	11.9	0.65194(6)	0.00	–	–	10.62 ^{+0.34} _{–0.36}	0.47 ± 0.05	–	56 ⁺²³ _{–24}	–	–0.23 ± 0.22
Q 2335+1501	3.8 ^d	27.0	0.67989(2)	1.36	–	0.11 ^{+0.13} _{–0.08}	9.83 ^{+0.20} _{–0.22}	4.47 ± 0.17	6.31 ± 2.51	12 ⁺⁶ _{–5}	8.96 ^{+0.09} _{–0.26}	0.33 ± 0.34

Notes. Values for $z_{\text{em}}^{\text{SPEC}}$ refer to the heliocentric rest-frame corrected measurement, with the bracket notation reflecting the uncertainty in the profile-fit. θ is the angular separation between quasar and host, measured in arcsec from known photometry. θ is translated into an impact parameter (b) measured in kpc using the spectroscopically determined emission-line redshift and the assumed cosmology. $E_{B-V}^{\text{nebulular}}$ refers to the nebular extinctions (SED, BDEC, SFR) derived from the χ^2 -minimising SED solution; the Balmer decrement; and based on the ratio of the SFR in H α and [O II] under the assumption that they trace similar time-scales, respectively. Stellar mass estimates were determined from the maximum likelihood analysis of the SEDs χ^2 -distributions. The star-formation rate estimates were corrected for intrinsic and Galactic extinction, and were converted to a Chabrier IMF. σ corresponds to the velocity dispersion based on the profile fits to the emission lines after resolution correction using Eq. (1), and [O/H] to the preferred oxygen abundance derived from emission line ratios according to the M08 prescriptions. [M/H]_{em} refers to the metallicity in emission, inferred by applying a correction factor and truncation radius to the absorption metallicity. (*) Un-binned angular distance. (**) Inferred from the rescaled S16 Magellan II spectrum (Sects. 3.3, 3.6 and 3.8). (‡) Upper limit on E_{B-V} imposed from dust-content priors (Sect. 3.6). (†) O₂ diagnostic measurement. (††) O₃ diagnostic measurement. (‡) R₂₃ diagnostic measurement.

References. (a) Chen & Lanzetta (2003); (b) Rao et al. (2011); (c) this work, based on Rao et al. (2011) K-band image (Sect. 2.4); (d) this work.

We then perturbed the FWHM measurements using the measurement uncertainty in the FWHM (see Table 3) to characterise the width of the distribution, centred on the measurement. Having simulated the data, we determined dispersions and errors as the median, 16th- and 84th percentile in the cumulative distribution function (CDF) of the real values below the square-root in Eq. (1).

3.3. Galaxy associations in the Q 1436–0051 field

Past observations indicate that absorbing galaxies can be related to galaxy associations in dense environments (Kacprzak et al.

2010; Rao et al. 2011; Christensen et al. 2014; Péroux et al. 2017). We found a remarkable example of such associations in the field Q 1436–0051, which was observed to host multiple galaxies that coincide with the redshifts of two damped absorbers ($\log_{10}[N_{\text{H I}} (\text{cm}^{-2})] = 20.08^{+0.10}_{-0.12}$ at $z_{\text{abs}} = 0.737$, and $\log_{10}[N_{\text{H I}} (\text{cm}^{-2})] = 18.40 \pm 0.98$, consistent with the lower limit of the definition for a sub-DLA, at $z_{\text{abs}} = 0.928$). We confirm the presence of three galaxies at the $z_{\text{abs}} = 0.737$ absorber redshift and two galaxies at the $z_{\text{abs}} = 0.928$ absorber redshift, all remarkably lying within a single slit-position. We show the spatial configuration of these systems in the 2D FORS2 spectrum in Fig. A.1. Based on impact-parameter and redshift information

[b , z_{em}] of the objects in the slit (see Table A.1), we found the most likely counterparts to be located at [45.5, 0.73749] and [34.9, 0.92886], which is consistent with Object 6 and Object 5, respectively, assuming the nomenclature of Meiring et al. (2011) and Straka et al. (2016). We also note that the host of the $z_{\text{abs}} = 0.737$ absorber is likely part of an interacting system. This issue is discussed further in Sects. 3.6 and 3.8.

3.4. Unlikely host in the Q 1209+107 PA2 field

The subsequent analysis of our entire sample (see Sect. 4) in relation to known scaling relations and luminosity-selected samples reveals that the candidate absorbing galaxy in the Q 1209+107 PA2 field occupies a unique place in the MZ (Sect. 4.3); on the star-forming main-sequence (Sect. 4.4); and in the metallicity-gradient (Sect. 4.5) parameter spaces. In particular, it is worrying that a low-mass ($\log_{10}[M_{\star}(M_{\odot})] \sim 8.2$) star-burst galaxy has a super-solar metallicity at a distance of 38 kpc from its luminosity-centre, when the emission-line diagnostics yield a low central oxygen abundance of $[\text{O}/\text{H}] \sim 8.05$.

Guided by these results and discussions, we flag the absorbing galaxy as an unlikely host. Rather, its redshift, mass, metallicity and SFR are suggestive of a smaller member in a group environment around the real host. More likely, the real host is a more massive galaxy which is hiding below the quasar PSF. We note that the SPSF-subtraction did not reveal any hidden line-flux below the quasar trace. We therefore report upper limits on the line-flux from an object under the quasar trace as the 3σ residuals in a $\pm 5 \text{ \AA}$ spectral window centred on the predicted emission lines in the SPSF-subtracted 1D-spectrum. We found consistent upper limits at a $\sim 2 \times 10^{-17} \text{ ergs s}^{-1} \text{ cm}^{-2}$ flux-level at the predicted position of $[\text{O II}]$ and $\text{H}\beta$ alike. In the following analysis we treated this candidate as the host, but flagged it where possible, and excluded it in calculations of the statistical properties of the sample as it most likely is not the real host of the absorber. For more details, see the relevant sections.

3.5. Non-detections in the Q 2353–0028 and Q 1209+107 PA1 fields

In this section we discuss the two fields Q 2353–0028 and Q 1209+107 PA1. In these fields, our analyses was unable to identify the absorbing galaxies.

For Q 2353–0028 we observed a single prominent spectral feature associated with the candidate object at $\lambda_{\text{obs}} = 6565.2 \text{ \AA}$. However, this does not coincide with any of the emission lines for the assumed absorber redshift. At the absorber redshift ($z_{\text{abs}} = 0.6044$), this corresponds to redshift differences of $|\Delta z_{[\text{O II}]}| = 0.16$, $|\Delta z_{\text{H}\beta}| = 0.25$, and $|\Delta z_{[\text{O III}]}| = 0.29$, or equivalently to velocity offsets of $|\Delta v_{[\text{O II}]}| = 293378 \text{ km s}^{-1}$, $|\Delta v_{\text{H}\beta}| \sim 47427 \text{ km s}^{-1}$, and $|\Delta v_{[\text{O III}]}| \sim 54778 \text{ km s}^{-1}$. This leads us to refute the object as the host galaxy. We note that the emission feature is $\sim 2 \text{ \AA}$ redwards of the $\text{H}\alpha$ $\lambda 6563 \text{ \AA}$ rest-wavelength, which would place the galaxy at a redshift $z_{\text{gal}} \sim 0.0003$. However, with no additional emission lines to corroborate with, we consider the low redshift solution unlikely. We note that the quasar itself is located at redshift 0.765 (Rao et al. 2006), and displays a strong $[\text{O II}] \lambda\lambda 3727, 3729 \text{ \AA}$ narrow-line doublet at the expected wavelength $\lambda_{[\text{O II}], \text{QSO}} = 6578 \text{ \AA}$. Interpreting the galaxy feature as $[\text{O II}]$ emission at the quasar redshift gives a velocity blue-shift $\Delta v_{[\text{O II}]}(z_{\text{QSO}}) \sim 592 \text{ km s}^{-1}$ between

the quasar and object, which suggests that the observed emission originates from a galaxy in a group at the quasar redshift⁴. This is also consistent with the uncertain redshift solution based on broad-band photometry, $z_{\text{phot}} = 0.844 \pm 0.300$ (Rao et al. 2006).

In the case of PA1 of the Q 1209+107 field we did not find any spectral features of a host at the absorber redshift ($z_{\text{abs}} = 0.6295$) in the SPSF-subtracted frame, nor a stellar continuum at the position of the candidate host. The stellar-continuum of the candidate host is too faint and too proximate ($\sim 1.67 \text{ arcsec}$) to be spatially resolved from the quasar PSF. This prevents us from detecting the object, also from an expected Balmer discontinuity around $\lambda 5940 \text{ \AA}$.

3.6. Modelling the spectral energy distribution

We inferred stellar masses of the absorbing galaxies from modelling the spectral energy distribution (SED) with the LePhare code (Arnouts et al. 1999; Ilbert et al. 2006), fitted to broad-band photometric magnitudes corrected for Galactic extinction (Table 1) using the spectroscopically determined emission-line redshifts (Table 4). For matching the photometry, we used Bruzual & Charlot (2003; BC03) simple stellar population (SSP) spectral templates based on Padova 1994 stellar evolutionary tracks and a Chabrier (2003) IMF. The SSPs have exponentially declining star-formation rates, parametrised with fiducial stellar population ages and e-folding time-scales in the ranges $[0.01 : 13.5] \text{ Gyrs}$ and $[0.1 : 30] \text{ Gyrs}$, respectively. To model the flux in each photometric band, the filter transmission curves for each instrument used to measure the original magnitudes were retrieved.

The best-fit SED minimises the χ^2 -statistic across a user-defined grid of free parameters. Our grid encompassed (i) an LMC attenuation-curve (Fitzpatrick & Massa 2007); (ii) a large range of intrinsic reddenings with $E_{B-V} \in [0.00 : 1.00]$ in incremental steps of 0.05 to ensure the preferred E_{B-V} is associated with a χ^2 -minimum rather than a grid-boundary; (iii) the option to evaluate fits including- and excluding flux contribution from nebular emission.

The resulting SEDs of the absorbing galaxies are shown in Fig. 2, and stellar masses together with the E_{B-V} values are reported in Table 4. Stellar masses and their uncertainties were determined as the median value and from the 16th- and 84th percentiles of a maximum likelihood analysis of the SED-fits χ^2 -distributions, respectively. We note that for the Q 1323–0021 field, we have priors on the nebular emission and on the E_{B-V} based on detected emission lines and the dust-obscured star formation (Møller et al. 2018). For this object, we therefore prefer a model excluding the nebulae emission lines, and restrict the range of reddening to $E_{B-V} \in [0.00 : 0.30]$.

For Q 1323–0021, the i -band magnitude was removed from the SED-fit, motivated by strong residuals from the QSO PSF-subtraction (Rao et al. 2011). In the Q 1436–0051 field, we solved for M_{\star} for both of the interacting components (see Sects. 2.4 and 3.3). In agreement with Rao et al. (2011), we found that the K -band photometry was unreliable. We therefore excluded it from the SED-fitting analysis. This resulted in stellar masses of $\log_{10}[M_{\star}(M_{\odot})] = 10.41 \pm 0.10$ and $\log_{10}[M_{\star}(M_{\odot})] = 9.79 \pm 0.07$, placing the absorbing galaxy in the category of a minor-merger.

⁴ The object is located at an impact parameter of $\sim 5 \text{ arcsec}$, which at the quasar redshift for the assumed cosmology corresponds to a projected distance of 36.5 kpc.

3.7. Intrinsic extinction correction

For three galaxies in the fields of Q 0153+0009, Q 1209+107 PA2, and Q 1436–0051 we detected higher order Balmer-lines (see Table 3 for individual measurements). This allowed us to correct line-fluxes for intrinsic dust extinction based on the Balmer decrement (Eq. (2)). The broad-band colour excess is tied to the deviation in observed-to-intrinsic line-ratios as

$$E_{B-V} = \frac{2.5}{\kappa(\text{H5}) - \kappa(\text{H}\beta)} \log_{10} \left(\frac{(\text{H}\beta/\text{H5})_{\text{obs}}}{(\text{H}\beta/\text{H5})_0} \right), \quad (2)$$

where κ is the value of the attenuation curve at the rest-wavelength of the labelled line-transition and $(\text{H}\beta/\text{H5})_{\text{obs}}$ is the observed flux ratio based on the entries in Table 3. $(\text{H}\beta/\text{H5})_0$ is the intrinsic flux ratio with an adopted value of 2.137 assuming case B recombination at $T = 10^4$ K and $n_e \sim 10^2$ – 10^4 cm $^{-3}$ (Osterbrock & Ferland 2006). We adopted the Fitzpatrick & Massa (2007) LMC attenuation-curve with $R_V = A_V/E_{B-V} = 3.1$, but note that extinction corrections based on Balmer lines are relatively insensitive to the choice of attenuation-curve as these behave similar redwards of the 2175 Å extinction bump.

We also attempted to use H6, H7 and H8 measurements (see Table 3) to constrain the intrinsic extinction where these lines were observed. However, the flux in the higher order lines decreased rapidly, which introduced large errors. We also attempted to model the observed line-ratios simultaneously, with extinction as a free parameter. However, the large measurement errors in the higher order lines prevented us from better constraining the fit. We therefore took a conservative approach, and used the values based on the strongest Balmer decrement ($\text{H}\beta/\text{H5}$) in all cases. We intentionally avoided combining our FORS2 $\text{H}\beta$ measurements with literature $\text{H}\alpha$ measurements (see for example Møller et al. 2018 for a Q 1323–0021 $\text{H}\alpha$ measurement based on Sinfoni IFU data), since such a combination would introduce systematic effects.

Under the assumption that the $\text{H}\alpha$ and [O II] star formation rate indicators (Sect. 3.8, Eqs. (5) and (6)) trace similar timescales, any discrepancy between the two can be attributed to abundance effects and dust reddening (Kewley & Geller 2004). Requiring that the two star formation rate indicators be equal, the extinction can be solved for as

$$E_{B-V} = \frac{2.5}{\kappa_{[\text{O II}]} - \kappa_{\text{H}\alpha}} \log_{10} \left(\frac{\text{SFR}_{\text{H}\alpha}}{\text{SFR}_{[\text{O II}]}} \right), \quad (3)$$

where we infer $\text{SFR}_{\text{H}\alpha}$ from the measured $\text{H}\beta$ flux (see Sect. 3.8). Where no direct spectroscopic measurements can be used to quantify the reddening, the E_{B-V} can instead be inferred from the spectral energy distribution fits (see Sect. 3.6). The colour excess of the stellar continuum was empirically tied to the colour excess derived from the nebular emission lines (Calzetti 1997; Calzetti et al. 2000), such that

$$E_{B-V}^{\text{stellar}} = 0.44 \times E_{B-V}^{\text{nebular}}. \quad (4)$$

The resulting E_{B-V} values are reported in Table 4. For completeness, we report all E_{B-V} estimates. Hereafter, we distinguish them using the abbreviations BDEC (Balmer decrement), SFR (star formation rate), and SED (spectral energy distribution) to reflect the method with which the measurements were inferred. We did not detect all emission lines required to determine the E_{B-V} based on both BDEC and SFR for any object. Without having to select between the two methods, we therefore proceeded

to apply intrinsic E_{B-V} corrections evaluated from the line measurements when computing the SFRs and [O/H]s reported in Table 4. SED-based E_{B-V} are provided to display our best-fit SED results and for comparing measurements of E_{B-V} with different techniques, but we did not correct any flux measurements with these values. The SED-based E_{B-V} were poorly constrained by the lack of UV-photometry, and were only used to define a grid on which to optimise the SED fits to obtain stellar masses (see Sect. 3.6).

3.8. Star formation

We measured the unobscured star formation rates of the host galaxies with nebulae emission-line diagnostics assuming the standard $\text{H}\alpha$ $\lambda 6563$ Å Kennicutt (1998) – and the re-calibrated [O II] $\lambda\lambda 3727, 3729$ Å Kewley & Geller (2004) relations:

$$\begin{aligned} \text{SFR}_{\text{H}\alpha, 10 \text{ Myr}} [M_{\odot} \text{ yr}^{-1}] &= 7.9 \times 10^{-42} L_{\text{H}\alpha} [\text{ergs s}^{-1}] \\ &= 2.3 \times 10^{-41} L_{\text{H}\beta} [\text{ergs s}^{-1}], \end{aligned} \quad (5)$$

$$\text{SFR}_{[\text{O II}], 10 \text{ Myr}} [M_{\odot} \text{ yr}^{-1}] = 6.58 \times 10^{-42} L_{[\text{O II}]} [\text{ergs s}^{-1}]. \quad (6)$$

L_i refers to the dust-corrected intrinsic luminosity in SFR calibrator i . It was determined using the flux f_i and the luminosity-distance d_L using the python `astropy.cosmology` tool (Astropy Collaboration 2013) for the assumed cosmology, evaluated for the absorbing galaxy emission-line redshift z_{em} (see Sect. 3.2 and Table 4), as $L_i = L_{\text{obs}} \times 10^{0.4\kappa(\lambda)E_{B-V}^{\text{nebular}}}$. Here, $L_{\text{obs}} = f_i 4\pi d_L^2$. We note that in the absence of a dust-correction from reliable spectroscopic E_{B-V} measurements (see Sect. 3.7), the SFR can be assumed as a lower limit. The $\text{H}\alpha$ luminosity was inferred from a conversion of the $\text{H}\beta$ luminosity, assuming the intrinsic line ratio $\text{H}\alpha/\text{H}\beta = 2.86$ for standard case B recombination (Osterbrock & Ferland 2006).

The calibration of these relations assumes solar abundances and a Salpeter initial mass function (IMF; Salpeter 1955) with lower- and upper stellar mass cutoffs at 0.1 and 100 M_{\odot} respectively. As a Hydrogen recombination line, the $\text{H}\alpha$ flux is sensitive to the incident radiation bluewards of the 912 Lyman limit. This makes recombination lines direct probes of young (≤ 10 Myr) massive ($> 10 M_{\odot}$) stars which dominate the ionising photon budget, and therefore tracers of the near-instantaneous SFR on time-scales of ~ 10 Myr. The $\text{SFR}_{[\text{O II}]}$ relation is based on the [O II] $\lambda\lambda 3727, 3729$ Å collisionally excited forbidden-line doublet, empirically calibrated against $\text{H}\alpha$ to give a quantitative SFR tracer on a similar time-scale (Gallagher et al. 1989; Kennicutt 1992; Kewley & Geller 2004). For internal consistency, we shifted the values to a Chabrier IMF (Chabrier 2003) by applying a downward correction factor of 1.8. For objects where both SFR measurements are possible, we assigned preference to $\text{SFR}_{\text{H}\beta}$ as this is the most direct probe of star formation, and since $\text{SFR}_{[\text{O II}]}$ is calibrated to this recombination line (see Sect. 4.4 for more information). The resulting SFRs based on both diagnostics and their associated measurement errors are summarised in Table 4.

Emission from the [O II] doublet was used by (Straka et al. 2016; hereafter S16) to measure the SFR of the interacting system in the Q 1436–0051 field (their object 6 and 7, see Sect. 2.4 for more information). They could not resolve the flux from the interacting components. Using a Salpeter IMF, they therefore reported a combined SFR, which they split according to photometric flux-ratios, giving $\text{SFR}_{[\text{O II}]}^{\text{S16}}(\text{obj } 6) = 26 M_{\odot} \text{ yr}^{-1}$ and $\text{SFR}_{[\text{O II}]}^{\text{S16}}(\text{obj } 7) = 22 M_{\odot} \text{ yr}^{-1}$.

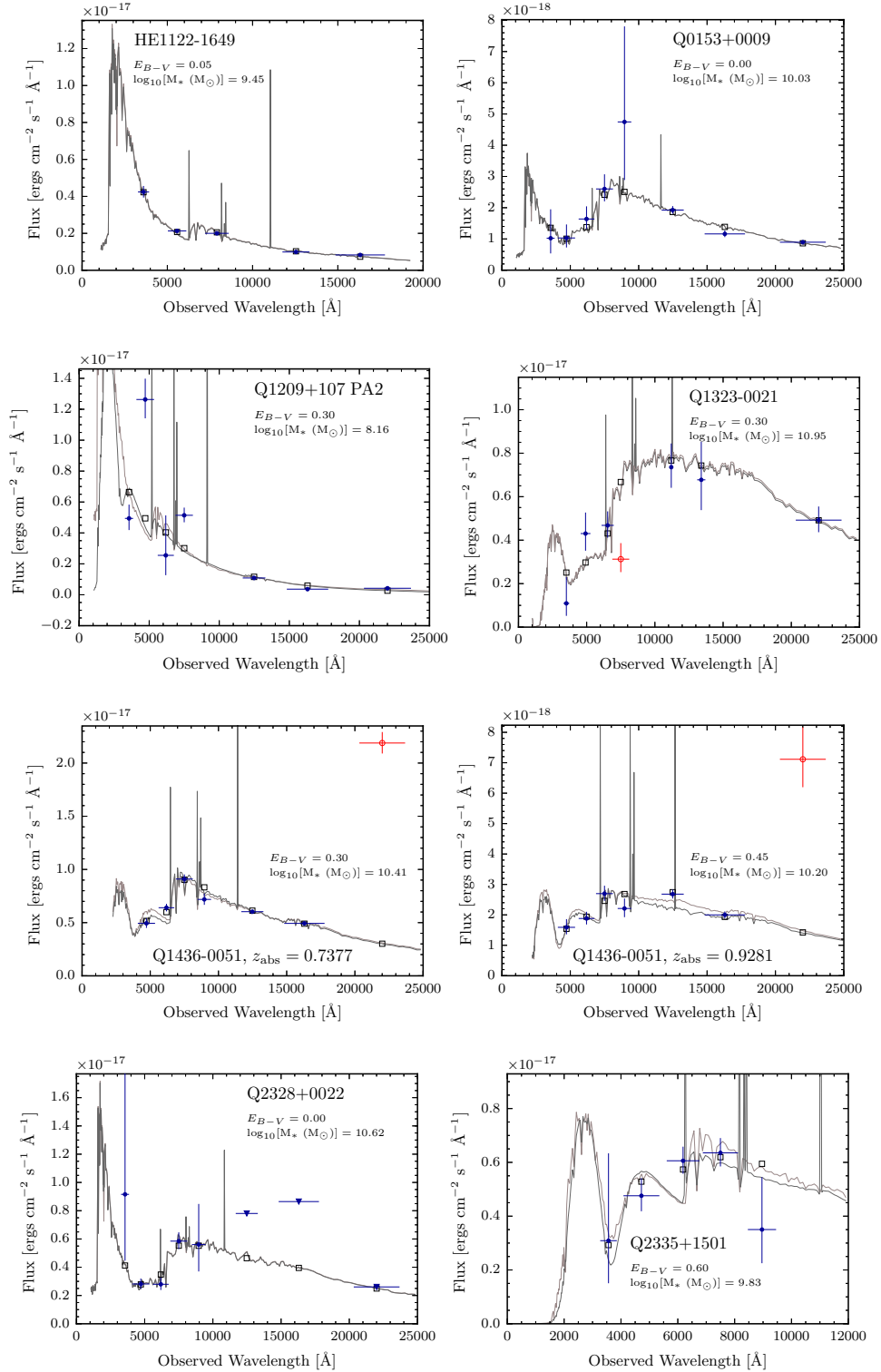


Fig. 2. Spectral energy distribution fits minimising the χ^2 -statistic for each of the spectroscopically identified host-galaxies. In each panel, we plot the solutions including and excluding nebular emission lines to show its impact on the derived stellar masses. Blue (red) data points refer to included (excluded) magnitudes, with vertical and horizontal error-bars indicating the uncertainty in the photometry and the FWHM of each filter, respectively. Grey squares refer to the transmission-weighted flux in each filter, calculated based on the best-fit SED solution. Upper limits are denoted by triangles. Each panel text displays the LEPHARE best fit reddening before we apply the stellar-to-nebular conversion (Eq. (4)), and the resulting stellar mass.

Our FORS2 spectrum is able to resolve the individual components of the interacting system (see Appendix A), giving a $\text{SFR}_{\text{H}\beta} = 0.48 \pm 0.10 M_{\odot} \text{yr}^{-1}$ of the confirmed host (see Table 4). The strong contrast between the $\text{SFR}_{[\text{O II}]^{\text{S16}}}$ and our $\text{SFR}_{\text{H}\beta}$ diagnostic makes this field a unique case, granting additional analysis. Our FORS2 spectrum does not cover the [O II] doublet. We therefore matched the continuum light in the calibrated Magellan II spectrum used for the S16 analysis (Straka et al. 2016, and priv. comm. with Lorrie Straka) to the combined *i*-band magnitude reported in Rao et al. (2011). Under the assumption that the reported S16 flux-level of $\times 10^{-17} \text{ergs s}^{-1} \text{cm}^{-2}$ is in fact $\times 10^{-18} \text{ergs s}^{-1} \text{cm}^{-2}$, the continuum fluxes are consistent. With this rescaling of the flux level, and converting to a Chabrier IMF, we recovered a $\text{SFR}_{[\text{O II}]^{\text{This work}}} = 1.02 \pm 0.07 M_{\odot} \text{yr}^{-1}$, which we also report in Table 4. To within a factor of two, this value is consistent with our FORS2 $\text{SFR}_{\text{H}\beta}$ measurement.

3.9. Metallicity

We inferred the metallicity of the absorbing galaxy in two independent ways based on (i) strong-line diagnostics with dereddened line-fluxes according to Sect. 3.7 where possible; and (ii) applying a metallicity gradient correction to the known absorption metallicity. Despite being interchangeable, we distinguish between absorption and emission based measurements by referring to the metallicity ([M/H]) and Oxygen abundance $12 + \log(\text{O}/\text{H})$, respectively.

Emission-line fluxes in [O II], H β and [O III] enabled us to calculate specific line-ratios which correlate with metallicity (Pagel et al. 1979; Maiolino et al. 2008). In the following, we report the results based on the R₂₃, O₃₂, O₂ and O₃ line-ratios, defined as

$$\begin{aligned} R_{23} &= (f_{[\text{O II}]\lambda\lambda 3727,3729} + f_{[\text{O III}]\lambda\lambda 4959,5007}) / f_{\text{H}\beta} \\ O_{32} &= f_{[\text{O III}]\lambda\lambda 4959,5007} / f_{[\text{O II}]\lambda\lambda 3727,3729} \\ O_2 &= f_{[\text{O II}]\lambda\lambda 3727,3729} / f_{\text{H}\beta} \\ O_3 &= f_{[\text{O III}]\lambda 5007} / f_{\text{H}\beta}, \end{aligned} \quad (7)$$

respectively. These line-ratios are sensitive to the nebular conditions that govern the individual line-strengths, and observed line-ratios are often compatible with multiple abundances (Osterbrock & Ferland 2006). We therefore assumed the standard R₂₃ diagnostic, invoking the O₃₂ ratio to account for ionisation corrections and break the degenerate solutions in abundance from a characteristic double-branched diagnostic. For systems with limited line-coverage, we report solutions based on the O₂ and O₃ line-ratios. Where these line-ratios give double-valued abundance-solutions, we report the abundance which closest matches the value inferred from a $z = 0.7$ mass-metallicity relation (Maiolino et al. 2008, hereafter M08). For internal consistency, these diagnostic line-ratios were converted to oxygen abundances assuming the M08 calibration (see Table 4). The reported uncertainties reflect the uncertainties in derived line-ratios, excluding the internal scatter present in the M08 relations. For notes on individual objects, see Appendix B.

The use of different strong-line diagnostics, each displaying its own internal scatter, makes it difficult to analyse the sample in a homogenous way. By combining SED stellar masses with absorption- and emission line metallicities, Christensen et al. (2014) reinterpreted $C_{[\text{M}/\text{H}]}$ (see Sect. 1) as an average metallicity gradient Γ acting over the impact parameter b connecting the absorption- and emission measurements, $C_{[\text{M}/\text{H}]} = \Gamma b$. They retrieved a mean linear metallicity gradient $\langle \Gamma \rangle = -0.022 \pm 0.004 \text{ dex kpc}^{-1}$. In Sect. 4.5 we re-examine

their analysis including the results from our work, which gives a revised value of $\langle \Gamma \rangle = -0.022 \pm 0.001 \text{ dex kpc}^{-1}$. Applying this updated correction factor and a 12 kpc truncation radius (see Sect. 4.5) to the absorption-metallicities allowed us to infer a standardised metallicity measurement in emission for each absorbing galaxy as

$$[\text{M}/\text{H}]_{\text{em}} = [\text{M}/\text{H}]_{\text{abs}} + \langle \Gamma \rangle b |_{b \leq 12 \text{ kpc}}. \quad (8)$$

The calibration of Eq. (8) is tied to the M08 MZ-relation, which in turn uses the Kewley & Dopita (2002) functional form of the R₂₃ and the O₂₃ diagnostics to convert between observed line-ratios and metallicity. We used zinc as a tracer element of the absorption-metallicity where possible, since it is minimally depleted. Where only iron or chromium measurements exist, we included a standard depletion and α -enhancement correction to the absorption metallicity, $[\text{M}/\text{H}]_{\text{abs}} = [\text{Fe}/\text{H}] + 0.3 \text{ dex}$ (Rafelski et al. 2012). We note, however, that such a constant correction does not account for metallicity-dependent depletion, and De Cia et al. (2018) suggest that even zinc can be subject to marginal dust depletion, albeit to a lesser extent than for iron. For this reason, the reported zinc-measurements represent lower limits on the metallicity measurements.

4. Discussion

In the following, our sample is discussed in relation to other luminosity- and absorption selected samples. Luminosity-selected data is not illustrated for individual galaxies. We strictly adhere to plotting the scaling relations derived from such samples. The luminosity-selected MZ-relations are taken from M08, whereas the luminosity-selected star-forming main sequences are taken from Whitaker et al. (2014). We refer to each relation's reference with the abbreviation M08 and W14, respectively. Likewise, we refer to Møller et al. (2013) as M13—in particular when referring to the predicted M13 MZ-relation. Where relevant parameters are known, individual galaxies in the absorption-selected reference sample are plotted⁵. This reference sample constitutes the spectroscopically confirmed systems presented in Krogager et al. (2012) and Christensen et al. (2014), referred to as K12 and C14, respectively. In Sect. 4.4 we extend the comparison sample to include the objects in Kanekar et al. (2018).

4.1. Impact parameter as probe of average size

The impact parameter, b , measures the projected distance between the luminosity-centre and a random quasar sightline piercing the gaseous component of a galaxy. Therefore, the distribution of impact parameters conveys information on the average spatial scales and sizes of the gaseous HI regions probed, having folded in detection- and strategy-biases. In Fig. 3, we therefore plot the distribution of b as a function of $\log_{10}[N_{\text{HI}}(\text{cm}^{-2})]$ (left) and as a function of $[\text{M}/\text{H}]_{\text{abs}}$ (right). The data refer to damped absorbers with spectroscopically confirmed hosts in the reference sample (circles) with the added objects from this work (squares). Our sample effectively extends the observed distributions of Fig. 3 towards (i) lower redshifts;

⁵ We note that two new stellar masses of absorbing galaxies were recently published in Augustin et al. (2018). The paper appeared too late for us to include those objects in our reference sample, but a quick comparison confirms that the new objects fall on the relations presented in this paper.

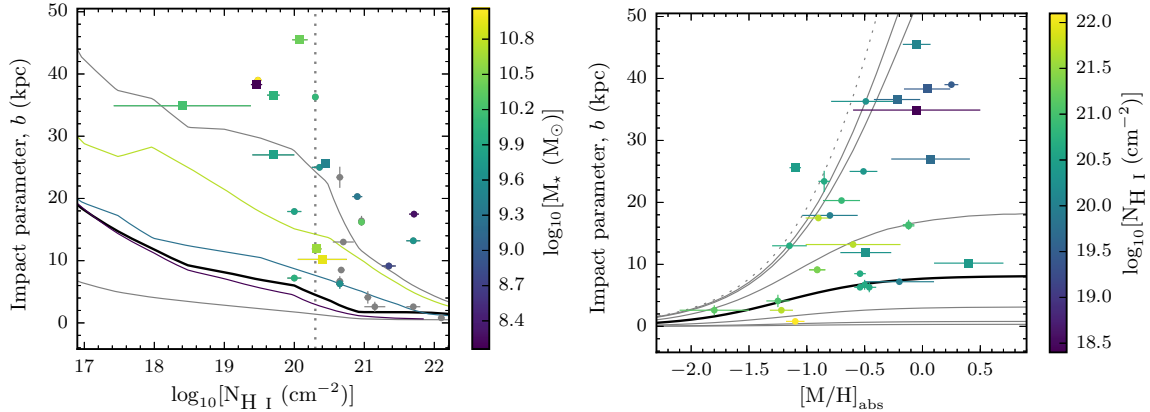


Fig. 3. *Left panel:* distribution of impact parameter plotted as a function of the column density $\log_{10}[N_{\text{HI}} (\text{cm}^{-2})]$, colour-coded by stellar mass. Circles refer to data from literature. Our new identifications are plotted as squares. Grey data points represent spectroscopically confirmed absorbing galaxies without stellar mass estimates. The black line represents the median- and the grey lines represent the 1σ scatter in simulated distributions (Rahmati & Schaye 2014) at $z = 2$. Colour-coded lines represent the median impact parameters for those stellar mass bins, from the same simulations. *Right panel:* distribution of impact parameters as a function of the absorber metallicity $[M/H]_{\text{abs}}$, colour-coded by column density. The black line marks the median- and the grey lines mark the 1σ , 2σ and 3σ contours based on the model-predictions from Krogager et al. (2017). The grey dotted line marks the distribution envelope.

(ii) lower H I column-densities; and (iii) higher absorption-line metallicities.

Building on the results of previous studies (see Sect. 1), the left panel of Fig. 3 conforms to the idea that sub-DLAs and DLAs trace different relations to their hosts; the former having higher scatter- and higher mean impact parameters than the latter, on average. Similar conclusions were reached by Rahmani et al. (2016) who found a transition region at ~ 20 kpc, above which no $\log_{10}[N_{\text{HI}} (\text{cm}^{-2})] > 21.0$ absorbing galaxy was detected. We find a similar value, which for the combined sample becomes $b \sim 25$ kpc. Rao et al. (2011) found that DLAs are statistically closer to the candidate host sightline than sub-DLAs by a factor of two, with $\langle b \rangle_{\text{R11,DLA}} = 17.4$ kpc and $\langle b \rangle_{\text{R11,sub-DLA}} = 33.3$ kpc, respectively. This is remarkably consistent with our findings, which give median impact parameters of $\langle b \rangle_{\text{DLA}} = 11.1$ kpc and $\langle b \rangle_{\text{sub-DLA}} = 35.8$ kpc. These results suggest a characteristic scale-length associated with the column-density distribution of gas in absorption-selected galaxies, and may be connected to the fall-off in gas density with radius.

We overplot the median (black) and 1σ (grey) lines of the impact parameter distribution from the Rahmati & Schaye (2014) simulations. We colour-code the data to the SED $\log_{10}[M_{\star} (M_{\odot})]$ (the point is flagged grey if no stellar mass value exists) and overplot the median curves for $\log_{10}[M_{\star} (M_{\odot})]$ bins of 7.0–8.5; 8.5–10.0; and 10.0–11.5 (Rahmati & Schaye 2014), in representative colours. This allows us verify whether the observed distribution in the data is captured by the simulations, and to assess whether the retrieved column-density scale-length is mass-dependent. With the current small sample, we find no such dependence.

Overall, the observed scatter is larger, and the median impact parameter increases sharper with decreasing H I column density, relative to the simulations. One suggestion is that this difference is driven by false-positive host galaxy identifications (Rahmati & Schaye 2014). However, such a false-positive identification rate would have to be sensitive to the column-density of the absorber -acting stronger on lower column density absorbers in order to reconcile the observations with simulations. That sub-DLAs are located at large impact parameters

does not make them less likely to be the host, an issue discussed in Meiring et al. (2011). In addition, the imposed cut in metallicity limits this bias if absorbing galaxies follow a mass-metallicity relation (M 13).

Instead, the interpretation is complicated by sample pre-selection; detection-bias; strategy-bias, and there may be a size-evolution with redshift. Fundamentally, an absorption-selection introduces a bias towards gaseous systems with large neutral gas cross-sections. In combination with a lower cut on absorption metallicity, this pre-selects towards large, massive, bright galaxies independent of the absorber H I column density, biasing the observations towards large impact parameters. This selection is enhanced by the brightness of the background quasar, which prevents the detection of low luminosity systems -especially at low impact parameters if the region below the quasar trace is not scanned with an SPSF analysis (see Sect. 3.1). In addition, our $z < 1$ data is a long-slit follow-up of systems with photometric candidate hosts, whereas the $z \geq 2$ galaxies are identified from Ly α emission in the Ly α trough or from strong optical emission lines found along any of the three slit position angles configured to cover as much of the region around the quasar as possible, without any pre-selection on candidate host (Fynbo et al. 2010; Krogager et al. 2017). Intuitively the latter observing strategy leads to a higher effective exposure time in the slit-coverage overlap, and therefore to a preferential identification of hosts at low impact parameters.

This strategy-bias is quantified in the right panel of Fig. 3, which shows how the impact parameters (circles and squares) are distributed relative to the modelled expectation (grey contours; Krogager et al. 2017) as a function of absorption metallicity. The data is now colour-coded to the H I column density, with an expected correlation assuming the existence of a luminosity-metallicity relation for damped absorbers (M 13), and that luminosity correlates with size of the absorbing galaxy (K12). In their paper, Krogager et al. (2017) show a remarkable statistical agreement; the 1σ model contours encompassing 69% of their data. This implies that the strategy bias is effectively negligible in their DLA sample, relative to the pre-selection towards large systems.

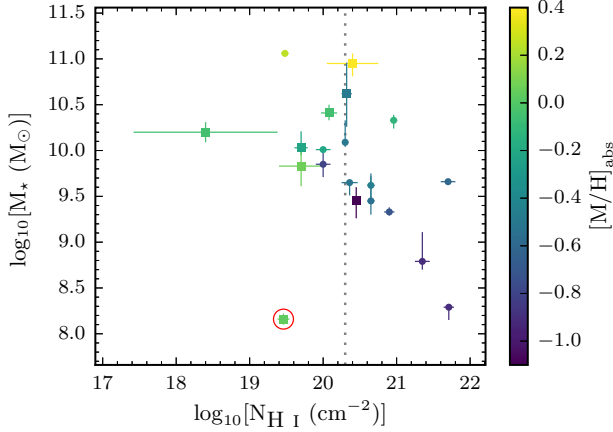


Fig. 4. Stellar masses of spectroscopically confirmed absorbing galaxies as a function of the absorber neutral hydrogen column density, colour-coded by the absorption metallicity. The dotted line marks the traditional distinction between sub-DLAs and DLAs at $\log_{10}[N_{\text{H I}}(\text{cm}^{-2})] = 20.3$. The object encircled in red represents the outlier from Q 1209+107 PA2.

It is remarkable that the model, developed for $z \sim 2-3$ DLAs, has an envelope that encompasses 96% of the spectroscopically confirmed systems (i.e. 27/28 systems, with one outlier) extending towards sub-DLAs and to $z \sim 0.7$. To investigate this statistically, we computed the fraction of systems locked into the 1σ -, 2σ -, 3σ -model contours, for which we find 46%; 82%; and 89% of the combined data, respectively. This factor two increase between the 1 - and 2σ contours indicates that the model does not statistically match a combined sample of sub-DLAs and DLAs. This is supported by the H I column-densities, which show that the factor of two increase is attributed to the more metal-enriched ($[M/H]_{\text{abs}} \geq -0.5$) sub-DLAs.

4.2. Drivers of the apparent $M_{\star} - N_{\text{H I}}$ correlation

It has been suggested that sub-DLAs and DLAs arise in galaxies of different masses (Kulkarni et al. 2010; Meiring et al. 2011) – a suggestion which may alleviate the statistical tension between sub-DLAs and DLAs in the b - $[M/H]_{\text{abs}}$ model expectation (see Sect. 4.1 and Fig. 3). To address this question, in Fig. 4 we plot the stellar mass of spectroscopically identified hosts as a function of the H I column density of the associated quasar absorber, colour-coded to the absorption-metallicity, $[M/H]_{\text{abs}}$.

The data suggest an anti-correlation, with higher-mass systems observed to host progressively lower column-density absorbers; and a secondary correlation between the absorption-metallicity and stellar mass, reminiscent of a mass-metallicity relation. But the observed anti-correlation could be a manifestation of multiple effects acting simultaneously; (i) a selection-bias against dusty – and therefore massive, metal-rich systems; and (ii) the cross-section selection biasing the sample number-count to large, massive galaxies with relatively larger projected areas of lower-density gas; the combination of the two making the sampling of the underlying distribution mimic a correlation.

We know that visual attenuation, A_V , which is used to parametrise the dust content and the overall reddening of a source is related to the total column of metals. The metal column is itself the product of the neutral hydrogen gas column density and the metallicity. Recent studies have shown that the metal column correlates with the visual attenuation, such that

$\log_{10}(A_V/\text{mag}) \propto \log_{10} N_{\text{H I}} + [M/H]$ (see Zafar & Watson 2013; Zafar & Møller 2018). Such a preferential dust-bias against high column-density absorbers is therefore consistent with the observed column-density dependent cutoff in stellar mass that we observe in the data, and can – at least in part, be explained by a dust bias against red quasars.

Recent work from the High A_V Quasar survey (HAQ; Fynbo et al. 2013b; Krogager et al. 2015; Zafar et al. 2015) – and the extended HAQ (eHAQ; Krogager et al. 2016; Fynbo et al. 2017) survey suggest that a traditional quasar selection is indeed biased against reddened quasars. This is consistent with Noterdaeme et al. (2015) who found that the high column-density ($\log_{10} N_{\text{H I}} \sim 22$), high metallicity ($\geq 1/10$ solar) DLAs induce a colour-change in the background quasar caused by both dust- and hydrogen absorption. This propagates into a dust-bias which preferentially acts on high $N_{\text{H I}}$, massive, metal-rich, dusty galaxies selected against quasar sight-lines.

4.3. The mass-metallicity relation

We investigated how the absorption-selected galaxy population is distributed relative to known mass-metallicity (MZ) relations of luminosity-selected galaxies. In Fig. 5, we plot two metallicity measurements as a function of the stellar mass. The data represent spectroscopically confirmed absorbing galaxies, with squares denoting the measurements in this work, and circles representing the compiled reference sample. We colour-code the data according to the redshift of each system, and overplot the M08 MZ relations at redshifts $z = 0.07$, $z = 0.7$, $z = 2.2$, and $z = 3.5$, matched in colour. Here, we also add a 0.15 dex conservative estimate of the intrinsic scatter in each relation as the shaded regions (Kewley & Ellison 2008, M08).

In Fig. 5 top panel, we use the absorption metallicity as an indicator of the integrated emission metallicity. In addition, we convert the M13 functional form for M_{\star} into a mass-metallicity relation (M13 MZ-relation) for absorption-selected galaxies, setting $C_{[M/H]} = 0$. These are plotted for the same four redshifts as the M08 relations to give a fair comparison. Two observations can be made. Firstly, with the exception of $z = 3.5$, the M08- and M13 MZ relations tangentially match in the near linear low-mass regime, but diverge towards larger masses. Secondly, the data fall systematically below both the M08 and the M13 MZ-relations at their respective redshifts. To quantify how well the models describe the data, we calculated the reduced chi-square statistic, χ^2_{ν} . For M08, we interpolated the functional forms to the redshifts of the data. Including the 0.15 dex intrinsic scatter in the relation, we found a value $\chi^2_{\nu, \text{M08}} = 11.70$. This can be compared to the corresponding M13 MZ-relation which, by including their intrinsic scatter of 0.38 dex yields a value $\chi^2_{\nu, \text{M13}} = 3.21$. We here note that whilst the M13 model is statistically a better fit to the data, this result is driven by a large internal scatter, and does not mitigate the systematically lower metallicities for a given stellar mass and redshift.

Following the prescription outlined in Sect. 3.9, in the bottom panel of Fig. 5, we corrected the absorption metallicity for the average metallicity gradient solved in Sect. 4.5. Local galaxies are found to have effective radii ~ 6 kpc, with oxygen abundance gradients extending to around ~ 2 disc effective radii followed by flat gradients (the CALIFA survey, Sánchez et al. 2014). Motivated by these results, in combination with the metallicity gradient we also applied a truncation-radius at 12 kpc to the data. This effectively converts the absorption measurement into an indirect emission measurement of the metallicity at the galaxy luminosity centre.

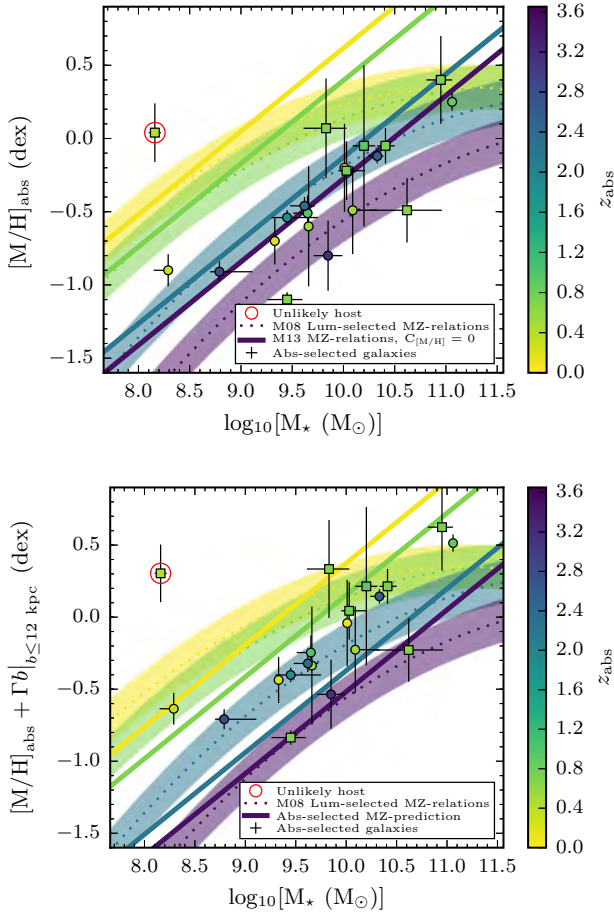


Fig. 5. Metallicity as a function of stellar mass for spectroscopically confirmed absorbing galaxies, colour-coded by redshift. Squares indicate the results of this work, whereas circles refer to the absorption-selected reference sample. The M08 mass-metallicity relations based on luminosity-selected samples, and the M13 predicted mass-metallicity relations for absorption-selected samples are overplotted at four representative redshifts. *Top panel:* results assuming the metallicity measured in absorption. *Bottom panel:* results with an impact-parameter dependent correction factor and a gradient cut-off at a truncation radius of 12 kpc. The object encircled in red represents the outlier from Q 1209+107 PA2.

It is worth noting that the M08 MZ-relations were calibrated to metallicity measurements averaged over the emission line regions of star forming galaxies. We can therefore ask whether applying a correction factor to the absorption metallicity will overestimate the luminosity-selected measurement, rendering the comparison meaningless. The individual surveys used to calibrate the M08 MZ relations at different redshifts have apertures of 0.75–1.3 arcsec (Savaglio et al. 2005, $z \sim 0.7$); 0.76 arcsec (Erb et al. 2006, $z \sim 2.2$) and 0.75 arcsec (Maiolino et al. 2008, $z \sim 3.5$). A source centred on - and filling the aperture therefore have physical radii of the order 2.8–4.7 kpc; 3.6 kpc and 3.0 kpc for those representative redshifts, respectively. This gives a conservative estimate of the overshooting in the range $r_{\text{aperture}} \times \langle \Gamma \rangle \sim 0.06$ –0.10 dex. Recognising that this range is significantly below individual absorption metallicity uncertainties, and that the exact overshooting is sensitive to the light-distribution across the aperture, we

conclude that its net systematic effect on our conclusions are negligible.

In the lower panel, we also overplot the same M08 relations, and include $C_{[M/H]}$ to the M13 predicted MZ-relation. To be consistent with the original functional form based on a pure DLA-sample, we reformulated the constant as $C_{[M/H]} = \langle \Gamma \rangle \times \langle b \rangle_{\text{DLA}}$, for $\langle \Gamma \rangle = -0.022 \text{ dex kpc}^{-1}$ (see Sect. 4.5), and $\langle b \rangle_{\text{DLA}} = 11.1 \text{ kpc}$ (see Sect. 4.1). Having applied the corrections to the data and to the relations, we now make two new observations. Firstly, rather than overlapping with the M08 relations at low stellar masses, including $C_{[M/H]}$ renormalises the M13 MZ-relation and generates convergence at larger stellar masses, on average. Secondly, the systematic bias in the data towards lower metallicity for a given stellar mass and redshift bin is reduced. These conclusions are supported by recalculating the reduced chi-square statistics, which give values of $\chi^2_{\nu, \text{M08}} = 7.95$ and $\chi^2_{\nu, \text{M13}} = 0.98$ by replacing the intrinsic scatter from M13 with the updated value of 0.32 (see Sect. 4.5).

We therefore conclude that the absorber based MZ-relation provides a better fit to the data. We recognise that this fit is dominated by a large intrinsic scatter that prevents us from discerning any clear redshift evolution. Despite this, the inclusion of a mean metallicity gradient and a truncation radius is physically motivated and has a significant effect on the χ^2 -statistic, reducing it by a factor ~ 3 . This suggests that we can statistically predict global properties from local measurements.

4.4. Absorbing galaxies probing sub-main-sequence star-formation

Møller et al. (2018) and Kanekar et al. (2018), based on a recent ALMA survey of molecular gas (Neeleman et al. 2016b; Møller et al. 2018), tried to characterise the relation between the neutral- and molecular gas content and the SFR in absorption-selected galaxies. Based on a sample of two, the former suggested that absorption-selected galaxies sample a missing phase in galaxy evolution; a “post-starburst” phase, characterised by low star-formation and large gas- and molecular fractions (Møller et al. 2018). This is driven by the preceding onset of a starburst phase that drives molecular- and neutral gas to large distances, making such systems susceptible to the H I cross-section selection. In the latter, Kanekar et al. (2018) from a sample of seven, argued that absorption-selected galaxies are consistent with the star-forming main-sequence. However, they retain large molecular masses at all redshifts. The insensitivity of the SFR on molecular gas mass is therefore interpreted as evidence for low molecular gas-densities which inhibit the molecular-gas from converting into stars.

Here, we do not consider CO-detections. This allows us to look at a larger data-set to quantify the absorbing galaxy population relative to the star-formation main sequence as a whole. In Fig. 6, we show how the sample of absorbing galaxies fall relative to the main sequence of star-formation. Square symbols represent the results of this work (SED-based M_* and extinction-corrected SFRs, as reported in Table 4); circles refer to literature samples. For completeness, we add to our sample the two systems (B 1629+120g and J 0058+0155g) from Kanekar et al. (2018), not covered by the C14 sample or this study. These two systems are represented by triangles. For galaxies with multiple SFR-tracers ([O II] and H β), we assign preference to the H β measurement, since this is a direct measure of the SFR based on recombination theory. We note however that in general, the [O II] SFRs show good agreement with the H β based measurements.

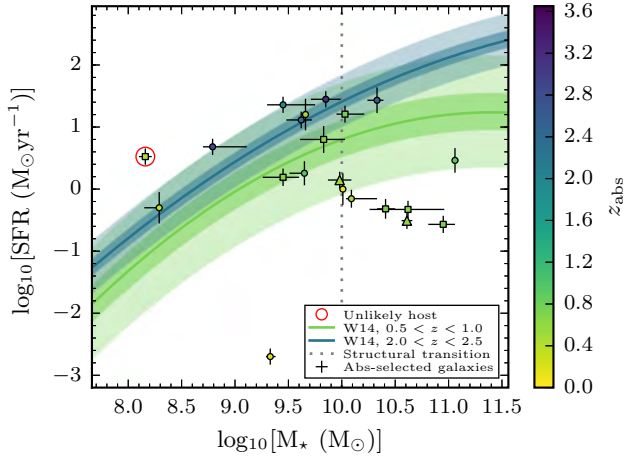


Fig. 6. Star-formation rate as a function of stellar mass for spectroscopically confirmed absorbing galaxies, colour-coded by redshift. Squares indicate the results of this work; circles refer to work by others. Triangles represent CO detected galaxies. For reference, we plot the Whitaker et al. (2014) redshift-dependent star-forming main sequence for two representative redshift ranges together with their 1σ - and 3σ scatter, represented by the dark- and light- shaded regions centred on each relation, respectively. See text in Sect. 4.4 for more details. The object encircled in red represents the outlier from Q 1209+107 PA2.

In addition to the measurement errors reported in Table 4, we include a 30% uncertainty to each SFR to account for scatter between the H β and the [O II] diagnostic calibrations (Kennicutt 1998; Kewley & Geller 2004). We then colour-code the absorbing galaxies by redshift. For reference, we overplot the star-forming main-sequences at redshift ranges $0.5 < z < 1.0$ and $2.0 < z < 2.5$ for a Chabrier IMF (Whitaker et al. 2014). We have matched the colours for each relation to representative redshifts of $z = 0.75$ and $z = 2.25$, respectively. In addition, we include the 1σ - and 3σ dispersions as the dark- and light shaded regions around each of the relations. These are estimated based on a reported scatter of 0.14 dex for $z \sim 2$ and 0.30 dex for $z < 1$ (Whitaker et al. 2015).

The high-redshift ($z \sim 2$) absorbing galaxies are consistent with the 3σ scatter of the star-forming main sequence at that redshift, whereas a significant fraction of systems at low ($z \lesssim 1$) redshifts suggest sub-main-sequence star-formation. Despite individual systems showing large scatter, we note that this bias appears significant and real, since the data are not stochastically distributed around the main sequence. With the current sample, we therefore ask whether this suppression, if real, is evolutionary or inherent to the nature of absorption-selected galaxies.

Despite the temptation to see the results as indicative of an evolutionary transition, with galaxies “breaking off” the star-forming main sequence to become quenched at some characteristic redshift $z \sim 0.7$ in line with the CO detected DLA galaxies in Kanekar et al. (2018), this is not supported by our data. A majority of the systems with suppressed SFRs lie at the high-mass end of the distribution, whereas the majority of systems at lower stellar masses are consistent with the 3σ scatter. Empirically, this suggests that suppressed SFRs are inherent to absorption-selected galaxies above stellar mass $\log_{10} M_{\star} (M_{\odot}) \gtrsim 10$, indicated by the grey dotted line in Fig. 6. 88% (7/8 systems) with $\log_{10} M_{\star} (M_{\odot}) \gtrsim 10$ fall below their respective redshift-relation. Out of these, 63% (5/8 systems) are inconsistent with the 3σ scatter. Despite the low number

of systems at high- z , this interpretation is consistent with the Q 0918+1636 system ($z_{\text{abs}} = 2.583$, $\log_{10} M_{\star} (M_{\odot}) \sim 10.3$), with a single outlier in Q 0738+313 ($z_{\text{abs}} = 0.221$, $\log_{10} M_{\star} (M_{\odot}) \sim 9.3$) displaying suppressed SFR at lower mass.

The natural question to ask is whether this suppression can be explained by selection effects or a dust bias. Indeed, pre-selecting against HAQ galaxies (Fynbo et al. 2013b; Krogager et al. 2015; Zafar et al. 2015), large fractions of obscured star formation and lack of applying extinction corrections to the SFR will systematically deplete the high mass, high star formation domain of Fig. 6. Ma et al. (2015) showed that massive ($10.3 \leq \log_{10}[M_{\star} (M_{\odot})] \leq 11.5$), dusty galaxies are usually highly star forming, with values of $510\text{--}4800 M_{\odot} \text{ yr}^{-1}$. The extinction corrected SFRs for our galaxies (see Table 4) are low, which suggests that the detected galaxies on average are not very dusty. Based on the high fraction of identified hosts, a dust bias therefore does not appear to affect this study. Albeit difficult to motivate why, we therefore suggest that the suppression of star formation in absorption-selected galaxies is mass-dependent, and not evolutionary.

4.5. The existence of an average metallicity gradient

Cosmological hydrodynamic simulations such as the Galaxies-Intergalactic Medium Calculation (GIMIC, Crain et al. 2009) predict systematic flattening of metallicity-gradients in star-forming disc-galaxies with redshift, from $z = 2$ to $z = 0$. In such simulations, this flattening is caused by declining inflows of pristine gas; enrichment by in situ star-formation; and the redistribution of metal-enriched gas from the inner to outer disc, leading to progressive outer disc enrichment. Observations of spatially resolved star-forming galaxies are comparable to these results (Swinbank et al. 2012). Likewise, Stott et al. (2014) suggested that the specific SFR (sSFR), which parametrises how intensely a galaxy is forming stars, drives the observed differences in metallicity gradients. In their framework, observations of high-sSFR systems associated with metal-poor centres and flat- and inverted metallicity-gradients are a consequence of mergers (Rupke et al. 2010) and cold flows (Dekel et al. 2009; Cresci et al. 2010). Similar results were also reported by Queyrel et al. (2012), who found examples of positive gradients in $z = 1.2$ star-forming galaxies. These mechanisms will channel pristine gas into the galaxy central regions, providing fuel and triggering intense star-formation that increases the sSFR whilst diluting the metallicity in the galactic cores. This leads us to expect a synergy between the metallicity-gradient’s observed dependence on sSFR and redshift, consistent with the fundamental metallicity relation for which galaxies at fixed stellar mass are progressively metal poor for increased SFR (Mannucci et al. 2010).

To see whether we can resolve such evolutionary diagnostics, we first determined individual metallicity-gradients $\Gamma_i [\text{dex kpc}^{-1}]$. We recognise, however, that there are important differences between gradients measured in emission on spatially resolved systems to those measured by combining emission with absorption measurements. Despite internal consistency in the derived oxygen abundances reported in Table 4 using the M08 calibrations, the individual measurements as well as those from literature use different emission-line diagnostics, and therefore represent a heterogeneous sample. Additionally, absorption metallicities sample pencil-beams and therefore trace the local metallicity, typically offset from the galaxy centre. In slit spectra however, a spectroscopic emission-line metallicity represents the mean metallicity across the slit-width. For a galaxy at $z = 0.7$, a representative redshift of our sample,

a slit-width of $\theta = 1.31$ arcsec yields a metallicity-estimate averaged over spatial scales of ~ 9.5 kpc. We therefore caution against a direct combination of absorption and emission metallicities, since they likely probe different enrichment histories and sample local and global enrichment time-scales, respectively.

To determine Γ_i homogeneously, we instead used the relation $\Gamma_i = C_{[M/H],i}/b_i$ (C14). $C_{[M/H],i}$ refers to the predicted metallicity parameter (M13, their Eq. (6)), evaluated for a system i assuming its SED stellar mass as

$$C_{[M/H],i} = \frac{\log_{10}[M_{\star,i}^{\text{SED}}(M_{\odot})]}{1.76} - [M/H]_{\text{abs},i} - 0.35z_{\text{abs},i} - 5.04, \quad (9)$$

and b_i refers to the measured impact parameter. We then determined an empirical expectation value of the average metallicity gradient, $\langle \Gamma \rangle$, adopting the $C_{\text{d.o.f.}}^2$ -minimisation method used in M13 and C14. Recognising that Eq. (9) has a natural intrinsic scatter, σ_{nat} , we desire the combination $[\sigma_{\text{nat}}, \langle \Gamma \rangle]$ which minimises σ_{nat} and for which the $C_{\text{d.o.f.}}^2$ -statistic is unity. In effect, we seek the solution to

$$0 = \left(\frac{1}{\text{d.o.f.}} \sum_{i=1}^N \frac{(C_{[M/H],i} - \langle \Gamma \rangle b_i)^2}{\sigma_{\text{nat}}^2 + \sigma_{C_{[M/H],i}}^2} \right) - C_{\text{d.o.f.}}^2, \quad (10)$$

where the degrees of freedom (d.o.f.) is $N-1$ and not $N-2$, since by construction we fix σ_{nat} to its minimum value. $\sigma_{C_{[M/H],i}}$ is the propagated uncertainty from the absorption metallicity and from the stellar mass measurements.

For our total FORS2 sample, we found a solution $[0.66 \pm 0.05, 0.015 \pm 0.001]$. Combining the new sample with C14, we found $[0.44 \pm 0.01, 0.018 \pm 0.001]$. These gradients are shallower than the findings of C14, who found $\langle \Gamma \rangle_{\text{C14}} = -0.022 \pm 0.004$ dex kpc $^{-1}$, and only marginally consistent to within the reported errors in our respective studies. We note, however, that we reformulated a method that searched a pre-defined parameter-grid for the minimum σ_{nat} into a method seeking the roots of Eq. (10). Having confirmed that the two methods yield consistent values on the same data, we excluded the probable misidentification in Q1209+107 PA2 (see Sect. 3.4). With this exclusion we retrieved an intrinsic dispersion $\sigma_{\text{nat}} = 0.32 \pm 0.01$ and an average gradient of $\langle \Gamma \rangle_{\text{new}} = -0.022 \pm 0.001$ dex kpc $^{-1}$. This value is in perfect agreement with $\langle \Gamma \rangle_{\text{C14}}$, and lends further support to the galaxy in Q1209+107 PA2 being an unlikely host.

In the same work, C14 solved for gradients measured from the direct comparison of metallicity measurements in emission- and absorption line measurements, $([M/H]_{\text{em}} - [M/H]_{\text{abs}})/b_i$, for which they found a mean value of -0.023 ± 0.015 dex kpc $^{-1}$. Similar work comparing direct measurements yield a median value of -0.022 dex kpc $^{-1}$ (Péroux et al. 2016), and performing a weighted mean on the three direct measurements reported in Rahmani et al. (2016) gives a metallicity gradient of -0.04 ± 0.01 dex kpc $^{-1}$. We note however, that Rahmani et al. (2016) reported a best-fit gradient to a compilation of all known measurements, excluding limits and non-detections of -0.002 ± 0.007 dex kpc $^{-1}$. This would indicate an insignificant metallicity gradient – in contrast with our results, and may reflect the combination of heterogenous diagnostics and local- and global scale metallicity-measurements. Stott et al. (2014) retrieved an average gradient of $\Delta Z/dr = -0.002 \pm 0.007$ dex kpc $^{-1}$ based on 20 disc galaxies at $z = 1$. Swinbank et al. (2012) recovered metallicity gradients in discs ($\lesssim 10$ kpc) that are negative or flat for seven spatially resolved galaxies at $z = 0.84 - 2.23$, with an average gradient of $\Delta \log_{10}(\text{O}/\text{H})/\Delta R = -0.027 \pm 0.005$ dex kpc $^{-1}$.

Table 5. Retrieved metallicity-gradient correlations.

Independent variable (x)	$\Delta\Gamma/\Delta x$ (θ_1)
$\log_{10}[N_{\text{HI}} (\text{cm}^{-2})]$	-0.016 ± 0.003
z_{abs}	0.07 ± 0.03
$\log_{10}[M_{\star} (M_{\odot})]$	-0.02 ± 0.01
$\text{SFR} (M_{\odot} \text{yr}^{-1})$	-0.003 ± 0.001
$\log_{10}[\text{sSFR} (\text{yr}^{-1})]$	0.002 ± 0.02

Having robustly identified the existence of an average metallicity gradient in absorption-selected galaxies with a grid-based and a solver-based model alike, we now consider whether $\langle \Gamma \rangle$ correlates with galaxy evolution parameters. In particular, we desire to see whether $\langle \Gamma \rangle$ is sensitive to the inclusion of sub-DLAs; whether it shows a redshift-evolution; and whether it correlates with galaxy evolution parameters such as M_{\star} or sSFR. Such correlations were found in luminosity-selected star-forming disc-galaxies at $z = 1$ (Stott et al. 2014). Since the scatter in the sample is larger than the individual measurement errors, we proceeded with the methodology developed, but replaced $\langle \Gamma \rangle$ by a linear function of the form $\langle \Gamma \rangle = \theta_1 x + \theta_2$ in Eq. (10). Here, θ represents the new parameters we seek to optimise, and x is the independent variable.

The resulting correlations are summarised in Table 5. We find a $\sim 5\sigma$ correlation with the H I column density, and a formal 3σ correlation with SFR. A correlation with H I column density may be related to the ionisation-corrections applied to the absorption metallicity, which itself correlates inversely with H I column density. Whether such ionisation corrections explain the observed correlation is beyond the scope of this paper.

If real, the correlation with SFR may suggest that absorption-selected galaxies have sSFRs which are driven by a different mechanism relative to luminosity-selected systems. Such systems show a correlation with sSFR, with slopes of 0.023 ± 0.004 , driven by a correlation with M_{\star} of the order -0.022 ± 0.009 (Stott et al. 2014). We note however, that with errors of 0.01 and 0.02 on the correlations with M_{\star} and sSFR, respectively, the data are consistent with the disc-galaxy correlations, but we lack the number statistics to test the Stott et al. (2014) result.

5. Conclusions

In this paper we spectroscopically confirm seven galaxies harbouring damped absorption systems at redshift $z < 1$. In addition, we detected a low-mass, star-bursting galaxy at low impact-parameter in the Q1209+107 quasar field. Further analysis suggests that this is an unlikely host. This has two implications. Firstly, the galaxy hosts for the two damped absorbers in Q1209+107 are still unidentified. Secondly, the proximity of the unlikely host to the quasar line of sight suggests that the low-redshift $z_{\text{abs}} = 0.3930$ absorber is hosted by a galaxy that belongs to a larger galaxy-group. We also report one non-detection in the Q1209+107 PA1 field and on a galaxy at the wrong redshift to be related to the absorbing system in the Q2353–0028 field. With a conservative estimate, our FORS2 campaign therefore had a success-rate of 70%. Combining spectroscopic data in emission with the known properties in absorption and deep multi-band photometry in the quasar fields, we conducted an extensive analysis to characterise the absorbing galaxies. In the following paragraphs we summarise the results.

Despite statistical differences, the observed distribution of impact parameters with HI column-density and with absorption metallicity can be extended from DLAs to sub-DLAs; from high ($z \sim 2-3$) redshifts to low ($z \sim 0.7$) redshifts; and to higher absorption metallicities. Our observations can be used to constrain the models further.

We find no solid evidence for the claim that sub-DLAs and DLAs arise in galaxies of different masses. We argue that the apparent correlation is driven by selection effects, including a dust-bias against massive metal-rich systems and the fact that projected cross-section of low-column-density sub-DLA gas is geometrically larger. This favours the detection of sub-DLAs in large galaxies.

We find a significant mean metallicity gradient of $\langle \Gamma \rangle = -0.022 \pm 0.001 \text{ dex kpc}^{-1}$ based on the absorber properties and known SED stellar masses. This value is consistent with literature values, but has a significantly reduced uncertainty achieved by avoiding the combination of different strong-line diagnostics in emission and by not directly combining metallicity measurements on local (absorption) and global (emission) spatial scales.

Correcting the absorption-metallicities for our mean metallicity-gradient and assuming a physically motivated truncation-radius of 12 kpc, absorption-selected galaxies fall on top of predicted MZ-relations. Applying these corrections significantly reduces the scatter around the relations, and suggests that global properties can indeed be predicted from local absorption measurements.

Based on the current sample, absorption-selected galaxies with stellar masses above $\log_{10}[M_{\star} (M_{\odot})] \sim 10$ show sub-main-sequence star formation. Whereas this has been interpreted as an effect of probing a particular evolutionary phase or as a transition from the nature of absorbing galaxies between high- and low redshifts, the fact that such a suppression is not seen at lower masses is indicative of a mass-dependence.

Acknowledgements. This work was supported by grant ID DFF-4090-00079. We would also like to extend our gratitude to Sandhya Rao and Lorrie Straka for sharing data; and to Jens-Kristian Krogager and Alireza Rahmati for sharing their model- and simulation predictions. This research made use of Astropy, a community-developed core Python package for Astronomy. In addition, it has made use of SDSS DR10. Funding for SDSS-III has been provided by the Alfred P. Sloan Foundation, the Participating Institutions, the National Science Foundation, and the US Department of Energy Office of Science. The SDSS-III web site is <http://www.sdss3.org/>. SDSS-III is managed by the Astrophysical Research Consortium for the Participating Institutions of the SDSS-III Collaboration including the University of Arizona, the Brazilian Participation Group, Brookhaven National Laboratory, Carnegie Mellon University, University of Florida, the French Participation Group, the German Participation Group, Harvard University, the Instituto de Astrofísica de Canarias, the Michigan State/Notre Dame/JINA Participation Group, Johns Hopkins University, Lawrence Berkeley National Laboratory, Max Planck Institute for Astrophysics, Max Planck Institute for Extraterrestrial Physics, New Mexico State University, New York University, Ohio State University, Pennsylvania State University, University of Portsmouth, Princeton University, the Spanish Participation Group, University of Tokyo, University of Utah, Vanderbilt University, University of Virginia, University of Washington, and Yale University.

References

Ahn, C. P., Alexandroff, R., Allende Prieto, C., et al. 2014, *ApJS*, 211, 17
 Appenzeller, I., Fricke, K., Furtig, W., et al. 1998, *The Messenger*, 94, 1
 Arnouts, S., Cristiani, S., Moscardini, L., et al. 1999, *MNRAS*, 310, 540
 Astropy Collaboration (Robitaille, T. P., et al.) 2013, *A&A*, 558, A33
 Augustin, R., Péroux, C., Møller, P., et al. 2018, *MNRAS*, 478, 3120
 Berg, T. A. M., Ellison, S. L., Prochaska, J. X., et al. 2017, *MNRAS*, 464, L56
 Berry, M., Somerville, R. S., Gawiser, E., et al. 2016, *MNRAS*, 458, 531
 Bertin, E., & Arnouts, S. 1996, *A&AS*, 117, 393

Boffin, H. M. J., Dumas, C., & Kaufer, A. 2015, *VLT-MAN-ESO-13100-1543*
 Boissé, P., Le Brun, V., Bergeron, J., & Deharveng, J.-M. 1998, *A&A*, 333, 841
 Bouché, N., Murphy, M. T., Kacprzak, G. G., et al. 2013, *Science*, 341, 50
 Bruzual, G., & Charlot, S. 2003, *MNRAS*, 344, 1000
 Calzetti, D. 1997, *AIPC Conf. Proc.*, 408, 403
 Calzetti, D., Armus, L., Bohlin, R. C., et al. 2000, *ApJ*, 533, 682
 Chabrier, G. 2003, *PASP*, 115, 763
 Chen, H.-W., & Lanzetta, K. M. 2003, *ApJ*, 597, 706
 Christensen, L., Wisotzki, L., Roth, M. M., et al. 2007, *A&A*, 468, 857
 Christensen, L., Møller, P., Fynbo, J. P. U., & Zafar, T. 2014, *MNRAS*, 445, 225 (C14)
 Crain, R. A., Theuns, T., Vecchia, C. D., et al. 2009, *MNRAS*, 399, 1773
 Cresci, G., Mannucci, F., Maiolino, R., et al. 2010, *Nature*, 467, 811
 Cristiani, S. 1987, *A&A*, 175, L1
 De Cia, A., Ledoux, C., Petitjean, P., & Savaglio, S. 2018, *A&A*, 611, A76
 Dekel, A., Sari, R., & Ceverino, D. 2009, *ApJ*, 703, 785
 de la Varga, A., Reimers, D., Tytler, D., Barlow, T., & Burles, S. 2000, *A&A*, 363, 69
 Dessauges-Zavadsky, M., Ellison, S. L., & Murphy, M. T. 2009, *MNRAS*, 396, 61
 Ellison, S. L. 2006, *MNRAS*, 368, 335
 Erb, D. K., Shapley, A. E., Pettini, M., et al. 2006, *ApJ*, 644, 813
 Fitzpatrick, E. L., & Massa, D. 2007, *ApJ*, 663, 320
 Freudling, W., Romaniello, M., Bramich, D. M., et al. 2013, *A&A*, 559, A96
 Fumagalli, M., O'Meara, J. M., Xavier Prochaska, J., Rafelski, M., & Kanekar, N. 2015, *MNRAS*, 446, 3178
 Fynbo, J. P. U., Møller, P., & Warren, S. J. 1999, *MNRAS*, 305, 849
 Fynbo, J. P. U., Prochaska, J. X., Sommer-Larsen, J., Dessauges-Zavadsky, M., & Møller, P. 2008, *ApJ*, 683, 321
 Fynbo, J. P. U., Laursen, P., Ledoux, C., et al. 2010, *MNRAS*, 408, 2128
 Fynbo, J. P. U., Ledoux, C., Noterdaeme, P., et al. 2011, *MNRAS*, 413, 2481
 Fynbo, J. P. U., Geier, S. J., Christensen, L., et al. 2013a, *MNRAS*, 436, 361
 Fynbo, J. P. U., Krogager, J.-K., Venemans, B., et al. 2013b, *ApJS*, 204, 14
 Fynbo, J. P. U., Krogager, J.-K., Heintz, K. E., et al. 2017, *A&A*, 606, A13
 Gallagher, J. S., Bushouse, H., & Hunter, D. A. 1989, *ApJ*, 97, 700
 Hanuschik, R. W. 2003, *A&A*, 407, 1157
 Hewett, P. C., & Wild, V. 2007, *MNRAS*, 379, 738
 Horne, K. 1986, *PASP*, 98, 609
 Ilbert, O., Arnouts, S., McCracken, H. J., et al. 2006, *A&A*, 457, 841
 Kacprzak, G. G., Murphy, M. T., & Churchill, C. W. 2010, *MNRAS*, 406, 445
 Kanekar, N., Prochaska, J. X., Christensen, L., et al. 2018, *ApJ*, 856, L23
 Karim, A., Schinnerer, E., Martínez-Sansigre, A., et al. 2011, *ApJ*, 730, 61
 Kennicutt, R. C. J. 1992, *ApJ*, 388, 310
 Kennicutt, R. C. 1998, *ARA&A*, 36, 189
 Kewley, L. J., & Dopita, M. A. 2002, *ApJS*, 142, 35
 Kewley, L. J., & Geller, M. J. 2004, *ApJ*, 127, 2002
 Kewley, L. J., & Ellison, S. L. 2008, *ApJ*, 681, 1183
 Komatsu, E., Smith, K. M., Dunkley, J., et al. 2011, *ApJS*, 192, 18
 Krogager, J.-K., Fynbo, J. P. U., Møller, P., et al. 2012, *MNRAS*, 424, 1 (K12)
 Krogager, J.-K., Fynbo, J. P. U., Ledoux, C., et al. 2013, *MNRAS*, 433, 3091
 Krogager, J.-K., Geier, S., Fynbo, J. P. U., et al. 2015, *ApJS*, 217, 5
 Krogager, J.-K., Fynbo, J. P. U., Heintz, K. E., et al. 2016, *ApJ*, 832, 21
 Krogager, J.-K., Møller, P., Fynbo, J. P. U., & Noterdaeme, P. 2017, *MNRAS*, 469, 2959
 Kulkarni, V. P., Khare, P., Péroux, C., et al. 2007, *ApJ*, 661, 88
 Kulkarni, V. P., Khare, P., Som, D., et al. 2010, *New Astron.*, 15, 735
 Le Brun, V., Bergeron, J., Boissé, P., & Deharveng, J. M. 1997, *A&A*, 321, 733
 Ledoux, C., Bergeron, J., & Petitjean, P. 2002, *A&A*, 385, 802
 Ledoux, C., Petitjean, P., Møller, P., Fynbo, J., & Srianand, R. 2005, *Proc. IAU*, 199, 433
 Ledoux, C., Petitjean, P., Fynbo, J. P. U., Møller, P., & Srianand, R. 2006, *A&A*, 457, 71
 Ma, J., Gonzalez, A. H., Spilker, J. S., et al. 2015, *ApJ*, 812, 88
 Maiolino, R., Nagao, T., Grazian, A., et al. 2008, *A&A*, 488, 463 (M08)
 Mannucci, F., Cresci, G., Maiolino, R., Marconi, A., & Gnerucci, A. 2010, *MNRAS*, 408, 2115
 Meiring, J. D., Kulkarni, V. P., Lauroesch, J. T., et al. 2008, *MNRAS*, 384, 1015
 Meiring, J. D., Lauroesch, J. T., Kulkarni, V. P., et al. 2009, *MNRAS*, 397, 2037
 Meiring, J. D., Lauroesch, J. T., Habertzell, L., et al. 2011, *MNRAS*, 410, 2516
 Møller, P. 2000, *The Messenger*, 99, 31
 Møller, P., & Warren, S. J. 1998, *MNRAS*, 299, 661
 Møller, P., Warren, S. J., Fall, S. M., Jakobsen, P., & Fynbo, J. U. 2000, *The Messenger*, 99, 33
 Møller, P., Warren, S. J., Fall, S. M., Fynbo, J. U., & Jakobsen, P. 2002, *ApJ*, 574, 51
 Møller, P., Fynbo, J. P. U., & Fall, S. M. 2004, *A&A*, 422, 33
 Møller, P., Fynbo, J. P. U., Ledoux, C., & Nilsson, K. K. 2013, *MNRAS*, 430, 2680 (M13)

- Møller, P., Christensen, L., Zwaan, M. A., et al. 2018, *MNRAS*, **474**, 4039
- Monier, E. M., Turnshek, D. A., & Rao, S. 2009, *MNRAS*, **397**, 943
- Neeleman, M., Wolfe, A. M., Prochaska, J. X., & Rafelski, M. 2013, *ApJ*, **769**, 54
- Neeleman, M., Prochaska, J. X., Ribaudo, J., et al. 2016a, *ApJ*, **818**, 113
- Neeleman, M., Prochaska, J. X., Zwaan, M. A., et al. 2016b, *ApJ*, **820**, L39
- Nestor, D. B., Pettini, M., Hewett, P. C., Rao, S., & Wild, V. 2008, *MNRAS*, **390**, 1670
- Noeske, K. G., Weiner, B. J., Faber, S. M., et al. 2007, *ApJ*, **660**, 43
- Noterdaeme, P., Petitjean, P., Ledoux, C., & Srianand, R. 2009, *A&A*, **505**, 1087
- Noterdaeme, P., Laursen, P., Petitjean, P., et al. 2012a, *A&A*, **540**, A63
- Noterdaeme, P., Petitjean, P., Carithers, W. C., et al. 2012b, *A&A*, **547**, L1
- Noterdaeme, P., Petitjean, P., & Srianand, R. 2015, *A&A*, **578**, L5
- Osterbrock, D. E., & Ferland, G. J. 2006, in *Astrophysics of gaseous nebulae and active galactic nuclei*, 2nd, eds. D. E. Osterbrock, & G. J. Ferland (Sausalito, CA: University Science Books)
- Pagel, B. E. J., Edmunds, M. G., Blackwell, D. E., Chun, M. S., & Smith, G. 1979, *MNRAS*, **189**, 95
- Péroux, C., Dessauges-Zavadsky, M., D'Odorico, S., Kim, T.-S., & McMahon, R. G. 2003, *MNRAS*, **345**, 480
- Péroux, C., Meiring, J. D., Kulkarni, V. P., et al. 2006, *MNRAS*, **372**, 369
- Péroux, C., Meiring, J. D., Kulkarni, V. P., et al. 2008, *MNRAS*, **386**, 2209
- Péroux, C., Bouché, N., Kulkarni, V. P., York, D. G., & Vladilo, G. 2011, *MNRAS*, **410**, 2237
- Péroux, C., Bouché, N., Kulkarni, V. P., York, D. G., & Vladilo, G. 2012, *MNRAS*, **419**, 3060
- Péroux, C., Quiret, S., Rahmani, H., et al. 2016, *MNRAS*, **457**, 903
- Péroux, C., Rahmani, H., Quiret, S., et al. 2017, *MNRAS*, **464**, 2053
- Pettini, M., Smith, L. J., Hunstead, R. W., & King, D. L. 1994, *ApJ*, **426**, 79
- Pontzen, A., Governato, F., Pettini, M., et al. 2008, *MNRAS*, **390**, 1349
- Prochaska, J. X., Gawiser, E., Wolfe, A. M., Castro, S., & Djorgovski, S. G. 2003, *ApJ*, **595**, 9
- Prochaska, J. X., Herbert-Fort, S., & Wolfe, A. M. 2005, *ApJ*, **635**, 123
- Queyrel, J., Contini, T., Kissler-Patig, M., et al. 2012, *A&A*, **539**, A93
- Rafelski, M., Wolfe, A. M., Prochaska, J. X., Neeleman, M., & Mendez, A. J. 2012, *ApJ*, **755**, 89
- Rafelski, M., Neeleman, M., Fumagalli, M., Wolfe, A. M., & Prochaska, J. X. 2014, *ApJ*, **782**, L29
- Rahmani, H., Péroux, C., Turnshek, D. A., et al. 2016, *MNRAS*, **463**, 980
- Rahmati, A., & Schaye, J. 2014, *MNRAS*, **438**, 529
- Rao, S. M., Turnshek, D. A., & Nestor, D. B. 2006, *ApJ*, **636**, 610
- Rao, S. M., Ele Belfort-Mihalyi, M., Turnshek, D. A., et al. 2011, *MNRAS*, **416**, 1215
- Rupke, D. S. N., Kewley, L. J., & Barnes, J. E. 2010, *ApJ*, **710**, L156
- Salpeter, E. E. 1955, *ApJ*, **121**, 161
- Sánchez, S. F., Rosales-Ortega, F. F., Iglesias-Páramo, J., et al. 2014, *A&A*, **563**, A49
- Sandin, C., Becker, T., Roth, M. M., et al. 2010, *A&A*, **515**, A35
- Savaglio, S., Glazebrook, K., Le Borgne, D., et al. 2005, *ApJ*, **635**, 260
- Schlafly, E. F., & Finkbeiner, D. P. 2011, *ApJ*, **737**, 103
- Schlegel, D. J., & Finkbeiner Davis, M. 1998, *ApJ*, **500**, 525
- Som, D., Kulkarni, V. P., Meiring, J., et al. 2013, *MNRAS*, **435**, 1469
- Som, D., Kulkarni, V. P., Meiring, J., et al. 2015, *ApJ*, **806**, 25
- Songaila, A., & Cowie, L. L. 2010, *ApJ*, **721**, 1448
- Stott, J. P., Sobral, D., Swinbank, A. M., et al. 2014, *MNRAS*, **443**, 2695
- Straka, L. A., Johnson, S., York, D. G., et al. 2016, *MNRAS*, **458**, 3760
- Swinbank, A. M., Sobral, D., Smail, I., et al. 2012, *MNRAS*, **426**, 935
- Tremonti, C. A., Heckman, T. M., Kauffmann, G., et al. 2004, *ApJ*, **613**, 898
- van Dokkum, P. G. 2001, *PASP*, **113**, 1420
- Whitaker, K. E., Franx, M., Leja, J., et al. 2014, *ApJ*, **795**, 104, (W14)
- Whitaker, K. E., Franx, M., Bezanson, R., et al. 2015, *ApJ*, **811**, L12
- Wolfe, A. M., Turnshek, D. A., Smith, H. E., & Cohen, R. D. 1986, *ApJS*, **61**, 249
- Zafar, T., & Møller, P. 2018, *MNRAS*, submitted
- Zafar, T., & Watson, D. 2013, *A&A*, **560**, A26
- Zafar, T., Møller, P., Ledoux, C., et al. 2011, *A&A*, **532**, A51
- Zafar, T., Péroux, C., Popping, A., et al. 2013a, *A&A*, **556**, A141
- Zafar, T., Popping, A., & Péroux, C. 2013b, *A&A*, **556**, A140
- Zafar, T., Møller, P., Watson, D., et al. 2015, *A&A*, **584**, A100
- Zafar, T., Møller, P., Péroux, C., et al. 2017, *MNRAS*, **465**, 1613

Appendix A: Group analysis in Q1436–0051

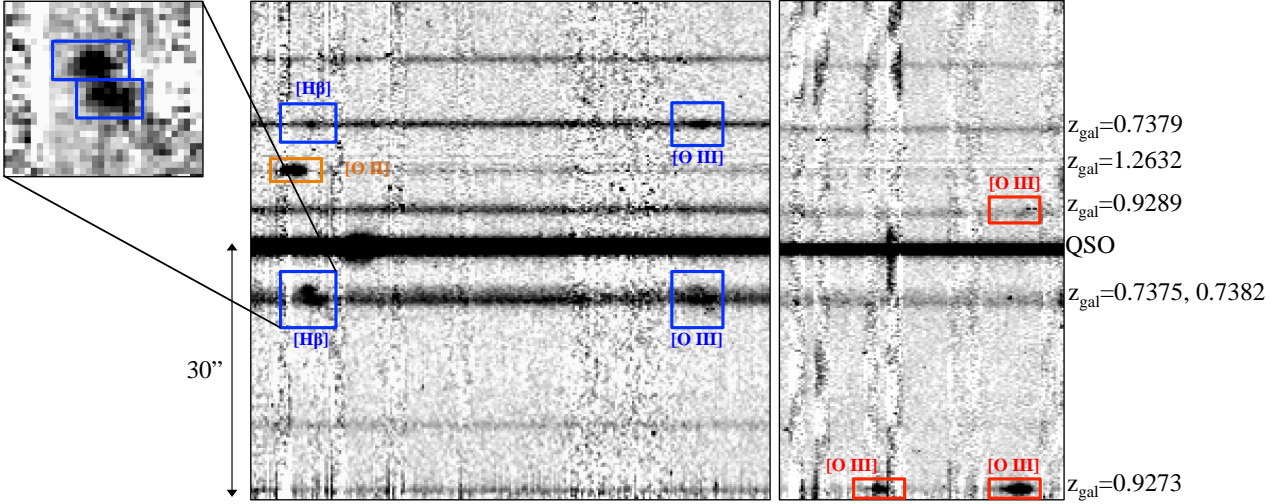


Fig. A.1. Negative colour-mapped FORS2 spectral segments of the Q1436–0051 field, observed during our campaign. Boxes highlight the identified emission lines, colour-coded to emphasize systems at similar redshifts.

Table A.1. Galaxies at relatively small projected distances from the quasar Q1436–0051.

Q1436–0051 Field Galaxy identifiers		
θ^a	b^b	$z_{\text{em}}^{\text{SPEC}}$
(–)5.0	36.7	0.7375
(–)7.5	46.3	0.7382
4.4	34.9	0.9289
9.1	77.0	1.2632
14.5	106.5	0.7379
29.0	230.1	0.9273

Notes. The identified emission lines (see Fig. A.1) suggests the presence of galaxy groups at the absorbing systems redshifts (see Sect. 3.3 for further discussion). ^(a) Un-binned angular distance relative to the quasar. ^(b) Projected distance in kpc relative to the quasar, measured at the spectroscopic redshifts.

Appendix B: Notes in individual abundance measurements

Here, we present the abundance measurements based on flux-ratios for individual objects. We evaluated the flux-ratios as the median-value with lower and upper uncertainties based on the 16th- and 84th percentile of the CDF. The CDF was generated from $1\text{E}6$ realisations of the flux-ratios assuming normal-distributed fluxes centred on the measurement, with a width characterised by the flux uncertainty. In order to differentiate between abundances measured with different diagnostics, we use the following notation: $[\text{O}/\text{H}]_{\text{diagnostic}}$ where the subscript refers to the diagnostic line-ratio as defined in Eq. (7) used. If the line-ratio is consistent with two abundances, we refer to these with “*l*” or “*u*” superscripts to denote the lower branch and upper branch value, respectively. When a comparison to the mass-metallicity relation is made, we refer to this value as $[\text{O}/\text{H}]_{\text{MZ,M08}}$. In this comparison, we do not consider internal scatter present in the M08 MZ-relation. *HE 1122–1649*. The O_2 line-ratio gives an oxygen abundance $[\text{O}/\text{H}]_{\text{O}_2} = 8.70^{+0.17}_{-0.20}$. This

is consistent with the value inferred from the mass-metallicity relation, $[\text{O}/\text{H}]_{\text{MZ,M08}} = 8.57$.

Q 0153+0009. The O_3 line-ratio gives a double-valued abundance, with a lower- and upper abundance branch value of $[\text{O}/\text{H}]_{\text{O}_3}^l = 7.02^{+0.03}_{-0.03}$ and $[\text{O}/\text{H}]_{\text{O}_3}^u = 8.75^{+0.03}_{-0.03}$, respectively. The upper-branch abundance is consistent with the value inferred from the mass-metallicity relation, $[\text{O}/\text{H}]_{\text{MZ,M08}} = 8.81$. We note that the reported uncertainties are underestimated. This is in part because we have not accounted for internal scatter in the M08 calibration, and in part because the abundance calibration is insensitive to variations in the flux-ratio around the measured value.

Q 1209+107 PA2. The R_{23} line-ratio, to within the 1σ uncertainty, does not constrain the abundance. Interpreting the large line-ratio as indicative of a unique abundance at the maximum line-ratio gives $[\text{O}/\text{H}]_{\text{R}_{23}} = 8.05$. The O_2 line-ratio gives a double-valued abundance, with a lower- and upper branch value of $[\text{O}/\text{H}]_{\text{O}_2}^l = 8.55^{+0.05}_{-0.04}$ and $[\text{O}/\text{H}]_{\text{O}_2}^u = 8.83^{+0.03}_{-0.04}$, respectively. Likewise, the O_3 line-ratio also gives a double-valued abundance, with a lower- and upper branch value of $[\text{O}/\text{H}]_{\text{O}_3}^l = 7.62^{+0.05}_{-0.04}$ and $[\text{O}/\text{H}]_{\text{O}_3}^u = 8.16^{+0.04}_{-0.05}$, respectively, and the O_{32} line-ratio gives an abundance $[\text{O}/\text{H}]_{\text{O}_{32}} = 8.35^{+0.02}_{-0.02}$. The inferred abundance from the mass-metallicity relation gives $[\text{O}/\text{H}]_{\text{MZ,M08}} = 8.02$. This is consistent with our interpretation of the R_{23} . We therefore report the R_{23} value.

Q 1436–0051. We infer $f_{[\text{O III}]4959}$ assuming the standard line-strength conversion $f_{[\text{O III}]4959} = 0.34 f_{[\text{O III}]45007}$. Combining our FORS2 measurements with our re-measured $f_{[\text{O II}]3727,3729}$ line-flux in the Magellan II spectrum (Straka et al. 2016, see Sect. 3.8), we find an R_{23} line-ratio consistent with a double-valued abundance. The lower- and upper branch values are $[\text{O}/\text{H}]_{\text{R}_{23}}^l = 7.93^{+0.12}_{-0.33}$ and $[\text{O}/\text{H}]_{\text{R}_{23}}^u = 8.16^{+0.35}_{-0.11}$, respectively. The O_2 line-ratio is outside the range to constrain the abundance. The O_3 line-ratio gives an upper branch abundance $[\text{O}/\text{H}]_{\text{O}_3}^u = 8.82^{+0.08}_{-0.08}$, but we note that the flux-ratio is marginally consistent with a lower-branch abundance $[\text{O}/\text{H}]_{\text{O}_3}^l \sim 7.02$. The O_{32} line-ratio gives an abundance $[\text{O}/\text{H}]_{\text{O}_{32}} = 9.11^{+0.07}_{-0.06}$. We believe that the large scatter in abundances as determined with the different diagnostics

is driven by the combination of spectroscopic data from different telescopes, at different slit-placements, and taken in different conditions. To avoid introducing such systematic differences in the abundance measurements, and noting the consistency with the value inferred from the mass-metallicity relation $[\text{O}/\text{H}]_{\text{MZ,M08}} = 8.92$, we assumed the $[\text{O}/\text{H}]_{\text{O}_3}$ upper branch abundance.

Q 2335+1501. The O_2 line-ratio gives a double-valued abundance, with a lower- and upper branch value of $[\text{O}/\text{H}]_{\text{O}_2}^l = 8.34_{-0.19}^{+0.36}$ and $[\text{O}/\text{H}]_{\text{O}_2}^u = 8.96_{-0.26}^{+0.09}$, respectively. We note that the upper branch abundance is consistent with the value inferred from the mass-metallicity relation, $[\text{O}/\text{H}]_{\text{MZ,M08}} = 8.82$.

Paper II

The nature of strong HI absorbers probed by cosmological simulations: satellite accretion and outflows

N. H. P. Rhodin,^{1*} O. Agertz,² L. Christensen,¹ F. Renaud,² and J. P. U. Fynbo,^{3,4}

¹*DARK, Niels Bohr Institute, University of Copenhagen, Lyngbyvej 2, DK-2100 Copenhagen Ø, Denmark*

²*Lund Observatory, Department of Astronomy and Theoretical Physics, Box 43, SE-221 00 Lund, Sweden*

³*Cosmic DAWN Center NBI/DTU-Space*

⁴*Niels Bohr Institute, University of Copenhagen, Lyngbyvej 2, DK-2100, Copenhagen Ø, Denmark*

Accepted 2019 May 24. Received 2019 January 30

ABSTRACT

We use cosmological hydrodynamic zoom simulations to study the neutral gas distribution in and around galaxies that gives rise to high column density HI Ly- α absorption (damped Ly- α systems (DLAs) and sub-DLAs) in background quasar spectra. Such simulations often sacrifice numerical resolution for volume which affects the lower-density galaxy halo gas, and simulations have difficulties reproducing the span of projected separations (b) between absorbing clouds and their hosts. Our simulations produce (sub-)DLAs over the entire probed parameter space ($b \lesssim 50$ kpc and metallicity $-4 \lesssim [M/H] \lesssim 0.5$) at all redshifts ($z \sim 0.4 - 3.0$), enclosing spectroscopically confirmed absorber-galaxy pairs. Recovering (sub-)DLAs at $b \gtrsim 20 - 30$ kpc from a massive host galaxy requires high numerical resolution and efficient feedback, and we show that these lines-of-sight are associated with dwarf satellites in the main halo, stripped metal-rich gas and outflows. HI disc- and halo gas significantly contributes to (sub-)DLAs around galaxies. At large redshifts the halo plays an increasingly important role, while at $0.4 < z < 1$ the disc and halo contribute with $\sim 60(80)$ and $\sim 40(20)$ per cent to column densities above the sub-DLA (DLA) lower limits. The distribution of b for sub-DLAs and DLAs overlap at $z \sim 2 - 3$, but evolves so that sub-DLAs on average are located at twice larger b by $z \sim 0.5$. A weak correlation suggests that sub-DLA covering fractions increase with stellar mass more rapidly than those of DLA. This can explain why sub-DLAs are preferentially selected in more massive galaxies in the low- z Universe.

Key words: galaxies: formation – galaxies: evolution – galaxies: haloes – galaxies: intergalactic medium – quasars: absorption lines

1 INTRODUCTION

The chance alignment of neutral gas clouds intervening the line of sight (LOS) towards background quasi-stellar objects (quasars) imprints characteristic absorption features in the quasar power-law continua. In neutral hydrogen (HI), the most HI-rich absorbers are the Damped Lyman- α Absorbers (DLAs; $\log_{10}[N_{\text{HI}} (\text{cm}^{-2})] \geq 20.3$, Wolfe et al. (1986)) and the sub-DLAs ($19.0 \leq \log_{10}[N_{\text{HI}} (\text{cm}^{-2})] < 20.3$, e.g., Péroux et al. (2003); Zafar et al. (2013)). Unless otherwise specified, we refer to sub-DLAs and DLAs uniformly as strong HI absorbers. Both classes of absorbers are always accompanied by low-ionization metal line complexes (Prochaska et al. 2003; Noterdaeme et al. 2012; Rafelski et al. 2014) which suggests an association with a gaseous medium af-

fectured by chemical enrichment. Yet, the origin and nature of strong HI absorbers and their relation to galactic environments remains highly debated.

Absorption velocities and asymmetric line-profiles with leading edges (Prochaska & Wolfe 1997), as well as models of disc formation (Mo et al. 1998), support the idea that DLAs preferentially probe rapidly rotating galaxy discs (Wolfe et al. 1986). However, using cosmological hydrodynamic simulations, Haehnelt et al. (1998) demonstrated that the absorption kinematics could equally well be explained by irregular proto-galactic clumps in dark matter halos subject to a combination of rotation, random motions, gas flows, and mergers. A picture is emerging in which strong HI absorbers trace neutral gas on scales of tens of kpc in galaxies (Møller & Warren 1998; Christensen et al. 2007; Pontzen et al. 2008; Monier et al. 2009; Fynbo et al. 2010, 2011; Meiring et al. 2011; Rao et al. 2011; Krogager et al. 2012; Péroux et al.

* E-mail: henrikrhodin@dark-cosmology.dk

2012; Fynbo et al. 2013b; Krogager et al. 2013; Rahmati & Schaye 2014; Rahmani et al. 2016; Rhodin et al. 2018).

A number of analytical models have been successful in reproducing observed bulk properties of DLAs (Fynbo et al. 2008; Krogager et al. 2017, from hereon the “F08+K17 model”) (also Freudling et al. 2019, in prep.). By construction, these models depend on mean scaling relations of galaxies, and cannot capture processes related to galactic sub-structure or gas structures in the intergalactic medium (IGM). Large-scale cosmological hydrodynamic simulations have the potential to mitigate these shortcomings, and have been employed for over a decade (e.g. Nagamine et al. 2007; Pontzen et al. 2008; Fumagalli et al. 2011; Cen 2012; Rahmati et al. 2013; Faucher-Giguère et al. 2015; Liang et al. 2016). Such simulations have been successful in reproducing a broad range of observables, including the H I column density distribution function and the distribution of DLA metallicities. However, such simulations struggle with reproducing the observed absorption kinematics (Pontzen et al. 2008; Bird et al. 2014, 2015); lack resolution to capture small scale features of cold gas in halos (McCourt et al. 2018; Hummels et al. 2018); and require very strong stellar feedback in order to produce cold gas at large impact parameters, destroying the star forming gas discs in the process (Liang et al. 2016, 2018).

Formal numerical convergence on the spatial scales advocated by McCourt et al. (2018) to resolve fragmented, cold gas clouds in the CGM ($\sim 0.003 - 0.1$ pc) is far beyond the current limits of cosmological simulations. However, recent work is capable of marginally resolving the the total path length of cold gas along the LOS, estimated to span a range of $0.1 - 100$ pc (McCourt et al. 2018). Such simulations are the so called ‘zoom-in simulations’ which focus on the assembly of individual galaxies, and they provide a viable pathway towards understanding the distribution of strong H I absorbers, their significance as reservoirs of neutral gas, and their role in the cosmic baryon cycle. In particular, van de Voort et al. (2019) showed that already a uniform 1 kpc resolution to the virial radius significantly altered radial profiles of H I column densities, and lead to enhanced covering fractions of Lyman-Limit Systems (LLS; $\log_{10}[\text{N}_{\text{HI}} (\text{cm}^{-2})] \geq 17.2$, Tytler (1982)) within 150 kpc by a factor of two. Echoing the results of Hummels et al. (2018), Peeples et al. (2019) showed that whilst numerical resolution has a large impact on the physical state of the cold CGM gas and on its underlying kinematic structure, integrated quantities changed at $\lesssim 30\%$ level as the resolution was varied. These results suggest that resolving the CGM is crucial to our understanding of strong H I absorbers around galaxies.

The detection of strong H I absorbers at high impact parameters (b [kpc]) from their tentative host galaxies (see e.g. Møller & Christensen 2019; Christensen et al. 2019) provide clues to their nature and clustering. Fumagalli et al. (2011) suggest that cold streams accreting smoothly onto massive ($M_{\text{vir}} = 10^{10} - 10^{12} M_{\odot}$) galaxies contribute $>50\%$ of the covering factor in strong H I absorption above $z = 4$; but that such stream’s significance is replaced by contributions from galaxies, which dominate the cross-section below $z \sim 2$. Whereas cold stream accretion undeniably plays a vital role, Fumagalli et al. (2011)’s simulations severely under-predicted the equivalent widths of metal absorption lines, and their limited outflow- and feedback implemen-

tations renders conclusions biased to smooth, metal-poor, cold accretion. In addition, work using large scale cosmological simulations have called into question the detection of these high- b absorbers, suggesting instead that observations suffer from a selection bias towards the most luminous (but unrelated) galaxy in the projected sky vicinity (Rahmati & Schaye 2014). Finally, we note that comparing impact parameters from simulations to those associated with confirmed galaxy counterparts of strong H I absorbers are difficult, as observational campaigns often pre-select on absorption-metallicity to ensure high detection rates. Given the uncertain numerical resolution requirements for capturing neutral gas in halos, these issues warrants a revisit using higher resolution models with realistic feedback implementations.

In this work, we employ high resolution cosmological zoom simulations to build probability-functions of the distribution of strong H I absorption in and around galaxies. These probability-functions are matched to the most recent compilation of such spectroscopically confirmed absorber-galaxy pairs (Møller & Christensen 2019; Christensen et al. 2019, from hereon, the “MC19” compilation) and the analytical F08+K17 model, and are used to explore the physical origin of strong H I absorption. Throughout the analysis, we confine the comparison to a circular beam of 50 kpc radius, centred on the galaxy. This value is observationally motivated, and selected to enclose the current compilation of detections. The paper is organised as follows: Section 2 describes our simulations, with particular emphasis given to the feedback recipes and resolution, Section 3 presents our results, and Section 4 summarises our conclusions.

2 SIMULATIONS

2.1 Simulation setup

We carry out a cosmological hydrodynamic+ N -body zoom-in simulation of a Milky Way mass galaxy using the adaptive mesh refinement (AMR) code RAMSES (Teyssier 2002), assuming a flat Λ -cold dark matter cosmology with $H_0 = 70.2 \text{ km s}^{-1} \text{ Mpc}^{-1}$, $\Omega_m = 0.272$, $\Omega_{\Lambda} = 0.728$, and $\Omega_b = 0.045$. From a dark matter only simulation, with a simulation cube of size $L_{\text{box}} = 85 \text{ Mpc}$ at $z = 0$, a halo of $R_{200,m} = 334 \text{ kpc}$ (radius within which the mass density is 200 times the mean matter density) and $M_{200,m} = 1.3 \times 10^{12} M_{\odot}$ was selected for re-simulation at high resolution. Particles within $3R_{200,m}$ at $z = 0$ were traced back to $z = 100$, and the Lagrangian region they defined was regenerated at high resolution, still embedded within the full lower-resolution volume, using the MUSIC code (Hahn & Abel 2011). The simulation was then run to $z = 0$, with outputs every $\Delta a = 0.01$. These are the same initial conditions as the “m12i” halo from Hopkins et al. (2014) and Wetzel et al. (2016), drawn from the volume used in the AGORA galaxy formation comparison project (Kim et al. 2014, 2016).

The dark matter particle mass in the high resolution region is $m_{\text{dm}} = 3.5 \times 10^4 M_{\odot}$, with a gas mass resolution of $7070 M_{\odot}$. Star formation is sampled using $10^4 M_{\odot}$ particles, with stellar evolution reducing this by up to 50%, see below. The adaptive mesh is allowed to refine if a cell contains more than eight dark matter particles. This allows the local force

softening to closely match the local mean inter-particle separation, which suppresses discreteness effects (e.g., [Romeo et al. 2008](#)). A similar criterion is employed for the baryonic component, where the maximum refinement level is set to allow for a mean constant physical resolution of ~ 20 pc in the dense interstellar medium. As such, this simulation is a significant improvement over previous cosmological zoom simulation used to study cold gas in and around galaxies (e.g. [Liang et al. 2016](#)).

The adopted star formation and feedback physics is presented in [Agertz et al. \(2013\)](#) and [Agertz & Kravtsov \(2015, 2016\)](#). Briefly, star formation is treated as a Poisson process occurring on a cell-by-cell basis according to the star formation law,

$$\dot{\rho}_\star = \epsilon_{\text{ff}} \frac{\rho_g}{t_{\text{ff}}}, \quad (1)$$

where $\dot{\rho}_\star$ is the star formation rate density, ρ_g the gas density, $t_{\text{ff}} = \sqrt{3\pi/32G\rho_g}$ is the local free-fall time and ϵ_{ff} is the local star formation efficiency per free-fall time of gas in the cell. The efficiency is computed following the relation from [Padoan et al. \(2012\)](#), derived from simulations of star formation in magnetised supersonic turbulence¹.

Each formed star particle is treated as a single-age stellar population with a [Chabrier \(2003\)](#) initial mass function. We account for injection of energy, momentum, mass and heavy elements over time from Type II and Type Ia supernovae (SNe), stellar winds and radiation pressure (allowing for both single scattering and multiple scattering events on dust) on the surrounding gas. Each mechanism depends on the stellar age, mass and gas/stellar metallicity (through the metallicity dependent age-mass relation of [Raiteri et al. 1996](#)), calibrated on the stellar evolution code STARBURST99 ([Leitherer et al. 1999](#)).

Furthermore, to accurately account for SN feedback we adopt the SN momentum injection model recently suggested by [Kim & Ostriker \(2015\)](#), see also [Martizzi et al. 2015](#). A SN explosion is considered resolved when its cooling radius² is captured by at least 6 grid cells. In this case the explosion is initialised in the energy conserving phase by injecting the relevant energy (10^{51} erg per SN) into the nearest grid cell. If this criterion is not fulfilled, the SN is initialised in its momentum conserving phase, i.e. the total momentum generated during the energy conserving Sedov-Taylor phase is injected into the cells surrounding a star particle. It can be shown (e.g. [Blondin et al. 1998](#); [Kim & Ostriker 2015](#)) that at this time, the momentum of the expanding shell is approximately $4 \times 10^5 (E_{\text{SN}}/10^{51} \text{ erg})^{16/17} (n/1 \text{ cm}^{-3})^{-2/17} M_\odot \text{ km s}^{-1}$.

We track iron (Fe) and oxygen (O) abundances separately, and advect them as passive scalars. When computing the gas cooling rate, which is a function of total metallicity, we construct a total metal mass as

$$M_Z = 2.09M_{\text{O}} + 1.06M_{\text{Fe}} \quad (2)$$

¹ $\epsilon_{\text{ff}} = 0.5 \exp(-1.6t_{\text{ff}}/t_{\text{dyn}})$, where the dynamical time is $t_{\text{dyn}} = L/2\sigma$, and σ is the local velocity dispersion compute using neighbouring gas cells over a region of size $L = 3$ grid cells per spatial dimension.

² The cooling radius in gas of density n and metallicity Z scales as $r \approx 30(n/1 \text{ cm}^{-3})^{-0.43} (Z/Z_\odot + 0.01)^{-0.18}$ pc for a supernova explosion with energy $E_{\text{SN}} = 10^{51}$ erg (e.g. [Cioffi et al. 1988](#); [Thornton et al. 1998](#)).

according to the mixture of alpha (C, N, O, Ne, Mg, Si, S) and iron (Fe, Ni) group elements relevant for the sun ([Asplund et al. 2009](#)). The code accounts for metallicity dependent cooling by using tabulated cooling functions of [Sutherland & Dopita \(1993\)](#) for gas temperatures of $10^{4-8.5}$ K, and rates from [Rosen & Bregman \(1995\)](#) for cooling down to lower temperatures. Heating from the ultraviolet background radiation is accounted for by using the model of [Haardt & Madau \(1996\)](#), assuming a reionization redshift of $z = 8.5$. Self-shielding is modelled following the model of [Aubert & Teyssier \(2010\)](#). Finally, we follow [Agertz et al. \(2009\)](#) and adopt an initial metallicity of $Z = 10^{-3} Z_\odot$ in the high-resolution zoom-in region in order to account for enrichment from unresolved population III star formation (e.g. [Wise et al. 2012](#)).

2.2 Model verification and analysis

By accounting for the above stellar feedback budget, [Agertz & Kravtsov \(2015, 2016\)](#) simulated the cosmological assembly of Milky Way-mass galaxies, demonstrating that it led to a realistic late-type galaxy matching observed properties such as disc size, the presence of a thin and thick stellar disc, stellar and gas surface density profiles, the Kennicutt-Schmidt relation, the stellar mass-gas metallicity relation (and its evolution), and a specific angular momentum typical of spiral galaxies of the Milky Way mass (stellar mass of $\approx 5 \times 10^{10} M_\odot$).

The simulation considered in this work reaches a significantly higher mass and spatial resolution, and matches the above mentioned observational relations (to be presented in [Agertz et al. in prep.](#)). Furthermore, we find that HI column density distributions, $f(N_{\text{HI}})$, at all redshifts feature a turnover at column densities $N_{\text{HI}} \sim 10^{21} \text{ cm}^{-2}$, as observed both at high and low redshifts ([Zwaan et al. 2005](#); [Noterdaeme et al. 2009](#)), and in the ISM of individual local galaxies (see analysis by [Erkal et al. 2012](#)). Our simulation does therefore not suffer from an excess of high column density HI ($N_{\text{HI}} \gg 10^{21} \text{ cm}^{-2}$) in the inner few kpc of galaxies, as found by [Erkal et al. \(2012\)](#) in their high resolution simulations with inefficient stellar feedback³. As such, our zoom simulation is a relevant platform for studying the nature of DLA and sub-DLA LOS in and around massive disc galaxies.

Using the dark matter halo finder HOP ([Eisenstein & Hut 1998](#)), we identify all dark matter halos⁴ within the simulated high resolution volume, in all simulation snapshots (see Section 2.1). For each halo, we generate two-dimensional maps of N_{HI} and metallicity ($[M/H]$). We obtain HI from the neutral gas density in each cell by correcting for its molecular hydrogen content using the model by [Krumholz et al. \(2008, 2009\)](#), as implemented in [Agertz & Kravtsov \(2015\)](#).

All maps cover an area of $200 \times 200 \text{ kpc}^2$, and are centered on the dark matter and stars using a shrinking sphere

³ Using simulations at lower numerical resolution, [Altay et al. \(2011\)](#) found that the HI–H₂ transition was sufficient to explain the observed turnover, in contrast to [Erkal et al. \(2012\)](#) (see also [Altay et al. 2013](#)) who argued that establishing a realistic star formation-feedback cycle is crucial for explaining the column density distribution of DLAs.

⁴ Substructures are not robustly identified using HOP, but as we are mainly interested in *central* galaxies, this is no issue.

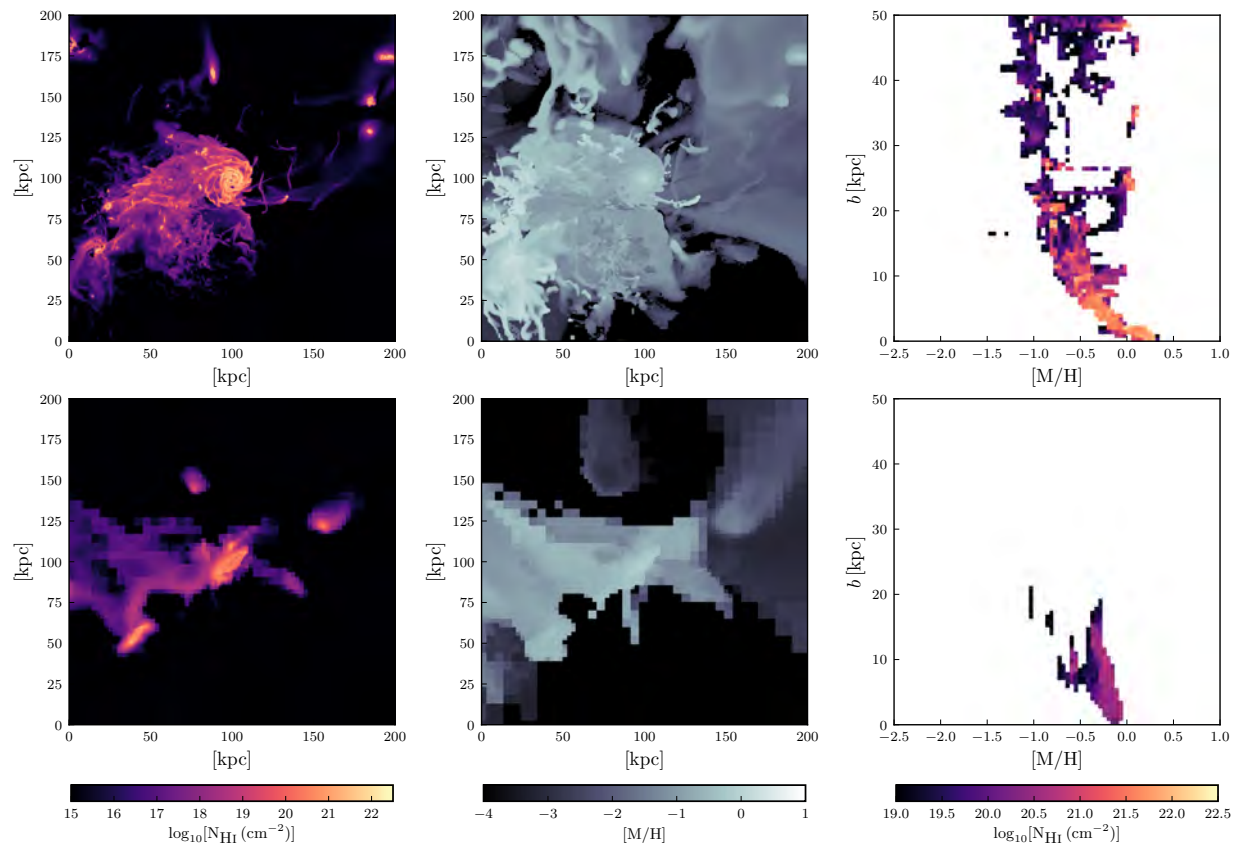


Figure 1. H I column density projection (*left*), neutral gas metallicity (*center*), and projected separation as a function of metallicity for gas above the lower sub-DLA column density limit (*right*). The top row features the simulated central galaxy at fiducial resolution (see Section 2.1), with the bottom row presenting a low resolution version, comparable to the typical numerical resolution achieved in large volume cosmological simulations discussed in Section 2.2. The enhanced resolution increases the strong H I ($\log_{10}[\text{N}_{\text{HI}} (\text{cm}^{-2})] > 19$) covering fractions at large projected radii, and reveals a complex, turbulent disc-halo interface with small-scale H I-structures.

algorithm (Power et al. 2003). The pixels have the same sizes as the finest cell sizes available in the simulation at the given snapshot, typically $\Delta x \sim 20$ pc. In each pixel, the quantities have been computed as

$$N_{\text{HI}} = \sum_i n_{\text{HI},i} \Delta x_i \quad (3)$$

and

$$[\text{M}/\text{H}] = \frac{\sum_i n_{\text{HI},i} [\text{M}/\text{H}]_i}{\sum_i n_{\text{HI},i}}, \quad (4)$$

where the sum runs over all cells along a given pixel LOS along the simulation volume (with a 200 kpc depth), $n_{\text{HI},i}$ is the local cell density of neutral hydrogen, $[\text{M}/\text{H}]_i$ the local cell gas metallicity, and Δx_i the size of a cell. For each snapshot we compute maps from the three Cartesian directions. In subsequent sections we will present results both for single snapshots and directions to illustrate our findings, as well as results averaged over all analysed directions and different redshift ranges. Finally, quoted impact parameters b are defined as the projected distance from the center of the main galaxy to a point of interest.

Numerical studies of DLAs have generally focused on

large simulation volumes in order to capture a statistical sample of galaxies, at the sacrifice of numerical resolution (see Section 1). Indeed, modern cosmological simulations of galaxy formation in domains with sizes of over tens of Mpc, aimed at reproducing the stellar luminosity function, e.g. EAGLE (Schaye et al. 2015) and Illustris (Vogelsberger et al. 2014), have been restricted to spatial resolutions of $\sim 0.5 - 1$ kpc. In contrast, we are here interested in a specific set of observations relating DLAs and sub-DLAs, at impact parameters up to $b \sim 50$ kpc, to confirmed host galaxies, here predominantly massive and star forming (see Section 3.1), making a comparison to high resolution zoom simulations more appropriate.

The importance of high numerical resolution is illustrated in Figure 1. The top row shows N_{HI} and $[\text{M}/\text{H}]$ maps, as well as b vs. $[\text{M}/\text{H}]$, at $z = 1$ for the most massive galaxy in our zoom region ($M_{\star} \sim 5 \times 10^{10} M_{\odot}$). The bottom row shows the same quantities, but for the simulation run at 32 times lower spatial resolution ($\Delta x \sim 640$ pc), and dark matter particle masses of $1.4 \times 10^6 M_{\odot}$, compatible with the aforementioned large volume simulations. While the low resolution simulation also leads to an extended disc, with a

similar stellar mass at $z = 0$ (made possible by the stellar feedback driven galactic outflows), the lack of detail in the circum-galactic medium (CGM) compared to the fiducial high resolution model is striking. In this work, we have not performed convergence tests. However, the cold, dense gas is not artificial, but an emergent feature at the fiducial resolution of our simulations. This gas will not disappear by further enhancing resolution. On the contrary, it will reveal more cold gas at large galactocentric distances until formal convergence is reached (McCourt et al. 2018; Hummels et al. 2018), and our qualitative results on the cold gas contents can therefore conservatively be treated as lower limits.

The fiducial model resolves a greater number of low mass satellites, all found to contribute to DLA and sub-DLA detections (see also Section 3.2). In addition, galaxy interactions, inflows and feedback driven outflows create complex gas structures with large covering fractions (see Sections 3.2 and 3.4). A significant fraction of these gas structures show high levels of metal-enrichment for which feedback and satellite accretion is key; most prominently observed as potential strong HI detections at $b > 20$ kpc in the b -[M/H] plane (Section 3.1). All of the above are crucial in order to interpret the observations presented in the next following analysis.

3 RESULTS

3.1 Comparing simulations to analytical models

The simple analytical F08+K17 model was built to capture very basic statistical properties of DLAs and their galaxy counterparts such as relations between impact parameter, metallicity and luminosity. The model does not include physical properties such as the role of environment, inflows and outflows, and does not account for radiative transfer effects and density gradients. Despite its simplicity, it is able to reconcile the metallicity distributions of Gamma Ray Bursts (GRBs), quasar DLAs and Lyman-break galaxies (LBGs) - suggesting that these objects are selections of the same underlying galaxy population (Fynbo et al. 2008). When combined with the Krogager et al. (2017) recipe for UV-luminosity and expected SFR, the model accurately predicts the fraction of identified counterparts in surveys of absorption selected galaxies that utilise different observing strategies.

The model describes DLAs as resulting from random LOS through infinitely thin, inclined slabs of "DLA-gas" smeared across a disc-like geometry, calibrated to ensure the cross-section matches the observed line density of DLAs at $z = 3$ (Prochaska et al. 2005). It combines a $z \sim 3$ UV luminosity function (Reddy et al. 2008); a $z \sim 3$ metallicity-luminosity relation (Pettini et al. 2001); a $z \sim 0$ local Holmberg relation to describe the size of the HI-disc as a function of the galaxy luminosity (following Wolfe et al. 1986, and originally derived from local discs in the Virgo- and Hercules clusters (Holmberg, E. et al. 1975; Peterson et al. 1979)); and a prescription for the metallicity gradient following Boissier & Prantzos (2001). In light of its success, with our simulations we now ask if the assumed scaling relations are reproduced in the simulations and if so at which redshifts.

To answer this, we use HOP to identify the most massive dark matter halo, and follow its evolution in redshift from $z = 3$ to $z = 0.4$. This halo grows in stellar mass from $9.6 \leq \log_{10}[M_{\star} (M_{\odot})] \leq 10.8$, which matches the LBG population stellar mass distribution $\log_{10}[M_{\star} (M_{\odot})] = 9.87 \pm 0.53$ (Reddy & Steidel 2009) from whose luminosity function the F08+K17 model was constructed. We compute b (kpc), [M/H], and $\log_{10}[N_{\text{HI}} (\text{cm}^{-2})]$ at each redshift and along each side of the simulation-box using the method described in Section 2.2. Binning in redshift intervals, we calculate the angle-averaged detection-fractions ($f_{\text{detections}}$) at each locus. The results are presented in Fig 2 and consists of probability-functions in the b (kpc) - [M/H] -and the b (kpc) - $\log_{10}[N_{\text{HI}} (\text{cm}^{-2})]$ parameter space, with $f_{\text{detections}}$ normalised for each panel. We show these results together with predictions from the F08+K17 model (with the mean relation (black solid), the 1σ -, 2σ - and 3σ intrinsic dispersions (grey solid) contours and model envelope (grey dashed)), and the MC19 compilation for a sequence of redshifts (columns). It is worth noting that galaxies above $b \gtrsim 30$ kpc from quasar LOSs have historically been considered unlikely counterparts to strong HI absorbers. Therefore, the accumulated observational data may by selection only probe the lower range of possible impact parameters. Row one shows a simulation snapshot centred on the galaxy; rows two- and three show the space spanned by b (kpc) - [M/H] with a cut on the column-density at the sub-DLA and at the DLA lower limits, respectively; and row four spans the b (kpc) - $\log_{10}[N_{\text{HI}} (\text{cm}^{-2})]$ parameter space.

Figure 2 reveals significant detection probabilities of LOS above the DLA column density threshold extending to impact parameters of 50 kpc from the host center, across all redshifts. It can also be seen that the distribution clearly changes with redshift. Qualitatively, this can be understood as follows; at higher redshifts the higher density of galaxies inherent to hierarchical structure formation give rise to higher merger frequencies, and more tidal interactions and turbulent disturbances. At $z > 2$, this inhibits gas from settling into coherent and long-lived structures such as extended HI discs. We therefore see $f_{\text{detections}}$ across a broad range of grid-points in the b (kpc) - [M/H] -and the b (kpc) - $\log_{10}[N_{\text{HI}} (\text{cm}^{-2})]$ parameter spaces alike. This is particularly clear in the highest redshift panel ($z = 2 - 3$, Fig 2 *bottom left*), for which our simulations generate detections across the whole parameter-space.

Towards progressively lower redshift, merger-rates and densities drop, and the HI gas is allowed to settle. This includes the formation of an HI disc which encodes information on a metallicity-gradient, most prominently observed as the diagonal stripe of high detection-probability (Fig. 2 *third row, rightmost panel*, but see also Section 3.2 for a direct observation of the disc in this parameter-space). In the same row, we also find a region of diffuse (lower detection probability per unit grid-point) $f_{\text{detections}}$ but extending to large impact parameters. This is indicative of a significant contribution from the circum-galactic medium and the extended halo to the DLA cross-section (see Sections 3.2 and 3.3).

In Table 1 we quantify the agreement between the F08+K17 model and our simulation by calculating the summed detection-fraction enclosed within the 1σ - 2σ - and 3σ limits. The DLA LOS detection fractions in simulations

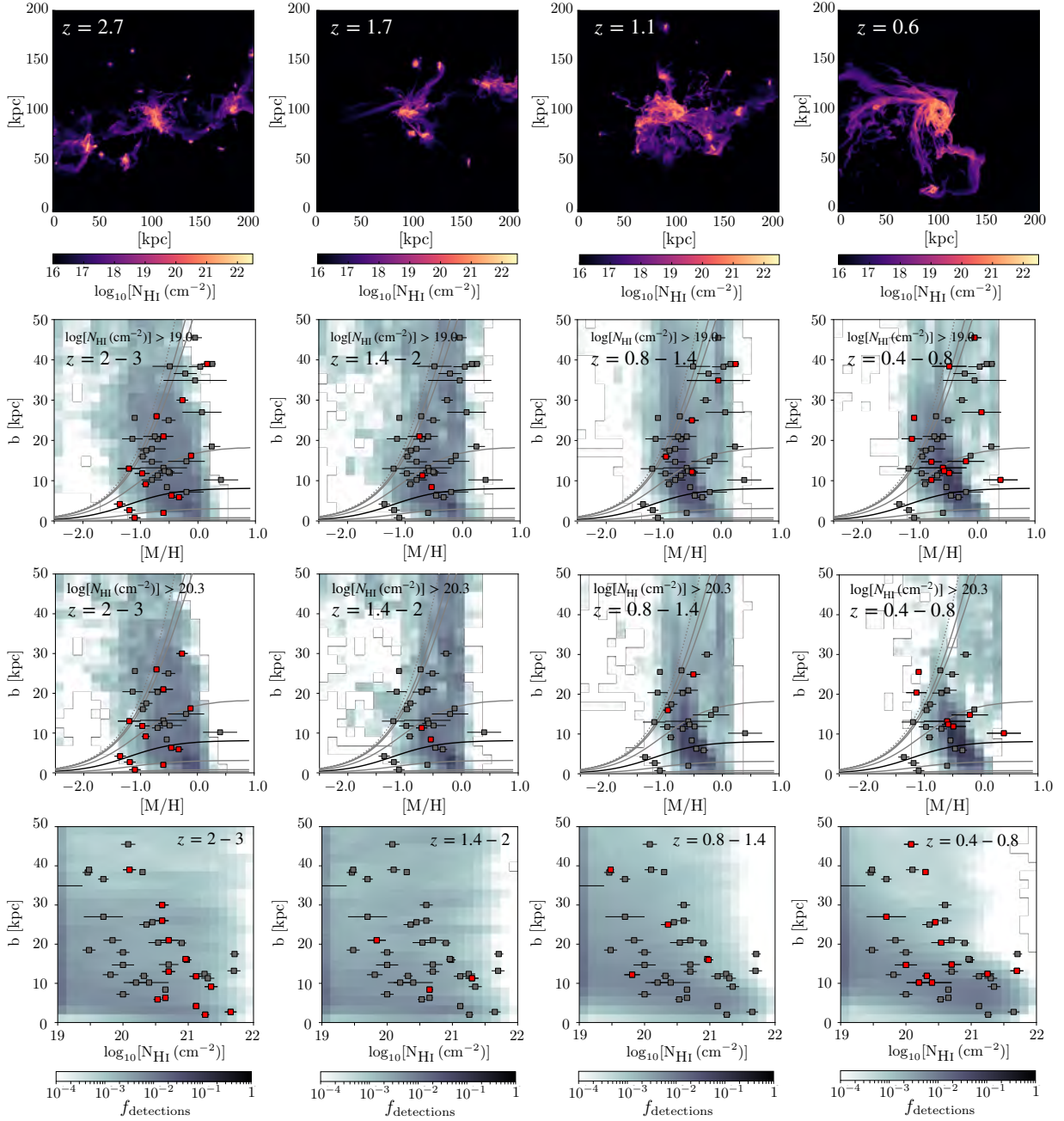


Figure 2. *First row:* H I column-density projections of the simulated central galaxy. *Second row:* Angle-averaged detection-fractions of sight-lines above the sub-DLA column-density limit ($\log_{10}[N_{\text{HI}} (\text{cm}^{-2})] = 19$) within an observationally motivated beam of 50 kpc radius (in projected separation). *Third row:* Same as second row, cut at the DLA column-density limit ($\log_{10}[N_{\text{HI}} (\text{cm}^{-2})] = 20.3$). *Fourth row:* Angle-averaged detection-fractions in the space spanned by projected distance and H I column-density. Image columns depict the redshift-evolution in the relations, moving from high (*left column*) to progressively lower redshifts. The MC19 compilation of observations has been overplotted as individual data-points. The data has been filtered to the column-density threshold of the row, and is colour-coded to depict the data in the redshift-range of the image column in red. In rows two and three, we have overlotted the mean (black solid), 1σ -, 2σ - and 3σ -contours (grey solid) and the model envelope (grey dashed line) of the analytical F08+K17 model.

Table 1. Simulation-based detection fractions of DLA-LOS enclosed within the F08+K17 model 1σ -, 2σ -, and 3σ -confidence regions.

Redshift range	1σ (0.68)	2σ (0.95)	3σ (0.99)
3.0 – 2.0	0.41	0.74	0.77
2.0 – 1.4	0.41	0.81	0.85
1.4 – 0.8	0.58	0.89	0.91
0.8 – 0.4	0.78	0.97	0.98

Table 2. Same as Table 1, but including sub-DLA LOS.

Redshift range	1σ (0.68)	2σ (0.95)	3σ (0.99)
3.0 – 2.0	0.41	0.70	0.74
2.0 – 1.4	0.39	0.76	0.81
1.4 – 0.8	0.42	0.77	0.81
0.8 – 0.4	0.54	0.84	0.87

converge to model predictions towards progressively lower redshifts, reaching a good agreement at $z \sim 0.8$. This may be related to the evolution and stability of the HI disc, in which case the model assumption of a geometrically thin, but optically thick slab of gas above the DLA column density limit is valid below $z \sim 0.8$ (see Section 3.2). If true, this can explain the statistical convergence of observational data, model-confidence regions and simulation results towards low redshift when an HI disc is present.

Relaxing the threshold on the column-density to include detection-fractions from sub-DLA LOS in b (kpc) – [M/H] (Figure 2, *second row*), we find that $f_{\text{detections}}$ becomes less concentrated and covers a larger region in the parameter-space at all redshifts. Phenomenologically, this suggests that sub-DLA LOS fill the void between islands of DLA- $f_{\text{detections}}$, and could be related to a density gradient such that sub-DLAs on average trace lower-density gas. We pursue this by separating the galaxy into a halo and a disc (Section 3.2) and quantify statistical differences between the average DLA and sub-DLA LOS in Sections 3.3 and 3.4.

In Table 2 we demonstrate how the inclusion of sub-DLA column densities affects the match between simulation $f_{\text{detections}}$ and the analytical disc model predictions. We find that such an inclusion results in a worse match at all redshifts. This most probably reflects the underlying Holmberg relation in the construction of the model, which works well down to the lower limit of DLA column densities. Indeed, this statistical discrepancy also matches the observational results of Rhodin et al. (2018), who found an excess of sub-DLAs beyond the predicted 1σ model region. We therefore conclude that in order to match simulations and observational data below the formal DLA limit, the analytical disc-model must be amended or expanded.

3.2 The fraction of DLA/sub-DLA systems in discs and halos

The relative contributions of interstellar (“disc”) and circumgalactic (“halo”) gas to DLA and sub-DLA detections are not yet known. Despite employing an infinitely thin circular disc to define a geometry on which to distribute the DLA cross-section, the F08+K17 model does not claim to describe galactic HI discs. In simulations, such a separation is complicated as these gaseous components are ill-defined, especially for the earliest stages of disc formation. This is especially true for gas in the interface between the disc and the halo, related to accretion and outflows. The results below should hence be treated as indicative.

We adopt the following simple approach for separating neutral disc gas from halo gas, and apply it to our most massive galaxy in the zoom-in region. For each simulation snapshot, the angular momentum vector is computed for all baryons residing within $3r_{1/2}$ of the central galaxy, where $r_{1/2}$ is the (baryonic) half mass radius. This defines a disc plane, for which we compute the density profile $n(r)$ of *neutral gas*, where r is the spherical radius. Such profiles are nearly exponential, with a fall-off below $n(r) \sim 10^{-2} \text{ cm}^{-3}$ due to the inability of gas to self-shield against the background UV field (also found in the radiative transfer calculations by Aubert & Teyssier 2010). We define the size of the disc to be the radius r_d where $n(r)$ falls below $n = 10^{-3} \text{ cm}^{-3}$, but note that our conclusions are not very sensitive to cut-off densities in the range to $n = 10^{-4} - 10^{-2} \text{ cm}^{-3}$. At $z < 1$, r_d fall in the range $\sim 15 - 30$ kpc. For each simulation snapshot, all neutral gas inside of the cylindrical radius r_d and below an altitude above the disc plane of $h = 8$ kpc is defined as ‘disc’, and the gas outside of this domain is defined as ‘halo’.

At high redshifts ($z \gtrsim 1 - 2$), mergers and galaxy interactions yield mostly transient discs - if at all. To allow for a cleaner disc-halo separation, we restrict our analysis to $z < 1$, and in order to convey that a robust (as opposed to a transient) disc is identified, we stack the results between $z = 0.4 - 1$. In this way, we ensure that our methodology is not biased to the conditions of a single snapshot. The results of the component separation are shown in Figure 3, for which the top row displays an HI column density map of the galaxy (*left*), the HI disc (*center*) and halo (*right*) at $z = 0.6$. Row two and three display the associated detection fractions in the b –[M/H] plane, with lower column-density thresholds set to sub-DLA and DLA limits, respectively. Our simple approach allows a clear disc component to be extracted, with the residual halo gas containing satellites, stripped filamentary gas, and gas at smaller impact parameters residing just outside, but soon to be accreted onto, the disc.

The disc component is visually distinct in the b –[M/H] relation, both for DLA LOS alone, and when sub-DLA LOS are included, and extends all the way to the 3σ confidence relation of the analytical F08+K17 model. In fact, 99.6%(88%) of all simulated DLA sightlines lie within the $2(1)\sigma$ relation, indicating that the F08+K17 model does not necessarily represent the physical nature of turbulent discs, but illustrates why this model has been highly successful in capturing observational properties of DLAs (Krogager et al. 2017). For the above disc definition, $\sim 40\%$ (60%) of LOS with $\log_{10}[\text{N}_{\text{HI}} (\text{cm}^2)] > 19$ intersect ‘halo’ (‘disc’) gas, and $\sim 20\%$ (80%) for $\log_{10}[\text{N}_{\text{HI}} (\text{cm}^2)] > 20.3$. By allowing for a disc def-

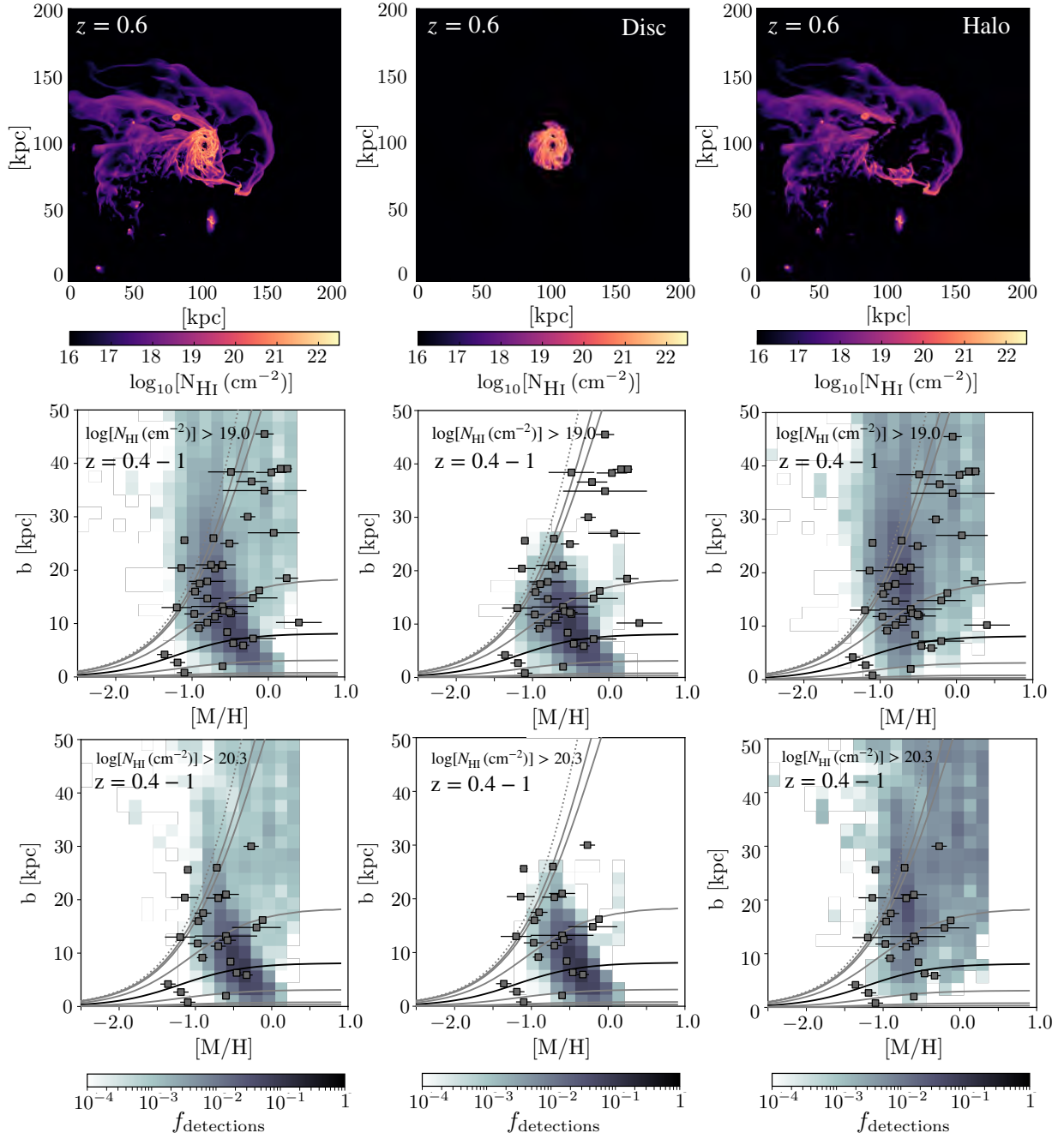


Figure 3. H I column density projection of the central halo (*top*) split into three panels depicting the total H I gas projection (*left*), the disc component (*center*) and halo (*right*). The bottom panels display the associated distributions of detection-fractions in the $b - [M/H]$ plane, with cuts at the sub-DLA and DLA threshold, respectively. The integral of detection-fractions in a panel measures the contribution of that structure to the total number of LOS producing strong H I absorption above the associated column-density threshold.

initiation with $h = 4$ kpc, rather than 8 kpc, we find identical results, indicating that our results are robust to reasonable parameter changes. In summary, our experiments illustrate that for the extended disc galaxy of the type analysed here, compatible with L_{\star} galaxies ($M_{\star} \sim \text{few} \times 10^{10} M_{\odot}$) and for

$z < 1$, DLAs predominantly originate in extended H I discs, but with halo gas playing a role at all impact parameters - especially at high impact parameters and in the sub-DLA regime.

Both simulations and observations indicate a significant

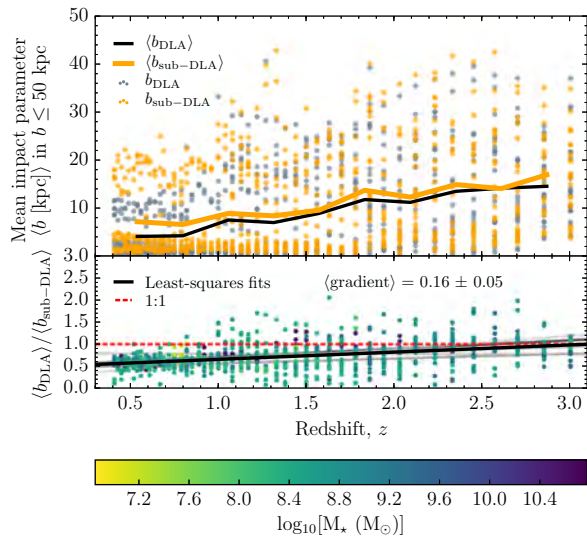


Figure 4. Angle-averaged mean impact parameters (b [kpc]) of sub-DLA and DLA sight-lines in seven halos followed in our simulations. *Top panel:* Mean impact parameter of DLA (grey) and sub-DLA (orange) LOS of individual snapshots. Binned mean trends for DLA and sub-DLAs impact parameters as a function of redshift are depicted as solid lines following the same colour-coding. *Bottom panel:* Data represents the mean DLA to sub-DLA impact parameter ratio for each snapshot and from each side of the simulation box, colour-coded to stellar mass. The dashed red line marks a one to one ratio. Solid grey lines show fits to separate halos. The solid black line depicts the mean relation.

amount of metal rich DLA/sub-DLA LOS at high impact parameters ($b \gtrsim 25$ kpc). From the simulated component separation, it is clear that most of the gas contributing to these LOS is of halo origin. We interpret this as a clear sign of metal rich gas stripped from dwarf satellites, as the shallow potential wells in these galaxies allow for efficient unbinding of enriched gas via outflows, ram pressure and tidal stripping. This is supported by the metallicity map in Figure 1 which shows high metallicity gas extending from the satellites; and visually by the presence of satellites and stripped tidal tails in the halo component of the main galaxy in Figure 3. We caution that this is a qualitative assessment. Rigorously tracing the precise origins of metals and mixing of gas requires particle tracing methods (e.g. Genel et al. 2013; Cadiou et al. 2019). Such methods will help us understand flows through the CGM and the disc-halo interface, and to quantify the contribution from satellites, which we leave for future work.

3.3 A redshift evolution in the mean impact parameters

The results of Section 3.1 suggest that there is a redshift evolution in the internal distribution of sub-DLA and DLA LOS through a galaxy, and that this evolution may be different for sub-DLAs and DLAs. We know from observations that strong HI absorbers follow a column-density dependent distribution of impact parameters (Christensen et al. 2007;

Monier et al. 2009; Fynbo et al. 2010, 2011; Meiring et al. 2011; Rao et al. 2011; Rahmani et al. 2016). Marginalizing over redshifts, these observations state that DLA LOS are found systematically closer to their host galaxy than sub-DLA LOS by a factor of ~ 2 (Rao et al. 2011; Rhodin et al. 2018). Likewise, investigations of the $\Delta v_{90} - [M/H]_{\text{abs}}$ relation (e.g. Ledoux et al. 2006; Møller et al. 2013; Neeleman et al. 2013) have shown that DLAs have smaller mean velocity widths and lower metallicities than sub-DLAs (e.g. Som et al. 2015). Taken together, these observations suggest that the two classes of absorbers on average trace different parts of their hosts.

We now explore whether we can quantify such average differences. The simplest non-parametric statistic to quantify the difference is the mean impact parameters of sub-DLA and DLA LOS. From here onwards, these will be referred to as $\langle b_{\text{sub-DLA}} \rangle$ and $\langle b_{\text{DLA}} \rangle$ respectively. These quantities are particularly interesting from an observational point of view, as impact parameters are amongst the simplest observables and readily available for 43 absorber-galaxy pairs in the MC19 compilation. In addition, the analysis presented in Section 3.1 suggest that DLA LOS can be found at large impact parameters with significant probabilities.

We first calculate $\langle b_{\text{sub-DLA}} \rangle$ and $\langle b_{\text{DLA}} \rangle$. To ensure that the galaxy analysed in previous sections is not an outlier, we allow HOP (see Section 2.2) to identify the seven most massive halos. This allows us to cover diverse galaxy environments, a stellar mass range of $6.7 < \log_{10}[M_{\star}(M_{\odot})] < 10.8$ which covers most observations, and to span a redshift range $0.4 < z < 3.0$. Using the information on $\langle b_{\text{sub-DLA}} \rangle$ and $\langle b_{\text{DLA}} \rangle$ together with the associated redshift and stellar mass from the three Cartesian directions and for each of the halos, we present the results in Figure 4. The top panel displays the individual data of $\langle b_{\text{sub-DLA}} \rangle$ (orange) and $\langle b_{\text{DLA}} \rangle$ (grey) together with their binned-mean relations in the respective colours, as a function of redshift. The results indicate a co-evolution in mean DLA -and- sub-DLA impact parameters towards progressively smaller values with time. However, perhaps the most striking feature is the large scatter in the mean values at any redshift. The scatter is set from the range of galaxy-sizes spanned by the seven halos, and the effect of a fixed 50 kpc beam. To cancel the size-dependence and enhance any differential change in the mean impact parameters with redshift, in the bottom panel, we therefore proceed to plot the ratio of the means; $\langle b_{\text{DLA}} \rangle / \langle b_{\text{sub-DLA}} \rangle$. A horizontal line implies a scale-free fraction, which at unity translates to identical mean impact parameters for sub-DLA and DLA LOS. For reference, we display such a 1 : 1 relation as a red dashed line.

To ensure that any correlation in $\langle b_{\text{DLA}} \rangle / \langle b_{\text{sub-DLA}} \rangle$ with redshift is indeed real, and not a consequence of an underlying correlation with stellar mass, we calculate the Pearson (PC) coefficient, the Spearman rank-order correlation (SC) coefficient, and their associated null-hypothesis's p-values. Expressed Test (parameter1, parameter2) = [coefficient, p-value] we find $\text{PC}(\langle b_{\text{DLA}} \rangle / \langle b_{\text{sub-DLA}} \rangle, \log_{10}[M_{\star}(M_{\odot})]) = [0.073, \sim 10^{-2}]$ and $\text{SC}(\langle b_{\text{DLA}} \rangle / \langle b_{\text{sub-DLA}} \rangle, \log_{10}[M_{\star}(M_{\odot})]) = [0.144, \sim 10^{-5}]$, whereas significantly higher correlation coefficients are identified for $\text{PC}(\langle b_{\text{DLA}} \rangle / \langle b_{\text{sub-DLA}} \rangle, z) = [0.396, \sim 10^{-31}]$, $\text{SC}(\langle b_{\text{DLA}} \rangle / \langle b_{\text{sub-DLA}} \rangle, z) = [0.399, \sim 10^{-32}]$. With consistent results from a Pearson and a Spearman test, both strongly

suggesting that redshift is indeed the primary driver in the impact parameter evolution, we proceed to ask whether it is driven by a particular halo.

We find consistent correlation coefficients of the same magnitude using both the Pearson and the Spearman test (six positive and one negative correlation) for the individual halos. The magnitude of these coefficients for individual halos are similar to that of the population as a whole, but at elevated p-values in a broad range $\sim [10^{-33} : 10^{-1}]$. We therefore proceed to explicitly calculate linear fits to individual halos (Figure 4, grey lines). These fits yield similar gradients that systematically favour an evolution in the mean impact parameter ratio with time. With a fit to all data, we find a mean gradient of 0.16 ± 0.05 per unit redshift, i.e. at a formal 3.2σ significance (Figure 4, black solid line).

This mean evolution in the ratio $\langle b_{\text{DLA}} \rangle / \langle b_{\text{sub-DLA}} \rangle$ with redshift is remarkably consistent with the analysis presented in Section 3.1. At $z \sim 3$ the ratio intercepts the 1:1 correlation. This is in part caused by the *presence* of multiple galaxies within the 50 kpc projected radius beam - each one generating its own internal distribution of DLA and sub-DLA LOSs - which on average will tend to average out any difference between the mean impact parameters discovered in the beam. In part, it is caused by the *interaction* between galaxies in the beam, which causes irregular gas flows that inhibit the formation of coherent structures, rendering a stochastic distribution. Moving down in redshift, the distribution of sub-DLA and DLA LOS diverge such that, on average, they are separated by a factor of two below redshifts $z \sim 0.5$.

It is striking that such a factor of ~ 2 difference in mean projected separation between sub-DLA and DLA LOS is retrieved in observations at redshifts $z < 1.0$ (Rao et al. 2011; Rhodin et al. 2018). Indeed, even the absolute mean impact parameters derived in these studies ($\langle b_{\text{DLA}}^{\text{empirical}} \sim 15$ kpc, $\langle b_{\text{sub-DLA}}^{\text{empirical}} \sim 30$ kpc) are marginally consistent with some of the high means retrieved for individual galaxies in our simulations at comparable redshifts (see Figure 4, top panel). As per Section 3.1 and Figure 2 bottom row, however, we find significant detection fractions of both sub-DLA and DLA LOS to projected separations ~ 50 kpc at all redshifts, and marginal inconsistencies in the absolute mean values between simulations and observations may reflect (observational) low number statistics and that cosmological zoom simulations have not converged on the spatial scales required to resolve cold gas in the CGM (McCourt et al. 2018; Hummels et al. 2018). We also note that Rahmati & Schaye (2014, R14) identify an anti-correlation between median impact parameter and N_{HI} , for which they report $\langle b_{\text{sub-DLA}}^{\text{R14}} \sim 7$ pkpc and $\langle b_{\text{DLA}}^{\text{R14}} \sim 2$ pkpc. Albeit a large intrinsic scatter in the data, with 15-85 per cent percentiles which we estimate to extend from 2 – 29 kpc and 0.5 – 4 kpc for sub-DLAs and DLAs, respectively (Rahmati & Schaye 2014, private communication), their median values are significantly lower than those identified in observations and in our simulations. Additionally, despite a consistent factor of two difference in the means, their analysis is based on redshift $z = 3$, whereas our analysis of the redshift evolution suggests that such a clear separation is only in place at $z \lesssim 0.7$.

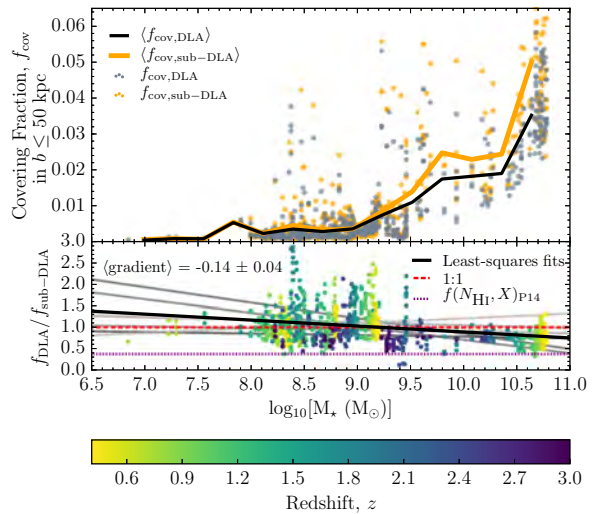


Figure 5. Same as Figure 4, but for covering-fractions (f_{cov}) of sub-DLA and DLA LOS as a function of stellar mass. The *bottom panel* additionally includes the expected cosmological ratio of the number of DLAs to sub-DLAs, based on the P14 column-density distribution function (dotted purple line, see text for more details).

3.4 Do sub-DLA and DLA sight-lines probe galaxies of different mass?

An alternative explanation to the idea that sub-DLA and DLA LOS trace different relations *within* a galaxy, is that they on average probe intrinsically *different* galaxy populations; sub-DLA LOS on average probing more massive galaxies than do DLA LOS (e.g. Khare et al. 2007; Kulkarini et al. 2010). Similar conclusions were also reached with deep ground-based imaging of sub-DLA hosts, which suggest that these systems preferentially sample more luminous - and therefore more massive galaxies than DLAs (Meiring et al. 2011). By measuring the stellar mass of the absorbing galaxies from matching spectral energy distribution galaxy templates to photometry, Augustin et al. (2018) and Rhodin et al. (2018) directly confirmed the apparent anti-correlation between the host’s stellar mass and the H I column-density of the absorber.

If real, this correlation is remarkable as we expect both high- and low column-density LOS to pass through a given galaxy. In addition, the shape of the column-density frequency distribution function ($f(N_{\text{HI}}, X)$) forces the frequency of sub-DLAs to outnumber that of DLAs. From Prochaska et al. (2014, P14) and with integration limits $[19.00, 20.30]_{\text{sub-DLA}}$ and $[20.30, 25.00]_{\text{DLA}}$, one finds $N_{\text{DLA}}/N_{\text{sub-DLA}} \sim 0.38$, which together with the apparent correlation described above implies an excess of massive gas-rich galaxies relative to low-mass galaxies, at odds with naive expectations from galaxy luminosity functions. A viable alternative is that the correlation is driven by sample selection effects.

Indeed Dessauges-Zavadsky et al. (2009) argue for a metallicity bias at low-redshifts, while at $z > 1.7$ DLA and sub-DLA selections show statistically consistent metallicity

distributions. Recent work on dust attenuation and quasar surveys confirms that we expect a dust-bias to preferentially act on high N_{HI} , massive, metal-rich, dusty galaxies selected against quasar LOS (Vladilo & Péroux 2005; Zafar & Watson 2013; Fynbo et al. 2013a; Noterdaeme et al. 2015; Krogager et al. 2015; Zafar et al. 2015; Krogager et al. 2016; Fynbo et al. 2017). In Rhodin et al. (2018) we argue that the detection void in the low mass, low HI column-density parameter space could be explained by a functional dependence of the ratio in covering fraction of sub-DLA to DLA LOS with stellar mass, such that sub-DLAs are preferentially detected in more massive galaxies.

To test this prediction, we calculate the covering fraction (f_{cov}) of sub-DLA and DLA LOSs in each halo, and repeat the statistical analysis described in Section 3.3. Utilising the column-density maps created with Equation 3, we define f_{cov} as the fractional area with column densities above the (sub-)DLA limit in a circular beam with 50 kpc galactocentric projected separation. We present the angle-averaged results in Figure 5. In the top panel, we plot the data for individual galaxies f_{cov} in DLA (grey) and sub-DLA (orange) LOS, together with binned-mean relations in the respective colours, as a function of stellar mass. f_{cov} for sub-DLA and DLA LOS correlate with stellar mass such that larger stellar masses, on average, are associated with larger f_{cov} . At stellar mass $\log_{10}(M_{\star} [M_{\odot}]) \sim 10$ the entire central region sees an increase in neutral gas, which leads to a rapid increase in the final covering fractions. For the most massive disc galaxy in our sample, this increase correlates with rapid disc growth at $z \sim 1.5$. This increase in gas disc sizes of galaxies forming in Milky Way-mass halos, around this redshift and stellar mass, is found in larger samples of zoom simulations (Kretschmer et al. in prep), as well as observationally in terms of the stellar size-mass relation (see compilation by Agertz & Kravtsov 2015).

Calculating the Pearson correlation coefficient; the Spearman rank-order correlation coefficient, and their associated null-hypothesis's p-value, we find $\text{PC}(z, f_{\text{DLA}}/f_{\text{sub-DLA}}) = [-0.162, \sim 10^{-6}]$ and $\text{SC}(z, f_{\text{DLA}}/f_{\text{sub-DLA}}) = [-0.164, \sim 10^{-6}]$, whereas $\text{PC}(\log_{10}(M_{\star} [M_{\odot}]), f_{\text{DLA}}/f_{\text{sub-DLA}}) = [-0.273, \sim 10^{-15}]$ and $\text{SC}(\log_{10}(M_{\star} [M_{\odot}]), f_{\text{DLA}}/f_{\text{sub-DLA}}) = [-0.244, \sim 10^{-12}]$. With consistent results, we conclude that a correlation in differential covering fraction with stellar mass indeed dominates over a correlation with redshift by a factor of ~ 2 . In Figure 5 lower panel, we show the ratio of DLA to sub-DLA covering fractions to envisage the differential scaling with stellar mass, and colour-code the data by redshift.

Having established the subordinate role of redshift to stellar mass in the covering fraction ratio, we proceed to ask whether the correlation is driven by a particular halo. Individual halos display similar correlation coefficients to the that of the population as a whole, but at elevated p-values in the range $\sim [10^{-3} : 10^{-1}]$, suggesting that each halo contributes to the final p-value and correlation-strength of the population. We therefore proceed to calculate linear fits to the data of individual halos (overplotted as grey lines). With consistent trends, we find a mean differential covering fraction ratio per unit logarithmic stellar mass of -0.14 ± 0.04 . This corresponds to a weak functional dependence at a 3.5 σ significance which we over-plot as a black solid line. Qualita-

tively, this correlation with stellar mass is consistent with the results of Faucher-Giguère et al. (2015) who report that the covering fraction of gas at different column-density thresholds is sensitive to individual dark matter halo masses for LBGs at $z \sim 2$.

Despite weak, if real and acting across the three decades in stellar mass $\sim [8.0 < M_{\star} [M_{\odot}] < 11.]$ identified in observations, we expect this gradient to account for $3 \times 0.14 \sim 0.4$, i.e. a 40% measured effect. We consider a more realistic value to be that produced within the 1σ dispersion in the stellar mass distribution of confirmed hosts. For the sample used in Rhodin et al. (2018), with mean and dispersion in stellar mass of 9.87 ± 0.66 , we expect a measured effect of $\sim 20\%$. Whereas we expect this effect to contribute to the observed anti-correlation, a direct comparison to the current set of data is beyond the scope of this work, as such a comparison has to account for sample selection functions and observational strategy bias.

As a reference-point, we instead calculate the predicted ratio of the number of DLAs to sub-DLAs, based on $f(N_{\text{HI}}, X)$. With the P14 parametrisation, $f(N_{\text{HI}}, X)_{\text{P14}}$, we expect a ratio $N_{\text{DLA}}/N_{\text{sub-DLA}} = 0.38$. We over-plot this estimator as a dotted purple line. Using the $f(N)$ statistic as an unbiased proxy for the cosmic average covering fraction ratio in DLAs to sub-DLAs, we find an over-density of DLA (or equivalently, an under-density of sub-DLA) LOS within a 50 kpc projected radius beam from the mass center of the hosting halo. From this, we conclude that the majority of sub-DLAs are located at separations $b > 50$ kpc.

4 CONCLUSIONS

In this work, we have used a cosmological zoom-in hydrodynamics simulation of the assembly of a Milky Way mass galaxy to study beams of 50 kpc radius centered on galaxies to study the environments capable of producing sub-DLA and DLA LOS. Building probability functions of observables and logging their redshift evolution, we have matched these to the most up-to-date compilation of spectroscopically confirmed absorbing galaxies (Møller & Christensen 2019; Christensen et al. 2019), and to analytic models (Fynbo et al. 2008; Krogager et al. 2017). The main results can be summarised as follows:

- Recent advances have shown that increased numerical resolution leads to increased long-lived cool gas content on progressively smaller size scales (Hummels et al. 2018); a doubling in covering fraction of Lyman limit systems within 150 kpc (van de Voort et al. 2019); and improved match to observed kinematic structure of the absorbing gas (Peeples et al. 2019). Our results are in qualitative agreement, suggesting that increased numerical resolution leads to an excess of HI coverage in galaxy halos and the CGM. This increases the mean impact parameters of strong HI absorbers and produces detection probabilities at all observed values.
- High numerical resolution and an effective feedback prescription allow us to reproduce the column density distribution function of blind quasar surveys and for individual galaxies. This validates the application of these simulations to study sub-DLA and DLAs in a galactic context.
- At redshift $z \lesssim 1$ we statistically match the distribution

of impact parameters with metallicity based on the analytical F08+K17 model for DLAs. For higher redshifts, and when including the contribution from sub-DLAs, we find a greater statistical miss-match and excess detection probability beyond the envelope of the analytical model.

- To understand the physical origin of the detection-fractions, we perform a disc-halo separation using the baryonic angular momentum vector and the density profile of neutral gas. We find that $\sim 80\%$ of DLAs originate in extended H I discs, with the remaining 20% originating in the halo. Including sub-DLAs increases the relative contribution of the halo to 40%. We note that this separation relies on the existence of a clearly defined H I disc, and our results are limited to redshifts $z < 1$.

- We find a 3.2σ significance redshift evolution in the mean impact parameters of sub-DLA and DLA LOS. At high redshifts the mean impact parameters overlap, but separate at successively lower redshifts with sub-DLA LOS on average identified at a factor two larger projected separations than DLAs at $z \sim 0.4$. At all redshifts, our simulations can match the observational data.

- We find a 3.5σ significance anti-correlation in differential covering-fraction of DLA to sub-DLA LOSs with stellar mass. This suggests an observational selection effect that causes the preferential detection of sub-DLAs in more massive galaxies in the low-redshift universe.

Despite the remarkable agreement with observations - which may suggest that strong H I absorption predominantly form in typical gas-rich disc galaxies - we caution against over-interpreting the results. Whereas our simulation qualitatively capture and explain the current set of observations, the results should be anchored in the next generation of zoom-in simulations performed across a large grid to account for environmental dependence and sample the underlying dark matter halo distribution.

ACKNOWLEDGEMENTS

We thank the referee for valuable comments which greatly improved the scientific content, language, and clarity of the work presented here. This work was supported by grant ID DFF-4090-00079. The cosmic Dawn center is funded by the DNRF. This work used the COSMA Data Centric system at Durham University, operated by the Institute for Computational Cosmology on behalf of the STFC DiRAC HPC Facility (www.dirac.ac.uk). This equipment was funded by a BIS National E-infrastructure capital grant ST/K00042X/1, DiRAC Operations grant ST/K003267/1 and Durham University. DiRAC is part of the National E-Infrastructure. OA acknowledges support from the Swedish Research Council (grant 2014- 5791). OA and FR acknowledge support from the Knut and Alice Wallenberg Foundation.

REFERENCES

Agertz O., Kravtsov A. V., 2015, *ApJ*, **804**, 18
 Agertz O., Kravtsov A. V., 2016, *ApJ*, **824**, 79
 Agertz O., Teyssier R., Moore B., 2009, *MNRAS*, **397**, L64
 Agertz O., Kravtsov A. V., Leitner S. N., Gnedin N. Y., 2013, *ApJ*, **770**, 25

Altay G., Theuns T., Schaye J., Crighton N. H. M., Dalla Vecchia C., 2011, *ApJ*, **737**, L37
 Altay G., Theuns T., Schaye J., Booth C. M., Dalla Vecchia C., 2013, *MNRAS*, **436**, 2689
 Asplund M., Grevesse N., Sauval A. J., Scott P., 2009, *ARA&A*, **47**, 481
 Aubert D., Teyssier R., 2010, *ApJ*, **724**, 244
 Augustin R., et al., 2018, *MNRAS*, **478**, 3120
 Bird S., Vogelsberger M., Haehnelt M., Sijacki D., Genel S., Torrey P., Springel V., Hernquist L., 2014, *MNRAS*, **445**, 2313
 Bird S., Haehnelt M., Neeleman M., Genel S., Vogelsberger M., Hernquist L., 2015, *MNRAS*, **447**, 1834
 Blondin J. M., Wright E. B., Borkowski K. J., Reynolds S. P., 1998, *ApJ*, **500**, 342
 Boissier S., Prantzos N., 2001, *MNRAS*, **325**, 321
 Cadiou C., Dubois Y., Pichon C., 2019, *A&A*, **621**, A96
 Cen R., 2012, *ApJ*, **748**, 121
 Chabrier G., 2003, *PASP*, **115**, 763
 Christensen L., Wisotzki L., Roth M. M., Sánchez S. F., Kelz A., Jahnke K., 2007, *A&A*, **468**, 587
 Christensen L., Møller P., Rhodin N. H. P., Heintz K., Fynbo J. P. U., 2019, *MNRAS*
 Cioffi D. F., McKee C. F., Bertschinger E., 1988, *ApJ*, **334**, 252
 Dessauges-Zavadsky M., Ellison S. L., Murphy M. T., 2009, *MNRAS*, **396**, L61
 Eisenstein D. J., Hut P., 1998, *ApJ*, **498**, 137
 Erkal D., Gnedin N. Y., Kravtsov A. V., 2012, *ApJ*, **761**, 54
 Faucher-Giguère C.-A., Hopkins P. F., Kereš D., Muratov A. L., Quataert E., Murray N., 2015, *MNRAS*, **449**, 987
 Freudling W., Møller P., Krogager J.-K., Christensen L., 2019
 Fumagalli M., Prochaska J. X., Kasen D., Dekel A., Ceverino D., Primack J. R., 2011, *MNRAS*, **418**, 1796
 Fynbo J. P. U., Prochaska J. X., Sommer-Larsen J., Dessauges-Zavadsky M., Møller P., 2008, *ApJ*, **683**, 321
 Fynbo J. P. U., et al., 2010, *MNRAS*, **408**, 2128
 Fynbo J. P. U., et al., 2011, *MNRAS*, **413**, 2481
 Fynbo J. P. U., Krogager J.-K., Venemans B., Noterdaeme P., Vestergaard M., Møller P., Ledoux C., Geier S., 2013a, *ApJS*, **204**, 6
 Fynbo J. P. U., et al., 2013b, *MNRAS*, **436**, 361
 Fynbo J. P. U., et al., 2017, *A&A*, **606**, A13
 Genel S., Vogelsberger M., Nelson D., Sijacki D., Springel V., Hernquist L., 2013, *MNRAS*, **435**, 1426
 Haardt F., Madau P., 1996, *ApJ*, **461**, 20
 Haehnelt M. G., Steinmetz M., Rauch M., 1998, *ApJ*, **495**, 647
 Hahn O., Abel T., 2011, *MNRAS*, **415**, 2101
 Holmberg, E. in Sandage A., Sandage M., Kristian J., 1975, *Galaxies and the Universe*. "Chicago: University of Chicago Press", p. 123
 Hopkins P. F., Kereš D., Oñorbe J., Faucher-Giguère C.-A., Quataert E., Murray N., Bullock J. S., 2014, *MNRAS*, **445**, 581
 Hummels C. B., et al., 2018, arXiv e-prints,
 Khare P., Kulkarni V. P., Péroux C., York D. G., Lauroesch J. T., Meiring J. D., 2007, *A&A*, **464**, 487
 Kim C.-G., Ostriker E. C., 2015, *ApJ*, **802**, 99
 Kim J.-h., Abel T., Agertz O. e. a., 2014, *ApJS*, **210**, 14
 Kim J.-h., et al., 2016, *ApJ*, **833**, 202
 Krogager J.-K., Fynbo J. P. U., Møller P., Ledoux C., Noterdaeme P., Christensen L., Milvang-Jensen B., Sparre M., 2012, *MNRAS*, **424**, L1
 Krogager J.-K., et al., 2013, *MNRAS*, **433**, 3091
 Krogager J.-K., et al., 2015, *ApJS*, **217**, 5
 Krogager J.-K., et al., 2016, *ApJ*, **832**, 49
 Krogager J.-K., Møller P., Fynbo J. P. U., Noterdaeme P., 2017, *MNRAS*, **469**, 2959
 Krumholz M. R., McKee C. F., Tumlinson J., 2008, *Astrophysical Journal*, **689**, 865

- Krumholz M. R., McKee C. F., Tumlinson J., 2009, *Astrophysical Journal*, 693, 216
- Kulkarni V. P., Khare P., Som D., Meiring J., York D. G., Péroux C., Lauroesch J. T., 2010, *New Astron.*, 15, 735
- Ledoux C., Petitjean P., Fynbo J. P. U., Møller P., Srianand R., 2006, *A&A*, 457, 71
- Leitherer C., et al., 1999, *ApJS*, 123, 3
- Liang C. J., Kravtsov A. V., Agertz O., 2016, *MNRAS*, 458, 1164
- Liang C. J., Kravtsov A. V., Agertz O., 2018, *MNRAS*, 479, 1822
- Martizzi D., Faucher-Giguère C.-A., Quataert E., 2015, *MNRAS*, 450, 504
- McCourt M., Oh S. P., O’Leary R., Madigan A.-M., 2018, *MNRAS*, 473, 5407
- Meiring J. D., Lauroesch J. T., Habertzettl L., Kulkarni V. P., Péroux C., Khare P., York D. G., 2011, *MNRAS*, 410, 2516
- Mo H. J., Mao S., White S. D. M., 1998, *MNRAS*, 295, 319
- Møller P., Christensen L., 2019, *MNRAS*
- Møller P., Warren S. J., 1998, *MNRAS*, 299, 661
- Møller P., Fynbo J. P. U., Ledoux C., Nilsson K. K., 2013, *MNRAS*, 430, 2680
- Monier E. M., Turnshek D. A., Rao S., 2009, *MNRAS*, 397, 943
- Nagamine K., Wolfe A. M., Hernquist L., Springel V., 2007, *ApJ*, 660, 945
- Neeleman M., Wolfe A. M., Prochaska J. X., Rafelski M., 2013, *ApJ*, 769, 54
- Noterdaeme P., Petitjean P., Ledoux C., Srianand R., 2009, *A&A*, 505, 1087
- Noterdaeme P., et al., 2012, *A&A*, 547, L1
- Noterdaeme P., Petitjean P., Srianand R., 2015, *A&A*, 578, L5
- Padoan P., Haugbølle T., Nordlund Å., 2012, *ApJ*, 759, L27
- Peeples M. S., et al., 2019, *ApJ*, 873, 129
- Péroux C., Dessauges-Zavadsky M., D’Odorico S., Kim T.-S., McMahon R. G., 2003, *MNRAS*, 345, 480
- Péroux C., Bouché N., Kulkarni V. P., York D. G., Vladilo G., 2012, *MNRAS*, 419, 3060
- Peterson B. M., Strom S. E., Strom K. M., 1979, *AJ*, 84, 735
- Pettini M., Shapley A. E., Steidel C. C., Cuby J.-G., Dickinson M., Moorwood A. F. M., Adelberger K. L., Giavalisco M., 2001, *ApJ*, 554, 981
- Pontzen A., et al., 2008, *MNRAS*, 390, 1349
- Power C., Navarro J. F., Jenkins A., Frenk C. S., White S. D. M., Springel V., Stadel J., Quinn T., 2003, *MNRAS*, 338, 14
- Prochaska J. X., Wolfe A. M., 1997, *ApJ*, 487, 73
- Prochaska J. X., Gawiser E., Wolfe A. M., Castro S., Djorgovski S. G., 2003, *ApJ*, 595, L9
- Prochaska J. X., Herbert-Fort S., Wolfe A. M., 2005, *ApJ*, 635, 123
- Prochaska J. X., Madau P., O’Meara J. M., Fumagalli M., 2014, *MNRAS*, 438, 476
- Rafelski M., Neeleman M., Fumagalli M., Wolfe A. M., Prochaska J. X., 2014, *ApJ*, 782, L29
- Rahmani H., et al., 2016, *MNRAS*, 463, 980
- Rahmati A., Schaye J., 2014, *MNRAS*, 438, 529
- Rahmati A., Pawlik A. H., Raičević M., Schaye J., 2013, *MNRAS*, 430, 2427
- Raiteri C. M., Villata M., Navarro J. F., 1996, *A&A*, 315, 105
- Rao S. M., Belfort-Mihalyi M., Turnshek D. A., Monier E. M., Nestor D. B., Quider A., 2011, *MNRAS*, 416, 1215
- Reddy N. A., Steidel C. C., 2009, *ApJ*, 692, 778
- Reddy N. A., Steidel C. C., Pettini M., Adelberger K. L., Shapley A. E., Erb D. K., Dickinson M., 2008, *ApJS*, 175, 48
- Rhodin N. H. P., Christensen L., Møller P., Zafar T., Fynbo J. P. U., 2018, preprint, ([arXiv:1807.01755](https://arxiv.org/abs/1807.01755))
- Romeo A. B., Agertz O., Moore B., Stadel J., 2008, *ApJ*, 686, 1
- Rosen A., Bregman J. N., 1995, *ApJ*, 440, 634
- Schaye J., et al., 2015, *MNRAS*, 446, 521
- Som D., Kulkarni V. P., Meiring J., York D. G., Péroux C., Lauroesch J. T., Aller M. C., Khare P., 2015, *ApJ*, 806, 25
- Sutherland R. S., Dopita M. A., 1993, *ApJS*, 88, 253
- Teyssier R., 2002, *A&A*, 385, 337
- Thornton K., Gaudlitz M., Janka H.-T., Steinmetz M., 1998, *ApJ*, 500, 95
- Tytler D., 1982, *Nature*, 298, 427
- Vladilo G., Péroux C., 2005, *A&A*, 444, 461
- Vogelsberger M., et al., 2014, *MNRAS*, 444, 1518
- Wetzel A. R., Hopkins P. F., Kim J.-h., Faucher-Giguère C.-A., Kereš D., Quataert E., 2016, *ApJ*, 827, L23
- Wise J. H., Abel T., Turk M. J., Norman M. L., Smith B. D., 2012, *MNRAS*, 427, 311
- Wolfe A. M., Turnshek D. A., Smith H. E., Cohen R. D., 1986, *ApJS*, 61, 249
- Zafar T., Watson D., 2013, *A&A*, 560, A26
- Zafar T., Popping A., Péroux C., 2013, *A&A*, 556, A140
- Zafar T., et al., 2015, *A&A*, 584, A100
- Zwaan M. A., van der Hulst J. M., Briggs F. H., Verheijen M. A. W., Ryan-Weber E. V., 2005, *MNRAS*, 364, 1467
- van de Voort F., Springel V., Mandelker N., van den Bosch F. C., Pakmor R., 2019, *MNRAS*, 482, L85

This paper has been typeset from a $\text{\TeX}/\text{\LaTeX}$ file prepared by the author.

Paper III

Absorption-selected galaxies trace the low-mass, late-type, star-forming population at $z \sim 2 - 3$

N. H. P. RHODIN,¹ J.-K. KROGAGER,^{2,1} L. CHRISTENSEN,¹ F. VALENTINO,³ K. E. HEINTZ,^{4,3} P. MÖLLER,⁵ T. ZAFAR,⁶
AND J. P. U. FYNBO³

¹*DARK, Niels Bohr Institute, University of Copenhagen, Lyngbyvej 2, DK-2100 Copenhagen Ø, Denmark*

²*Institut d'Astrophysique de Paris, CNRS-UPMC, UMR7095, 98bis bd Arago, 75014 Paris, France*

³*Cosmic Dawn Center (DAWN), Niels Bohr Institute, University of Copenhagen, Lyngbyvej 2, DK-2100 Copenhagen Ø, Denmark*

⁴*Centre for Astrophysics and Cosmology, Science Institute, University of Iceland, Dunhagi 5, 107 Reykjavík, Iceland*

⁵*European Southern Observatory, Karl-Schwarzschildstrasse 2, 85748 Garching bei München, Germany*

⁶*Australian Astronomical Optics, Macquarie University, 105 Delhi Road, North Ryde, NSW 2113, Australia*

(Received -; Revised -; Accepted -)

Submitted to ApJ

ABSTRACT

We report on the stellar content, half-light radii, and star formation rates of seven new and three known high redshift ($z \gtrsim 2$) galaxies detected from neutral hydrogen (H I) absorbers (Damped Ly α Absorbers (DLAs) and sub-DLAs) toward background quasars. We characterise the galactic environments of such absorbers and their associated host galaxy counterparts, and perform the first systematic morphological characterisation of such absorption-emission pairs at high redshifts. Leveraging the spatial resolution of the Hubble Space Telescope (*HST*) Wide Field Camera 3 (WFC3), we image the counterparts in the quasar-subtracted fields in the F105W, the F160W, and the F606W filters. Our analysis reveals complex, irregular hosts with multiple star-forming clumps. Consistent with expectations from luminosity-selected surveys, we measure half-light radii in the range $r_{1/2} \sim 0.5 - 2.5$ kpc based on the reddest (F160W) band to trace the oldest stellar populations; stellar masses in the range $\log_{10}[M_{\star} (M_{\odot})] \sim 8 - 10$ derived from broadband photometry with realistic magnitude errors; and spectroscopic- and spectral energy distribution-based star formation rates $\lesssim 30 M_{\odot} \text{ yr}^{-1}$. Placed on the mass-size relation and on the main sequence of star formation, our results indicate that absorbing galaxies at high redshift are consistent with late-type, gas-rich, star-forming galaxy populations.

Keywords: galaxies: evolution — galaxies: photometry — galaxies: stellar content — (galaxies:) quasars: absorption lines

1. INTRODUCTION

Galaxies can be selected via their gas cross-section when there is a chance alignment with a background quasar along the line of sight. In neutral hydrogen (H I), the most H I-rich absorbers are the Damped Lyman- α Absorbers (DLAs; $\log_{10}[N_{\text{HI}} (\text{cm}^{-2})] \geq 20.3$, Wolfe et al. (1986)) and the sub-DLAs ($19.0 \leq \log_{10}[N_{\text{HI}} (\text{cm}^{-2})] < 20.3$, e.g., Péroux et al. (2003); Zafar et al. (2013b)). These classes imprint deep H I absorption lines with characteristic Lorentzian damping wings in the quasar spectrum, and are always accompa-

nied by low-ionisation metal line complexes (Prochaska et al. 2003; Noterdaeme et al. 2012a; Rafelski et al. 2014). Unless otherwise specified, sub-DLAs and DLAs will collectively be referred to as *strong H I absorbers*.

DLAs alone account for $> 80\%$ of neutral gas out to redshift $z \sim 5$ (Prochaska et al. 2005; Noterdaeme et al. 2012a; Crighton et al. 2015; Sánchez-Ramírez et al. 2016), and combined with the contribution from sub-DLAs, strong H I absorbers efficiently probe the neutral, chemically enriched gaseous environments of galaxies. The connection that strong H I absorbers hold to their harbouring galaxies can be studied by correlating absorption properties with complementary information of the host in emission. Such analysis suggests that absorption-selected galaxies are consistent with

Corresponding author: N. H. P. Rhodin
henrikrhodin@dark-cosmology.dk

the faint end of Lyman-break galaxies (Møller et al. 2002), and that they probe a more representative portion (low mass, faint end of the luminosity function) of galaxy populations across cosmic time than conventional luminosity selections (Fynbo et al. 2008; Berry et al. 2016; Krogager et al. 2017). In particular, a recent string of observations indicate that galaxies hosting strong HI absorbers at $z \sim 0.7$ experience suppressed star formation rates (SFR) - either above stellar masses $\log_{10}[M_{\star} (M_{\odot})] \sim 10$ (Rhodin et al. 2018), as a consequence of redshift (Kanekar et al. 2018) or galaxy evolution (Møller et al. 2018). Independent of its cause, a low SFR is remarkable if strong HI absorbers truly represent the formation-sites for molecular gas and, in extension, reservoirs that maintain star formation.

The current status of how damped absorbers relate to their galactic environments hinges on low number-statistics of spectroscopically confirmed absorption-emission pairs. At cosmological redshifts $z \gtrsim 2$, this lack in sample size is caused by a combination of low angular separation and inherent brightness contrast between target galaxy and background quasar; increased surface brightness dimming with redshift; and the lower mean mass (and therefore luminosity) of galaxies selected by gas cross-section. Indeed, the lack of detections and reported survey statistics are consistent with scaling relation arguments, which suggest that the emission-line targets often fall below detection-limits in blind surveys; whilst pre-selecting on the absorption metallicity yields higher detection rates (Fynbo et al. 2010, 2011) as metal-rich galaxies tend to be more massive, and therefore more luminous (Krogager et al. 2017).

Yet, $z \sim 2-3$ allows for simultaneous measurements of the neutral hydrogen column density from the damped Ly α absorption profile and detailed absorption analysis of metal lines with ground-based spectroscopy (Noterdaeme et al. 2012a). This has ensured high fidelity data to base followup campaigns on in search of the counterparts in emission. Indeed, the damped Ly α absorption trough effectively blocks out the quasar light and can be used to search for Ly α emission from the hypothesised host. Owing to the resonance nature of Ly α , which is known to affect the emerging line-flux from high- z galaxy populations (Verhamme et al. 2008; Laursen et al. 2009; Hayes et al. 2010) and its efficient destruction by dust in more chemically enriched, massive and luminous galaxies (which could mitigate any selection on absorption metallicity), such Ly α searches often resulted in non-detections (Fynbo et al. 2011, 2013). However, taking advantage of the large wavelength coverage in modern spectrographs to simultaneously detect strong-rest-frame optical emission lines, ground-

based observational efforts have been increasingly successful, most prominently seen in the high detection-rate achieved with the Very Large Telescope (VLT) X-Shooter (VLT/X-Shooter, Vernet et al. 2011) campaign (Fynbo et al. 2010; Krogager et al. 2017).

Whereas previous spectroscopic searches for galaxy counterparts focused primarily on identifying the host in emission at the absorber redshift, analyses of the stellar emission components from the galaxies have typically been reported as individual case studies (Møller et al. 2002; Fynbo et al. 2013; Krogager et al. 2013; Augustin et al. 2018). Even though we have assembled a significant sample of $z \gtrsim 2$ DLA-galaxy pairs, a comprehensive investigation of the stellar contents of the galaxies as a population is lacking. Here, we take advantage of the detailed information available from ground-based spectra to search for the counterparts of damped H I absorbers at $z \sim 2-3$ with multi-band photometric Hubble Space Telescope (*HST*) imaging. With its exquisite spatial resolution and absent of the telluric atmosphere, *HST* allows us to disentangle the emission from the intervening galaxy and background quasar; and determine stellar masses and morphologies. This directly addresses the low-number statistics, and will enable scaling relations at high- z to be explored independent of samples at low redshift, as well as probing the low-mass extensions of any relations established from luminosity-selected galaxy samples.

The paper is organised as follows: Section 2 describes sample selection, observations, and data-reduction; Section 3 presents our imaging, photometry, morphological analysis, and spectral energy distribution (SED) based stellar mass measurements; and Section 4 places our findings in context. In Section 5 we summarise our conclusions. Throughout this paper, we assume a flat Λ cold dark matter (Λ CDM) cosmology, with $H_0 = 70.4 \text{ km s}^{-1} \text{ Mpc}^{-1}$ and $\Omega_{\Lambda} = 0.727$ (Komatsu et al. 2011) to ensure consistency with prior work (e.g. Christensen et al. 2014; Møller et al. 2018; Rhodin et al. 2018).

2. OBSERVATIONS AND DATA-REDUCTION

2.1. Sample selection

We select targets to study morphology and stellar mass content in high redshift ($z \gtrsim 2$) absorption-selected galaxies hosting strong HI absorbers using *HST* imaging (see Section 2.2). To break model degeneracies with only three broad-band magnitudes, we require the galaxies to be spectroscopically confirmed with emission lines detected at z_{abs} , and measured in quasar spectra (see Table 2 for individual entry references). In addition, spectroscopic redshifts and high spatial resolution allows

Table 1. Observation log for the *HST* imaging.

Quasar Field	R.A. ^a	Dec. ^a	$N_{\text{orb}} \times N_{\text{exp}} \times t_{\text{exp}}$		
	[J2000]	[J2000]	IR/F105W	IR/F160W	UVIS/F606W
	[hh:mm:ss]	[° : ' : '']	[s]	[s]	[s]
Q0124+0044	01 : 24 : 03.78	+00 : 44 : 32.74	$1 \times 4 \times 653$	$1 \times 4 \times 653$	$1 \times 4 \times 621$
Q0139-0824	01 : 39 : 01.41	-08 : 24 : 44.05	$1 \times 4 \times 653$	$1 \times 4 \times 653$	$1 \times 4 \times 622$
Q0310+0055	03 : 10 : 36.85	+00 : 55 : 21.66	$1 \times 4 \times 653$	$1 \times 4 \times 653$	–
Q1313+1441	13 : 13 : 41.20	+14 : 41 : 40.60	$1 \times 4 \times 653$	$1 \times 4 \times 653$	$1 \times 4 \times 623$
Q2059-0528	20 : 59 : 22.43	-05 : 28 : 42.78	$1 \times 4 \times 653$	$1 \times 4 \times 653$	$1 \times 4 \times 622$
Q2239-2949	22 : 39 : 41.77	-29 : 49 : 54.47	$1 \times 4 \times 653$	$1 \times 4 \times 653$	$1 \times 4 \times 626$
Q2247-6015	22 : 47 : 08.93	-60 : 15 : 45.30	$1 \times 4 \times 703$	$1 \times 4 \times 703$	$1 \times 4 \times 646$
Q0338-0005	03 : 38 : 54.78	-00 : 05 : 21.01	–	–	$2 \times 4 \times 627$
Q2222-0946	22 : 22 : 56.11	-09 : 46 : 36.29	$1 \times 4 \times 653$	$1 \times 4 \times 653$	$1 \times 4 \times 629$
Q0918+1636	09 : 18 : 26 : 16	+16 : 36 : 09.02	$1 \times 4 \times 653$	$1 \times 4 \times 653$	$1 \times 4 \times 631$

^aR.A. and Dec. refer to the coordinates of the quasar, taken from the SIMBAD database (Wenger et al. 2000).

accurate conversions of angular separations to physical distances, and therefore measurements of the projected spatial scales that connect the emission and absorption.

A large fraction of the confirmed hosts were originally selected on the absorption properties in intermediate resolution X-Shooter quasar spectra (for an overview of the X-Shooter observing strategy, see Krogager et al. 2017). These absorbers were themselves selected based on high Si II $\lambda 1526$ Å rest-frame equivalent widths measured in Sloan Digital Sky Survey (SDSS, Richards et al. 2001; Noterdaeme et al. 2009a) spectra, since these measurements act as an efficient proxy for high metallicity absorbers (Prochaska et al. 2008) - and therefore are more likely to be hosted by more luminous hosts (Fynbo et al. 2010, 2011; Krogager et al. 2012; Noterdaeme et al. 2012b; Péroux et al. 2012; Bouché et al. 2013; Fynbo et al. 2013; Krogager et al. 2013; Rahmani et al. 2016; Rhodin et al. 2018).

In summary, our sample consists of seven new, and three re-analysed $z_{\text{abs}} \sim 1.8 - 3.1$ spectroscopically confirmed galaxies hosting five DLAs and two sub-DLAs in quasar fields, with a sample selection biased towards high-metallicity absorbers.

2.2. *HST* data

To study stellar content and morphology, we acquired *HST* broad-band imaging in the Wide Field Camera 3 (WFC3) using the Ultraviolet-Visible (UVIS) channel UVIS/F606W, and the Infrared (IR) channel IR/F105W and IR/F160W filters (new detections: Cycle 23, ID 14122, PI. Christensen; re-analysed detections: Cycle 19, ID 12553, PI. Fynbo). At the absorber redshifts,

this allows us to map the stellar continuum around the rest-frame Balmer jump. Each target is imaged with one orbit per filter (except Q 0338-0005 which was observed with two orbits in F606W), subdivided into four exposures of equal lengths. We use a standard four-point dither strategy designed to provide an optimal sub-pixel PSF sampling (WFC3-UVIS-DITHER-BOX and WFC3-IR-DITHER-BOX-MIN patterns in the F606W, and the F105W- and F160W filters, respectively). For each target, the impact parameter and position-angle of the candidate absorbing galaxy based on long-slit spectra allows us to optimize the target orientation relative to the diffraction spikes and detector bleeding effects. The observation log is summarised in Table 1.

To reduce individual exposures we run a standard **AstroDrizzle** processing pipeline based on the Python **DrizzlePac**¹. With the Object Association (ASN) Table, this procedure constructs a parameter file which is used to align frames and perform sky subtraction and cosmic ray rejection. Individual exposures in each filter and for each object are drizzled into final, inverse variance (IVM) weighted science frames. For a detailed description of **AstroDrizzle**, we refer to the STScI DrizzlePac documentation. For each filter, we select combinations $[\text{final_pixfrac}, \text{final_scale} (\text{arcsec/pixel})]_{\text{filter}}$ of $[0.7, 0.066]_{\text{F105W}}$; $[0.7, 0.066]_{\text{F160W}}$ and $[0.7, 0.024]_{\text{F606W}}$. These values allow us to recover a high spatial resolution

¹ DrizzlePac is a product of the Space Telescope Science Institute (STScI), designed as a set of callable modules which can also be run as a single task: AstroDrizzle.

Table 2. Reference information on the properties of the targeted galaxy-absorber pairs. Spectroscopic quasar redshifts (z_{QSO}) are taken from the SIMBAD database. None of our targets are proximate absorbers ($\Delta v_{\text{QSO-abs}} < 5000 \text{ km s}^{-1}$). All SFRs are reported for a Chabrier IMF. Super-scripts give references to individual entries. Sub-scripts refer to the spectral line measurement on which the SFR was inferred. For Q 0124+0044 and Q 0139-0824 the impact parameters and SFRs refer to those derived based on the new identifications published in this work. Additionally for Q 0139-0824, we report the metallicity based on the absorption measurements in this work.

Quasar Field	z_{QSO}	z_{abs}	$\log_{10}(\text{N}_{\text{HI}})$ [$\log_{10}(\text{cm}^{-2})$]	$[\text{M}/\text{H}]_{\text{abs}}$		θ [arcsec]	b [kpc]	SFR [$M_{\odot} \text{ yr}^{-1}$]
				Tracer	[dex]			
Q0124+0044	3.84	2.2616 ^j	20.70 ± 0.15^j	Si II	-0.85 ± 0.15^j	1.3	10.9	$> 0.1^{(k)}$
Q0139-0824	3.01	2.6773 ^f	20.70 ± 0.15^f	Si II	-1.2 ± 0.2^k	1.6	13.0	$> 1.2^{(k)}$
Q0310+0055	3.78	3.1150 ^a	20.05 ± 0.05^a	—	—	3.8 ^a	29.6 ^a	$0.54 \pm 0.07_{\text{Ly}\alpha}^a$
Q1313+1441	1.89	1.7941 ^e	21.30 ± 0.10^e	Zn II	-0.70 ± 0.10^e	1.3 ^e	11.3 ^e	$> 0.3_{\text{Ly}\alpha}^e$
Q2059-0528	2.54	2.2101 ^b	21.00 ± 0.05^b	Zn II	-0.96 ± 0.06^b	$< 0.8^b$	$< 6.3^b$	$0.2_{\text{Ly}\alpha}^{b,e} < \text{SFR} < 1.4_{\text{H}\alpha}^l$
Q2239-2949	2.10	1.8250 ^{h,i}	19.84 ± 0.14^g	Si II	-0.67 ± 0.15^g	2.4 ^g	20.8 ^g	$0.07 \pm 0.01_{\text{Ly}\alpha}^g$
Q2247-6015	3.01	2.3288 ^{c,d}	20.62 ± 0.05^c	Zn II	-0.72 ± 0.05^m	3.1 ^{c,m}	26 ^{c,m}	$33_{-11}^{+40} \frac{e}{\text{H}\alpha}^m$
Q0338-0005	3.05	2.2298 ⁿ	21.09 ± 0.10^n	Zn II	-0.67 ± 0.18^e	0.49 ^o	4.1 ^o	$> 0.3^e$
Q2222-0946	2.93	2.35409 ⁿ	20.65 ± 0.05^p	Zn II	-0.46 ± 0.07^p	0.80 ^p	6.7 ^p	$13 \pm 1 \frac{e}{\text{H}\alpha}$
Q0918+1636	3.09	2.5832 ^q	20.96 ± 0.05^q	Zn II	-0.12 ± 0.05^p	2.0 ^f	16.4 ^f	$8 \pm 3 \frac{e}{\text{H}\alpha}$

NOTE—The table entry references are as follows: ^(a)Kashikawa et al. (2014), ^(b)Hartoog et al. (2015), ^(c)Bouché et al. (2012), ^(d)Lopez et al. (2002), ^(e)Krogager et al. (2017), ^(f)Wolfe et al. (2008), ^(g)Zafar et al. (2017), ^(h)Cappetta et al. (2010), ⁽ⁱ⁾Zafar et al. (2013b), ^(j)Berg et al. (2016), ^(k)This work, ^(l)Péroux et al. (2012), ^(m)Bouché et al. (2013), ⁽ⁿ⁾Bashir et al. (2019), ^(o)Krogager et al. (2012), ^(p)Fynbo et al. (2010), ^(q)Fynbo et al. (2011), ^(r)Fynbo et al. (2013)

in the drizzled images and ensure partial pixel-overlap to avoid image fragmentation. In addition, using the same drizzle settings for all objects in a given filter allows us to construct an empirical, non-parametric model of the quasar point spread function (PSF) (see Section 3.2).

2.3. Archival data

In this Section, we review the archival data extracted for individual quasar fields. For consistency, we convert Salpeter initial mass function (IMF) based star formation rates to the Chabrier IMF equivalent by applying a downwards correction factor of 1.8. For objects only observed in Ly α , we have implicitly assumed standard Case B recombination theory ($f_{\text{Ly}\alpha}/f_{\text{H}\alpha} = 8.7$) and escape fractions of unity to convert Ly α flux in the H α star formation rate indicator. For a summary of the quantities, we refer the reader to Table 2.

2.3.1. Q 0124 + 0044

This quasar was targeted in the large X-shooter legacy sample XQ-100 (López et al. 2016, Programme ID 189.A-0424). Having one of the most metal-rich DLAs in that sample (Berg et al. 2016), the X-shooter slit was placed at a single position angle at +130 deg East of North that serendipitously contained emission from the DLA host. In the 2-dimensional spectrum we detected

emission lines from Ly α and [O III] $\lambda 5007 \text{ \AA}$ offset spatially by 1.0–1.3 arcsec from the quasar trace. The Ly α emission is illustrated in Fig. 1. Integrating the line gives a line flux of $f(\text{Ly}\alpha) = (5.8 \pm 0.3) \times 10^{-18} \text{ erg cm}^{-2} \text{ s}^{-1}$ at $z_{\text{em}} = 2.2617$ after correction for Galactic reddening, and suggests a lower limit for the star-formation rate of $0.1 M_{\odot} \text{ yr}^{-1}$ based on a Chabrier IMF. Extinction corrections from the extinction maps of Schlafly & Finkbeiner (2011) are applied as follows, $A_{\text{F606W}} = 0.071$, $A_{\text{F105W}} = 0.022$ and $A_{\text{F160W}} = 0.014$ magnitudes.

2.3.2. Q 0139-0824

A tentative detection of Ly α emission was originally seen in VLT Visible Multi-Object Spectrograph (VLT/VIMOS, Le Fèvre et al. 2003) IFU data. Follow-up deeper observations with the VLT Focal Reducer and low dispersion Spectrograph (VLT/FORS1, Appenzeller et al. 1998) in Aug. and Sep. 2008 (Programme ID 081.A-0506) provided the proof of a detection of Ly α offset by ≈ 1.6 arcsec to the South-West from the trace of the quasar as illustrated in Fig. 2. During X-shooter observations aimed to identify additional emission lines besides Ly α (Programme ID 088.A-0378) the recorded seeing measured from the quasar PSF was 1.4–1.5 arcsec, and the chosen slit width was 1.2 arcsec was placed at a slit position angle of -98 deg. East of

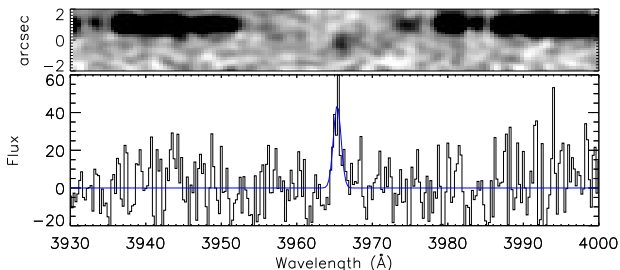


Figure 1. Section of the 2-dimensional X-shooter spectrum around the damped Ly α line towards Q0124+0044. The 2D spectrum has been smoothed by a Gaussian function with a FWHM of 3 pixels. At an impact parameter of ~ 1.3 arcsec from the quasar, Ly α emission is detected from the host galaxy. The best fit Gaussian function is overlaid on the 1D spectrum.

North. No additional emission lines were detected corresponding to the DLA redshift. We note that the slit position angles used for spectroscopy do not correspond exactly to the position angle of the galaxy measured directly in the *HST* images, as we did not at that time have sufficient spatial information to optimally orient the slit. Integrating the Ly α line gives a line flux of $f(\text{Ly}\alpha) = (2.2 \pm 0.2) \times 10^{-17} \text{ erg cm}^{-2} \text{ s}^{-1}$ at $z_{\text{em}} = 2.6791$ after correcting for Galactic extinction, and suggests a lower limit for the SFR of $0.7 M_{\odot} \text{ yr}^{-1}$ based on a Chabrier IMF. We adopt extinction correction factors at the position of the quasar, with retrieved values of $A_{\text{F606W}} = 0.068$, $A_{\text{F105W}} = 0.022$ and $A_{\text{F160W}} = 0.014$ magnitudes.

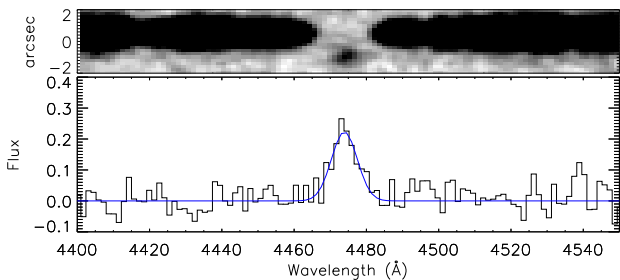


Figure 2. Section of the 2-dimensional FORS1 spectrum around the damped Ly α line towards Q0139-0824. The spectrum has been smoothed by a Gaussian function with a FWHM of 2 pixels. At an impact parameter of ~ 1.6 arcsec from the quasar, Ly α emission is detected from the host galaxy. The best fit Gaussian function is overlaid on the 1D spectrum.

2.3.3. Q 0310+0055

The absorbing galaxy in the Q0310+0055 field was confirmed as host with Subaru Faint Object Camera and Spectrograph (Subaru/FOCAS, Kashikawa et al. 2002) long-slit spectra (Kashikawa et al. 2014). With a 0.8 arcsec slit-width and a varying seeing of the order 0.5 - 1.0 arcsec, their observations may suffer from significant slit-losses. No dust-extinction- or slit-loss corrections were applied. The reported impact parameter is based on the peak position of extended Ly α emission.

We note that our PSF subtracted fields reveal two objects at lower impact parameters (blue circular apertures, see Figure 5). However, Kashikawa et al. (2014) do not detect Ly α emission at the absorber redshift, at lower impact parameters. Absent evidence for a physical connection, we therefore disregard them in the remainder of this work, but note that the detections may be related objects which do not emit in Ly α . Further investigation of the field must be done to ensure the nature of these objects. To accommodate the Subaru/FOCAS NB502 narrowband detection ($\text{mag}_{\text{NB502}} = 25.46 \pm 0.13$) (Kashikawa et al. 2014) in our stellar mass analysis (see Section 3.4) and mitigate the effects of the Ly α line-emission, we correct this magnitude for its associated narrow-band excess (NBe), reported as $\text{NBe} > 1.54$. This gives a NB continuum magnitude of $\text{NB502}_{\text{cont.}} = 27.00 \pm 0.13$. For the SED fits with LePhare (see Section 3.4), we then construct a simple box-shaped narrow-band filter at a central wavelength $\lambda_c = 5025 \text{ \AA}$ of width 60 \AA , based on the filter specification outlined on the Subaru homepage.² In addition, we also include their B- and V-band non-detections (25.32 and 25.50 magnitudes, respectively) reported as the 3σ limiting magnitudes in 2 arcsec apertures at the position of the narrow-band detection. Finally, all magnitudes (measurements and limits) are corrected for Galactic extinction prior to entering the LePhare setup. Individual values are as follows: $A_{\text{B}} = 0.414$, $A_{\text{NB502}} = 0.343$, $A_{\text{V}} = 0.305$, $A_{\text{F105W}} = 0.082$, $A_{\text{F160W}} = 0.052$.

2.3.4. Q 1313+1441

The galaxy host of the absorber in Q1313+1441 was confirmed by Krogager et al. (2017) based on Ly α emission in the trough of the damped Ly α absorption profile. The authors report an impact parameter based on X-Shooter slit-spectra triangulation. The Ly α measurement may suffer from slit-losses and dust-extinction, which is why the star formation rate is presented as a conservative lower limit. Based on detections in differ-

² <https://www.naoj.org/Observing/Instruments/FOCAS/camera/filters.htm>

ent slit positions, Krogager et al. (2017), suggest that the emission arise in a galaxy group environment.

2.3.5. *Q 2059–0528*

This object was observed by Hartoog et al. (2015), following the 3 slit position angle observational strategy of other X-Shooter campaigns (Fynbo et al. 2010; Krogager et al. 2017). This allowed simultaneous measurements in absorption and emission. Emission was detected at all PAs, suggesting an object at low impact parameter (< 0.75 arcsec, corresponding to an impact parameter of < 6.3 kpc) in the overlapping spectral region. With Ly α detections in all slit positions, the slit triangulation only yields an upper limit on the impact parameter. A 3σ detection of Ly α in emission at the trough of the damped Ly α absorption profile is found in a stacked spectrum. Converting the Ly α measurement to H α gives a lower bound on the SFR. The measurement may suffer from slit-losses and dust-extinction. The 1D quasar spectrum follows the shape of a dereddened composite quasar spectrum (Vanden Berk et al. 2001), hence the continuum extinction is not significant along the quasar line-of-sight. That does not exclude that galaxy counterpart by itself could have an amount of dust that affects the detected emission lines. Péroux et al. (2012) used SINFONI IFU observations to search the quasar field for the host galaxy in H α emission. This yielded an H α non-detection, which translates into a robust upper limit on the SFR. We adopt extinction correction factors of $A_{F606W} = 0.104$, $A_{F105W} = 0.033$, and $A_{F160W} = 0.021$ magnitudes.

2.3.6. *Q 2239–2949*

The absorber in quasar field Q 2239–2949 (Zafar et al. 2013b,a) and its host were investigated by Zafar et al. (2017). The absorber is a sub-DLA, and no ionization corrections were applied. However, the authors report a [Si/Fe] ratio which suggests that a combination of ionization- and dust effects are present. Observations revealed Ly α in emission at z_{abs} , offset from the spatial position of the absorber by an impact parameter measured from X-Shooter slit triangulation. Converting the Ly α measurement to H α gives a dust-uncorrected SFR with propagated flux-measurement errors, as reported in Table 2. Based on slit width and seeing, the authors quantify the slit-loss corrections to be less than a factor of 2. With a maximum correction factor of 20 to account for both dust and slit losses, they estimate an upper limit on the SFR of $\sim 1.4 M_{\odot} \text{ yr}^{-1}$. We adopt extinction correction factors of $A_{F606W} = 0.043$, $A_{F105W} = 0.013$, and $A_{F160W} = 0.009$ magnitudes.

2.3.7. *Q 2247–6015*

This quasar absorber was first analysed by Lopez et al. (2002) with a high S/N, high resolution UVES spectrum. Bouché et al. (2012, 2013) conducted comprehensive followup observations of the quasar field (alternative name; HE 2243–60) to look for the absorbing galaxy in emission using SINFONI IFU data. Not affected by slit-losses, the authors report a dust-corrected H α star formation rate. Their analysis also includes a re-analysis of the absorber, combining archival observations to achieve deeper observations. We therefore choose to report emission and absorption properties based on Bouché et al. (2012, 2013). We adopt extinction correction factors of $A_{F606W} = 0.047$, $A_{F105W} = 0.015$, and $A_{F160W} = 0.009$ magnitudes.

2.3.8. *Q 0338–0005*

This quasar has a DLA and a sub-DLA reported along its line of sight (Zafar et al. 2013a). Previously, Noterdaeme et al. (2009b) reported the H I column density of both absorbers and Bashir et al. (2019) re-determined the column densities using the high resolution UVES spectrum. The Ly α emission from the DLA host-galaxy is reported by Krogager et al. (2012) and was confirmed in the UVES spectrum by Bashir et al. (2019). Krogager et al. (2012) reported the galaxy at an impact parameter of $b = 0.49 \pm 0.13$ arcsec. From the measured Ly α flux of $f(\text{Ly}\alpha) = 1.3 \pm 0.2 \times 10^{-17} \text{ erg s}^{-1} \text{ cm}^{-2}$, Krogager et al. (2017) report a lower limit of $\text{SFR}(\text{Ly}\alpha) > 0.3 M_{\odot} \text{ yr}^{-1}$. In Fig. 3 we illustrate a tentative candidate counterpart detection, which is only visible after subtraction of the PSF, located 0.39 ± 0.02 arcsec from the quasar line of sight.

2.3.9. *Q 2222–0946*

The absorber towards Q 2222–0946 was reported by Noterdaeme et al. (2009a) and its host galaxy was detected by Fynbo et al. (2010) using the X-shooter triangulation strategy. The DLA was found to be at an impact parameter of 0.8 ± 0.1 arcsec (6 kpc at $z_{\text{abs}} = 2.354$), at a predicted position angle of 40 deg based on X-shooter slit triangulation. This was confirmed by Krogager et al. (2013) who identified the target at impact parameter 0.74 arcsec corresponding to 6.3 kpc at $z = 2.354$ at PA = 26.45 deg East of North. Ly α , [O II], [O III], and H α emission lines have been detected in the X-shooter spectrum (Fynbo et al. 2010). The SFR based on H α is calculated to be $13 \pm 1 M_{\odot} \text{ yr}^{-1}$ (Krogager et al. 2017). For the F606W, F105W and F160W magnitudes we adopt extinction correction factors of 0.103, 0.032 and 0.021 magnitudes, respectively.

2.3.10. *Q 0918+1636*

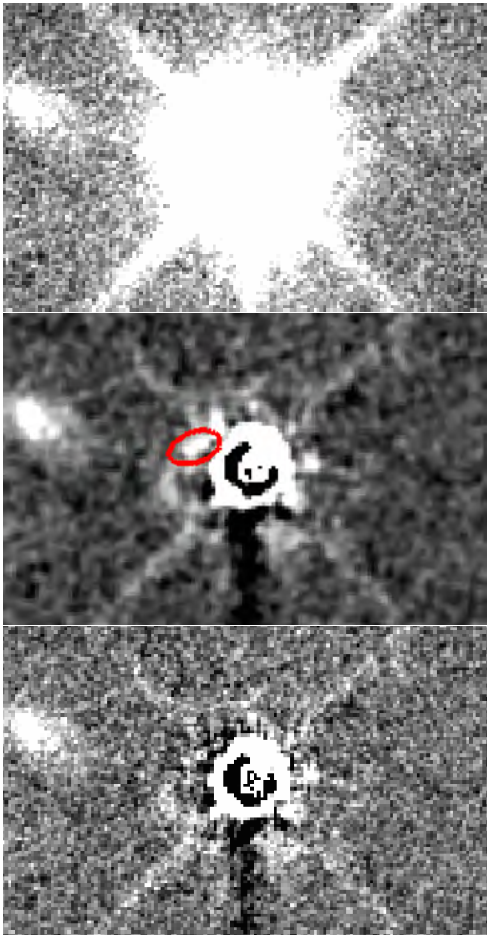


Figure 3. Tentative counterpart detection in the Q0338-0005 field. *Top:* A zoom-in of the quasar vicinity. *Centre:* Quasar PSF subtracted residuals, revealing tentative counterpart (red ellipsoid) at low projected separation. *Bottom:* Residual image after simultaneous fitting of quasar PSF and tentative DLA galaxy counterpart.

The quasar absorber in emission was detected under the X-shooter metal-rich DLA triangulation strategy method (Fynbo et al. 2011). Fynbo et al. (2011) reported emission from [O II] and [O III] and H₂ molecules in absorption are also detected. Later, Fynbo et al. (2013) detected H α and H β emission lines and using the *HST* data, performed the SED fit. Fynbo et al. (2013) find the DLA galaxy for $z_{abs} = 2.583$ absorber at impact parameter 1.98 ± 0.02 arcsec from quasar (proper distance of 16.2 kpc), at position angle -115 deg East of North. We confirm their finding. Second absorber at $z_{abs} = 2.412$, has a candidate detection located at a position angle of ~ 130 deg East of North, at impact parameter consistent with zero, with a conservative upper

limit of 0.25 arcsec corresponding to 2.0 kpc, based on a $\sim 3.5\sigma$ detection in a co-added 2D spectrum. We cannot confirm such an object with our quasar point spread function (qPSF) subtraction technique as detailed in Section 3.2. In addition to the re-reduced *HST* images and their associated magnitudes, we also include the SDSS u , g and Nordic Optical Telescope NOTCam (Abbott et al. 2000) NOTCam/ K_s band photometry reported in Fynbo et al. (2013), which have already been corrected for Galactic extinction. We also apply Galactic extinction corrections to the *HST* magnitudes based on the Schlafly & Finkbeiner (2011) re-calibrated extinction maps at the position of the quasar. For the F606W, F105W and F160W magnitudes we adopt extinction correction factors of 0.058, 0.018 and 0.012 magnitudes, respectively.

3. RESULTS

3.1. Absorption analysis of the Q0139-0824 DLA

The DLA in Q0139-0824 has a reported absorption metallicity of $[\text{Si}/\text{H}]_{abs} = -1.15 \pm 0.15$ dex (Krogager et al. 2012; Hartoog et al. 2015). This value emerged based on unpublished measurements, whereas an extensive literature search only returned a published iron abundance $[\text{Fe}/\text{H}]_{abs} = -1.62 \pm 0.02$, and a minimally depleted metallicity of $[\text{M}/\text{H}]_{abs} = -1.27 \pm 0.19$, with respect to solar (Wolfe et al. 2008). Despite marginally consistent measurements to within their respective uncertainties, the discrepancy warrants a re-examination to test whether the difference is systematic or driven by the uncertainties. We therefore use existing X-shooter (Vernet et al. 2011) data (programme ID 088.A-0378; PI: Christensen) and perform our own absorption analysis to determine the gas-phase abundance independently.

The quasar was observed with X-Shooter on 7. Jan 2012 with an integration time of 2×1800 s on target, with the target nodded along the slit. Slit widths of 1.3 arcsec and 1.2 arcsec were chosen for the UVB and VIS+NIR arms, respectively. The data were reduced using standard X-Shooter *esorex* scripts version 2.9.3 (Modigliani et al. 2010), and flux calibrated using observations of the spectrophotometric standard star, Feige 110, observed on the same night. Data from the UVB and VIS arms were reduced in stare mode, and 1D spectra were optimally extracted using custom routines and combined by weighting each spectrum with the average signal to noise ratio. To compute an accurate value for the instrument resolution, even though seeing during the observations was larger than the slit width, we measured spectral resolutions from telluric absorption lines in the quasar spectra to be $\mathcal{R}_{VIS} = 42$ km s⁻¹ and $\mathcal{R}_{NIR} = 70$ km s⁻¹. With a lack of telluric absorption

features in the UVB arm, we scale its nominal resolution to the ratio of observed-to-nominal resolution in the visual arm, giving $\mathcal{R}_{\text{UVB}} = 70 \text{ km s}^{-1}$, roughly consistent with $R = 4100$ reported for X-shooters UVB arm at a slit width of 1.3 arcsec (Vernet et al. 2011).

To measure the gas-phase metallicity of the absorber, we fit Voigt profiles to each velocity component of well-defined low-ionization absorption lines free of telluric contamination in the reduced 1D spectra. We use the python package VOIGTFIT (Krogager 2018), which uses line-lists with updated oscillator strengths (Cashman et al. 2017), and has the added advantage of fitting the continuum together with the line parameters. We select a Chebyshev polynomial of order two as the continuum function, which is fitted around the spectral region covering each line transition.

At the modest spectral resolution, we cannot resolve intrinsically narrow components originating in individual clouds and which may cause line asymmetries. We therefore resort to fit the resolved profile with a conservative two-component velocity structure after binning the spectrum by a factor of two (see Figure 4). We fit all lines simultaneously, tying the broadening-parameter and the redshift for each velocity component. Column densities for each velocity component and the total ion column are reported in Table 3. We also derive a neutral hydrogen column density consistent with the results presented in Wolfe et al. (2008). We, therefore, fix the neutral hydrogen column density to the reported value $\log_{10}[N_{\text{HI}} (\text{cm}^{-2})] = 20.70 \pm 0.15$ and measure gas-phase metallicities of $[\text{Al}/\text{H}] = -1.16 \pm 0.33$, $[\text{Si}/\text{H}] = -1.24 \pm 0.20$ and $[\text{Fe}/\text{H}] = -1.45 \pm 0.16$.

Less refractory elements such as S and Zn are less depleted onto dust grains and are thus more suitable tracers of the gas-phase metallicity. The sulphur lines $\text{S II } \lambda\lambda 1250, 1253, 1259\text{\AA}$ are, however, blended with the intermediate $\text{Ly}\alpha$ forest, and $\text{Zn II } \lambda\lambda 2026, 2062\text{\AA}$ show a different velocity profile which may be explained by proximate tellurics or a blend with an intervening component. However, we only identify an intervening C IV absorber at $z_{\text{abs}} = 2.36$, and a possible Mg II absorber at $z_{\text{abs}} = 2.23$ - none of which will produce strong lines at the position of the Zn II lines. We therefore report the metallicity of the absorbing gas as $[\text{Si}/\text{H}]$. This result is based on two transitions; the mildly saturated Si II $\lambda 1526\text{\AA}$ line which reveals velocity-structure and broadening-parameters, and the Si II $\lambda 1808\text{\AA}$ weak line transition to constrain the strength (see Figure 4).

3.2. Quasar point spread function subtraction

To detect the faint stellar continuum of the absorbing galaxy and to search for objects hiding in the bright

Table 3. Absorption analysis of the low-ionization line-complexes associated with the Q0139-0824 DLA at $z_{\text{sys}} = 2.6775$.

Complex	b	$\log_{10}[N (\text{cm}^{-2})]$
$[\lambda] = \text{\AA}, [v] = \text{km s}^{-1}$	$[\text{km s}^{-1}]$	
Al II $\lambda 1670$		
$v_1 = 0 \pm 1$	32 ± 2	13.40 ± 0.06
$v_2 = 104 \pm 2$	11 ± 1	13.85 ± 0.40
Total Column:		13.99 ± 0.29
Fe II $\lambda 1608, 2344, 2374, 2382$		
$v_1 = 0 \pm 1$	32 ± 2	14.51 ± 0.03
$v_2 = 104 \pm 2$	11 ± 1	14.39 ± 0.07
Total Column:		14.76 ± 0.04
Si II $\lambda 1526, 1808$		
$v_1 = 0 \pm 1$	32 ± 2	14.71 ± 0.14
$v_2 = 104 \pm 2$	11 ± 1	14.59 ± 0.20
Total Column:		14.97 ± 0.12

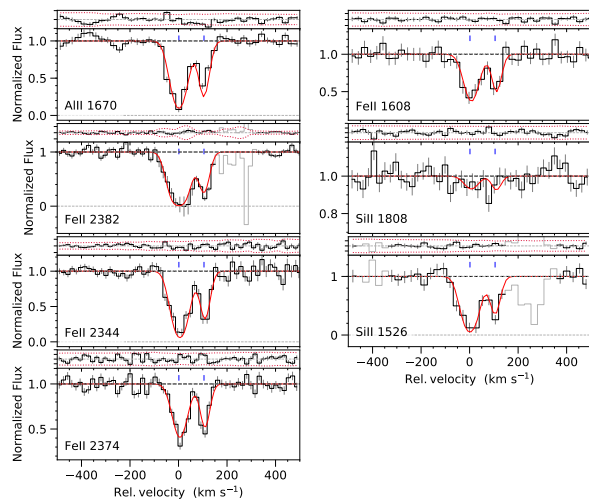


Figure 4. Voigt profile fits to the low-ionisation metal absorption lines of the $z = 2.6775$ DLA towards Q0139-0824. Each panel is subdivided into two sub-panels showing the velocity components of a single transition (*bottom*), and the fit residuals (*top*). The black line represents the observed spectrum, with its uncertainties depicted by grey vertical bars in each spectral bin. Grey regions without uncertainties are masked out in the fit. The red curve represents the best fit.

qPSF, we must isolate the flux from the quasar and subtract it from each image. Traditionally for *HST* images,

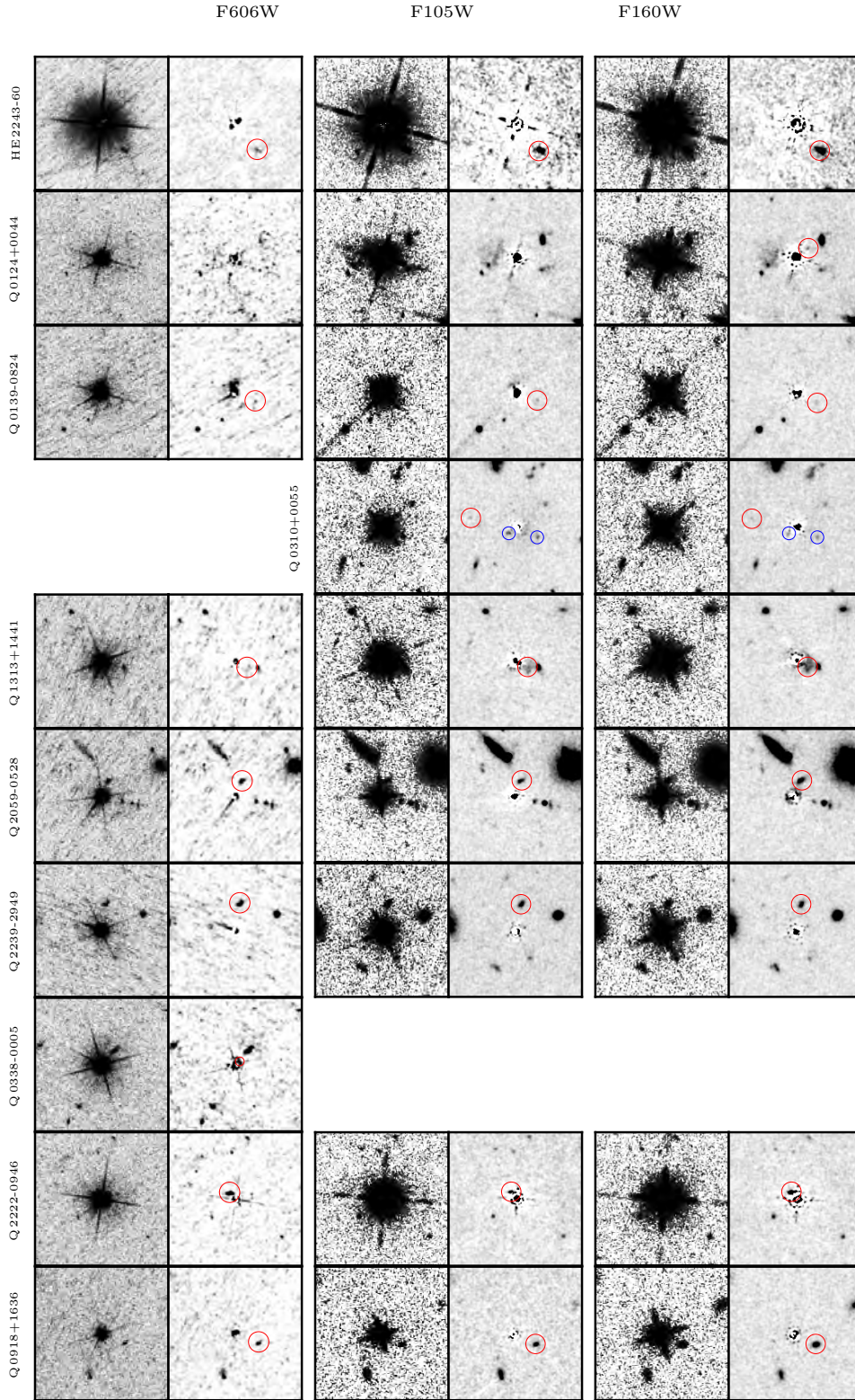


Figure 5. Mosaic of 11×11 arcsec quasar fields. Rows label individual fields. Column doublets label *HST* filters. Each doublet displays the science image (*left*) and qPSF subtracted residual image (*right*) with confirmed detections (red circle). Each panel is aligned North up East left. For clarity, science images are displayed with a histogram equalization to enhance faint structures, and residual images have been Gaussian smoothed with a fixed smoothing-length of 0.06 arcsec.

a PSF is artificially created with TINYTIM, or empirically modelled from bright, unsaturated stars in the same exposure (e.g. Kulkarni et al. 2000; Krogager et al. 2013; Fynbo et al. 2013). The former method is noiseless, can be constructed for the position of the quasar on the detector, and captures the profile of the outer PSF wings. However, the model is limited by the details in its construction; by the accuracy of the recorded telescope aberrations; and can produce unsatisfactory models for saturated objects (e.g. Krogager et al. 2013). The latter method takes advantage of high S/N and is observed simultaneous to the quasar, which mitigates temporal variations. However, it is sensitive to the position of the bright star on the detector plane; to telescope aberrations; is often unable to model the extended PSF wings as the out regions are dominated by noise in the sky background; is limited by the number of suitable stars in the field; and there may be a colour mismatch between the object of interest (on our case, the quasar) and stars (Warren et al. 2001).

Since our *HST* programme targeted multiple quasar fields with the same observing strategy, and since the final data products for each filter are drizzled with identical settings (see Section 2.2), the aforementioned caveats can be mitigated by modeling the qPSF from the targeted quasars themselves (e.g. Warren et al. 2001; Augustin et al. 2018). To each i -th quasar, we therefore proceed to construct empirical, non-parametric models of qPSF $_i$ from the median combined stack of all remaining n -th quasar PSFs after rebinning each to a $4\times$ finer grid, and recentering each of these on their respective quasar centroid. Finally, our empirically constructed qPSF $_i$ models are iteratively fitted to their respective quasar, and subtracted from the drizzled science image to search the field for faint stellar continuum emission from the absorber host galaxy (see Figure 5 and Section 3.3).

In the field of Q 0139–0824, we identify a bright object in the F606W band at low impact parameter. This object clearly overlaps with the quasar PSF, but is unidentified in the other bands. We therefore revisited the quasar spectrum to see whether this object has an absorber counterpart. The spectrum reveals a weak absorber at a redshift $z_{\text{abs}} = 2.233$, which we hypothesize is the counterpart of the bright object. However, the absorption lines are too weak to be compatible with a damped H I absorber, and we therefore leave it to be pursued in future work.

The PSF-subtracted Q 2059–0528 field reveals multiple objects, all of which have larger impact parameters than the limit ($b < 6.3$ kpc) reported in Hartoog et al. (2015). We note, however, that this limit is based on the

assumption that the individual Ly α signals in the three slits are detecting the same counterpart. Relaxing this assumption, we note that their reported detection in the PA = -60 deg slit is the only detection formally above 3σ significance. We therefore identify the bright object immediately North-West of the quasar as the most likely source of the Ly α emission, and as a candidate counterpart to the DLA, and based on that report our results in Table 4. Such a configuration with several components seen in emission appears similar to the DLA host galaxy system towards Q2206–1958, which was shown to be in an active stage of merger (Møller et al. 2002; Weatherley et al. 2005).

3.3. Modelling surface brightness profiles with GALFIT

Having identified the emission counterparts in each quasar-subtracted field, we employ GALFIT (Peng et al. 2002) to model their surface brightness profiles. Here, we do so by iteratively adding Sérsic components which GALFIT implicitly convolve with the PSF-model, and which are fitted simultaneously with the quasar until the galaxy emission is fully captured.

GALFIT has been used to derive structural parameters and magnitudes for individual objects in the past (e.g. Krogager et al. 2013; Fynbo et al. 2013; Augustin et al. 2018). We here make an effort to outline and emphasize certain aspects of the fitting procedure which differ for our particular science case, relative to standard retrieval of parameters for a galaxy on a flat sky background.

- Its brightness causes the quasar PSF profile to extend far into the field. It is therefore essential to use a large PSF model, capable of subtracting the flux in the PSF wings. If the PSF does not account for this, GALFIT will overestimate the sky background.
- The large PSF model necessitates a large fitting region. We found that a fitting region of 800×800 pixels for a pixel scale of 0.067 arcsec pixel $^{-1}$ was needed to ensure robust quasar magnitudes matching known SDSS photometry.
- The Sérsic function associates higher (central) light concentrations with larger extended wings. Any over/under estimation of either the sky background and/or the quasar PSF wing will therefore be compensated for by (wrongfully) adjusting the Sérsic index. This will minimize the χ^2 statistic at the expense of unrealistically large concentrations. It is therefore essential to fit the galaxy and quasar simultaneously, and determine the background independently. This is particularly important as our objects lie at small impact parameters,

and recognizing the brightness contrast between the quasar and the galaxy, a small change in the quasar magnitude may generate large differences in final galaxy parameter estimates.

We, therefore, fix the sky value to independent measurements determined from the mean of the pixel counts in sky regions free of sources and hot pixels. The zero-point (ZP) for each filter was calculated with the PHOTPLAM and the PHOTFLAM FITS header keywords, with values of $ZP_{F606W} = 26.104$; $ZP_{F105W} = 26.270$; and $ZP_{F160W} = 25.947$. Finally, we input the science image in the recommended units of counts. This is particularly relevant for our science case, as the brightness contrast between the quasar and the galaxy causes pixel values to span a large dynamic range.

We find that adopting a single Sérsic component does not capture the clumpy light distribution observed in many of the objects, and indeed results in large residuals. This behaviour is also reflected in the GALFIT solution, which under such conditions (or for faint objects) becomes unstable to perturbations in initial parameter guesses. We found that iteratively adding components which collectively capture the effective light distribution of the source stabilizes the parameter range within physically acceptable Sérsic indices ($0.5 \leq n \leq 8$) and effective radii $0.2 \leq r_{\text{eff}} [\text{pixels}] \leq 20$, although the international distribution of the parameters are sensitive to the initial guesses giving near-identical χ^2 -statistics for different combinations.

Previous studies, often motivated by observational considerations, choose to report structural parameters and morphology based on the band with the highest resolution. Here, we attempt a physically motivated approach, and report morphologies based on the reddest (F160W) band in order to capture the main stellar component. We then fix the morphology in the remaining bands to that derived in F160W, appropriately scaled and rotated to the resolution, pixel sampling and orientation of individual frames.

In order to systematically analyze and compare objects fitted with a single Sérsic profile to those that require multiple components, we therefore take a conservative approach and report non-parametric half-light radii ($r_{1/2}$) calculated from growth curves originating at the luminosity centre of the final galaxy-model; and total (summed over individual Sérsic components) magnitudes (mag_{AB}). For $r_{1/2}$ the final uncertainty reflects a weighted sum of the relative uncertainties from each component contributing to the model. We estimate the magnitude error directly from the quasar+galaxy subtracted residual image as $\Delta F = \sqrt{\sum_{i \in A} \sigma_{\text{tot},i}^2}$, where A

is the non-masked pixels in a circular aperture at the position of the galaxy-model luminosity centre with radius $5 \times r_{1/2}$, and $\sigma_{\text{tot},i}$ is the flux count in pixel i . These results are recorded in Table 4.

3.4. Modelling the spectral energy distribution

We determine the stellar mass content ($M_{\star}(M_{\odot})$) in each of the absorbing galaxies by fixing the redshift to the spectroscopic value, and iteratively match SED templates to broad-band magnitudes corrected for Galactic extinction. We use standard Bruzual & Charlot (2003, BC03) simple stellar population (SSP) spectral templates based on Padova 1994 stellar evolutionary tracks and a Chabrier (2003) IMF. We employ the LePhare code (Arnouts et al. 1999; Ilbert et al. 2006), which evaluates the template fit by minimising the χ^2 -statistic across a user pre-defined grid of parameters. Our grid encompasses (i) ages limited to be in the range 0 – 4 Gyrs which corresponds to the age of the Universe at the lowest absorption-redshift in our sample; (ii) e-folding time-scales in the range 0.1 - 30 Gyrs; (iii) a Calzetti et al. (2000) attenuation-curve as we are probing redshifts around the peak of cosmic star-formation; (iv) a set of intrinsic reddening, E_{B-V} in the range 0 - 0.3, sampled in steps of 0.05 and extended if needed to ensure that the preferred E_{B-V} value is associated with χ^2 -minima rather than a grid-boundary. The resulting SED fits of the absorbing galaxies are shown in Figure 6. The stellar masses and their associated measurement uncertainty are determined based on the median, 16th- and 84th percentile from a maximum likelihood analysis of the SED-fits χ^2 distribution, and reported in Table 4. Best fit SFRs and reddenings are reported in Table 5.

In the case of Q 2222-0946, we also correct the F160W broadband magnitude for a 33% nebular emission-line contribution, as determined in Krogager et al. (2013).

4. DISCUSSION

Our sample lies at a mean redshift of $z_{\text{abs}} = 2.3$, with a sample standard deviation of 0.4. In Figure 7 we show how our sample of absorption selected galaxies falls on the established mass-size relation (*left*), and the star-forming main sequence (*right*), both constructed on luminosity-selections and matching our sample in redshift.

For the mass-size relation, we show the $z = 2.25$ relations for early (red)- and late (blue) -type galaxies for the 3D-*HST*-CANDELS survey reported in van der Wel et al. (2014). The relations are based on measurements derived for a Chabrier initial mass function (Chabrier 2003) (and are therefore directly comparable to our results); have size-measurements based on effective radii

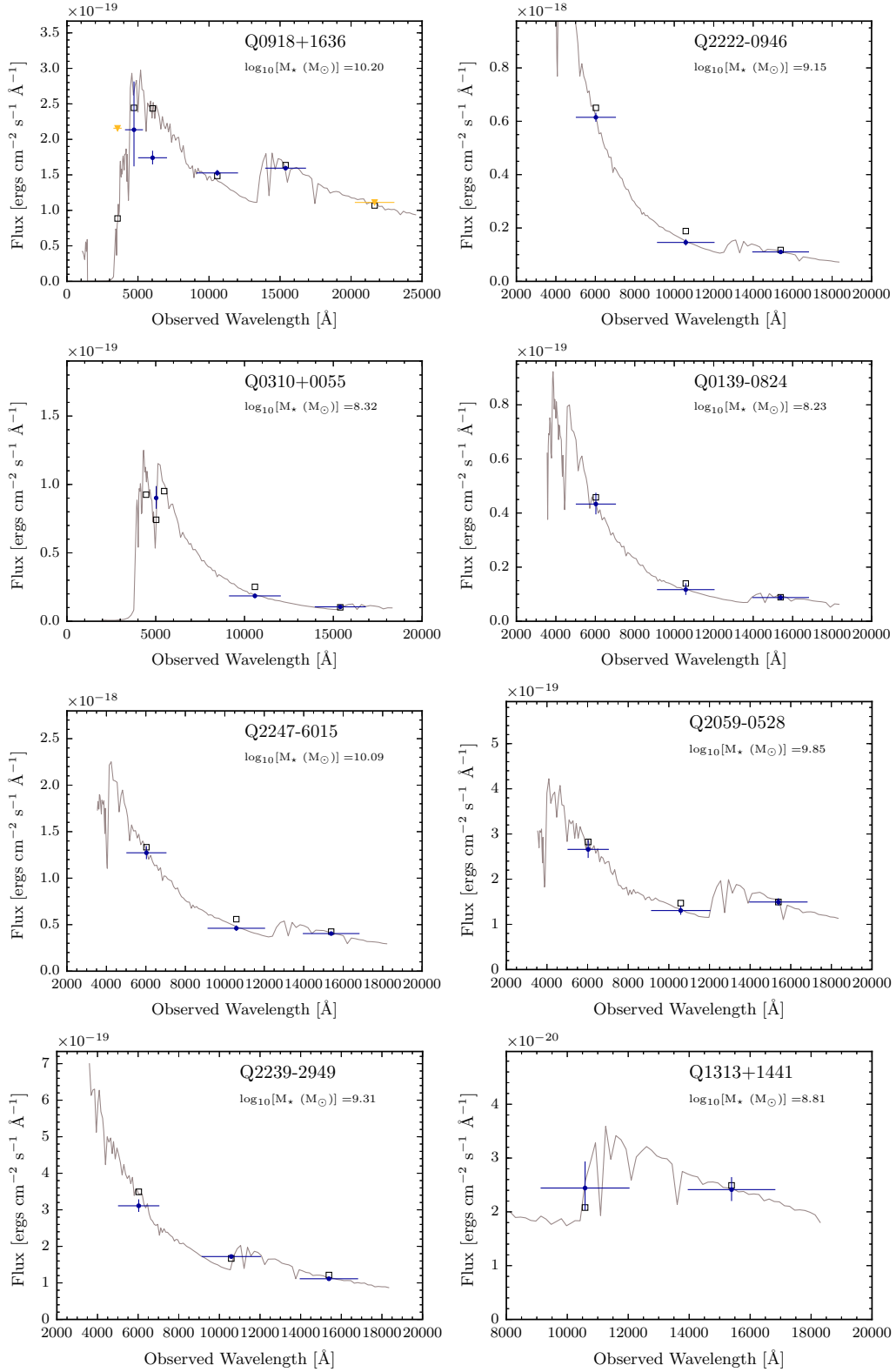


Figure 6. Spectral energy distribution fits minimising the χ^2 -statistic for each absorption-selected galaxy. Blue (yellow) filled symbols refer to included measurements (limits), with vertical and horizontal error-bars indicating magnitude uncertainties and the *FWHM* of each filter, respectively. Grey empty squares refer to the predicted transmission-weighted flux in each filter, calculated from the best-fit model. Each panel text displays the Object name and resulting stellar mass.

Table 4. Results of GALFIT and LePhare modelling of absorber counterparts.

Quasar Field	P.A.	θ	b	$r_{1/2}$	mag _{F606W}	mag _{F105W}	mag _{F160W}	$\log_{10}(M_{\star})$
	[Deg.]	[arcsec]	[kpc]	[kpc]	[AB]	[AB]	[AB]	[$\log_{10}(M_{\odot})$]
Q0124+0044	311 ± 1	1.25 ± 0.04	10.5 ± 0.3	0.4 ± 3.1	—	—	26.9 ± 0.2	—
Q0139-0824	244.6 ± 0.7	1.83 ± 0.03	14.8 ± 0.2	0.4 ± 1.5	27.2 ± 0.1	27.3 ± 0.2	26.8 ± 0.1	$8.2^{+0.2}_{-0.2}$
Q0310+0055	77.9 ± 0.5	3.77 ± 0.04	29.4 ± 0.3	0.5 ± 0.9	—	26.9 ± 0.1	26.7 ± 0.1	$8.3^{+0.3}_{-0.3}$
Q1313+1441	241 ± 2	1.20 ± 0.04	10.3 ± 0.4	2.2 ± 0.7	—	26.5 ± 0.2	25.7 ± 0.1	$8.8^{+0.3}_{-0.8}$
Q2059-0528	334.8 ± 0.3	1.43 ± 0.01	12.05 ± 0.09	1.7 ± 0.3	25.23 ± 0.08	24.71 ± 0.08	23.74 ± 0.06	$9.9^{+0.6}_{-0.7}$
Q2239-2949	348.8 ± 0.7	2.31 ± 0.03	19.8 ± 0.3	1.5 ± 0.4	25.00 ± 0.06	24.39 ± 0.03	24.05 ± 0.03	$9.31^{+0.06}_{-0.07}$
Q2247-6015	222.3 ± 0.3	2.99 ± 0.02	25.0 ± 0.2	2.6 ± 0.3	23.48 ± 0.06	23.33 ± 0.07	22.65 ± 0.04	$10.1^{+0.8}_{-0.8}$
Q0338-0005	305 ± 2	0.39 ± 0.02	3.3 ± 0.2	$1.5^* \pm 0.1$	$25.7^* \pm 0.1$	—	—	—
Q2222-0946	41.1 ± 0.2	0.74 ± 0.01	6.17 ± 0.02	0.52 ± 0.03	24.32 ± 0.03	24.59 ± 0.09	23.63 ± 0.06	$9.15^{+0.09}_{-0.10}$
Q0918+1636	245.78 ± 0.06	2.00 ± 0.01	16.37 ± 0.02	0.81 ± 0.03	25.65 ± 0.06	24.53 ± 0.03	23.66 ± 0.01	$10.2^{+0.1}_{-0.2}$

NOTE—The Position Angle (P.A.) is measured in degrees East of North. The spectroscopically inferred projected angular separation (θ) and associated impact parameter (b) reported in Table 2 have here been replaced the values measured directly in the *HST* images. Half-light radii, $r_{1/2}$, have been converted from image pixels to physical units of kpc with the drizzled pixel-scale and absorber redshift for the assumed cosmology. *The effective radius and the associated F606W magnitude of the object identified as the counterpart in the Q0338-0005 field required highly fine-tuned GALFIT setup, and these values should therefore be treated with caution.

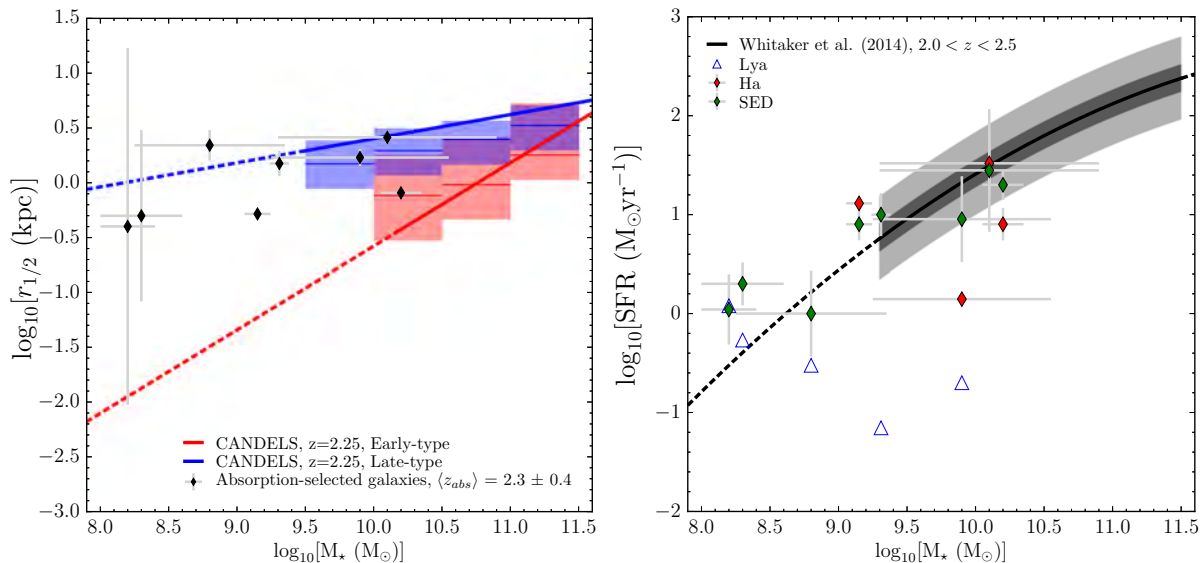


Figure 7. Our $z \sim 2.3$ *HST* sample of absorption selected galaxies placed on scaling relations derived from luminosity-selected samples. *Left:* the mass-size relation for early-type (red) and late-type (blue) galaxies. Lines reflect the relations derived based on effective radii measured along the major axis, with dashed segments emphasizing extrapolation beyond the reported completeness limits. Mass-binned statistics depict the mean and 1σ intrinsic scatter in circularized radii. *Right:* the main sequence of star forming galaxies (black line), with 1σ and 3σ intrinsic scatter as shaded regions, and extrapolation emphasized as dashed segment.

Table 5. LePhare SFR information.

Quasar Field	E_{B-V}	SFR
		$[M_{\odot} \text{ yr}^{-1}]$
Q0124+0044	–	–
Q0139–0824	0.00	1.1 ± 0.9
Q0310+0055	0.00	2 ± 1
Q1313+1441	0.05	1 ± 1
Q2059–0528	0.15	9 ± 9
Q2239–2949	0.15	10 ± 5
Q2247–6015	0.15	28 ± 40
Q0338–0005	–	–
Q2222–0946	0.00	8 ± 3
Q0918+1636	0.25	20 ± 7

NOTE—The reported values correspond to those that minimize the χ^2 statistic in association with deriving the stellar mass.

along the major axis; and are plotted as dashed lines for extrapolation below the reported completeness limits. Also shown, are the stellar-mass binned statistics (mean and 1σ dispersion) of circularised r_{eff} , which in definition more closely resemble our non-parametric measurements of the half-light radii.

Albeit limited by sample size and individual measurement uncertainties, our absorption-selected sample lies on the luminosity-selected relations, and displays a marginal preference to late-type galaxy morphologies. This result is consistent with the notion that identifying galaxies in absorption preferentially selects less evolved, gas-rich galaxies. In addition, it is remarkable that $\sim 50\%$ of our sample has stellar masses below the formal completeness limit for luminosity-selected surveys. At face value, this is direct evidence that an absorption selection extends the parameter space towards lower masses at the faint end of luminosity functions. However, it is encouraging to see that even towards the low mass end, our galaxies fall on the extrapolated luminosity-selected mass-size relation.

Having shown that our galaxies have normal sizes for the derived stellar mass based on the extrapolated relations, we now seek how they lie on the plane spanned by stellar mass and star formation rate. As a reference, we plot the polynomial parametrisation of the main sequence of star-formation for luminosity-selected galaxies at $z \sim 2 - 2.5$ reported in Whitaker et al. (2014), with the associated 1σ - and 3σ scatter in the relation based on the intrinsic dispersion of $\sigma_{\text{intrinsic}} = 0.14$ reported in

Whitaker et al. (2015). For our sample, we have incomplete data from three different SFR tracers; lower limits from Ly α ; recombination-line measurements of H α which trace the near-instantaneous SFR on time-scales of ~ 10 Myrs; and SED-based values from LePhare retrieved in the process of deriving stellar masses (see Section 3.4), and constructed to trace the ongoing SFR (see the LePhare package’s documentation). To form a complete census, we plot all the SFR-tracers for each object.

The results of the various diagnostics can be summarised as follows. For objects with SFR measurements in Ly α and either SED or H α , Ly α systematically provide the lowest SFR measurements, in perfect agreement with our expectations based on its resonance nature and effects on inferred SFRs. Therefore, SFRs based on Ly α should only be treated as lower limits. In addition, and considering the limited number of photometric bands available to perform our SED fits, we find a remarkable agreement between H α and SED based SFRs when these are available. Indeed, these results suggest that our galaxies fall perfectly on the predicted main sequence of star forming galaxies.

In the context of absorbing galaxies in general, the fact that our sample so finely trace known scaling relations is interesting in particular, considering their sub-main sequence star forming analogues at $z \sim 0.7$ (Møller et al. 2018; Kanekar et al. 2018; Rhodin et al. 2018). Unfortunately, our $z \sim 2.3$ *HST* sample does not capture the high end of stellar mass range covered by the low redshift sample and luminosity-selected relations. This inhibits us from discriminating whether sub-main-sequence star-formation is inherent to the selection; related to galaxy evolution; or related to a typical stellar mass-scale $\log_{10}[M_{\star} (M_{\odot})] \gtrsim 10$.

5. CONCLUSIONS

In this work, we have performed a systematic *HST* imaging analysis of a sample of $z \sim 2 - 3$ high column density HI absorption selected galaxies. The sample consisted of seven new and three re-analysed quasar fields, homogeneously selected based on the presence of spectroscopically confirmed galaxy counterparts to metal-rich H I absorbers in the quasar spectra. We reported on the previously un-published absorption-line analysis of the DLA towards Q0139–0824; and the spectroscopic X-shooter and FORS1 detections of the counterparts towards Q0139–0824 and Q0124+0044. We report on a new photometric F606W detection of the counterpart in the re-analysed quasar field Q0338–0005.

After careful removal of the quasar PSFs, each absorbing galaxy was modelled with Sersic-components to describe the light distribution. The photometric detection

of the galaxy counterpart allowed us to derive accurate and precise impact parameters and position angles. The final galaxy models allowed us to derive broad-band photometric magnitudes; stellar masses; and half-light radii. The main sample-results can be summarised as follows:

- Our sample spans a large range in stellar mass, with $\log_{10}[M_{\star} (M_{\odot})] \sim 8 - 10.5$. Compared to luminosity-selected samples at similar redshifts, the absorption selections probes a broader range, particularly extending to lower stellar masses.
- Combined with half-light radii which fall in the range $r_{1/2} \sim 0.5 - 2.5$ kpc, our sample is consistent with the mass-size relation of luminosity-selected samples at $z = 2.25$; and appears preferentially similar to late-type galaxies.
- Combined with SFR estimates ($\lesssim 30 M_{\odot} \text{ yr}^{-1}$) based on spectroscopic H α - and SED-based measurements, our sample is consistent with the star forming main sequence derived for luminosity-selected samples at the same redshift.

Albeit a small sample-size, our results suggest that at redshift 2 – 3, a gas cross-section selection selects normal, gas-rich, late-type, star forming galaxies. Previously, an analysis of a smaller sample size of strong absorption selected galaxies revealed that these galaxies are consistent with being sampled at the faint end of the Lyman-break galaxies (Møller et al. 2002). With the addition of known stellar masses, we have demonstrated that absorption selected galaxies follow known scaling relations if extrapolated to even lower masses as sampled from luminosity selections.

NHPR and LC are supported by the Independent Research Fund Denmark (DFR - 4090-00079). KEH acknowledges support by a Project Grant (162948-051) from The Icelandic Research Fund.

Facilities: *HST*(WFC3), *VLT*(FORs1), *VLT*(X-Shooter)

Software: This research has made use of the SIMBAD database, operated at CDS, Strasbourg, France (Wenger et al. 2000). Astropy (Astropy Collaboration et al. 2013), Photutils (Bradley et al. 2016), Matplotlib (Hunter 2007), Drizzlepac (STSCI Development Team 2012).

REFERENCES

- Abbott, T. M., Aspin, C., Sorensen, A. N., et al. 2000, in Proc. SPIE, Vol. 4008, Optical and IR Telescope Instrumentation and Detectors, ed. M. Iye & A. F. Moorwood, 714-719
- Appenzeller, I., Fricke, K., Fürtig, W., et al. 1998, The Messenger, 94, 1
- Arnouts, S., Cristiani, S., Moscardini, L., et al. 1999, MNRAS, 310, 540, doi: [10.1046/j.1365-8711.1999.02978.x](https://doi.org/10.1046/j.1365-8711.1999.02978.x)
- Astropy Collaboration, Robitaille, T. P., Tollerud, E. J., et al. 2013, A&A, 558, A33, doi: [10.1051/0004-6361/201322068](https://doi.org/10.1051/0004-6361/201322068)
- Augustin, R., Péroux, C., Møller, P., et al. 2018, MNRAS, doi: [10.1093/mnras/sty1287](https://doi.org/10.1093/mnras/sty1287)
- Bashir, W., Zafar, T., Khan, F. M., & Chishtie, F. 2019, New Astronomy, 66, 9, doi: [10.1016/j.newast.2018.07.001](https://doi.org/10.1016/j.newast.2018.07.001)
- Berg, T. A. M., Ellison, S. L., Sánchez-Ramírez, R., et al. 2016, MNRAS, 463, 3021, doi: [10.1093/mnras/stw2232](https://doi.org/10.1093/mnras/stw2232)
- Berry, M., Somerville, R. S., Gawiser, E., et al. 2016, MNRAS, 458, 531, doi: [10.1093/mnras/stw231](https://doi.org/10.1093/mnras/stw231)
- Bouché, N., Murphy, M. T., Kacprzak, G. G., et al. 2013, Science, 341, 50, doi: [10.1126/science.1234209](https://doi.org/10.1126/science.1234209)
- Bouché, N., Murphy, M. T., Péroux, C., et al. 2012, MNRAS, 419, 2, doi: [10.1111/j.1365-2966.2011.19500.x](https://doi.org/10.1111/j.1365-2966.2011.19500.x)
- Bradley, L., Sipocz, B., Robitaille, T., et al. 2016, Photutils: Photometry tools, Astrophysics Source Code Library. <http://ascl.net/1609.011>
- Bruzual, G., & Charlot, S. 2003, MNRAS, 344, 1000, doi: [10.1046/j.1365-8711.2003.06897.x](https://doi.org/10.1046/j.1365-8711.2003.06897.x)
- Calzetti, D., Armus, L., Bohlin, R. C., et al. 2000, ApJ, 533, 682, doi: [10.1086/308692](https://doi.org/10.1086/308692)
- Cappetta, M., D’Odorico, V., Cristiani, S., Saitta, F., & Viel, M. 2010, MNRAS, 407, 1290, doi: [10.1111/j.1365-2966.2010.16981.x](https://doi.org/10.1111/j.1365-2966.2010.16981.x)
- Cashman, F. H., Kulkarni, V. P., Kisielius, R., Ferland, G. J., & Bogdanovich, P. 2017, ApJS, 230, 8, doi: [10.3847/1538-4365/aa6d84](https://doi.org/10.3847/1538-4365/aa6d84)
- Chabrier, G. 2003, PASP, 115, 763, doi: [10.1086/376392](https://doi.org/10.1086/376392)
- Christensen, L., Møller, P., Fynbo, J. P. U., & Zafar, T. 2014, MNRAS, 445, 225, doi: [10.1093/mnras/stu1726](https://doi.org/10.1093/mnras/stu1726)
- Crighton, N. H. M., Murphy, M. T., Prochaska, J. X., et al. 2015, MNRAS, 452, 217, doi: [10.1093/mnras/stv1182](https://doi.org/10.1093/mnras/stv1182)
- Fynbo, J. P. U., Prochaska, J. X., Sommer-Larsen, J., Dessauges-Zavadsky, M., & Møller, P. 2008, ApJ, 683, 321, doi: [10.1086/589555](https://doi.org/10.1086/589555)
- Fynbo, J. P. U., Laursen, P., Ledoux, C., et al. 2010, MNRAS, 408, 2128, doi: [10.1111/j.1365-2966.2010.17294.x](https://doi.org/10.1111/j.1365-2966.2010.17294.x)
- Fynbo, J. P. U., Ledoux, C., Noterdaeme, P., et al. 2011, MNRAS, 413, 2481, doi: [10.1111/j.1365-2966.2011.18318.x](https://doi.org/10.1111/j.1365-2966.2011.18318.x)
- Fynbo, J. P. U., Geier, S. J., Christensen, L., et al. 2013, MNRAS, 436, 361, doi: [10.1093/mnras/stt1579](https://doi.org/10.1093/mnras/stt1579)
- Hartoog, O. E., Fynbo, J. P. U., Kaper, L., De Cia, A., & Bagdonaite, J. 2015, MNRAS, 447, 2738, doi: [10.1093/mnras/stu2578](https://doi.org/10.1093/mnras/stu2578)
- Hayes, M., Östlin, G., Schaerer, D., et al. 2010, Nature, 464, 562, doi: [10.1038/nature08881](https://doi.org/10.1038/nature08881)
- Hunter, J. D. 2007, Computing In Science & Engineering, 9, 90, doi: [10.1109/MCSE.2007.55](https://doi.org/10.1109/MCSE.2007.55)
- Ilbert, O., Arnouts, S., McCracken, H. J., et al. 2006, A&A, 457, 841, doi: [10.1051/0004-6361:20065138](https://doi.org/10.1051/0004-6361:20065138)
- Kanekar, N., Prochaska, J. X., Christensen, L., et al. 2018, ApJL, 856, L23, doi: [10.3847/2041-8213/aab6ab](https://doi.org/10.3847/2041-8213/aab6ab)
- Kashikawa, N., Misawa, T., Minowa, Y., et al. 2014, ApJ, 780, 116, doi: [10.1088/0004-637X/780/2/116](https://doi.org/10.1088/0004-637X/780/2/116)
- Kashikawa, N., Aoki, K., Asai, R., et al. 2002, PASJ, 54, 819, doi: [10.1093/pasj/54.6.819](https://doi.org/10.1093/pasj/54.6.819)
- Komatsu, E., Smith, K. M., Dunkley, J., et al. 2011, ApJS, 192, 18, doi: [10.1088/0067-0049/192/2/18](https://doi.org/10.1088/0067-0049/192/2/18)
- Krogager, J.-K. 2018, ArXiv e-prints. <https://arxiv.org/abs/1803.01187>
- Krogager, J.-K., Fynbo, J. P. U., Møller, P., et al. 2012, MNRAS, 424, L1, doi: [10.1111/j.1745-3933.2012.01272.x](https://doi.org/10.1111/j.1745-3933.2012.01272.x)
- Krogager, J.-K., Møller, P., Fynbo, J. P. U., & Noterdaeme, P. 2017, MNRAS, 469, 2959, doi: [10.1093/mnras/stx1011](https://doi.org/10.1093/mnras/stx1011)
- Krogager, J.-K., Fynbo, J. P. U., Ledoux, C., et al. 2013, MNRAS, 433, 3091, doi: [10.1093/mnras/stt955](https://doi.org/10.1093/mnras/stt955)
- Kulkarni, V. P., Hill, J. M., Schneider, G., et al. 2000, ApJ, 536, 36, doi: [10.1086/308904](https://doi.org/10.1086/308904)

- Laursen, P., Razoumov, A. O., & Sommer-Larsen, J. 2009, *ApJ*, 696, 853, doi: [10.1088/0004-637X/696/1/853](https://doi.org/10.1088/0004-637X/696/1/853)
- Le Fèvre, O., Saisse, M., Mancini, D., et al. 2003, in *Proc. SPIE*, Vol. 4841, Instrument Design and Performance for Optical/Infrared Ground-based Telescopes, ed. M. Iye & A. F. M. Moorwood, 1670–1681
- Lopez, S., Reimers, D., D’Odorico, S., & Prochaska, J. X. 2002, *A&A*, 385, 778, doi: [10.1051/0004-6361:20020181](https://doi.org/10.1051/0004-6361:20020181)
- López, S., D’Odorico, V., Ellison, S. L., et al. 2016, *A&A*, 594, A91, doi: [10.1051/0004-6361/201628161](https://doi.org/10.1051/0004-6361/201628161)
- Modigliani, A., Goldoni, P., Royer, F., et al. 2010, in *Proc. SPIE*, Vol. 7737, Observatory Operations: Strategies, Processes, and Systems III, 773728
- Møller, P., Warren, S. J., Fall, S. M., Fynbo, J. U., & Jakobsen, P. 2002, *ApJ*, 574, 51, doi: [10.1086/340934](https://doi.org/10.1086/340934)
- Møller, P., Christensen, L., Zwaan, M. A., et al. 2018, *MNRAS*, 474, 4039, doi: [10.1093/mnras/stx2845](https://doi.org/10.1093/mnras/stx2845)
- Noterdaeme, P., Petitjean, P., Ledoux, C., & Srianand, R. 2009a, *A&A*, 505, 1087, doi: [10.1051/0004-6361/200912768](https://doi.org/10.1051/0004-6361/200912768)
- . 2009b, *A&A*, 505, 1087, doi: [10.1051/0004-6361/200912768](https://doi.org/10.1051/0004-6361/200912768)
- Noterdaeme, P., Petitjean, P., Carithers, W. C., et al. 2012a, *A&A*, 547, L1, doi: [10.1051/0004-6361/201220259](https://doi.org/10.1051/0004-6361/201220259)
- Noterdaeme, P., Laursen, P., Petitjean, P., et al. 2012b, *A&A*, 540, A63, doi: [10.1051/0004-6361/201118691](https://doi.org/10.1051/0004-6361/201118691)
- Peng, C. Y., Ho, L. C., Impey, C. D., & Rix, H.-W. 2002, *AJ*, 124, 266, doi: [10.1086/340952](https://doi.org/10.1086/340952)
- Péroux, C., Bouché, N., Kulikarni, V. P., York, D. G., & Vladilo, G. 2012, *MNRAS*, 419, 3060, doi: [10.1111/j.1365-2966.2011.19947.x](https://doi.org/10.1111/j.1365-2966.2011.19947.x)
- Péroux, C., Dessauges-Zavadsky, M., D’Odorico, S., Kim, T.-S., & McMahon, R. G. 2003, *MNRAS*, 345, 480, doi: [10.1046/j.1365-8711.2003.06952.x](https://doi.org/10.1046/j.1365-8711.2003.06952.x)
- Prochaska, J. X., Chen, H.-W., Wolfe, A. M., Dessauges-Zavadsky, M., & Bloom, J. S. 2008, *ApJ*, 672, 59, doi: [10.1086/523689](https://doi.org/10.1086/523689)
- Prochaska, J. X., Gawiser, E., Wolfe, A. M., Castro, S., & Djorgovski, S. G. 2003, *ApJL*, 595, L9, doi: [10.1086/378945](https://doi.org/10.1086/378945)
- Prochaska, J. X., Herbert-Fort, S., & Wolfe, A. M. 2005, *ApJ*, 635, 123, doi: [10.1086/497287](https://doi.org/10.1086/497287)
- Rafelski, M., Neeleman, M., Fumagalli, M., Wolfe, A. M., & Prochaska, J. X. 2014, *ApJL*, 782, L29, doi: [10.1088/2041-8205/782/2/L29](https://doi.org/10.1088/2041-8205/782/2/L29)
- Rahmani, H., Péroux, C., Turnshek, D. A., et al. 2016, *MNRAS*, 463, 980, doi: [10.1093/mnras/stw1965](https://doi.org/10.1093/mnras/stw1965)
- Rhodin, N. H. P., Christensen, L., Møller, P., Zafar, T., & Fynbo, J. P. U. 2018, *A&A*
- Richards, G. T., Fan, X., Schneider, D. P., et al. 2001, *AJ*, 121, 2308, doi: [10.1086/320392](https://doi.org/10.1086/320392)
- Sánchez-Ramírez, R., Ellison, S. L., Prochaska, J. X., et al. 2016, *MNRAS*, 456, 4488, doi: [10.1093/mnras/stv2732](https://doi.org/10.1093/mnras/stv2732)
- Schlafly, E. F., & Finkbeiner, D. P. 2011, *ApJ*, 737, 103, doi: [10.1088/0004-637X/737/2/103](https://doi.org/10.1088/0004-637X/737/2/103)
- STSCI Development Team. 2012, DrizzlePac: HST image software, Astrophysics Source Code Library. <http://ascl.net/1212.011>
- van der Wel, A., Franx, M., van Dokkum, P. G., et al. 2014, *ApJ*, 788, 28, doi: [10.1088/0004-637X/788/1/28](https://doi.org/10.1088/0004-637X/788/1/28)
- Vanden Berk, D. E., Richards, G. T., Bauer, A., et al. 2001, *AJ*, 122, 549, doi: [10.1086/321167](https://doi.org/10.1086/321167)
- Verhamme, A., Schaerer, D., Atek, H., & Tapken, C. 2008, *A&A*, 491, 89, doi: [10.1051/0004-6361:200809648](https://doi.org/10.1051/0004-6361:200809648)
- Vernet, J., Dekker, H., D’Odorico, S., et al. 2011, *A&A*, 536, A105, doi: [10.1051/0004-6361/201117752](https://doi.org/10.1051/0004-6361/201117752)
- Warren, S. J., Møller, P., Fall, S. M., & Jakobsen, P. 2001, *MNRAS*, 326, 759, doi: [10.1046/j.1365-8711.2001.04629.x](https://doi.org/10.1046/j.1365-8711.2001.04629.x)
- Weatherley, S. J., Warren, S. J., Møller, P., et al. 2005, *MNRAS*, 358, 985, doi: [10.1111/j.1365-2966.2005.08838.x](https://doi.org/10.1111/j.1365-2966.2005.08838.x)
- Wenger, M., Ochsenbein, F., Egret, D., et al. 2000, *A&AS*, 143, 9, doi: [10.1051/aas:2000332](https://doi.org/10.1051/aas:2000332)
- Whitaker, K. E., Franx, M., Leja, J., et al. 2014, *ApJ*, 795, 104, doi: [10.1088/0004-637X/795/2/104](https://doi.org/10.1088/0004-637X/795/2/104)
- Whitaker, K. E., Franx, M., Bezanson, R., et al. 2015, *ApJL*, 811, L12, doi: [10.1088/2041-8205/811/1/L12](https://doi.org/10.1088/2041-8205/811/1/L12)
- Wolfe, A. M., Prochaska, J. X., Jorgenson, R. A., & Rafelski, M. 2008, *ApJ*, 681, 881, doi: [10.1086/588090](https://doi.org/10.1086/588090)
- Wolfe, A. M., Turnshek, D. A., Smith, H. E., & Cohen, R. D. 1986, *ApJS*, 61, 249, doi: [10.1086/191114](https://doi.org/10.1086/191114)
- Zafar, T., Møller, P., Péroux, C., et al. 2017, *MNRAS*, 465, 1613, doi: [10.1093/mnras/stw2907](https://doi.org/10.1093/mnras/stw2907)
- Zafar, T., Péroux, C., Popping, A., et al. 2013a, *A&A*, 556, A141, doi: [10.1051/0004-6361/201321154](https://doi.org/10.1051/0004-6361/201321154)
- Zafar, T., Popping, A., & Péroux, C. 2013b, *A&A*, 556, A140, doi: [10.1051/0004-6361/201321153](https://doi.org/10.1051/0004-6361/201321153)